ADDITIVES FOR ACTIVE LAYER DESIGN & TRAP PASSIVATION IN ORGANIC PHOTOVOLTAICS

A Dissertation

Presented to

The Academic Faculty

by

Marcel M. Said

In Partial Fulfillment

of the Requirements for the Degree

Doctor of Philosophy in the

School of Chemistry and Biochemistry

Georgia Institute of Technology

August 2016

ADDITIVES FOR ACTIVE LAYER DESIGN & TRAP PASSIVATION IN ORGANIC PHOTOVOLTAICS

Presented to:

Dr. Seth R. Marder, Advisor
School of Chemistry and Biochemistry
Georgia Institute of Technology

Dr. David Bucknall, Advisor
School of Engineering and Physical Sciences
Heriot-Watt University

Dr. Jean-Luc Brédas
School of Physical Science and Engineering
King Abdullah University of Science and Technology

Dr. Bernard Kippelen
School of Electrical Engineering
Georgia Institute of Technology

Dr. John R. Reynolds
School of Chemistry and Biochemistry
School of Materials Science and Engineering
Georgia Institute of Technology

Date Approved: June 19, 2016

I dedicate this thesis to my parents,

whose support of me and my dreams has never wavered

ACKNOWLEDGEMENTS

As proud as I am of the work completed in the chapters of this thesis, I am prouder still to have earned the support of so many talented and knowledgeable individuals, without whom this achievement would not have been possible. First, I would like to thank my advisor Prof. Seth Marder, who granted me the opportunity to work in his laboratory in advance of my first semester, creating and fostering my passion for the field of organic photovoltaic devices. Throughout my years under his tutelage, he has tirelessly worked to sculpt me, in my thoughts and actions, into a scientist, however difficult the transition may have been. For his efforts I am eternally grateful. Next, I would like to thank Prof. David Bucknall, who primarily introduced me to the field of material science, and whose advisement has never ceased to renew my optimism in the face of daunting and complex scientific challenges. I would also like to acknowledge Prof. Bernard Kippelen, for teaching me the fundamentals of organic photovoltaic devices and for allowing me to benefit from his facilities and the expertise of his group members when I had neither at my disposal, Prof. John Reynolds, for kindly welcoming me to work alongside his students and forming the Solid State Device Laboratory, a partnership that moved my research forward immensely, and Prof. Jean-Luc Brédas, for his invaluable guidance and discussions during my graduate career. Of course, I recognize that I benefit from the efforts of my committee members beyond our direct interactions, and so I also thank them for their continual work within the university, as well as their departments and scientific centers, such as COPE and GTPN, which has made my graduate career possible.

There are many members of the Marder group, past and present, without whom I could not have made it to this point. First, I owe a great debt of gratitude to Dr. Stephen

Barlow, who, over many discussions and reviews of my research, has helped me to build a greater understanding of the fundamental concepts behind it and how to articulate them. My thanks go to Dr. Tim Parker for his assistance in my thesis, as well as his daily efforts in keeping our laboratory functioning. I also must thank Dr. Denise Bale and Walaa Compton, as I, and certainly many others, would not have made it through graduate school without their support. I must acknowledge my close peers, Dr. Fadi Jradi, Dr. Karttikay Moudgil, Dr. Siyuan Zhang, Matthew Cooper, and Janos Simon; their passion for philosophical discussion and constructive criticism has greatly developed my capacity for critical-thinking. Additionally, I must thank Dr. Maria-Cristina Rumi, Dr. Benjamin Wunsch, Dr. Jassem Abdallah, Dr. Dun-Yen Kang, Dr. Yadong Zhang, Dr. Tissa Sajoto, Dr. Swagat Mohapatra, Dr. Yulia Getmanenko, Dr. Raghunath Dasari, Dr. Junxiang Zhang, Dr. Anthony Giordano, Dr. O'Neil Smith, Dr. Sergio Paniagua and many, many others for their instruction, support, and friendship.

My research could not have been brought to fruition without the assistance of my collaborators and others in my department. For teaching me to fabricate my first efficient photovoltaic devices, I must recognize Dr. Michael Durstock and Dr. Benjamin Leever at the Wright Patterson Air Force Base. For their assistance in the Solid State Device Laboratory and with X-ray scattering analysis, I thank Dr. Caroline Grand, Dr. Nabankur Deb, and Jeffrey Hernandez from the Reynolds and Bucknall groups. For welcoming me as a member of their group, teaching me the finer details of highly efficient organic photovoltaic devices, and for the many projects that we built together, I acknowledge Prof. Aram Amassian, Dr. Kui Zhao, Dr. Lethy Jagadamma, Guy Ngongang, Hanlin Hu, Ahmed Mansour, Ahmad Kirmani, and Rahim Munir at the King Abdullah University of Science

and Technology. I would also like to thank Dr. Cameron Tyson and Dr. Kenyetta Johnson for their invaluable guidance.

Finally, none of this would have been possible without the support of my family. The hard work and sacrifice of my parents is the sole reason that my brother and I have had the ability to pursue our goals without hardship. Mom, Dad, and Oliver, this is for you.

TABLE OF CONTENTS

ACKNOWLEDGEMENTS IV

LIST OF TABLES XI

LIST OF FIGURES XII

LIST OF ABBREVIATIONS & SYMBOLS XVIII

SUMMARY XX

CHAPTER 1 INTRODUCTION 1

1.1 Reflection on Organic Photovoltaic Devices – Theory & History 1

1.1.1 Organic Semiconductors 1

1.1.2 Foundations of Organic Photovoltaics 7

1.1.3 Electronic Processes in Organic Heterojunction Photovoltaics 10

1.1.4 Rise of the Bulk Heterojunction 16

1.1.5 Modern Techniques for Morphological Control in OPV Active Layers 20

1.2 Fundamental Techniques for Organic Photovoltaic Device and Material Characterization 22

1.2.1 Organic Photovoltaics – Device Fabrication and Measurements 22

1.2.2 Incident Photon-to-Current Conversion Efficiency 30

1.2.3 Electrical Conductivity and Mobility 33

1.2.4 Photoelectron Spectroscopy 39

1.2.5 Atomic Force Microscopy 45

1.2.6 Grazing-Incidence X-Ray Scattering & Diffraction 47

1.3 Conclusion 52

1.4 Works Cited 53

CHAPTER 2 DUAL-ACCEPTOR PERYLENE DIIMIDE TERNARY BULK HETEROJUNCTIONS IN ORGANIC PHOTOVOLTAIC DEVICES 77

2.1 Introduction 77

2.1.1 Ternary Bulk Heterojunctions in Organic Photovoltaics 77

2.1.2 Dual-Acceptor Ternary Bulk Heterojunctions 78

2.2 Methods & Results 80
2.2.1 Synthesis 80
2.2.2 Differential Scanning Calorimetry 83
2.2.3 Scanning Electron Microscopy 86
2.2.4 Grazing-Incidence Wide Angle X-ray Diffraction and Scattering 89
2.2.5 Organic Photovoltaic Devices 92
2.2.6 Atomic Force Microscopy 94
2.2.7 Electrochemical Thin Film Studies 100
2.2.8 Time-Of-Flight Electron Mobility 103
2.3 Conclusion 107
2.4 Works Cited 110
CHAPTER 3 ULTRA-LOW P-DOPING OF POLY(3-HEXYLTHIOPHENE) AND ITS IMPACT ON POLYMER AGGREGATION AND PHOTOVOLTAIC PERFORMANCE 116
3.1 Introduction 116
3.1.1 Origins of Electrical Doping 116
3.1.2 Electrical Doping in Organic Semiconductors 117
3.1.3 Electrical Doping for Trap Passivation 118
3.2 Methods & Results 122
3.2.1 Conductivity & Mobility Measurements 122
3.2.2 Ultra-violet Photoelectron Spectroscopy 129
3.2.3 Organic Photovoltaic Devices 133
3.2.4 Transmission Electron Microscopy 135
3.2.5 Atomic Force Microscopy 140
3.2.6 H-Aggregate Modelling of Absorbance Spectra 142
3.2.7 Grazing-Incidence Wide Angle X-Ray Scattering 145
3.2.8 Rutherford Backscattering 147
3.2.9 Organic Photovoltaic Devices with a Planar Dopant 151
3.3 Conclusion 153
3.4 Additional Experimental Information 153
3.5 Works Cited 155

CHAPTER 4 ULTRA-LOW P-DOPING OF LOW SHORT-RANGE ORDER POLYMERS IN EFFICIENT ORGANIC PHOTOVOLTAICS .162
4.1 Introduction 162
4.1.1 Additives in Organic Thin Film Processing 162
4.1.2 Dopants Acting as Additives in Organic Photovoltaics 163
4.2 Methods & Results 165
4.2.1 Conductivity & Mobility Measurements 165
4.2.2 Ultra-violet Photoelectron Spectroscopy 171
4.2.3 Organic Photovoltaic Devices 175
4.2.4 Atomic Force Microscopy 183
4.2.5 Grazing-Incidence Wide Angle X-Ray Scattering 186
4.3 Conclusion 188
4.4 Works Cited 190
CHAPTER 5 ZINC OXIDE INCORPORATING PENTAMETHYL-RHODOCENE DERIVATIVES AS ELECTRON-TRANSPORT LAYERS FOR HIGHLY EFFICIENT ORGANIC SOLAR CELLS 196
5.1 Introduction 196
5.1.1 Semiconducting Oxide Interlayers in Organic Electronics 196
5.1.2 Additives in Low-Temperature Solution-Processed Oxides 197
5.1.3 Molecular Dopant Incorporation into Amorphous Zinc Oxide 198
5.2 Methods & Results 199
5.2.1 ZnO Preparation 199
5.2.2 Secondary Ion Mass Spectrometry 201
5.2.3 X-ray Photoelectron Spectroscopy 205
5.2.4 Ultra-violet Photoelectron Spectroscopy 208
5.2.5 Conductivity & Mobility Measurements 211
5.2.6 Absorbance & Photoluminescence 214
5.2.7 Organic Photovoltaic Devices 219
5.2.8 Atomic Force Microscopy 228
5.3 Conclusion 230
5.4 Works Cited 232
CHAPTER 6 CONCLUSION AND OUTLOOK 240

6.1 Overview 240
6.2 Non-fullerene Acceptors in Organic Photovoltaics 241
6.3 Electrical Dopants in Organic Photovoltaic Devices 243
6.4 Amorphous Oxide Interlayers in Organic Photovoltaics 246
6.5 Outlook 248
6.6 Works Cited 249

LIST OF TABLES

Table 2.1. Device performance values of 3:2 P3HT:Polymer PDI devices with percentages of PDI addition by total acceptor mass. 94

Table 2.2. Calculated charge mobilities of thick films of PDI, Polymer PDI, and P3HT, fitted to a zero-field value. P3HT films were cast from both chlorobenzene (a) and chloroform (b). 106

Table 3.1. OFET hole mobility values of P3HT thin films doped with 0.0001 to 1% $Mo(tfd\text{-}COCF_3)_3$, pristine and annealed. V_{Th} is unreliable due to hysteresis and was not compared to avoid confusion. 127

Table 3.2. OPV performance values for ITO/PEIE/P3HT/$PC_{61}BM$/MoO_3/Ag devices p-doped with $Mo(tfd\text{-}COCF_3)_3$ at concentrations corresponding to the sub-band-emptying regime. 134

Table 3.3. OPV performance values of P3HT/$PC_{61}BM$ devices p-doped with $Ni(tfd)_2$. 152

Table 4.1. OPV performance values of p-doped PTB7 (top) and PCDTBT (bottom) cells with the acceptor $PC_{71}BM$ doped with $Mo(tfd\text{-}CO_2Me)_3$ and $Mo(tfd\text{-}COCF_3)_3$, respectively. Averages are from over 25 cells. 179

Table 5.1. Atomic ratios of relevant elements in the films with differing concentrations of n-dopant, determined by O 1s, Zn 2p, and Rh 3d XPS peaks. O/Zn atomic ratio was adjusted by signal decay through the material and corrected for oxygen contribution from the ITO substrate, uncorrected values given in parenthesis. 206

Table 5.2. Electron mobility values, threshold voltages, and On/Off ratios of the doped ZnO transistors. 213

Table 5.3. The OPV performance values of inverted PTB7/$PC_{71}BM$ device with compact ZnO doped by different concentrations as indicated. 224

Table 5.4. The photovoltaic parameters of inverted PTB7:$PC_{71}BM$ device with rippled ZnO doped by n-dopant with different concentration. 225

Table 5.5. The parameters of inverted PTB7-Th:$PC_{71}BM$ device with rippled ZnO doped by different dopant concentration. 226

LIST OF FIGURES

Figure 1.1. A representation of the Fermi Dirac distribution, density of states, and E_F for conductors, intrinsic semiconductors, and insulators at a given temperature T at thermal equilibrium. 5

Figure 1.2. A depiction of relevant junctions between conductors and semiconductors that can be observed in organic semiconductor devices. In the Schottky junction, the Schottky barrier is indicated by the two-directional arrow. 9

Figure 1.3. Solar radiation distribution is represented as irradiance as a function of wavelength. This figure compares the profiles of a 5778 K blackbody (black line), the solar constant at the edge of the atmosphere (yellow), and the solar constant after atmospheric attenuation (red). 10

Figure 1.4. (a) Energy level diagram of the staggered semiconductor heterojunction in an OPV at short-circuit. IE_D and EA_A are the ionization energy of the donor and the electron affinity of the acceptor respectively. (b) State diagram outlining relevant processes in the operation of an OPV. 14

Figure 1.5. Renderings of a planar (a) and a bulk heterojunction (b) active layer. 17

Figure 1.6. (left) A diagram of the layers in an ITO/PEDOT:PSS/P3HT:$PC_{61}BM$/Ca/Al device prepared at the Solid State Device Laboratory at the Georgia Institute of Technology, and (right) an image of that very cell, before electrode evaporation. 25

Figure 1.7. *J-V* curves from an ITO/a-ZnO/PTB7:$PC_{71}BM$/MoO_3/Ag device highlighting parameters relevant to cell efficiency. The shaded region represents the fill factor in relation to the area of a box outline is dashed red lines that would correspond to $J_{SC} \times V_{OC}$. 29

Figure 1.8. IPCE spectra from an ITO/a-ZnO/PCDTBT:$PC_{71}BM$/MoO_3/Ag device. The dashed lines indicate that at λ = 500 nm, 67% of the incoming photons are converted into electrical current. 31

Figure 1.9. Solar irradiance (left y axis) at AM 1.5, compared with maximum J_{SC} (right y axis) assuming 100% IPCE at all wavelengths lower than the given absorption onset. 33

Figure 1.10. (left) Microscope image of a prepatterned gold/ITO electrode fingers on silicon oxide over silicon beneath a pristine 50 nm P3HT film. (right) Representative *J-E* curves of PTB7 films, undoped and doped from 0.001 wt. % up to 30 wt. % of the p-dopant Mo(tfd-CO_2Me)$_3$. 36

Figure 1.11. A simple illustration of a bottom-gate bottom-contact FET, like those prepared in Chapters 3, 4, and 5. The channel forms at the interface between

the semiconductor and the dielectric, along the length between the source and drain electrodes. 39

Figure 1.12. This plot shows the calculated λ_p in nm of photoelectrons through organic materials, using constants identified by Seah *et al*. The decay of intensity I at a certain depth (x) can be expressed as $Ix = I0e - x\lambda p$ where I_0 is the intrinsic intensity. 41

Figure 1.13. A UPS spectrum of ca. 15 nm PCDTBT on ITO, corresponding to the values given in Figure 5.5. The ionizing radiation is He I (21.2 eV). *BE* is given in the Y-axis, and the X-axis corresponds to intensity in arbitrary units. 44

Figure 1.14. Atomic force microscopy topographic (left) and phase (right) images for P3HT thin films taken in tapping mode, exhibited in Chapter 2. The lamellar order of the polymer domains, absent from the topographic scan, is clearly identified in the phase scan. 46

Figure 1.15. A simplistic representation of Bragg diffraction, where d is the distance between reflecting lattice planes, and θ is the angle of incident electromagnetic radiation. 48

Figure 1.16. (left) A 2D GIWAXS pseudocolor plot for a neat P3HT film. Lamellar peaks (100, 200, 300) are identified. The red lines outline the region integrated to create the corresponding 1D plot (right). 51

Figure 2.1. Hypothetical environment of the ternary P3HT/PDI/PDI polymer blend. 79

Figure 2.2. Reaction scheme outlining the formation of the two products, *N,N'*-di(2-decyl-tetradecyl)perylenetetracarboxylic-diimide and poly{[*N,N'*-bis(2-decyl-tetradecyl)-3,4,9,10-perylenediimide-1,7-diyl]-alt-(dithieno[3,2-*b*:2',3'-*d*]thiophene-2,6-diyl)}. 82

Figure 2.3. Differential scanning calorimetry of various blends of P3HT and PDI, given in wt. % of the PDI. 84

Figure 2.4. Differential scanning calorimetry (DSC) on neat P3HT, neat small molecule PDI, neat polymer PDI, and corresponding binary and ternary blends. 86

Figure 2.5. Scanning electron microscopy images of 1:4 P3HT:PDI (left), 1:1 P3HT:PDI (middle), and 1:1 P3HT:$PC_{61}BM$ (right) films spun-cast from *o*-dichlorobenzene, at 15000× magnification. 88

Figure 2.6. Comparison of observable features in grazing-incidence wide angle X-ray scattering images of films composed of neat small molecule PDI (left), a 1:4 by weight blend of P3HT and PDI (left middle), a 1:1 by weight blend of P3HT and PDI (right middle), and neat P3HT (right). 90

Figure 2.7. X-ray diffraction of organic photovoltaic cells prepared at the Wright Patterson Air Force Base with active layers deposited from *o*-dichlorobenzene. The diffraction peaks of PDI and P3HT appear at ca. 3.0º and 5.6º respectively; Polymer PDI does not exhibit any peaks in the region observed. 92

Figure 2.8. *J-V* curves demonstrating the decrease in performance due to PDI addition to photovoltaic devices of 3:2 P3HT:Polymer PDI. 94

Figure 2.9. Phase atomic force microscopy images of films composed of a 1:1 by weight blend of P3HT and small molecule PDI (left), a 1:1:1 by weight ternary blend (middle), and a 1:1 by weight blend of P3HT and polymer PDI (right). 97

Figure 2.10. Atomic force microscopy images of a PDI:Polymer PDI film deposited from *o*-dichlorobenzene. Before annealing (left) the film is rough and stepped, but afterwards (right) it becomes much smoother. 99

Figure 2.11. Square wave voltammetry of films of PDI, Polymer PDI, and a blend of the two prepared from *o*-dichlorobenzene, pre- and post-thermal annealing. The step size was 0.05 V with a current drop of 0.1 mA. 103

Figure 2.12. Time-of-flight carrier mobility of thick films of PDI, Polymer PDI, and P3HT, fitted to a zero-field value. 106

Figure 2.13. Hypothetical representation of the blended PDI and Polymer PDI phases surrounded by P3HT domains. 108

Figure 3.1. The introduction of dopants into a semiconductor can result in a shift in the Fermi level energy and the contribution of carriers to a charge transport band, the carrier sign and specific band dependent upon the type of dopant used. 117

Figure 3.2. Structures of poly(3-hexylthiophene) and molybdenum tris[1-(trifluoromethylcarbonyl)-2-(trifluoromethyl)-ethane-1,2-dithiolene], and a schematic illustrating passivation of low-density gap states by electron transfer to a p-dopant. 120

Figure 3.3. Conductivity trends of P3HT thin films doped with 0.0001 to 1% Mo(tfd-$COCF_3)_3$. The undoped value is shown as a dotted line. 124

Figure 3.4. An example of hysteresis in P3HT FETs deposited from chlorobenzene. 125

Figure 3.5. OFET hole mobility trends of P3HT thin films doped with 0.0001 to 1% Mo(tfd-$COCF_3)_3$, pristine and annealed. The undoped value is indicated by the dotted line. 127

Figure 3.6. OFET hole mobility trends of P3HT thin films prepared from toluene, doped with 0.001 to 0.1% Mo(tfd-$COCF_3$)$_3$. 129

Figure 3.7. (left) Tabulated work functions and ionization energies of P3HT films doped at ultra-low concentrations. Undoped values are indicated by dotted lines. (right) Semi-logarithmic plots of the evolution of the work function and the valence band/Fermi level difference at ultra-low doping concentrations. 131

Figure 3.8. He(I) UPS spectra showing the region between the valence-band onset and the Fermi level. 132

Figure 3.9. *J-V* curves for ITO/PEIE/P3HT/$PC_{61}BM$/MoO_3/Ag devices p-doped with Mo(tfd-$COCF_3$)$_3$ at concentrations corresponding to the sub-band-emptying regime. 134

Figure 3.10. Transmission electron microscopy scans of undoped, 1%, and 5% doped P3HT films, spun-cast on UV ozone-cleaned glass then floated on water and collected on a Ni TEM grid. 138

Figure 3.11. Energy dispersive spectrum during transmission electron microscopy, focused on a dopant aggregate inside a 5% p-doped P3HT film. 139

Figure 3.12**.** Atomic force microscopy height scans for pristine and 0.1 wt% Mo(tfd-$COCF_3$)$_3$-doped P3HT thin films, a) and b) respectively. The phase scans for the same regions are given in c) and d). 141

Figure 3.13. (left) Free-exciton bandwidth and fraction of aggregates estimated from UV-vis spectra for p-doped films of P3HT. Values for pristine films are displayed with dotted lines. (right) An example of H-aggregate fitting of the absorption spectrum of an undoped P3HT film. 143

Figure 3.14. Free-exciton bandwidth and fraction of aggregates estimated from UV-vis spectra for annealed p-doped films of P3HT. Values for undoped films are indicated with dotted lines. 145

Figure 3.15. 1D GIWAXS patterns for P3HT doped with various wt. % of Mo(tfd-$COCF_3$)$_3$. The region near the (010) feature is shown in the inset. 147

Figure 3.16. Rutherford backscattering spectra focusing on the Fluorine, Sulfur, and Molybdenum regions of undoped and doped P3HT films on glass. 150

Figure 3.17. *J-V* curves of P3HT/$PC_{61}BM$ devices p-doped with Ni(tfd)$_2$. 152

Figure 4.1. Structures and relevant energy levels of PTB7 (far left), Mo(tfd-CO_2Me)$_3$ (middle left), Mo(tfd-$COCF_3$)$_3$ (middle right), and PCDTBT (far right). 165

Figure 4.2. Hole mobility values of Mo(tfd-$CO_2Me)_3$-doped PTB7 upon the introduction of the p-dopant from concentrations of ca. 0.001 to 1 wt. %. The undoped value is indicated by the dotted line. 167

Figure 4.3. Conductivity evolutions of Mo(tfd-$CO_2Me)_3$-doped PTB7 and Mo(tfd-$COCF_3)_3$ PCDTBT upon the introduction of the respective p-dopants down to concentrations of ca. 0.001 wt. %. The undoped values are given by dotted lines. 168

Figure 4.4. Comparison of the conductivity evolutions of PCDTBT with the p-dopants Mo(tfd-$CO_2Me)_3$ and Mo(tfd-$COCF_3)_3$. The lower *EA* of Mo(tfd-$CO_2Me)_3$ restricts its ability to passivate the traps of the high *IE* polymer, observable from the very slight improvement in conductivity. The undoped value is indicated by the dotted line. 170

Figure 4.5. Conductivity values of Mo(tfd-$CO_2Me)_3$-doped PTB7 upon the introduction of the p-dopant from concentrations of ca. 0.001 to 30 wt. %. The undoped value is given by a dotted line. 171

Figure 4.6. Work function and ionization energy evolution of PTB7 (left) and PCDTBT (right) upon the introduction of p-dopants Mo(tfd-$CO_2Me)_3$ and Mo(tfd-$COCF_3)_3$, respectively, from concentrations of ca. 0.02 to 1 wt. %, determined by UPS. Undoped values are represented by dotted lines. 174

Figure 4.7. *J-V* curves of p-doped PTB7 (left) and PCDTBT (right) OPV cells with the acceptor $PC_{71}BM$ doped with Mo(tfd-$CO_2Me)_3$ and Mo(tfd-$COCF_3)_3$, respectively. 178

Figure 4.8. IPCE spectra of PTB7 (left) and PCDTBT (right) OPV cells with the acceptor $PC_{71}BM$, doped with varied concentrations of Mo(tfd-$CO_2Me)_3$ and Mo(tfd-$COCF_3)_3$ respectively. 180

Figure 4.9. *J-V* curves (left) and IPCE (right) of PCDTBT:$PC_{71}BM$ OPV cells doped with various concentrations of Mo(tfd-$CO_2Me)_3$. 182

Figure 4.10. Atomic force microscopy topography (left) and phase (right) images of PTB7 films with 0, 0.01, 0.1, and 1 wt. % Mo(tfd-$CO_2Me)_3$. 184

Figure 4.11. Atomic force microscopy topography (left) and phase (right) images of PCDTBT films with 0, 0.01, 0.1, and 1 wt. % Mo(tfd-$COCF_3)_3$. 185

Figure 4.12. GIWAXS images of PTB7 (top) and PCDTBT (bottom) films on silicon wafers p-doped with relevant concentrations of Mo(tfd-$CO_2Me)_3$ and Mo(tfd-$COCF_3)_3$ respectively. 188

Figure 5.1. Thermogravimetric analysis of $[RhCp^*Cp]_2$ at 10 °C min^{-1}. 201

Figure 5.2. SIMS data showing (a) the Rh^+ signal intensity measured for ZnO films as a function of the rhodium concentration in the (zinc oxide precursor + dopant) solution and (b) depth profiling of a thin ZnO layer deposited from the solution containing 10^{-3} mg/mL of dopant. 203

Figure 5.3. Mass spectra recorded for four thin layers produced using solutions of zinc oxide mixed with rhodium at concentration ranging from 10^{-1} down to 10^{-4} M. 204

Figure 5.4. Evolution of the Rh 3d peaks is observed in the higher concentration samples. 207

Figure 5.5. (left) Work-function and ionization-energy trends in ZnO films prepared with various concentrations of n-dopant. (right) Secondary cut-off edges illustrating the shift in work function with various concentrations of n-dopant. 210

Figure 5.6. Electron mobility and conductivity values of ZnO with different concentration of dopant (as indicated) by bottom gate/bottom contact thin film filed effect transistor. 213

Figure 5.7. UV-Vis absorption spectra of thin, compact (left) and thick, rippled (right) ZnO doped by different concentration (mg/mL) as indicated. 215

Figure 5.8. (left) Photoluminescence spectra of ZnO thin films containing molecular dopants. (right) Decay of the long-lived green photoluminescence (580 nm) of ZnO films with various dopant concentrations. 218

Figure 5.9. Chemical structure of (a) PTB7 polymer, (b) PTB7-Th polymer, (c) $PC_{71}BM$ fullerene and (d) the $[RhCp^*Cp]_2$ n-dopant. (e) Device architecture showing different functional layers and (f) estimated energy-level diagram of materials used in inverted BHJ device configurations. 220

Figure 5.10. The *J-V* characteristics (a) and EQE (b) of inverted PTB7/$PC_{71}BM$ device with compact ZnO doped by different concentrations as indicated. 223

Figure 5.11. *J-V* curves and device characteristics from doping of ZnO interlayers in PTB7/$PC_{71}BM$ OPVs with cobaltocene (left) and tetramethylammonium chloride (right). 227

Figure 5.12. AFM (1×1 μm) images of compact ZnO with dopant concentration (mg/mL) as indicated. 229

Figure 5.13. AFM (5×5 μm) images of rippled ZnO, (a) without and (b) with 10^{-1} mg/mL dopant. 230

LIST OF ABBREVIATIONS & SYMBOLS

g	Density of states
K	Kelvin
C	Celsius
E_F	Fermi level energy
Φ	Work function
k_B	Boltzmann's constant
T	Temperature
σ	Electrical onductivity
μ	Electrical mobility
h	Planck's constant
VB	Valence band
CB	Conduction band
EA	Electron Affinity
IE	Ionization Energy
D	Donor
A	Acceptor
HOMO	Highest occupied molecular orbital
LUMO	Lowest unoccupied molecular orbital
λ	Wavelength
W	Watts
mW	Milliwatts
^{o}	Degrees
AM 1.5	Air Mass 1.5
BE	Binding energy
KE	Kinetic energy
ε_r	Dielectric constant
q	Charge
vis.	Visible
UV	Ultra-violet
OPV	Organic photovoltaic device
FET	Field-effect transistor
TOF	Time-of-flight
PCE	Power conversion efficiency
IPCE	Incident photon-to-current conversion efficiency
I	Current
J	Current density
V	Voltage
E	Electric Field
J_{SC}	Short-circuit current density
V_{OC}	Open-circuit voltage
FF	Fill factor
CT	Charge transfer
CS	Charge separated

BHJ	Bulk heterojunction
DSC	Differential scanning calorimetry
UPS	Ultra-violet photoelectron spectroscopy
XPS	X-ray photoelectron spectroscopy
UHV	Ultra high vacuum
AFM	Atomic force microscopy
GIWAXS	Grazing-incidence wide angle X-ray scattering
min	Minutes
s	Seconds
et al.	*Et alia*
mol	Mole
mmol	Millimole
g	Gram
mg	Milligram
PDI	Perylene diimide
PL	Photoluminescence
EQE	External quantum efficiency
Abs.	Absorbance
a.u.	Arbitrary units
V	Volts
mV	Millivolts
eV	Electronvolts
meV	Millielectronvolts
mA	Milliamperes
m	Meters
cm	Centimeters
cm^{-1}	Wavenumber
ITO	Indium-Tin oxide
a-ZnO	Amorphous zinc oxide
µm	microns
nm	nanometers
Å	Ångström
vs.	versus
π	Pi
M	mol/L
L	Liter
mL	Milliliter
Hz	Hertz
ca.	Circa
FeCp	Ferrocene

Other abbreviations are explained in the text.

SUMMARY

This dissertation explores the employment of solid additives in organic photovoltaic devices with the goal of customizing the electronic properties of the semiconducting materials, as well as the morphological effects of their introduction into active layer bulk heterojunctions. The outcomes of additive introduction are characterized primarily by photovoltaic device measurements, photoelectron spectroscopy, scanning probe microscopy, and X-ray diffraction techniques; other methods are implemented in certain projects, and are explained within the respective chapters they are applied. Ternary blend active layers, where a new component is added as a method of additive-based morphological control in an attempt to improve electron transport through non-fullerene acceptor domains, is the focus of Chapter 2. Chapters 3 and 4 involve the use of molecular dopants for trap passivation with common donor homopolymers and heteropolymers, respectively, within the active layer, and probes their ability to be dispersed with the local order of the system. Finally, Chapter 5 describes the introduction of molecular dopants into an amorphous inorganic charge-transport interlayer, with unexpected effects on oxide composition and device performance.

CHAPTER 1 **INTRODUCTION**

1.1 Reflection on Organic Photovoltaic Devices – Theory & History

The first bisection of this chapter seeks to introduce the field of organic photovoltaics to the reader through a brief history of organic semiconductors, accompanied by a discussion of semiconductor theory to complement the account with relevant concepts. The focus then moves on to the photovoltaic effect and early photovoltaic devices, before addressing the inception of the organic heterojunction photovoltaic device and processes that occur within it. Finally, this section details the origin of the bulk heterojunction and its influence on OPV development, including techniques for morphological control, which leads to the topic of this thesis: additives for active layer design and trap passivation in organic photovoltaics.

1.1.1 Organic Semiconductors

In December 1956, King Gustaf VI presented William Bradford Shockley, John Bardeen, and Walter Houser Brattain with the Nobel Prize in Physics "for their researches on semiconductors and their discovery of the transistor effect". That same year, American chemist Martin Pope was adjusting to a transition into an academic career at New York University under the direction of Hartmut Kallmann, an eminent German physicist. In just a few years, their work together would bring the semiconductor field to a new era, beginning with the discovery that organic molecules can behave as semiconductors in 1960, when they observed hole current flowing through an anthracene crystal in contact with a positively-biased electrolyte.[1,2] This

work opened the door for a number of new fields under the umbrella of organic electronics, involving the use of semiconducting and conducting organic polymers and small molecules.

Electrically, solid-state materials can be considered to fall within one of three classes depending on their electrical conductivity (σ): insulators, semiconductors, or conductors. σ quantifies the ability of a solid to conduct electrical current under an external bias, and can be expressed as:

$$\sigma = nq\mu \qquad \text{Equation 1.1}$$

where n is the number density of free carriers, *i.e.*, the number of carriers in a given volume, q is the carrier charge, and μ is the charge mobility. μ quantifies the rapidity with which a charge carrier can move through a material under an electric field, which is elaborated upon in Section 1.2.3. n is the product of the density of allowed states, $g(\in)$, and the probability of their occupation, $f(\in)$, known as the Fermi-Dirac probability function, given in Equation 1.2. Fermi-Dirac statistics are employed to allow the approximation of the behavior of identical particles in systems with large numbers of particles and states. The particles that obey these statistics are called fermions, such as electrons and electron vacancies, the latter of which are commonly referred to as holes.

In inorganic materials such as metals, silicon, and certain metal oxides, high order can lead to a high $g(\in)$, that is, a large density of contributing, closely spaced energy levels with overlapping wavefunctions, that can be called an energy band. In amorphous organic materials, disorder in the solid state can lead to $g(\in)$ distributions that resemble bands, and are sometimes inappropriately referred to as such, but do not participate in band-like transport, as is described later on. Due to basic thermodynamics, electrons occupy the lowest energy levels that are available; the energy up to which these levels are occupied at 0 K is called the Fermi level energy

(E_F). The energy required to move an electron from E_F to vacuum, the energy of an electron at rest out of the electrostatic influence of the bulk material (E_{VAC}), is called the work function (Φ). At temperatures above absolute zero, the states above and below E_F are respectively occupied and unoccupied in a way such that levels at E_F have an equal probability of being full or empty at any given time under thermodynamic equilibrium, described by:[3]

$$f(\in) = \frac{1}{e^{(\in - E_F)/k_B T} + 1} \qquad \text{Equation 1.2}$$

Here $\in$ is the energy of the state, T is temperature, and k_B is Boltzmann's temperature-energy relation constant. As energy levels near the Fermi level energy will have a higher probability of carrier occupation, the proximity of E_F, energetically, to energy bands (or high g regions) and gaps plays a primary role in determining a material's conductivity and its class.

While for a conductor E_F is located within a band, seen later in Figure 1.1, and thus n is relatively large, in non-degenerate semiconductors and insulators it is situated in a gap between two bands, and the populations of states proximate to E_F, and therefore with a high probability of carrier occupation, is lower, as is n. For these latter systems, the highest lying band below E_F is called the valence band (VB), and the lowest lying band above is the conduction band (CB), though in a highly doped, degenerate semiconductor (where the Fermi level energy is within $3k_BT$ of a band edge), E_F can be located just within one of these bands. VB and CB have energy level distributions that tail into the energy gap; the energy difference between vacuum and the valence band maximum (E_{VB}) is defined as the ionization energy (IE), equivalent to the energy absorbed upon the removal of an electron from the material, and for the conduction band minimum (E_{CB}) is the electron affinity (EA), equivalent to the energy released upon the addition of an electron to the material. While these gaps are defined as being

devoid of states, in real materials there can be some low densities present. The origin of these gap, or trap states is discussed in later sections.

Therefore, for a semiconductor the number densities of electrons in the conduction band and holes in the valence band, respectively, in thermal equilibrium are given by:

$$n_0 = \int_{E_{CB}}^{\infty} g_{CB}(\in) f(\in) d \in \cong N_{CB} e^{E_F - E_{CB}/k_B T} \qquad \text{Equation 1.3}$$

$$p_0 = \int_{-\infty}^{E_{VB}} g_{VB}(\in)(1 - f(\in)) d \in \cong N_{VB} e^{E_{VB} - E_F/k_B T} \qquad \text{Equation 1.4}$$

where $g_{CB}(\in)$ and $g_{VB}(\in)$ are the densities of states in the conduction and valence bands, respectively, and N_{CB} and N_{VB} are the effective densities of states in each band when the Fermi-Dirac function is replaced by the simpler Maxwell-Boltzmann distribution function, which can be applied for non-degenerate semiconductors. In an intrinsic semiconductor, which is a pure, undoped semiconductor, carriers arise only from thermal excitation from the valence band to the conduction band, and therefore $n_0 = p_0$ as each free electron will have a corresponding free hole. The hole and electron densities can then be identified as the intrinsic carrier density (n_i), which can be expressed through the root of the mass action law as:

$$n_i = \sqrt{n_0 p_0} = \sqrt{N_{CB} N_{VB}} e^{-E_G/2k_B T} \qquad \text{Equation 1.5}$$

This expression reveals a dependence on the energy gap $E_G = E_{CB} - E_{VB}$, as E_F drops out of the equation, and for static effective densities of states a lower E_G corresponds to a higher n_i. This leads to a basic understanding of a semiconductor as exhibiting a smaller energy gap than an insulator, as the higher intrinsic carrier densities will often lead to a greater electrical conductivity, although this distinction does not

take carrier mobility or doping into account. This simple distinction of intrinsic semiconductors and insulators is illustrated in Figure 1.1.

Electrical doping of a semiconductor, which often involves the intentional or unintentional introduction of foreign atoms or molecules into the solid, can shift the Fermi level energy towards to E_{VB} or $E_{CB,}$ increasing the number density of one carrier relative to the other. Semiconductors can be doped into degeneracy, exhibiting very high conductivities. Further discussions of carrier transport and doping are continued in later sections.

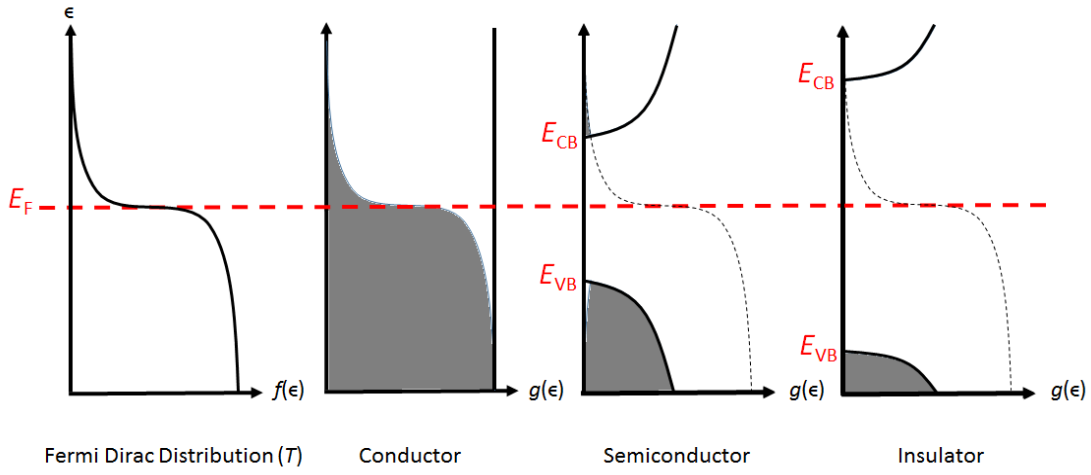

Figure 1.1. A representation of the Fermi Dirac distribution, density of states, and E_F for conductors, intrinsic semiconductors, and insulators at a given temperature T at thermal equilibrium. The vertical axis is energy while the horizontal axis is the probability of state occupancy on the left, or the density of states in the three examples on the right; $f(\epsilon)$ is superimposed on these plots in order to convey occupancy probabilities. Grey represents electron occupancy at thermodynamic equilibrium while white indicates vacancy.

Though partially conductive polyaniline was first synthesized by Henry Letheby in 1862,[4] the true potential of organic materials as electronic materials was not realized until the 1960s and 1970s.[5,6] Returning to New York, Pope and Kallmann, along with Mizuka Sano, observed electroluminescence from organic crystals in 1965,[7]

a precedent that led to the application of organics as the active component in semiconducting electronic devices, including organic light-emitting diodes (OLEDs), organic thin-film transistors (OTFTs), and organic photovoltaics (OPVs), which will be discussed in the next sections.[8–10] At around the same time, polypyrroles, prepared from tetraiodopyrrole, with conductivities up to 1 S/cm were observed by Weiss and coworkers in 1963,[11–13] paving the way for the work of Alan G. MacDiarmid, Alan J. Heeger, and Hideki Shirakawa on conductive polymers, which would earn them the Nobel Prize in Chemistry in 2000.

Conducting and semiconducting organic materials owe their electron transport to conjugated sp^2 carbon atoms. While engaging in three sigma bonds that typically occupy a plane intercepting the nucleus, a final electron is located in a delocalized p orbital orthogonally from the others. For conjugated polymers and single molecules of a similar dimensionality, neighboring p orbitals form delocalized molecular orbitals in a quasi-1-dimensional fashion, along the backbone (though in planar conjugated molecules it can be considered 2-dimensional). In solids, depending on the ordering of the molecules, intermolecular overlap can extend the dimensionality of this conjugation. The overlap of these orbitals between proximate molecules is the basis of charge transport in organic materials. This is in contrast to inorganic materials where charge transport is often isotropic, each atom contributing valence electrons to a much denser "sea" of electrons. High order and strong orbital overlap in many inorganic lattices results in carrier delocalization over many repeat units of the crystal and large charge carrier mobilities, while disorder in amorphous organic packing structures forces carriers to engage in intermolecular hopping as a primary method of transport.[14] As they do not engage in band-like transport, for organic molecules we call the equivalent of the valence band maximum the highest occupied molecular orbital

(HOMO) and that of the conduction band minimum as the lowest unoccupied molecular orbital (LUMO). These concepts will be expanded in later sections.

A neutral conjugated polymer can act as an insulator, or a semiconductor under an applied bias, as the size of the energy gap can hinder the number density of charge carriers and the conductivity. However, similar to inorganic materials, reduction or oxidation of the polymer, whether intentional or otherwise, can introduce mobile charges to the energy bands, vastly increasing charge mobility and conductivity. This electrical doping can increase σ up to 0.1 S/cm for many polymers at low dopant loading (<1 %) and, for certain polymers such as polyacetylene doped with iodine, over 10 kS/cm.[15–18] Further discussions of electrical doping in organic materials can be found in Chapters 3 and 4.

Another phenomenon observed by Pope and Kallmann in 1960 was the optical excitation of anthracene crystals resulting in charge injection into an adjacent electrode.[2] The sensitized photoconductivity observed in this early organic Schottky junction photodiode can be viewed as a precursor to modern organic photovoltaics.

1.1.2 Foundations of Organic Photovoltaics

In 1839, French physicist Alexandre-Edmond Becquerel observed an electric current upon the illumination of an electrochemical cell.[19] This effect was repeated in solids over four decades later, when in 1883 Charles Fritts coated selenium with gold, following the claims of selenium's photoconductivity made by Willoughby Smith a decade earlier.[20] Only two years subsequent, Shelford Bidwell discovered the root of this effect to be silver impurities within the selenium, which also happened to be one of the first known observations of doping, as will be discussed in Chapter 3.[21]

Continuing the work of Fritts, in 1888 Aleksandr Stoletov designed a solar cell based on Heinrich Hertz's research on the photoelectric effect, a phenomenon that

would be explained by Albert Einstein in 1905, earning the 1921 Nobel Prize in Physics.[22–25] The prototype for the modern solar cell did not appear until the 1940s; though Vadim Lashkaryov reported p-n junction photocells composed of cuprous oxide and silver sulfide in 1941,[26] by May of the same year Russell Ohl had already filed his patent for a "Light-sensitive electric device" detailing a modern junction semiconductor solar cell, that was later awarded in 1946.[27] Bell Laboratories demonstrated the first silicon solar cell 8 years later.[28]

To differentiate the aforementioned devices, a key aspect of the operationof a cell are material junctions. The junction points of conductors and semiconductors can have a range of behaviors, depending on the contact resistance and the energy level distributions of the two materials. A non-rectifying contact, through which current may flow symmetrically from one of the semiconductor's transport bands into the conductor or vice-versa depending on the bias, is called an ohmic contact. A non-ohmic contact does not have this symmetry due to the formation of an energetic barrier, which must be overcome for the semiconductor to inject a specific type of charge from the transport band into the metal, referred to as the Schottky barrier. As this barrier, which according to the Schottky-Mott rule is proportional to the difference between E_F of the conductor and the energy of the semiconductor's transport band, becomes sufficiently higher than the ambient thermal energy, this contact becomes rectifying in nature, exhibiting a large rectification ratio between current flow in either direction, and is known as a Schottky diode. It is worth noting that the Schottky-Mott rule is not entirely accurate, as the barrier can be heavily influenced by bonding between the two materials or by surface states on the semiconductor prior to contact,[29] making the prediction of junction type between two materials somewhat complex.

Additionally, the junction of two semiconductors can also act as a diode. The interface of two dissimilar semiconductors is called a heterojunction, and in the case of large differences in E_F can result in a p-n junction, which is discussed further in Chapter 3. Examples of these junctions are shown in Figure 1.2.

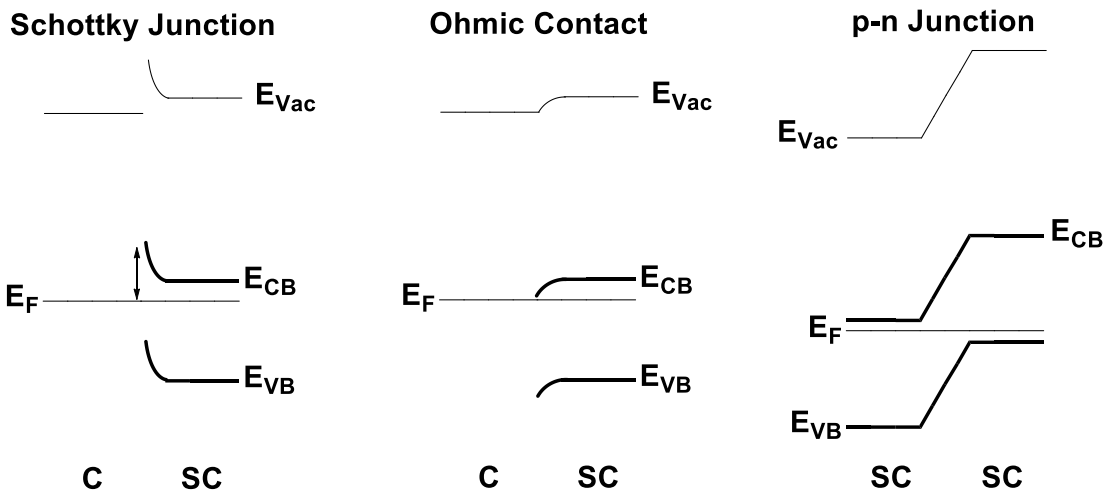

Figure 1.2. A depiction of relevant junctions between conductors and semiconductors that can be observed in organic semiconductor devices. In the Schottky junction, the Schottky barrier is indicated by the two-directional arrow.

In 1958, as silicon cells (now more efficient and marketable largely through the efforts of Les Hoffman) were making their way into orbit aboard the Vanguard I, Melvin Calvin was reporting the photovoltaic effect with organic semiconductor active layers, specifically magnesium phthalocyanine, implemented as a single layer sandwiched between two metal electrodes.[30] Though these early Schottky diode organic cells performed very poorly, several attempts were published, using conjugated polymers such as polyacetylenes or polythiophene.[31–34] It was not until 1986 that Ching W. Tang, considered to be the father of OLEDs, reported the first bilayer organic heterojunction solar cell,[35] which directed the next thirty years of research on OPVs.

1.1.3 Electronic Processes in Organic Heterojunction Photovoltaics

The function of a photovoltaic device is, by definition, the conversion of incoming light to electric power. The primary, and most practical, source of this electromagnetic radiation is our sun, which constantly outputs 1,368 W/m^2 at a distance of one astronomical unit (ca. the distance from the sun to the earth). The energy profile of this radiation, displayed in Figure 1.3, is very consistent with a blackbody at 5778 K, with an approximately 1:1 distribution between ultra-violet-visible (λ < 700 nm) and infrared (λ > 700 nm).[36,37] However, attenuation through Earth's atmosphere filters out a majority of the UV and specific absorbance bands of the atmospheric gases (observable in the infrared (IR) and near-IR), lowering the solar constant to ca. 1000 W/m^2 at the surface when considered at an angle of 48º, a standard for photovoltaic testing referred to as Air Mass 1.5 (AM 1.5).

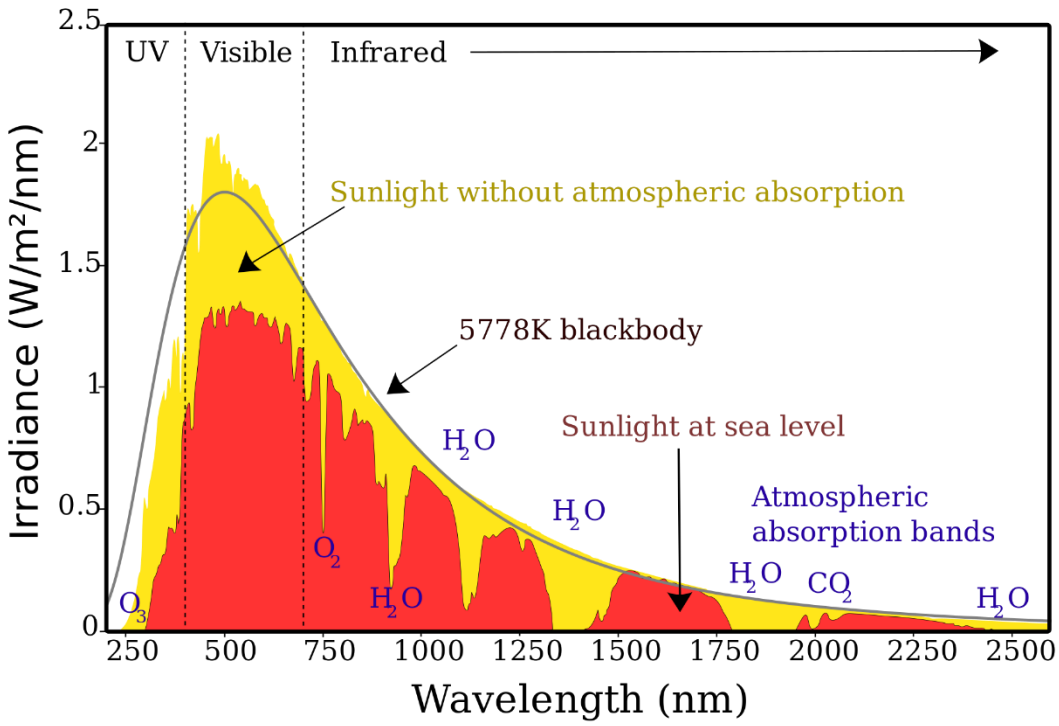

Figure 1.3. Solar radiation distribution is represented as irradiance as a function of wavelength. This figure compares the profiles of a 5778 K blackbody (black line), the solar constant at the edge of the atmosphere (yellow), and the solar constant after

atmospheric attenuation (red). Curves are adapted from references provided by the American Society for Testing and Materials (http://rredc.nrel.gov/solar/spectra/am1.5/).

Many organic semiconductors are well-suited for absorbance in the visible region, where solar irradiance, the power per area for a specific wavelength (λ), is greatest. This is governed by the size, in energy-space, of the energy gap defined in Section 1.1.1 (ca. 1.5 – 2.0 eV for organics), which can be controlled by orbital delocalization along the molecule or polymer and between molecules, if allowed by intermolecular packing.

If they are of sufficient energy, the absorption of incident photons by a semiconductor can result in the excitation of electrons in occupied energy levels, such as those in the valence band, into unoccupied levels, such as those in the conduction band. Organic semiconductors can exhibit very strong transitions, as orbital overlap between high energy occupied levels and low energy unoccupied levels can be quite significant. This transition can be considered as an excitation from one state to another; the state where electrons occupy the lowest allowed energy levels (with the occupancy of levels near the Fermi level energy in thermodynamic equilibrium dependent on the Fermi-Dirac distribution) is known as the ground state. In conjugated organic molecules this is almost always a singlet, which means that the total spin multiplicity cancels to zero, and is commonly denoted as S_0. The lowest energy allowed transition is thus to the excited state S_1, this transition accordingly resulting in a singlet exciton, which is a Coulombically bound charge pair composed of the excited electron and hole.[38] In many organic semiconducting materials, $S_0 \rightarrow S_1$ can be assumed as a transition of the electron from the HOMO to the LUMO.

Charge separation in a material, *M*, can be defined as $M^* + M \rightarrow M^+ + M^-$, where M^* is the excited material, and M^+ and M^- are the cation and anion respectively. Coulomb binding energy is essentially the energy required to overcome the electrical attraction and separate an exciton into a hole and electron, thus:

$$BE = IE_M - EA_M - E_{op} \qquad \text{Equation 1.6}$$

where E_{op} is the energy of the optical excitation. The binding energy of the exciton is partially dependent on the ability of the semiconductor to screen the Coulomb force, a factor called the dielectric constant (ε_r). For organic semiconductors this value is relatively low, ε_r ~ 3-4, compared to inorganic materials due to low polarizability, a property that can assist in electrostatic shielding of charges, resulting in binding energies on the order of hundreds of meV.[39–42] To put this into perspective, in crystalline silicon the ε_r is ~ 11.7,[43] providing low enough binding energies, ca. 15 meV,[44] that they can be overcome by thermal energy at room temperature $E = k_B T$, ca. 26 meV. As such, the separation of bound excitons in organic species would greatly benefit by forming an energetic driving force to achieve charge dissociation.

The implementation and benefit of such a driving force has shaped the field of organic photovoltaics for the last three decades. Returning to the work of Dr. Tang in 1986, layers of copper phthalocyanine and perylenetetracarboxyl-bisbenzimidazole were thermally evaporated in series, forming an organic heterojunction within the active layer. He determined that this interface was crucial for charge generation, moving exciton dissociation dependence away from the organic-metal contacts of single-layer cells. These prior cells had relied upon exciton generation near one of the metal electrodes, where the binding energy could be overcome by injection of a carrier into the metal, the other being blocked by a Schottky-type barrier and required to travel to the opposing electrode to generate current. At an organic heterojunction, the binding

energy is overcome by an energetic offset in the transport bands of the charge-donating and accepting materials, which allows the transfer and separation of electrons and holes. Accordingly, successful charge generation from both semiconductors requires a staggered gap heterojunction, with a one material having a lower *EA* and *IE*, referred to as the donor (D), and the other with a higher *EA* and *IE*, referred to as the acceptor (A). This heterojunction is visually depicted in Figure 1.4a. The energetic driving force to achieve charge dissociation, ΔG_{CS}, is derived for an exciton in D or A respectively as:

$$\Delta G_{CS}^{D^*} = IE_D - EA_A - E_{op}^D \qquad \text{Equation 1.7}$$

$$\Delta G_{CS}^{A^*} = IE_D - EA_A - E_{op}^A \qquad \text{Equation 1.8}$$

After charge separation, electrical current is generated as electrons and holes are transported to opposing electrodes by a built-in potential originating from their differing work functions, providing there is sufficient hole and electron transport in D and A, respectively.[45,46]

Overlooking exciton diffusion for the time being, the dissociation process at the heterojunction interface can be described as occurring in several stages. Immediately following electron transfer from D to A (or hole transfer from A to D) the Coulombic binding force has decreased relative to the singlet exciton, but is still prevalent. States where this force is still felt are called charge-transfer states (CT) and have a probability, based on their excess kinetic energy and environment, of recombining geminately to the S_0 state. Only when the two charges have separated to an extent that the force they exert on each other is zero, are states referred to as charge-separated (CS). Recombination of liberated charges subsequent to this step is referred to as bimolecular recombination. A depiction of these states is given in Figure 1.4b.

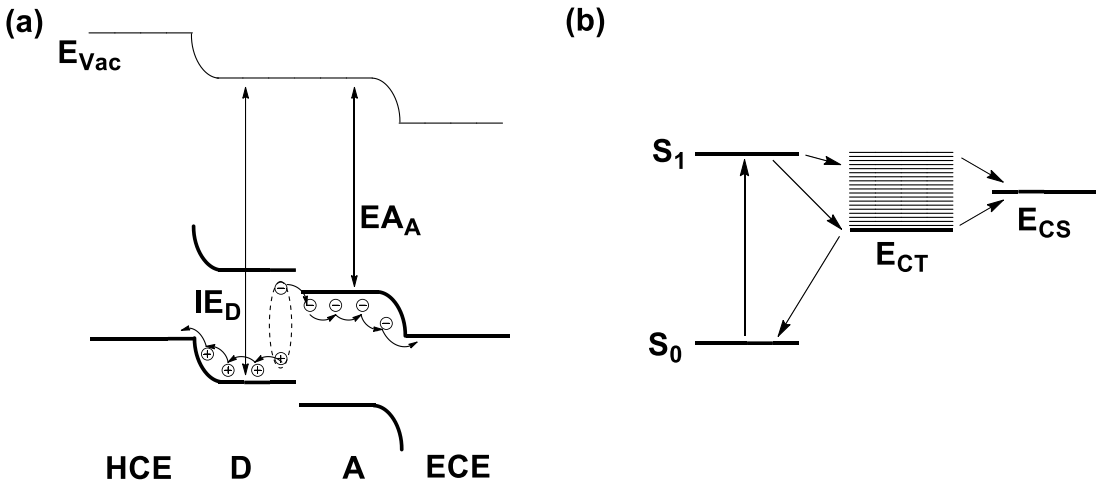

Figure 1.4. (a) Energy level diagram of the staggered semiconductor heterojunction in an OPV at short-circuit. IE_D and EA_A are the ionization energy of the donor and the electron affinity of the acceptor respectively. HCE and ECE are the hole- and electron-collecting electrodes respectively. The formation of the bound exciton in the donor is used as an example. Coloumbic binding energies are represented qualitatively in the distance from the HOMO/LUMO, and the band-bending at metal-organic contacts do not account for surface effects or energetic barriers. (b) State diagram outlining relevant processes in the operation of an OPV. The x-axis is not meant to represent physical distance. Adapted from Kippelen *et al.*[41]

The energy of CT states shown in Figure 1.4b can be estimated as $E_{CT} = (IE_D - EA_A) - \frac{q^2}{4\pi\varepsilon_r\varepsilon_0 r}$[42,47] where ε_r is the dielectric constant, ε_0 is the vacuum permittivity, and r is the distance between the electron and hole. The final term represents the Coulombic binding energy, a force that decreases linearly with distance, and as such higher lying states could be interpreted as having greater distances between the charge-carriers, with the lowest energy CT state having the electron and hole in adjacent A and D molecules. This is based on theory rooted in the work of Lars Onsager,[48] which has been applied to charge separation in OPVs to propose that freshly injected, "hot" carriers from excitons on opposing transport materials enter with excess thermal energy, allowing a thermalization distance, a, to form between the geminate charges.[49–52] Onsager proposed that charge recombination can occur within a Coulomb capture radius $r_c = \frac{q^2}{4\pi\varepsilon_r\varepsilon_0 k_B T}$ if $a < r_c$. Within this radius, the probability to achieve

charge separation becomes $P(E) = e^{-r_c/a}\left(1 + \frac{qr_c}{2k_BT}E\right)$, where E is the magnitude of the electric field. Conversely the probability for geminate recombination is 1 – $P(E)$. Since the understanding of OPVs has begun to rely on it, Onsager theory has been adjusted to account for CT state lifetimes and varied charge mobilities to improve accuracy, yielding estimations fairly consistent with experimental values.[42,50,53–55] As a note, in CS states the geminate radius r is effectively infinity, leading to an estimation of $E_{CS} = IE_D - EA_A$, where E_{CS} is the energy of the charge separated state, which becomes relevant when calculating open-circuit potentials, as will be discussed in Section 1.2.1. These liberated charges can still recombine through a process known as bimolecular recombination, which can arise due to a number of factors, including structural and energetic disorder, low carrier mobilities, poor blend morphologies (which is discussed in the next section), and trap states. These trap states lie within the energetic gap and can be the result of impurities or structural imperfections. Addressing these states is the focus of Chapters 3 and 4; this discussion is continued in those chapters.

Returning to excitons, the period between generation and dissociation / recombination is known as the lifetime, and is considered one of the major limiting factors in OPV performance. Accompanying the electron excitation comes a relaxation of local molecular structure, which in organic materials can often manifest in the shifting of conjugated C-C bond lengths to semiquinoidal structures.[40,42] In larger molecules, like polymers, this reorganization is shown to occur over a finite section of the molecule, extending up to 6 monomer units in polyphenylene vinylenes, for example, beyond which ground state bond arrangement is restored.[56] This exciton must find its way to the aforementioned heterojunction interface, hopping from site to site via what has been described as incoherent Förster energy transfer. This process lowers

the energy of the exciton with diffusion, and as such these charge-pairs can fall victim to traps (discussed further in Chapter 3).

The distance that an exciton can travel in material before relaxing back to the ground state is often referred to as the diffusion length, and for organic materials commonly employed in OPVs, such as polythiophene derivatives, can be ca. 10 nm.[57,58] If the heterojunction interface is not located within this distance, dissociation will not occur. Unfortunately, limiting film thickness of a planar heterojunction to 10 nm is not a viable option for effective light harvesting; absorption coefficients for organic semiconductors, though typically much higher than inorganics at ca. 10^5 cm^{-1} in the visible, would only result in ca. 10% absorption efficiency, severely limiting generated current.[41,59] Although some organic materials have demonstrated much larger exciton diffusion lengths, up to 70 nm for pentacene,[60] this remains an issue for a vast majority of materials implemented in OPVs. This concept was the limiting factor in the work of Ching Tang, and indeed for many bilayer planar heterojunction, and prior single layer, device configurations. The apparent solution came as a dispersed heterojunction, often called the bulk heterojunction (BHJ), beginning with the application of co-evaporated films by Masaaki Yokoyama in 1991, which was applied to solution-processing and polymers by the groups of Alan J. Heeger, Fred Wudl, Richard H. Friend, and Andrew B. Holmes in 1995.[61–63] While achieving the desired combination of interfacial area and absorbance, this technique nontrivially complicated OPV device design.

1.1.4 Rise of the Bulk Heterojunction

The bulk heterojunction, shown qualitatively in comparison to a bilayer planar heterojunction in Figure 1.5, is a mixture of D and A materials that have a variable degree of phase separation throughout the bulk of the film, where the size, order, distribution, and purity of the domains (the “microstructure”) are dependent on the

deposition method and post-processing conditions as well as on material properties such as miscibility, solubility in the given solvent, and packing. The BHJ needs to have sufficiently small domain sizes to allow for exciton diffusion to the interface, while still providing pathways through "pure" domains for hole and electron transport to their respective electrodes with sufficient mobilities. 3-dimensional morphological control is paramount to device performance, yet predicting BHJ nanostructures for new material blends remains a challenge.[64–69]

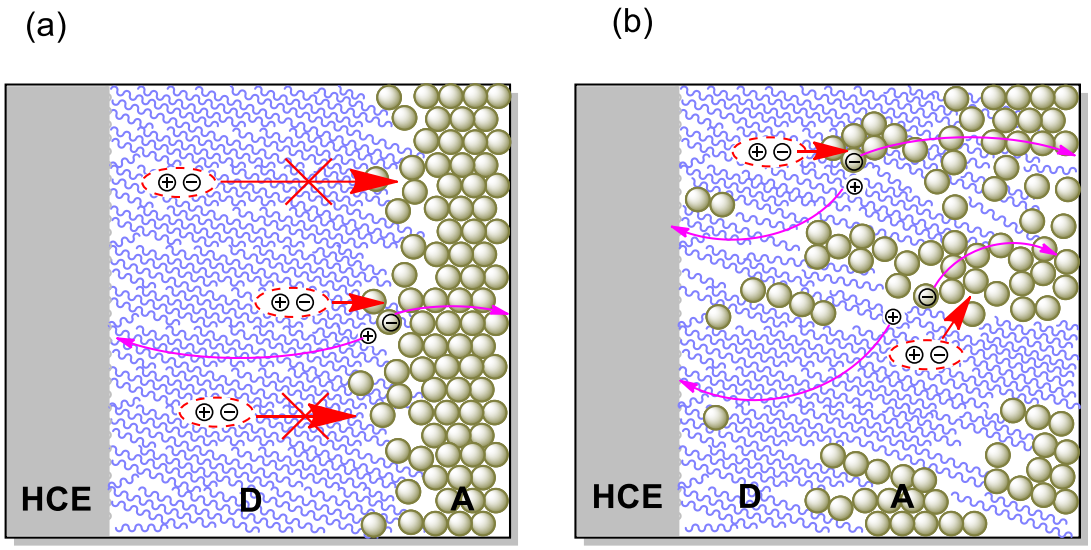

Figure 1.5. Renderings of a planar (a) and a bulk heterojunction (b) active layer. Donor polymers (D) are represented by blue wavy lines and acceptor molecules (A) are represented by tan circles; HCE is the hole-collecting electrode. Excitons are represented by grouped positive and negative charges. Exciton diffusion is shown with red straight arrows, charge carrier hopping pathways are shown by pink curved arrows. Molecular size is exaggerated for clarity and to distinguish between neat and mixed domains.

A problem that consistently emerges in flawed BHJ active layers, relative to planar heterojunctions, is increased charge recombination. If domains are smaller than r_c, charges may not be able to reach the thermalization length a due to confinement, resulting in increased geminate recombination.[70] Additionally, bimolecular

recombination has been linked to lower or uneven bulk charge mobilities,[71–73] higher interfacial area,[74–76] and phase segregation,[77] essentially providing inadequate pathways for charge transport to the electrodes. Many of these problems stem from the miscibility of D and A; while poor miscibility can result in segregated pure domains, strong miscibility can undermine neat phase order and charge transport. Certain material blends have even been shown to co-crystallize; these systems can undergo rapid recombination, unable to transport charge carriers through the film.[78–80] However, well mixed regions in a film do exhibit effective exciton dissociation; it has been speculated that, for many material systems, the ideal BHJ should not only include continuous neat phases for charge transport, but also mixed regions for exciton dissociation.[78,81] To address these challenges, numerous methods of morphological control in BHJ films have emerged; these will be discussed in the next section.

As a product of their π-conjugation, organic semiconductors are typically planar and rigid, especially in the case of small molecules, a feature that can often lead to anisotropic charge transport.[14,82–85] For materials that would otherwise have impressive charge mobilities, absorption coefficients, and exciton diffusion lengths, the environment of a bulk heterojunction can severely limit their applicability, as was observed for early planar perylene diimide derivatives.[77,86,87] On cue to serve as a solution entered buckminsterfullerene, a spherical conjugated carbon molecule comprised of 60 sp^2 carbons, named for the architect Buckminster Fuller, whose geodesic domes it resembles. The 60 atoms complete the truncated icosahedron as a composite of 32 shapes, 20 hexagons and 12 pentagons, that share 90 edges, exhibiting a van der Waals diameter of 1.01 nm and an average bond length of 1.4 Å, although π-bonds are considered to lie between neighboring hexagons. Though present in nature and as a product of combustion (albeit rarely),[88] the molecule was first synthesized

intentionally by Kroto *et al*. in 1985.[89] Sparingly soluble in common organic solvents, the fullerene was functionalized for solubility ten years later by the group of Fred Wudl, as a derivative known colloquially as phenyl-C_{61}-butyric acid methyl ester ($PC_{61}BM$),[90] which was employed as an acceptor by Alan J. Heeger the same year in his first bulk heterojunction OPVs.[62]

The high mobility and isotropic transport of the fullerene derivatives,[91] and high electron affinity (ca. 3.8 - 4.0 eV by inverse photoelectron spectroscopy, first reduction is ca. -1.0 V vs. $FeCp^+/FeCp$),[92–94] is only slightly affected by the application of functional groups,[95–97] and consistently arranges in packing structures conducive to charge transport.[98] Though not a strongly absorbing species with a somewhat large bandgap of ca. 1.8 eV, nor an inexpensive material at ca. $200-500 / g depending on purity (for $PC_{61}BM$ in 2016), its excellent charge accepting and transport properties in BHJs made it very difficult for other organic molecules to compete in terms of performance. As a result, fullerene derivatives largely dominated, and to some extent controlled, the OPV field for a significant portion of the last two decades, especially when combined with common, low-cost, crystalline homopolymers that rely on π-π intermolecular transport through highly-ordered phases, such as poly(3-hexylthiophene) (P3HT) and poly[methoxy-(dimethyloctylocy)-phenylen](vinylene) (MDMO-PPV).[99–102] The application of fullerene alternatives in an attempt to mimic their isotropic transport is the focus of Chapter 2; this discussion is continued there.

Since the mid to late 2000s, new types of donor heteropolymers, called "push-pull" have received a great deal of attention, leading to some of the highest performing OPVs to date.[103–109] These polymers have a repeating donor-acceptor chromophore system, which allows very fine control of the electronic properties via the substitution of various heterocyclic groups.[110,111] However, as a result of complex heterocycles and

branched side-chains, these materials have moved away from a reliance on short-range, π-π stacking order for effective charge transport in BHJs, and it has been suggested that charges are primarily transported along the backbone.[112–116] As the requirements of short-range order for the donor have decreased, non-fullerene acceptors have returned to prominence with rival performances.[117–120] Of course, these new materials and systems have their own morphological requirements and concerns.

1.1.5 Modern Techniques for Morphological Control in OPV Active Layers

For OPVs, the most common method of solution processing to achieve the desired ca. 100 nm films has been, by far, spin-coating, although examples of other methods, such as doctor-blading, spray-coating, and slot-die coating can be found in the literature. The given technique will have a great effect on drying times and, consequently, film morphology. At this point the discussion will focus on the process components; a more in-depth overview of these techniques given in the next section. For solution processed BHJs, the earliest and simplest methods of morphological control have been solvent manipulation and thermal annealing, taking advantage of simple material properties such as solvent volatility, material miscibility, and thermal transitions to control domain growth and purity. With homopolymers like MDMO-PPV and P3HT, it was determined that halogenated aromatic solvents, such as chlorobenzene and *o*-dichlorobenzene, gave optimum performance due to the higher solubility of fullerene derivatives, which led to smaller, well-dispersed domains.[99–101,121–123] Thermal annealing, first reported by Padinger *et al*.,[124] allows for the diffusion of small molecules and the reorganization of polymers which, depending on material miscibilities, can increase phase size and purity.[125,126] This technique is almost always necessary to achieve higher performances with P3HT.

Other techniques, such as solvent annealing or vacuum annealing, attempt to prolong or shorten the drying time of the cast film. This can be achieved most simply by using low-volatility solvents, such as *o*-dichlorobenzene or 1,2,4-trichlorobenzene, which will be significantly present in the film after casting, and placing the film in a sealed vessel, which will significantly increase the vapor pressure of the exiting solvent.[100,127] This can also be achieved by placing the dried film in a Petri dish containing a volatile solvent, allowing reentry into the film.[128–130] While this treatment has been shown to allow continued reorganization and domain growth, vacuum or mild thermal (50-80° C) annealing can quicken drying time to kinetically trap the microstructure.[71,131,132]

Coming to the present day, one of the most recent techniques to prolong drying time and alter domain growth is the use of solvent additives, high-boiling point solvents that are added in small quantities to solutions, which can alter material miscibility in solution as well, changing the initial state of the cast film.[133–137] Low-volatility solvents, such as diiodooctane or chloronapthalene, have been shown to drastically alter domain size and aggregate order in bulk heterojunctions, enhancing performance when properly administered.[136–139] Other, non-volatile agents, such as insulating polymers and hydrogen-bonding small molecules, can act as nucleation sites within a film, directing phase growth.[140–142]

This leads to the work in this thesis; the introduction of new materials into the active layer, essentially solid additives, with the goal of customizing and improving the electronic transport of the semiconductors in OPVs is very much a morphological study, as the introduction of new materials into these already disordered layers will certainly have an effect on the microstructure. This is elaborated upon in this chapter's conclusion and the following chapters.

1.2 Fundamental Techniques for Organic Photovoltaic Device and Material Characterization

Many techniques have been employed to characterize OPV devices, and the properties of the layer and materials (separate and blended) that compose them. This section surveys some of these methods, focusing on those used to probe device performance, electronic properties, and morphology. Note that this is not meant to represent a comprehensive review of all techniques relevant to OPVs, mainly those that were most extensively employed in this thesis. Additional techniques are appropriately discussed in Chapters 2-5, at the point that they are relevant.

1.2.1 Organic Photovoltaics – Device Fabrication and Measurements

As discussed in the previous sections, the structure of the OPV devices has progressed substantially since Melvin's first cell in 1948. While the composition of the active layer has advanced, so have the charge-extraction junctions that frame it. Modern cells can be referred to as having one of two possible formats, conventional or inverted, which refer to the direction of charge flow, during operation, out of the active layer relative to the substrate on which the cell is constructed, dictated by the Φ of the extracting materials. This is elaborated upon in the next few paragraphs.

The substrate, through which light typically enters the device, is typically a transparent dielectric, such as SiO_X or possibly a flexible polymer, coated with a thin, transparent conducting layer (TCL). This is usually an oxide, most often tin-doped indium oxide (ITO), with high transparency and conductivity,[143,144] although alternatives such as conductive polymers, silver nanowires, and graphene have been employed, with generally lower performances but the promise of higher flexibility.[145,146] Φ of ITO is largely dependent on surface cleaning methodology[147] and,

at ca. 4.5 – 5.0 eV, is not always appropriately placed for electron or hole transfer to/from the valence and conduction bands of many materials that are employed in OPVs without losses in energy, resulting in lower open-circuit voltages.[148–151] To improve alignment with organic semiconductor transport levels, interlayers, often semiconducting metal oxides with large bandgaps, have been employed between ITO and the active layer.[152–155]

The interlayer directly above the TCL is most often solution processed for polymer/fullerene BHJ cells. For a cell in the conventional format, this interlayer can be a high work function hole transport layer (HTL) or electrode replacement, or a surface modifier that increases the Fermi level energy by oxidizing the surface and / or creating a dipole pointing out from the surface. The most common interlayer material for this format is the ionomer mixture poly(3,4-ethylenedioxythiophene) polystyrene sulfonate (PEDOT:PSS),[153] though some attention has been given to solution-processed metal oxides, such as molybdenum oxide (MoO_X) and nickel oxide (NiO_X).[156–158] In an inverted cell, this interlayer is typically an electron transporting layer (ETL) and serves to do the opposite, moving E_F towards vacuum, again commonly metal oxides such as zinc oxide (ZnO_X) and titanium oxide (TiO_X),[159–167] although thin surface-modifying polymer films, such as ethoxylated-polyethylenimine (PEIE) and poly[(9,9-bis((dimethylamino)propyl)-2,7-fluorene)-2,7-(9,9–dioctylfluorene)] (PFN) have been reported to give substantial improvements in performance as well.[104,168] As a note, solution-processed thin film oxides will often exhibit rather low order and purity; this actuality and its possible solutions are discussed in Chapter 5.

Active layer deposition can be accomplished in a number of ways, as mentioned in Section 1.1.5. Thermal evaporation is a technique that has been used since the first report of single and bilayer devices and allows substantial control of the film

composition out-of-plane to the substrate. Small molecules can be evaporated in parallel or in series, with adjustable rates, and morphological control can even be achieved by temperature modulation of the substrate; however, this is the most limiting method in terms of eventual scale-up for production, as it is not compatible with polymers or large molecules and has a very low through-put due to the requirement of low pressures (ca. 10^{-6} Torr). Spin-coating involves the spreading of a solution across a substrate with centrifugal force by rotating it at hundreds or thousands of rpm.[169,170] Thicknesses are related to viscosity and solvent volatility. It remains the most common solution-processing method in the academic laboratory, producing reliable and smooth films, yet is not compatible with scale-up and is quite wasteful, with less than 1% of the material in solution being incorporated into the final film. Example device structure diagrams and images of an ITO/PEDOT:PSS/P3HT:PC_{61}BM/Ca/Al device prepared in the SSDL are shown in Figure 1.6.

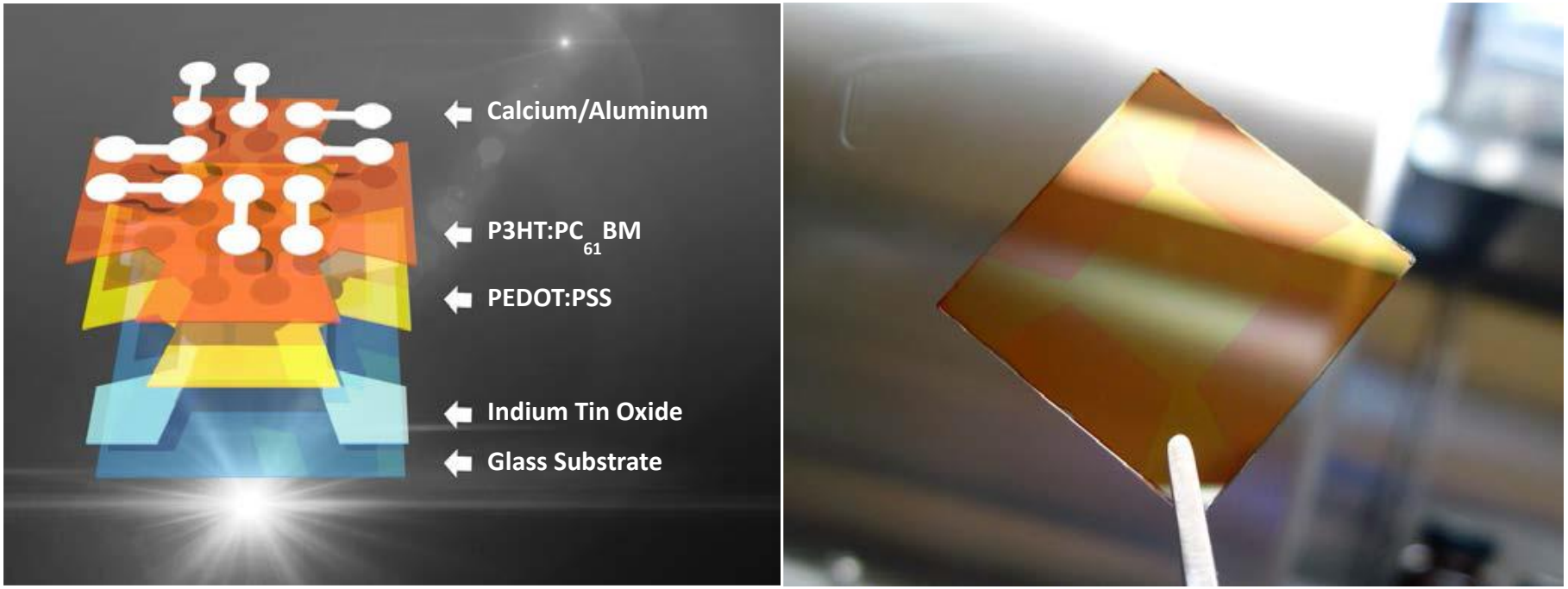

Figure 1.6. (left) A diagram of the layers in an ITO/PEDOT:PSS/P3HT:$PC_{61}BM$/Ca/Al device prepared at the Solid State Device Laboratory at the Georgia Institute of Technology, and (right) an image of that very cell, before electrode evaporation. This figure highlights the ITO and mask pattern that controls the device area, i.e. the overlap of the ITO and Ca/Al electrodes, which is 0.07 cm^2 for this format. The image and diagram are borrowed and adapted with permission from Marcin Kielar.

Solution-processing methods that are less commonly used in academia but are more practical for scale-up, have also been implemented in OPVs. Doctor-blading, or blade-coating, spreads a small volume of solution in a meniscus across a substrate at a controlled rate and height.[171,172] Temperature, surface energy, and fluid surface tension can influence film formation, and can lead to substantial order in active layer phase growth. OPV performance for some systems has been reported to be comparable with spin-coating.[173–175] Spray-coating pushes a solution through a pressurized nozzle, leading to a continuous flow of droplets, the size and speed of which can be adjusted.[176] While it has low waste and high throughput, the drying dynamics are very different than for solution-spreading techniques, requiring nontrivial optimization as film morphology and microstructure are generally different.[177–179] Lastly, slot-die coating is a large-area method, similar to blade-coating, where material is dispensed from an adjustable steel coating head upon a moving substrate.[171] Thickness can be controlled by coating rate, head width, and fluid rate. This method has already been used in the large scale for OPVs, but is not widely tested in academic laboratories, due to the quantity of material required.[180–183]

Due to the difficulties of solution processing on organic films, which include surface tension, dissolution of the previous layer, and possibly decomposition of organic materials by aqueous solutions, final layers are most often deposited by thermal evaporation, with notable exceptions.[184–186] In a conventional device, these will be low Φ electrodes, such as calcium; molybdenum or vanadium oxides are often implemented in inverted devices. When conductors are used, the E_F of the semiconductor blend close to the top electrode will be pinned close to its *EA* or *IE* respectively via electron or hole transfer to/from the semiconductor, reducing energetic losses.[14] Finally, a sizable

thickness of a common metal conductor is generally deposited on the electrodes to allow Ohmic contacts to external metal pins, through which bias will be induced.

Power generation in OPVs can be described using four parameters, short-circuit current density (J_{SC}), open-circuit voltage (V_{OC}), fill factor (*FF*), and power conversion efficiency (PCE). J_{SC}, in mA/cm^2, is the current density produced under illumination with no external bias, and can be derived as:[41,187,188]

$$J_{SC} = -\frac{1}{1 + {R_S}/{R_{SH}}}\left[J_{ph} - J_0\left(e^{\frac{|J_{SC}|R_S A}{k_B T/q}} - 1\right)\right] \qquad \text{Equation 1.9}$$

The series resistance (R_S) is related to the active layer conductivity, as well as the resistance of all contacts and junctions in the device and the external pins, and should be minimized, while the shunt resistance (R_{SH}) is affected by sources of leakage current, such as pinholes or impurity-induced recombination, and should be maximized.[41] J_{ph} and J_0 are the saturated current densities produced at a reverse bias under illumination and in the dark, respectively, and *A* is cell area. As R_S and J_0 go to 0 and R_{SH} goes to infinity, J_{SC} becomes ~ -J_{ph}. The maximum J_{SC} can be described by the integration of incident photon-to-current conversion efficiency (IPCE), which depends on the product of photocarrier generation, exciton separation, and charge collection, multiplied by photon flux across the AM 1.5 solar spectrum shown in Figure 1.3. For example, 100% IPCE of photons from 300 to 800 nm will give a J_{SC} of ca. 26.7 mA/cm^2. This will be expanded upon in the next section.

V_{OC}, the external bias in V at which injected current and photocurrent cancel one another, can be expressed as:

$$V_{OC} = \frac{k_B T}{q} \ln\left[1 + \frac{J_{ph}}{J_0}\left(1 - \frac{V_{OC}}{J_{ph} R_{SH} A}\right)\right] \quad \text{Equation 1.10}$$

where, as R_{SH} goes to infinity, the terms in parentheses approach 1, revealing the dependence on the ratio of J_{SC} over dark reverse saturation current density (as J_{SC} approaches ~ -J_{ph} as explained earlier). The maximum achievable V_{OC} for a material system is limited by the difference of IE_D and EA_A;[189] however, minimizing the staggering of D and A energy levels to increase V_{OC} may also decrease driving force for charge separation, as derived in Section 1.1.3. Additional losses in the V_{OC} relative to E_{CS} have been linked to low dielectric constants, energetic disorder in the density of states, and molecular orientation at the interface, among other factors.[190–193]

The relationship of the two previously mentioned properties to the PCE is outlined in the following equation:

$$PCE = (FF)\frac{J_{SC} V_{OC}}{P_{in}} \times 100\% \quad \text{Equation 1.11}$$

P_{in} is the incoming power density, which as previously discussed is 1000 W/m^2 (or more conveniently 100 mW/cm^2) at sea level for AM 1.5. As the product of the current density and the voltage is a power density, there will be a point at which this product is maximized corresponding to J_{max} and V_{max}. This product is equal to J_{SC} × V_{OC} × FF, which, when divided by the incoming power density returns a PCE, often given in % (by multiplying by 100%). These values are determined experimentally by sweeping a cell from negative to positive voltage (or positive to negative), measuring current output, and plotting J against V. An example plot taken from an ITO/a-ZnO/PTB7:$PC_{71}BM$/MoO_3/Ag device (work completed in Chapter 5) is shown in Figure 1.7.

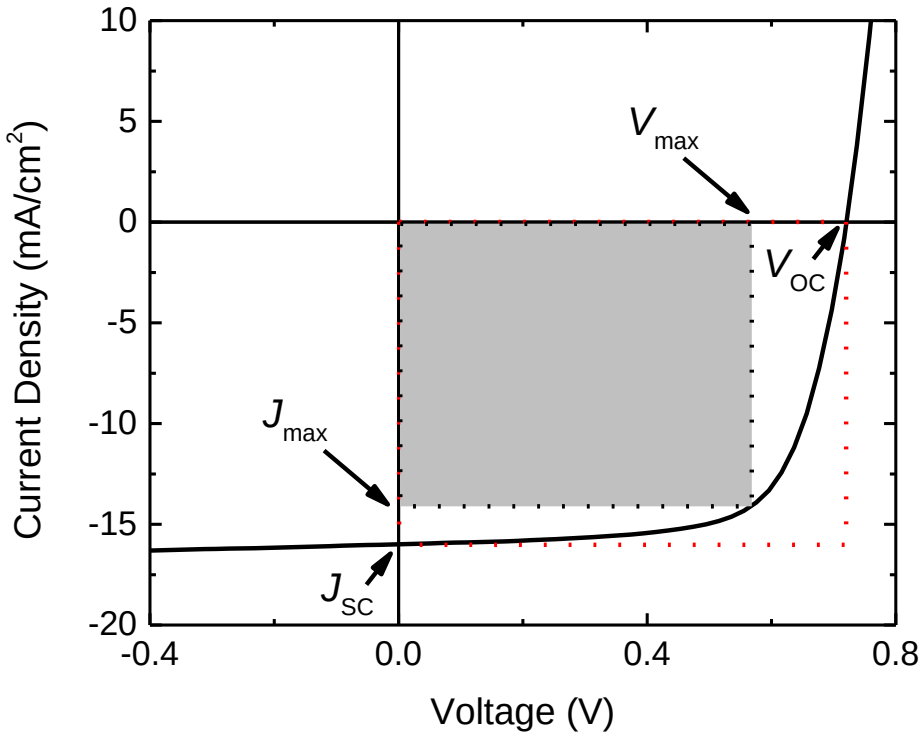

Figure 1.7. *J-V* curves from an ITO/a-ZnO/PTB7:$PC_{71}BM$/MoO_3/Ag device highlighting parameters relevant to cell efficiency. The shaded region represents the fill factor in relation to the area of a box outline is dashed red lines that would correspond to $J_{SC} \times V_{OC}$. From the *J-V* plot, we can determine that J_{SC} = 16 mA/cm^2, V_{OC} = 0.72 V, and $J_{max} \times V_{max}$ = 8.0 mW/cm^2. From these values, using the Equation 1.7 we can determine that PCE = 8.0%, and *FF* = 0.70.

The maximum achievable *FF* shares a relationship with V_{OC} when normalized to thermal voltage in the expression $v_{OC} = qV_{OC}/nk_BT$, where *n* is the diode ideality factor based on the mechanisms of recombination (*n* = 1 if recombinations are band-to-band, and increases up to *n* = 2 where recombination occurs via states in the energy gap), derived from Martin Green's empirical expression in the instance that R_S is very low and R_{SH} is very high:[194]

$$FF_0 = \frac{v_{OC} - \ln(v_{OC} + 0.72)}{v_{OC} + 1} \quad \text{Equation 1.12}$$

*FF*s achieved in OPVs tend to fall below FF_0; noting the substantial disorder and trap states present in organic materials, especially in a BHJ, relative to crystalline inorganics, this deviation in the ideality factor is quite understandable.[41]

Organic photovoltaic devices are prepared in each of Chapters 2 – 5 with a variety of different formats, most often implemented as a definitive tool to determine the effects of additives within the OPV device. Devices have been prepared at the Wright Patterson Air Force Base (2011-2012), the Solid State Device Laboratory at the Georgia Institute of Technology (2012-2016), and at the King Abdullah University of Science and Technology (2014-2015). Greater detail is given in the respective chapters.

1.2.2 Incident Photon-to-Current Conversion Efficiency

As mentioned in the previous section, J_{SC} is the product of the IPCE and the photon flux density, integrated across the solar spectrum:[41]

$$J_{SC} = \int_{AM\ 1.5} q\eta_{IPCE}(\lambda) N_{ph}(\lambda) d\lambda \quad \text{Equation 1.13}$$

Here IPCE is represented as η_{IPCE}, and the photon flux density at AM 1.5 is represented as N_{ph}, each of these being a λ-dependent quantity. IPCE can be determined by recording electrical current under monochromatic light; the ratio of the produced current and the highest possible current (determined by a calibrated reference) yields the conversion efficiency. By varying λ, a full spectrum representing carrier generation under white light illumination can be obtained. By integrating this spectrum over AM 1.5, using Equation 1.9, the J_{SC} of the OPV can be calculated. A sample spectrum from an ITO/a-ZnO/PCDTBT:$PC_{71}BM$/MoO_3/Ag device, similar to those exhibited in Chapter 4, is shown in Figure 1.8. As a note, this method describes the external quantum

efficiency (EQE), i.e. conversion efficiency from radiation incident on the solar cell, and indeed EQE and IPCE are often used interchangeably in the literature. This technique can also be used to determine internal quantum efficiency (IQE), the conversion efficiency from incident photons that are actually absorbed by the device, but this requires instrumentation with the ability to measure transmitted or reflected light, and is less relevant to the determination of PCE.

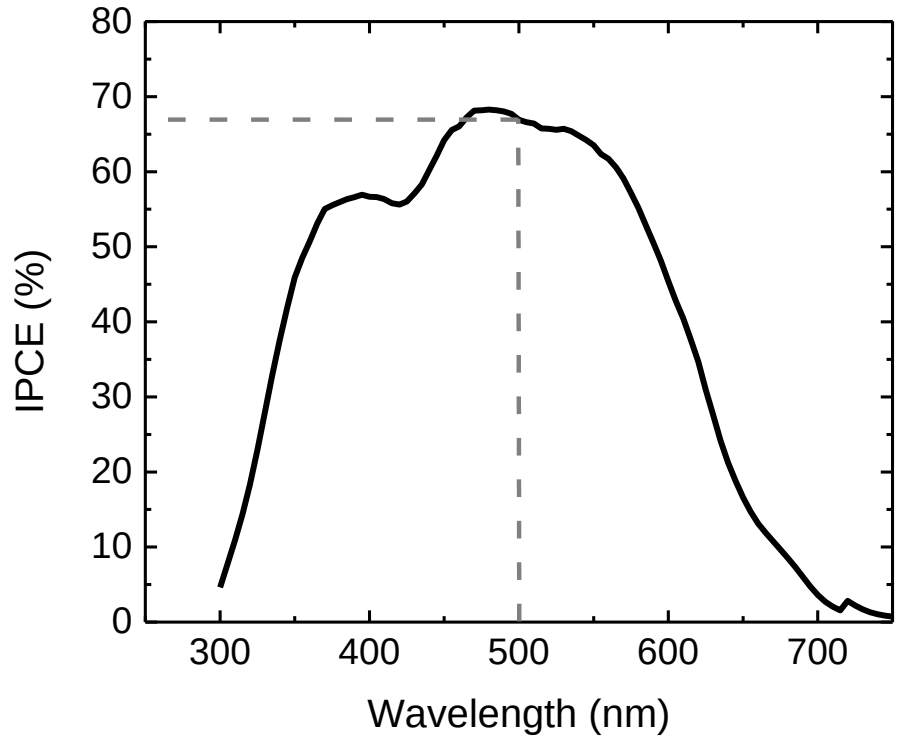

Figure 1.8. IPCE spectra from an ITO/a-ZnO/PCDTBT:$PC_{71}BM$/MoO_3/Ag device. The dashed lines indicate that at λ = 500 nm, 67% of the incoming photons are converted into electrical current. By integrating across the spectrum, it can be estimated that J_{SC} = 10 mA/cm^2, in good agreement with OPV *J*-*V* measurements on the same device.

For OPVs, the IPCE of an efficient cell will resemble the absorbance spectrum of the BHJ film of the D and A materials, and is thus partially dependent upon complementary spectral overlap to improve J_{SC}, but is also affected by the same

parasitic processes that lower the short-circuit current density, such as shunt resistance and recombination. Common acceptors, such as fullerene or rylene derivatives, will often have a larger optical gap than the donor, and in most cases are responsible for absorbance in the high-energy region of the spectrum. Therefore, the extent that efficient photon-to-current conversion extents into the near-IR will depend on the optical absorption of the donor, which for many materials, such as poly- and oligothiophene derivatives, can depend on morphological order and π-π overlap.[122,128,195] Thus, decreasing E_{op} of the donor from 1.80 eV (ca. 690 nm) to 1.55 eV (ca. 800 nm) has the potential to increase the J_{SC} by ca. 7 mA/cm^{-2}, reflected in the plot of maximum J_{SC} in Figure 1.9. Naturally, decreasing E_{op} can have a detrimental effect on V_{OC} or ΔG_{CS}, as discussed in previous sections. A somewhat advanced method to improve absorbance overlap with the solar spectrum is to employ more than two chromophores, as in ternary blend active layers or tandem devices, which have demonstrated fine control of spectral matching in OPVs.[184,196–198]

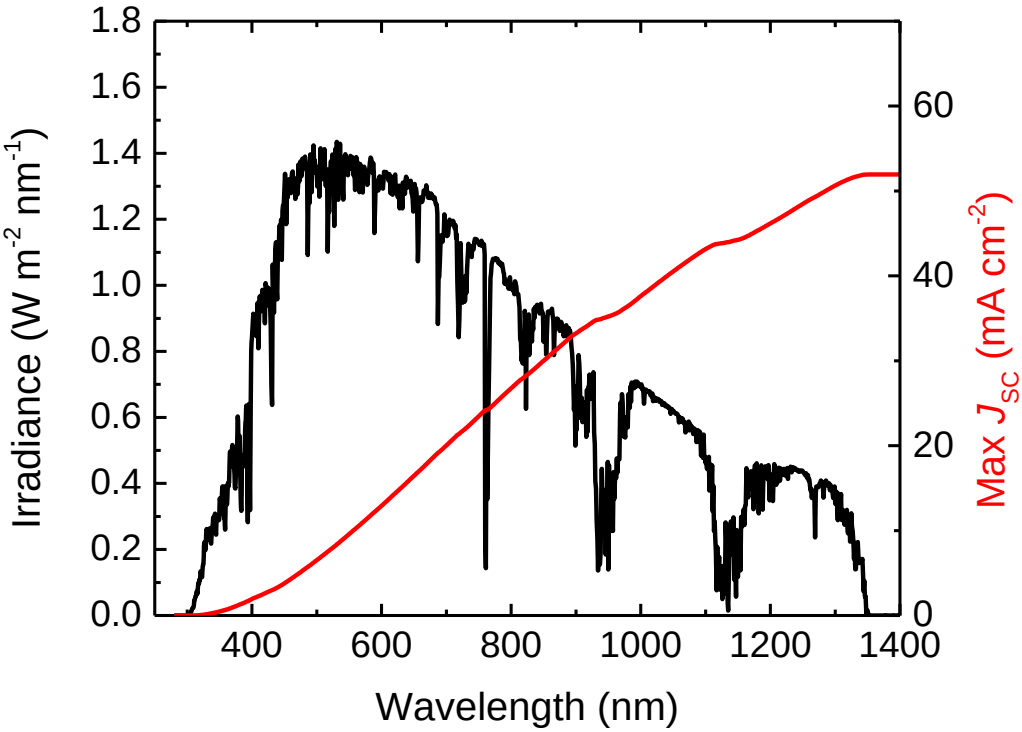

Figure 1.9. Solar irradiance (left y axis) at AM 1.5, compared with maximum J_{SC} (right y axis) assuming 100% IPCE at all wavelengths lower than the given absorption onset. Curves are adapted and/or calculated from references provided by the American Society for Testing and Materials (http://rredc.nrel.gov/solar/spectra/am1.5/).

IPCE was implemented in Chapters 4 and 5 as a method of studying J_{SC} enhancements in organic photovoltaic devices. The technique was performed at the Solid State Device Laboratory at the Georgia Institute of Technology (2012-2016) and at the King Abdullah University of Science and Technology (2014-2015). Greater detail is given in the respective chapters.

1.2.3 Electrical Conductivity and Mobility

Electrical conductivity is an intrinsic intensive property of a material that quantifies its ability to conduct an electric current under an external bias. It is the reciprocal of electrical resistivity (ρ). Conductivity is derived as:

$$\sigma = G\frac{l}{A} = \frac{Il}{VA} = \frac{J}{E}$$ Equation 1.14

Electrical conductance (*G*) is an extensive property and is given by current divided by voltage. Combined with the physical properties *l*, which is the distance between the two electrical contact points, and *A*, the cross-sectional area of the sample, conductivity can be simply expressed as the current density over the electric field (*E*), in Siemens per centimeter.

In Chapters 3, 4, and 5, conductivity progression was studied at low dopant concentrations in semiconductors, as has been done previously by the Kahn group.[199,200] σ was estimated from the ohmic (linear) regime of current-voltage curves, at $E < 1000$ V/cm, measured parallel to the film between source and drain electrodes, converting current to current density using film thickness and channel width, which in all cases were 50-100 nm and 2 mm respectively, and voltage to field using channel length, which were 2, 5, 10 or 20 μm. An image of a typical pixel is shown in Figure 1.10. Conductivities measured at all four channel lengths gave similar values for low conductivity films, indicating that contact resistance, the contribution of contacting electrode interfaces to the total resistance of a system, is negligible relative to film resistance. At higher values the conductivity was also determined with 4-point probe measurements, which minimizes the contact resistance by divorcing the current-carrying and voltage-sensing probes. Comparing these measurements relative to the 2-point measurements indicated a maximum contact resistance on the order of 10s of kΩ in the latter, which is negligible (< 1% total resistance) at the majority of ultra-low doping concentrations. Though this approximation does not account for changes in semiconductor/probe junctions as a result of electrical doping, it is assumed that the conductivity trends remain consistent as values were fairly equivalent with literature reports and 4-terminal measurements. As an example plot, the complete series of *J-E*

curves for PTB7 doped with $Mo(tfd\text{-}CO_2Me)_3$, which are presented as conductivity vs. dopant concentration plots in Figures 4.2 and 4.4, is shown in Figure 1.10. Greater detail is given in the respective chapters.

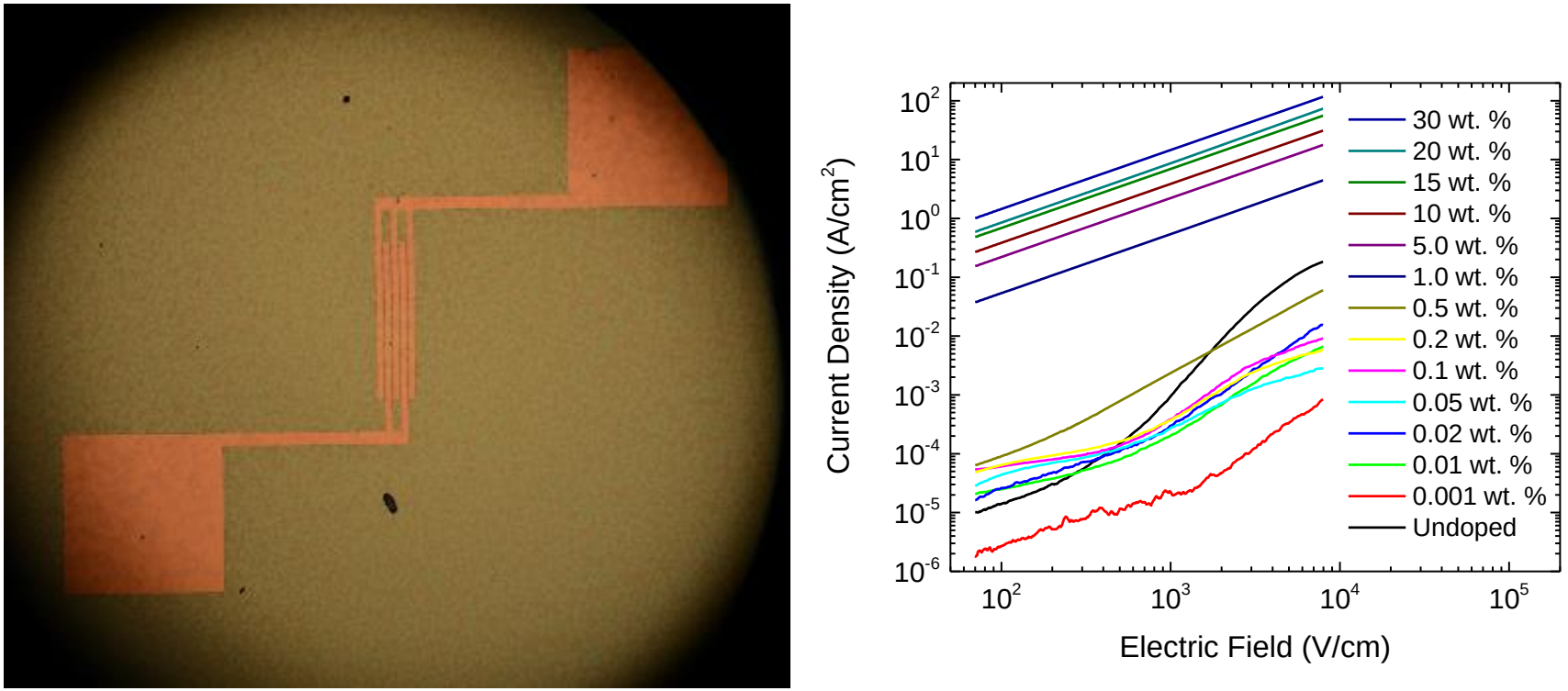

Figure 1.10. (left) Microscope image of a prepatterned gold/ITO electrode fingers on silicon oxide over silicon beneath a pristine 50 nm P3HT film. For this example pixel, channel width and length are 20 μm and 2 mm respectively. (right) Representative *J-E* curves of PTB7 films, undoped and doped from 0.001 wt. % up to 30 wt. % of the p-dopant Mo(tfd-CO_2Me)$_3$. The increase in slope between 10^3 and 10^4 has been linked to trap charge limited current (TCLC) which is greatest in the undoped film and present at dopant concentrations < 1.0 wt. %, above which deep traps are passivated (see Chapter 4).[200]

In the absence of an electric field, charge carriers move randomly in solid materials. Upon the application of a field, carriers are accelerated to a finite average velocity called the drift velocity (v_d), a limit resulting from scattering due to impurities, defects, and quasiparticles such as phonons. Electron, or hole, mobility (μ) quantifies how rapidly a charge carrier can move through a material under an electric field in relation to the magnitude of v_d, defined as $v_d = \mu E$, where E is the magnitude of the electric field. μ is most often given in $cm^2\ V^{-1}\ s^{-1}$. Mobilities of electrons and holes are generally related to electrical conductivity as:

$$\sigma = nq\mu_e + pq\mu_h \qquad \text{Equation 1.15}$$

although one term or the other is usually dominant under given conditions. The number densities of electrons and holes are given as n and p respectively. Inorganic materials, such as metals and silicon, have high order and extensive interatomic orbital overlap, and will typically have mobilities in the 100s to 1000s of $cm^2\ V^{-1}\ s^{-1}$.[201] In metals, due to high carrier densities from contributing valence electrons, ca. $10^{22}\ cm^{-3}$, very high conductivities result, typically ca. $10^5\ S\ cm^{-1}$. In many organic materials, disorder and/or poor intermolecular/interchain orbital overlap forces charge transport to occur via a hopping process, as discussed previously, which is less efficient than in well-ordered inorganic solids. As a result the mobilities are quite low, typically $< 1\ cm^2\ V^{-1}\ s^{-1}$, although there are notable exceptions in polymers and fullerenes.[114,202]

μ can be determined through a variety of different experiments, such as time-of-flight (TOF), space-charge limited current (SCLC), time resolved conductivity, and field-effect transistors (FETs). TOF experiments were used in Chapter 2 to measure changes in the bulk electron mobility of blended perylenediimide derivatives; further theory and experiment detail is provided in Section 2.2.8. SCLC measurements are another way of observing bulk mobility, by applying a field to an electrode-contacted

material of sufficient magnitude that the current becomes dominated by injected carriers, allowing mobility to be estimated by fitting the *I*-*V* curve. Unlike the linear ohmic (low bias) regime, this region is identified by an approximately quadratic relationship between current and voltage ($I \sim V^2$).[203,204] Time-resolved conductivity uses high frequency electromagnetic radiation to probe photo-induced carrier motion over short time and length scales, claiming relevance in the examination of charge behavior during charge separation.[205,206]

An FET uses an external electric field to form a discrete, conductive channel for a single charge carrier type within a semiconductor. Though this type of device was first patented by Julius Edgar Lilienfeld in 1926, practical devices were not fabricated until over 20 years later by Shockley's group at Bell Laboratories.[207,208] FETs can have differing configurations, such as top or bottom-contact, and top or bottom-gate, referring to the electrode location in reference to the semiconductor, but the general format includes source (S) and drain (D) electrodes that outline a channel of a specific length (*L*) and width (*W*), and a gate (G) electrode, isolated from S, D, and the semiconductor by a dielectric. By applying bias at G relative to S (V_{GS}), a channel can be opened or closed along the interface of the semiconductor and the dielectric, which can then be populated by inducing a bias between S and D (V_{DS}). In Chapters 3, 4, and 5, mobility trends upon the incorporation of electrical dopants into organic and metal-oxide semiconductors were determined by FET measurements. FETs prepared at the King Abdullah University of Science and Technology had a bottom-gate bottom-contact configuration as illustrated in Figure 1.11. Greater detail is given in the respective chapters.

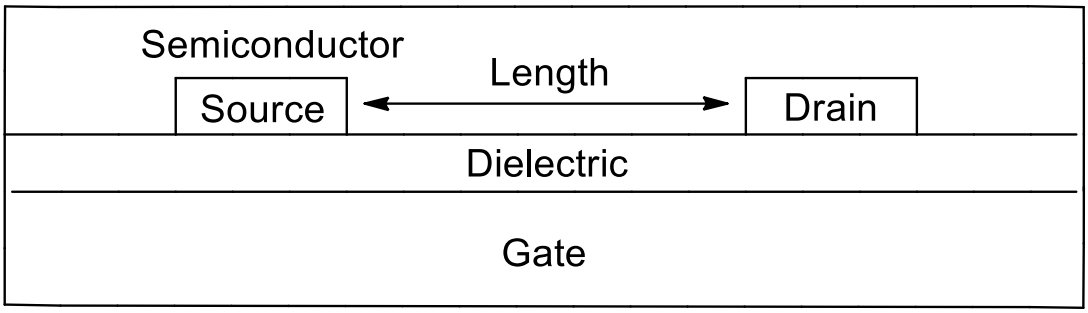

Figure 1.11. A simple illustration of a bottom-gate bottom-contact FET, like those prepared in Chapters 3, 4, and 5. The channel forms at the interface between the semiconductor and the dielectric, along the length between the source and drain electrodes.

These four experiments are quite diverse in their operation and resulting values, and as such there has been some debate over the relevance of certain techniques to charge transport in organic photovoltaics.[209–211] Both TOF and SCLC are considered to be bulk measurements, and can measure μ perpendicular to the film, which is often claimed as the most consistent reproduction of OPV conditions, yet thicknesses will generally need to be greater than those in the photovoltaic devices to allow sufficient sensitivity. Time-resolved conductivity μ values are often the highest, but have been criticized as representing local regions of the film that exhibit the most ideal transport, rather than the entirety of the material. FET measurements involve the formation of a discrete channel at the semiconductor interface, which is parallel to the film and may not represent the bulk. In the modern OPV literature, it is not surprising to see any one of these measurement types employed, which can coincide with technique preference and availability.

1.2.4 Photoelectron Spectroscopy

Photoelectron, or photoemission, spectroscopy (PES) refers to various surface measurement techniques that are employed to determine the binding energy (*BE*) of electrons ejected by incident electromagnetic radiation via the photoelectric

effect.[24,25,212,213] Depending on the energy of the incoming photons ($h\nu$), the energy levels of core or valence electrons can be identified by the kinetic energy (*KE*) of liberated photoelectrons *via* Einstein's relation:

$$KE = h\nu - BE - IE = h\nu - \Phi \qquad \text{Equation 1.16}$$

Photoelectron *BE* is determined by chemical structure, molecular bonding, and intermolecular wavefunction overlap, and thus can deliver an immense amount of information with great sensitivity. However, in solids, depending on photoelectron *KE* and the material density, the inelastic free mean path (λ_p) is limited leading to substantial signal decay beneath certain depths, which is what restricts PES to a surface-sensitive analytical technique. Decay is not considered beyond the material surface, as these experiments are typically conducted in ultra-high vacuum (UHV). Calculated λ_p is plotted against *KE* for organic materials in Figure 1.12.

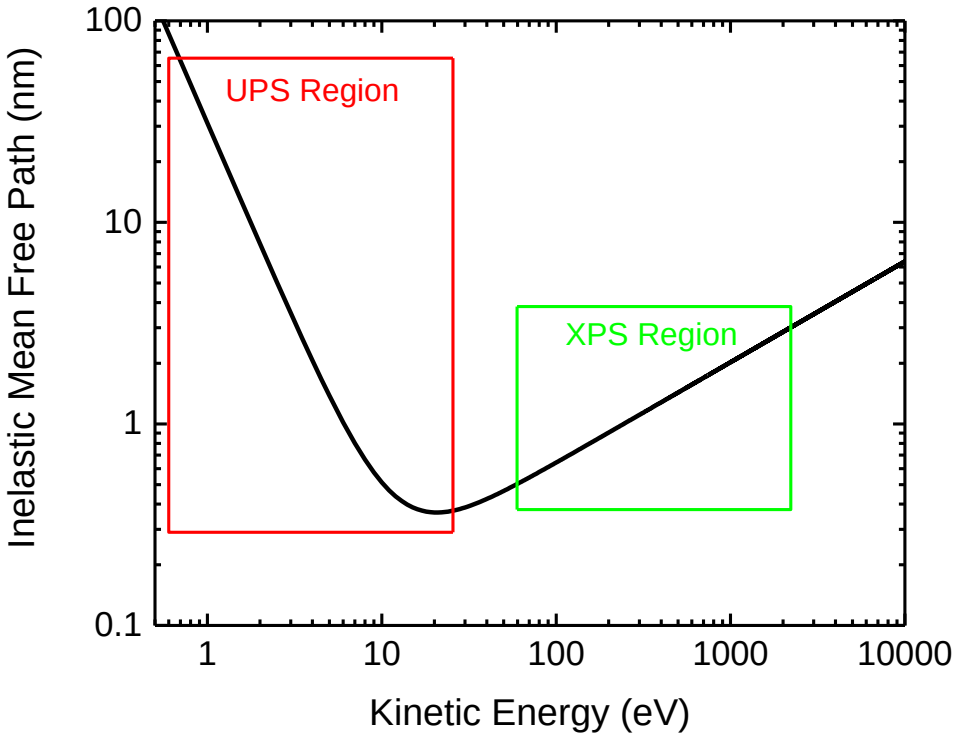

Figure 1.12. This plot shows the calculated λ_p in nm of photoelectrons through organic materials, using constants identified by Seah *et al*.[214] The decay of intensity I at a certain depth (x) can be expressed as $I(x) = I_0 e^{-x/\lambda_p}$ where I_0 is the intrinsic intensity. The energy regions analyzed in ultra-violet and x-ray photoelectron spectroscopy are indicated, respectively. Correcting for the signal decay is required for thin film analysis, and in some cases can be used to determine film thickness, as is performed in Chapter 5.

X-ray photoelectron spectroscopy (XPS) was first successfully demonstrated by Kai Siegbahn in 1957.[215] This technique uses an aluminum or magnesium source, which emits K_α X-rays upon bombardment with high energy electrons, to liberate electrons in atomic core energy levels on / near a material's surface. The intensity is recorded against *KE*, which is converted to *BE* using the Einstein relation above. The core binding energies of elements are uniquely characteristic, and therefore XPS allows the determination of elemental composition through their detection. Atomic ratios can be identified with the intensity of the peaks, as I is directly related to the elemental

concentration in the sample, when corrected for the ionization cross-section, the sensitivity of the detector, and the signal attenuation mentioned above. XPS was used in Chapter 5 to determine pentamethyl rhodocene derivative concentrations and O/Zn atomic ratios in oxide films. Greater detail is given in the chapter.

Ultra-violet photoelectron spectroscopy (UPS) uses UV light, between ca. 10-30 eV depending on the discharge source, to ionize valence electrons in gaseous or solid materials. The technique was developed by David W. Turner in 1962 implementing a helium discharge lamp emitting He I radiation at a wavelength of 58.4 nm (21.2 eV), which has remained the most common light source.[216,217] In the gas phase, UPS can determine the ionization energies free of intermolecular interactions.[218] In solid materials, UPS can be used to look at energy level distributions based on the kinetic energy and angular distribution of photoelectrons as well, taking into account the signal decay as mentioned above, but is also effectively used, regarding the work in this thesis, as an established method to determine Φ and *IE*.

To demonstrate this function, a UPS spectrum of ca. 15 nm PCDTBT on ITO ionized with He I radiation, corresponding to the values given in Figure 5.5, is shown in Figure 1.13. As the *KE* of incoming photoelectrons are determined relative to the Fermi level of the analyzer, in such an experiment, a conductor, or a thin semiconductor film on a conductor, is put into electrical contact with the analyzer to equalize the Fermi levels of the two materials, corresponding to 0 eV binding energy. Unfilled levels cannot be probed with UPS, as there are no electrons to liberate, so there can be no signal at negative binding energies. In a metal, a density of states can be seen directly at the lowest positive values of *BE* since E_F is located within an energy band. In semiconductors, like the polymer exhibited in Figure 1.13, E_F is in the gap between filled and empty bands (or densities of states in organics), so the intensity remains low

until the valence band onset (VBO). The *BE* of this onset is equivalent to the difference between *IE* and Φ.

With decreasing kinetic energy, the flux of inelastically scattered electrons will typically grow (along with λ_p) leading to an increase in intensity. As *BE* approaches $h\nu$, there will be a cutoff corresponding to a point at which photoelectrons no longer have enough kinetic energy to escape the material. This is called the secondary edge cutoff (SEC) and accordingly the work function can be determined as $\Phi = h\nu - SEC$. The value of *IE* can therefore be derived as $IE = (h\nu - SEC) + VBO$. As a note, the measured Φ of a thin semiconductor on a conductor will often be affected by the Φ of the conductor due to band-bending at the junction, as discussed previously, and should be considered when comparing UPS data of semiconductors on different conductive bases.

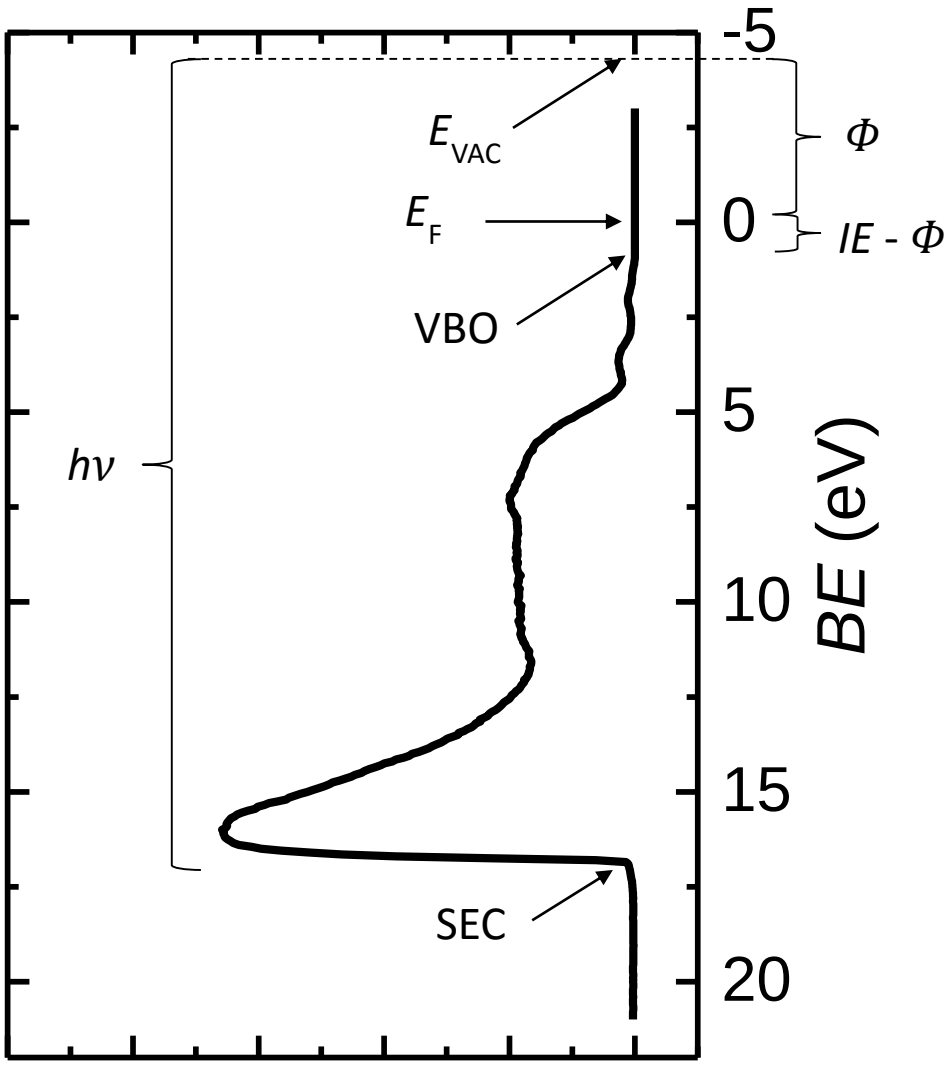

Figure 1.13. A UPS spectrum of ca. 15 nm PCDTBT on ITO, corresponding to the values given in Figure 5.5. The ionizing radiation is He I (21.2 eV). *BE* is given in the Y-axis, and the X-axis corresponds to intensity in arbitrary units.

UPS is employed in Chapters 3, 4, and 5 to study shifts in E_F upon the incorporation of electrical dopants into organic and metal-oxide semiconductors. Additional detail is given in the respective chapter.

1.2.5 Atomic Force Microscopy

Atomic force microscopy (AFM) is a type of scanning probe microscopy, a method of microscopy that overcomes the optical diffraction limit by scanning a mechanical probe to create an image of a surface, invented by Gerd K. Binning at IBM in 1982.[219,220] AFM can achieve sub-nanometer resolution through the use of an ultra-fine tip attached to a cantilever. Imaging is achieved by reflecting a laser beam off the cantilever onto a photodetector and moving the tip across the surface of a sample; as the sample imposes forces on the tip, the resulting movements of the cantilever are recorded by displacements of the reflected beam on the photodetector with respect to the equilibrium position, essentially translating atomic scale features into the macroscale. The image is formed by relating tip position to beam displacements, often represented as a pseudocolor plot. The tip itself is typically shaped as a ca. 5 μm tall pyramid with a ca. 30-50 nm wide point. This limits lateral resolution to the tens of nm, although higher resolutions have been achieved with functionalized tip terminations;[221–223] the vertical resolution is governed by the sensitivity of the photodetector, and can be fractions of a nanometer.

AFM tips can be acted upon by a number of forces, including mechanical, electrostatic, van der Waals, and capillary. Imaging is usually performed in one of three modes: contact mode, where the static tip is dragged across the surface, tapping mode, where the tip amplitude is oscillated over the surface, and non-contact mode, where the oscillating tip does not physically contact the surface at all, and is primarily acted upon by van der Waals forces.[220,224–226] In the latter two modes, the cantilever is oscillated by a piezoelectric element at its resonant frequency, the main difference between the two being that a tapping mode image is generated by the force of the contacts of the tip with the sample surface, while non-contact mode generates images from z-direction

feedback, adjusting its amplitude based on oscillation frequency changes due to surface forces to maintain a constant height. Each mode has advantages and disadvantages depending on material properties and environment; for example, non-contact mode does not result in sample degradation, making it useful with soft materials and biological samples, but can suffer from artifacts caused by fluids on the surface, which is common in atmospheric conditions.[227]

The two most common types of images produced by an AFM scan are topographic and phase. The topographic image is generated, depending on imaging mode as previously discussed, by oscillation frequency fluctuations or by the feedback used to adjust the cantilever height. Conversely, phase images map variations in the properties of the surface related to elasticity, friction, and adhesion, and can be collected simultaneously to topographic images. These images are generated by the phase lag between the input signal driving cantilever oscillation and the actual oscillation, which reflect changes in the surface mechanical properties. An example from Chapter 2, topographic and phase images for P3HT thin films taken in tapping mode, is shown in Figure 1.14. In the phase image, the boundaries of the fibrillary P3HT domains can easily be identified.

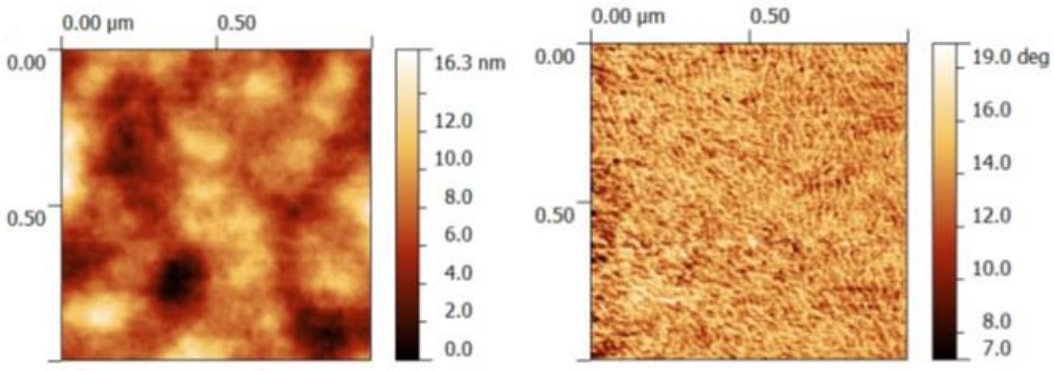

Figure 1.14. Atomic force microscopy topographic (left) and phase (right) images for P3HT thin films taken in tapping mode, exhibited in Chapter 2. The lamellar order of

the polymer domains, absent from the topographic scan, is clearly identified in the phase scan.

AFM has been used extensively to study active layer and interlayer surfaces in OPVs, including the development of techniques to measure local photoconductivity correlated with surface morphology.[228–233] In this thesis, AFM was used in each of Chapters 2, 3, 4, and 5 to study the effects of additives on the surface structure and mechanical properties of polymers, small molecules, and metal-oxides. Additional detail is given in the respective chapter.

1.2.6 Grazing-Incidence X-Ray Scattering & Diffraction

The nanoscale order of OPV thin films can be probed through their interactions with X-rays. This can be traced back to the phenomenon of Rayleigh scattering, the elastic scattering of x-rays resulting from interactions with electrons. Crystalline systems, where atoms or molecules are arranged in a highly ordered, repeating structure, can scatter waves in a specular manner, resulting in constructive and destructive interference between lattice planes. The resulting interference pattern is the root of an analysis method called Bragg diffraction, first proposed by William Lawrence Bragg and William Henry Bragg in 1913.[234]

For a crystal with a lattice plane spacing d, radiation with wavelength, λ, of a similar size will have path length differences, based on which plane they are scattering from, equal to $2dsin\theta$, where θ is the scattering angle relative to the plane, as shown in Figure 1.15. When this path length difference is equivalent to an integer multiple of λ the scattered waves interfere constructively producing a reflection spot in a diffraction pattern; this is essentially the derivation of Bragg's law:[235,236]

$$2d \sin\theta = n\lambda \qquad \text{Equation 1.17}$$

where *n* is a positive integer. This effect intensifies with reflection from successive lattice planes in the crystal. As a note, this effect can also be observed for moving particles, such as electrons, by treating them as waves with a de Broglie wavelength inversely proportional to their momentum. This is elaborated upon for particles at relativistic speeds in the electron microscopy section of Chapter 3 (3.2.4). Besides determination of the lattice spacing based on the diffraction angle, peak intensity and width can give information about particle or domain size, and sample crystallinity.

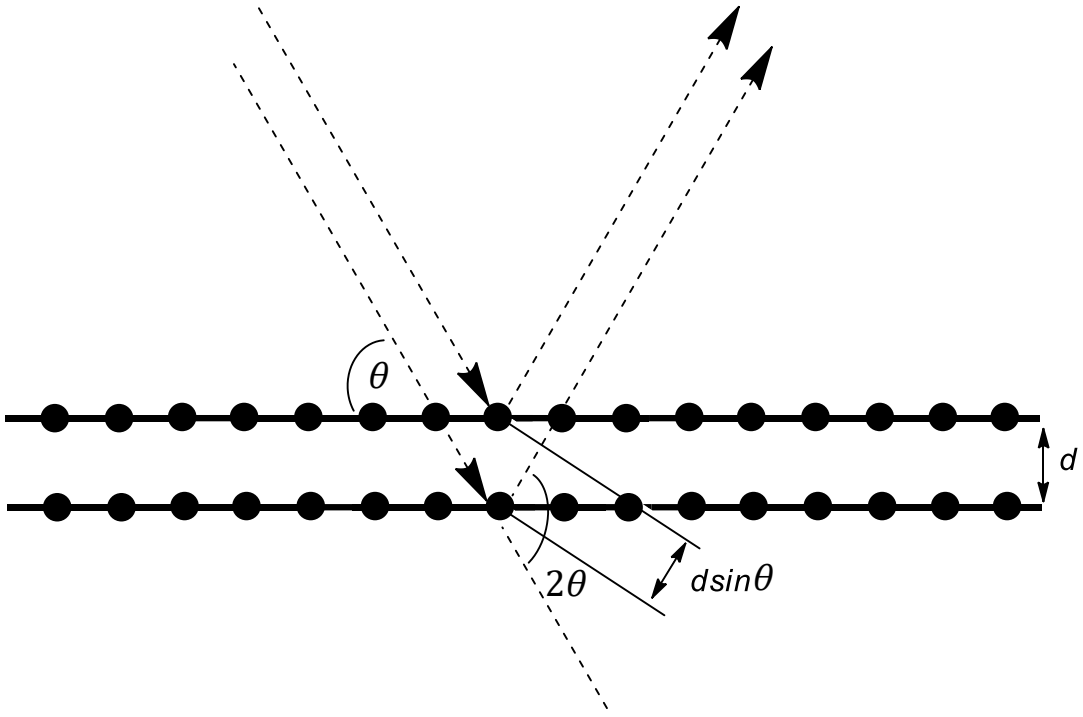

Figure 1.15. A simplistic representation of Bragg diffraction, where *d* is the distance between reflecting lattice planes, and θ is the angle of incident electromagnetic radiation.

Since 1912, X-ray diffraction has been heavily used to elucidate packing structures of inorganic and organic crystals, and, for organic crystals of sufficient purity, chemical structure down to mean chemical bond lengths, accelerating the understand of bonding, such as resonance and non-covalent interactions,[237–241] and

leading to over 20 Nobel prizes in chemistry, physics, and medicine. In a typical X-ray diffraction experiment, radiation is sourced from an X-ray tube, similar to that used in XPS, which is directed at the sample at an angle θ, the scattered radiation detected by a detector at 2θ. The source angle is increased over time, relative to the sample, to generate a diffraction pattern. When considering semi-crystalline organic thin films, such as the active layer in an OPV, a very low angle of incidence is used to increase the sensitivity to Bragg diffractions in the thin film relative to those in the substrate. In this experiment both the film and detector are radially scanned at a 1:2 ratio to probe lattice planes perpendicular to the film. Planes parallel to the film can be observed by rotating the film or moving the detector radially relative to the film surface. This technique sometimes referred to as grazing-incidence X-ray diffraction (GIXRD) and was developed by Marra *et al.* in 1979.[242]

A method of X-ray diffraction that is often used with polymer thin films is grazing-incidence wide angle X-ray scattering (GIWAXS), specifically referring to the wide scattering angles (large 2θ) that are typically observed for sub-nanometer structures.[243,244] This experiment provides a 2-dimensional diffraction pattern relative to the plane of the substrate, using a large stationary detector at a small distance from the sample, which allows the orientation of order and packing structures to be determined. The high radiation flux for this experiment is typically provided by a synchrotron source. Diffraction patterns of this type are often plotted in q-space, removing λ from the relationship to distance, but can converted to 2θ values for GIXRD comparisons:

$$q = \frac{4\pi}{\lambda}\sin\theta = \frac{2\pi}{d} \qquad \text{Equation 1.18}$$

As an example, a 2D GIWAXS pseudocolor plot for a neat P3HT film, from Chapter 3, is exhibited in Figure 1.16, with lamellar (edge-to-edge) diffractions

identified. These plots can be converted to 1D diffraction patterns by integrating across an angle, such as that outlined by the red lines. 1D patterns can sometimes reveal features difficult to observe in the pseudocolor plots, such as the weak π-π stacking feature at ca. 16.8 nm^{-1}, corresponding to a physical spacing of ca. 3.8 Å.

OPV active layers have often employed materials that arrange into highly ordered domains and as such GIXRD and GIWAXS have accordingly been used to determine degrees of order, π-π and lamellar packing distances.[99–102] In this thesis, these techniques were used in Chapters 2, 3, and 4 to characterize the effects of additives and material blending on the order of such active layers. Additional detail is given in the respective chapter.

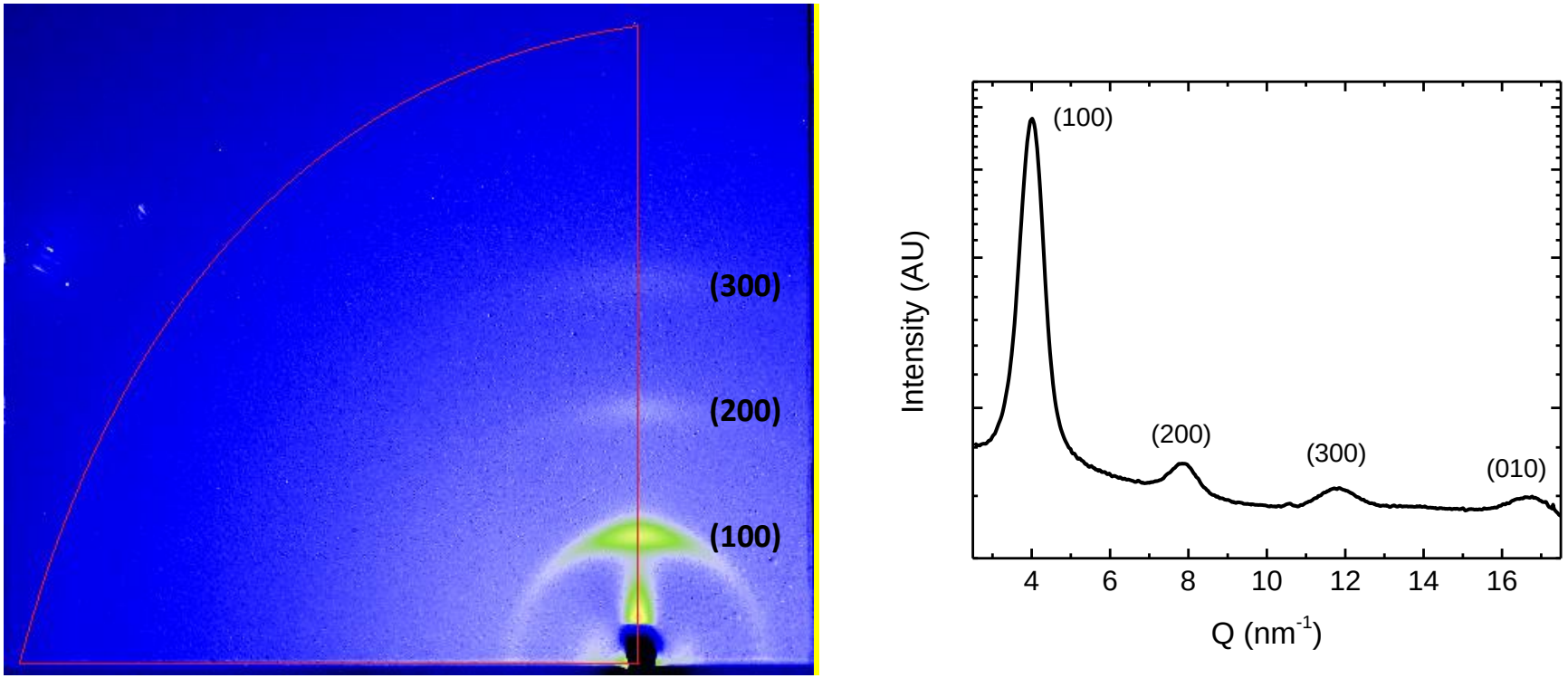

Figure 1.16. (left) A 2D GIWAXS pseudocolor plot for a neat P3HT film. Lamellar peaks (100, 200, 300) are identified. The red lines outline the region integrated to create the corresponding 1D plot (right). The lamellar feature at a ca. 4.0 nm^{-1} in q-space can be converted, via Equation 1.14, to 15.6 Å, and the π-π stacking feature at ca. 16.8 nm^{-1}, corresponds to a physical spacing of ca. 3.8 Å.

1.3 Conclusion

Great progress has been made in organic photovoltaics since the work of Kearns, Calvin, Kallmann, and Pope in the 1950s-60s, and especially in the last 20 years since the development of the bulk heterojunction by Heeger, Wudl, Friend, and Holmes, but many questions still remain. In particular, proper control of active layer morphology and microstructure as well as the effects of additive introduction on these properties are topics that require considerable attention as the field moves forward. The work in this thesis explores the employment of solid additives with the goal of customizing the electronic properties of the semiconductors in the OPV, as well as the morphological effects of their introduction in the BHJ, employing primarily the techniques described in Section 1.2 and others, explained within the respective chapters they are implemented. Ternary blend active layers, where a new component is added as a method of additive-based morphological control, attempting to improve electron transport through non-fullerene domains, is the focus of Chapter 2. Chapters 3 and 4 involve the use of molecular dopants for trap passivation with various polymers in the BHJ, and their ability to be dispersed with the local order of the system. Finally, Chapter 5 describes the introduction of molecular dopants into an amorphous inorganic charge-transport interlayer, with unexpected effects on oxide composition and device performance.

1.4 Works Cited

[1] H. Kallmann and M. Pope, “Positive Hole Injection into Organic Crystals,” *J. Chem. Phys.*, vol. 32, no. 1, p. 300, Jul. 1960.

[2] H. Kallmann and M. Pope, “Surface-controlled Bulk Conductivity in Organic Crystals,” *Nature*, vol. 185, no. 4715, pp. 753–753, Mar. 1960.

[3] C. Kittel and H. Kroemer, *Thermal Physics*. W. H. Freeman, 1980.

[4] A. G. MacDiarmid, “‘Synthetic Metals’: A Novel Role for Organic Polymers (Nobel Lecture),” *Angew. Chem. Int. Ed. Engl.*, vol. 40, no. 14, pp. 2581–2590, Jul. 2001.

[5] A. Bradley and J. P. Hammes, “Photoconductivity in Thin Organic Films,” *J. Electrochem. Soc.*, vol. 110, no. 6, p. 543, Jun. 1963.

[6] H. Inokuchi and H. Akamatu, “Electrical Conductivity of Organic Semiconductors,” *Solid State Phys.*, vol. 12, pp. 93–148, 1961.

[7] M. Sano, M. Pope, and H. Kallmann, “Electroluminescence and Band Gap in Anthracene,” *J. Chem. Phys.*, vol. 43, no. 8, p. 2920, May 1965.

[8] J. H. Burroughes, D. D. C. Bradley, A. R. Brown, R. N. Marks, K. Mackay, R. H. Friend, P. L. Burns, and A. B. Holmes, “Light-emitting diodes based on conjugated polymers,” *Nature*, vol. 347, no. 6293, pp. 539–541, Oct. 1990.

[9] W. Helfrich and W. G. Schneider, “Recombination Radiation in Anthracene Crystals,” *Phys. Rev. Lett.*, vol. 14, no. 7, pp. 229–231, Feb. 1965.

[10] C. W. Tang and S. A. VanSlyke, “Organic electroluminescent diodes,” *Appl. Phys. Lett.*, vol. 51, no. 12, p. 913, Sep. 1987.

[11] B. Bolto, R. McNeill, and D. Weiss, “Electronic Conduction in Polymers. III. Electronic Properties of Polypyrrole,” *Aust. J. Chem.*, vol. 16, no. 6, p. 1090, 1963.

[12] B. Bolto and D. Weiss, “Electronic Conduction in Polymers. II. The Electrochemical Reduction of Polypyrrole at Controlled Potential,” *Aust. J. Chem.*, vol. 16, no. 6, p. 1076, 1963.

[13] R. McNeill, R. Siudak, J. Wardlaw, and D. Weiss, “Electronic Conduction in Polymers. I. The Chemical Structure of Polypyrrole,” *Aust. J. Chem.*, vol. 16, no. 6, p. 1056, 1963.

[14] V. Coropceanu, J. Cornil, D. A. da Silva Filho, Y. Olivier, R. Silbey, and J.-L. Brédas, “Charge transport in organic semiconductors.,” *Chem. Rev.*, vol. 107, no. 4, pp. 926–52, Apr. 2007.

[15] A. J. Heeger, S. Kivelson, J. R. Schrieffer, and W.-P. Su, “Solitons in conducting polymers,” *Rev. Mod. Phys.*, vol. 60, no. 3, pp. 781–850, Jul. 1988.

[16] N. S. Sariciftci, L. Smilowitz, A. J. Heeger, and F. Wudl, “Photoinduced electron transfer from a conducting polymer to buckminsterfullerene.,” *Science*, vol. 258, no. 5087, pp. 1474–6, Nov. 1992.

[17] H. Shirakawa, E. J. Louis, A. G. MacDiarmid, C. K. Chiang, and A. J. Heeger, “Synthesis of electrically conducting organic polymers: halogen derivatives of polyacetylene, (CH) x,” *J. Chem. Soc. Chem. Commun.*, no. 16, p. 578, Jan. 1977.

[18] H. Sirringhaus, “Device Physics of Solution-Processed Organic Field-Effect Transistors,” *Adv. Mater.*, vol. 17, no. 20, pp. 2411–2425, Oct. 2005.

[19] W. Palz, *Power for the World: The Emergence of Electricity from the Sun*. Pan Stanford Publishing, 2010.

[20] W. Smith, “Effect of Light on Selenium During the Passage of An Electric Current,” *Nature*, vol. 7, no. 173, pp. 303–303, Feb. 1873.

[21] S. Bidwell, “On the Sensitiveness of Selenium to Light, and the Development of a similar Property in Sulphur,” *Proc. Phys. Soc. London*, vol. 7, no. 1, pp. 129–145, Feb. 1885.

[22] P. Gevorkian, *Sustainable Energy System Engineering: The Complete Green Building Design Resource*. McGraw Hill Professional, 2007.

[23] F. W. Sears, M. W. Zemansky, and H. D. Young, *University Physics, Part 1*. Addison-Wesley Pub. Co., 1982.

[24] A. Einstein, “Über einen die Erzeugung und Verwandlung des Lichtes betreffenden heuristischen Gesichtspunkt,” *Ann. Phys.*, vol. 322, no. 6, pp. 132–148, 1905.

[25] H. Hertz, “Ueber einen Einfluss des ultravioletten Lichtes auf die electrische Entladung,” *Ann. der Phys. und Chemie*, vol. 267, no. 8, pp. 983–1000, 1887.

[26] V. E. Lashkaryov, “Investigations of a Barrier Layer by the Thermoprobe Method,” *Izv. Akad. Nauk SSSR, Ser. Fiz.*, vol. 5, no. 4–5, pp. 442–446, 1941.

[27] R. S. Ohl, “Light-sensitive electric device,” US2402662 A, 25-Jun-1946.

[28] D. M. Chapin, C. S. Fuller, and G. L. Pearson, “A New Silicon p-n Junction Photocell for Converting Solar Radiation into Electrical Power,” *J. Appl. Phys.*, vol. 25, no. 5, p. 676, May 1954.

[29] J. Bardeen, “Surface States and Rectification at a Metal Semi-Conductor Contact,” *Phys. Rev.*, vol. 71, no. 10, pp. 717–727, May 1947.

[30] D. Kearns and M. Calvin, “Photovoltaic Effect and Photoconductivity in Laminated Organic Systems,” *J. Chem. Phys.*, vol. 29, no. 4, p. 950, Aug. 1958.

[31] A. K. Ghosh, D. L. Morel, T. Feng, R. F. Shaw, and C. A. Rowe, “Photovoltaic and rectification properties of Al/Mg phthalocyanine/Ag Schottky-barrier cells,” *J. Appl. Phys.*, vol. 45, no. 1, p. 230, Oct. 1974.

[32] S. Glenis, G. Tourillon, and F. Garnier, “Influence of the doping on the photovoltaic properties of thin films of poly-3-methylthiophene,” *Thin Solid Films*, vol. 139, no. 3, pp. 221–231, Jun. 1986.

[33] S. Karg, W. Riess, V. Dyakonov, and M. Schwoerer, “Electrical and optical characterization of poly(phenylene-vinylene) light emitting diodes,” *Synth. Met.*, vol. 54, no. 1–3, pp. 427–433, Mar. 1993.

[34] B. R. Weinberger, M. Akhtar, and S. C. Gau, “Polyacetylene photovoltaic devices,” *Synth. Met.*, vol. 4, no. 3, pp. 187–197, Mar. 1982.

[35] C. W. Tang, “Two-layer organic photovoltaic cell,” *Appl. Phys. Lett.*, vol. 48, no. 2, p. 183, Jan. 1986.

[36] M. A. El-Sharkawi, *Electric Energy: An Introduction*. CRC Press, 2004.

[37] E. V. Appleton, “Departure of Long-Wave Solar Radiation from Black-Body Intensity,” *Nature*, vol. 156, no. 3966, pp. 534–535, 1945.

[38] L. Salem, *The molecular orbital theory of conjugated systems*. W.A. Benjamin, 1966.

[39] S. Alvarado, P. Seidler, D. Lidzey, and D. Bradley, "Direct Determination of the Exciton Binding Energy of Conjugated Polymers Using a Scanning Tunneling Microscope," *Phys. Rev. Lett.*, vol. 81, no. 5, pp. 1082–1085, Aug. 1998.

[40] J.-L. Brédas, J. Cornil, and A. J. Heeger, "The exciton binding energy in luminescent conjugated polymers," *Adv. Mater.*, vol. 8, no. 5, pp. 447–452, May 1996.

[41] B. Kippelen and J.-L. Brédas, "Organic Photovoltaics," *Energy Environ. Sci.*, vol. 2, no. 3, p. 251, Mar. 2009.

[42] T. M. Clarke and J. R. Durrant, "Charge photogeneration in organic solar cells.," *Chem. Rev.*, vol. 110, no. 11, pp. 6736–67, Nov. 2010.

[43] W. C. Dunlap and R. L. Watters, "Direct Measurement of the Dielectric Constants of Silicon and Germanium," *Phys. Rev.*, vol. 92, no. 6, pp. 1396–1397, Dec. 1953.

[44] M. A. Green, "Improved value for the silicon free exciton binding energy," *AIP Adv.*, vol. 3, no. 11, p. 112104, Nov. 2013.

[45] I. Campbell, T. Hagler, D. Smith, and J. Ferraris, "Direct measurement of conjugated polymer electronic excitation energies using metal/polymer/metal structures.," *Phys. Rev. Lett.*, vol. 76, no. 11, pp. 1900–1903, Mar. 1996.

[46] P. W. M. Blom, V. D. Mihailetchi, L. J. A. Koster, and D. E. Markov, "Device Physics of Polymer:Fullerene Bulk Heterojunction Solar Cells," *Adv. Mater.*, vol. 19, no. 12, pp. 1551–1566, Jun. 2007.

[47] K. M. Pelzer and S. B. Darling, "Charge generation in organic photovoltaics: a review of theory and computation," *Mol. Syst. Des. Eng.*, vol. 1, no. 1, pp. 10-24, Feb. 2016.

[48] L. Onsager, "Initial Recombination of Ions," *Phys. Rev.*, vol. 54, no. 8, pp. 554–557, Oct. 1938.

[49] G. A. Buxton and N. Clarke, "Predicting structure and property relations in polymeric photovoltaic devices," *Phys. Rev. B*, vol. 74, no. 8, p. 085207, Aug. 2006.

[50] V. D. Mihailetchi, L. J. A. Koster, J. C. Hummelen, and P. W. M. Blom, “Photocurrent generation in polymer-fullerene bulk heterojunctions.,” *Phys. Rev. Lett.*, vol. 93, no. 21, p. 216601, Nov. 2004.

[51] V. D. Mihailetchi, L. J. A. Koster, and P. W. M. Blom, “Effect of metal electrodes on the performance of polymer:fullerene bulk heterojunction solar cells,” *Appl. Phys. Lett.*, vol. 85, no. 6, p. 970, Aug. 2004.

[52] V. D. Mihailetchi, L. J. A. Koster, P. W. M. Blom, C. Melzer, B. de Boer, J. K. J. van Duren, and R. A. J. Janssen, “Compositional Dependence of the Performance of Poly(p-phenylene vinylene):Methanofullerene Bulk-Heterojunction Solar Cells,” *Adv. Funct. Mater.*, vol. 15, no. 5, pp. 795–801, May 2005.

[53] M. Tachiya, “Breakdown of the Onsager theory of geminate ion recombination,” *J. Chem. Phys.*, vol. 89, no. 11, p. 6929, Dec. 1988.

[54] C. Deibel and V. Dyakonov, “Polymer–fullerene bulk heterojunction solar cells,” *Reports Prog. Phys.*, vol. 73, no. 9, p. 096401, Sep. 2010.

[55] C. L. Braun, “Electric field assisted dissociation of charge transfer states as a mechanism of photocarrier production,” *J. Chem. Phys.*, vol. 80, no. 9, p. 4157, May 1984.

[56] S. C. Graham, D. D. C. Bradley, R. H. Friend, and C. Spangler, “Raman and photoluminescence spectra of PPV oligomers,” *Synth. Met.*, vol. 41, no. 3, pp. 1277–1280, May 1991.

[57] J. E. Kroeze, T. J. Savenije, M. J. W. Vermeulen, and J. M. Warman, “Contactless Determination of the Photoconductivity Action Spectrum, Exciton Diffusion Length, and Charge Separation Efficiency in Polythiophene-Sensitized TiO 2 Bilayers,” *J. Phys. Chem. B*, vol. 107, no. 31, pp. 7696–7705, Aug. 2003.

[58] L. Luer, H. J. Egelhaaf, D. Oelkrug, G. Cerullo, G. Lanzani, B. H. Huisman, and D. de Leeuw, “Oxygen-induced quenching of photoexcited states in polythiophene films,” *Org. Electron.*, vol. 5, no. 1–3, pp. 83–89, Mar. 2004.

[59] A. Köhler and H. Bässler, *Electronic Processes in Organic Semiconductors: An Introduction*. John Wiley & Sons, 2015.

[60] S. Yoo, B. Domercq, and B. Kippelen, “Efficient thin-film organic solar cells based on pentacene/C_{60} heterojunctions,” *Appl. Phys. Lett.*, vol. 85, no. 22, p.

5427, Dec. 2004.

[61] J. J. M. Halls, C. A. Walsh, N. C. Greenham, E. A. Marseglia, R. H. Friend, S. C. Moratti, and A. B. Holmes, “Efficient photodiodes from interpenetrating polymer networks,” *Nature*, vol. 376, no. 6540, pp. 498–500, Aug. 1995.

[62] G. Yu, J. Gao, J. C. Hummelen, F. Wudl, and A. J. Heeger, “Polymer Photovoltaic Cells: Enhanced Efficiencies via a Network of Internal Donor-Acceptor Heterojunctions,” *Science (80-.).*, vol. 270, no. 5243, pp. 1789–1791, Dec. 1995.

[63] M. Hiramoto, H. Fujiwara, and M. Yokoyama, “Three-layered organic solar cell with a photoactive interlayer of codeposited pigments,” *Appl. Phys. Lett.*, vol. 58, no. 10, p. 1062, Mar. 1991.

[64] W. Cao and J. Xue, “Recent progress in organic photovoltaics: device architecture and optical design,” *Energy Environ. Sci.*, vol. 7, no. 7, p. 2123, Jun. 2014.

[65] W. Chen, M. P. Nikiforov, and S. B. Darling, “Morphology characterization in organic and hybrid solar cells,” *Energy Environ. Sci.*, vol. 5, no. 8, p. 8045, Jul. 2012.

[66] C. R. McNeill, “Morphology of all-polymer solar cells,” *Energy Environ. Sci.*, vol. 5, no. 2, p. 5653, Jan. 2012.

[67] J. S. Moon, J. Jo, and A. J. Heeger, “Nanomorphology of PCDTBT:$PC_{70}BM$ Bulk Heterojunction Solar Cells,” *Adv. Energy Mater.*, vol. 2, no. 3, pp. 304–308, Mar. 2012.

[68] S. H. Park, A. Roy, S. Beaupré, S. Cho, N. Coates, J. S. Moon, D. Moses, M. Leclerc, K. Lee, and A. J. Heeger, “Bulk heterojunction solar cells with internal quantum efficiency approaching 100%,” *Nat. Photonics*, vol. 3, no. 5, pp. 297–302, Apr. 2009.

[69] J. Peet, J. Y. Kim, N. E. Coates, W. L. Ma, D. Moses, A. J. Heeger, and G. C. Bazan, “Efficiency enhancement in low-bandgap polymer solar cells by processing with alkane dithiols.,” *Nat. Mater.*, vol. 6, no. 7, pp. 497–500, Jul. 2007.

[70] A. Ruseckas, P. E. Shaw, and I. D. W. Samuel, “Probing the nanoscale phase separation in binary photovoltaic blends of poly(3-hexylthiophene) and methanofullerene by energy transfer.,” *Dalt. Trans.*, no. 45, pp. 10040–3, Dec.

2009.

[71] D. Bartesaghi, I. D. C. Pérez, J. Kniepert, S. Roland, M. Turbiez, D. Neher, and L. J. A. Koster, “Competition between recombination and extraction of free charges determines the fill factor of organic solar cells.,” *Nat. Commun.*, vol. 6, p. 7083, Jan. 2015.

[72] H. Huang and J. Huang, Eds., *Organic and Hybrid Solar Cells*, vol. 25. Springer, 2014.

[73] S. Zhou and J.-X. Sun, “Mobility Dependent Efficiencies Of Organic Bulk-Heterojunction Solar Cells With Recombination Via Tail,” *Int. J. Mod. Phys. B*, vol. 27, no. 28, p. 1350167, Nov. 2013.

[74] S. R. Cowan, A. Roy, and A. J. Heeger, “Recombination in polymer-fullerene bulk heterojunction solar cells,” *Phys. Rev. B*, vol. 82, no. 24, p. 245207, Dec. 2010.

[75] V. Ramamurthy and K. S. Schanze, Eds., *Semiconductor Photochemistry And Photophysics/Volume Ten*. CRC Press, 2003.

[76] G. Lakhwani, A. Rao, and R. H. Friend, “Bimolecular recombination in organic photovoltaics.,” *Annu. Rev. Phys. Chem.*, vol. 65, pp. 557–81, Jan. 2014.

[77] S. Shoaee, T. M. Clarke, C. Huang, S. Barlow, S. R. Marder, M. Heeney, I. McCulloch, and J. R. Durrant, “Acceptor energy level control of charge photogeneration in organic donor/acceptor blends.,” *J. Am. Chem. Soc.*, vol. 132, no. 37, pp. 12919–26, Sep. 2010.

[78] E. Buchaca-Domingo, A. J. Ferguson, F. C. Jamieson, T. McCarthy-Ward, S. Shoaee, J. R. Tumbleston, O. G. Reid, L. Yu, M.-B. Madec, M. Pfannmöller, F. Hermerschmidt, R. R. Schröder, S. E. Watkins, N. Kopidakis, G. Portale, A. Amassian, M. Heeney, H. Ade, G. Rumbles, J. R. Durrant, and N. Stingelin, “Additive-assisted supramolecular manipulation of polymer:fullerene blend phase morphologies and its influence on photophysical processes,” *Mater. Horiz.*, vol. 1, no. 2, pp. 270–279, Feb. 2014.

[79] M. L. Chabinyc, M. F. Toney, R. J. Kline, I. McCulloch, and M. Heeney, “X-ray scattering study of thin films of poly(2,5-bis(3-alkylthiophen-2-yl)thieno[3,2-b]thiophene).,” *J. Am. Chem. Soc.*, vol. 129, no. 11, pp. 3226–37, Mar. 2007.

[80] I. McCulloch, M. Heeney, C. Bailey, K. Genevicius, I. Macdonald, M. Shkunov,

D. Sparrowe, S. Tierney, R. Wagner, W. Zhang, M. L. Chabinyc, R. J. Kline, M. D. McGehee, and M. F. Toney, “Liquid-crystalline semiconducting polymers with high charge-carrier mobility.,” *Nat. Mater.*, vol. 5, no. 4, pp. 328–33, Apr. 2006.

[81] D. Veldman, O. Ipek, S. C. J. Meskers, J. Sweelssen, M. M. Koetse, S. C. Veenstra, J. M. Kroon, S. S. van Bavel, J. Loos, and R. A. J. Janssen, “Compositional and electric field dependence of the dissociation of charge transfer excitons in alternating polyfluorene copolymer/fullerene blends.,” *J. Am. Chem. Soc.*, vol. 130, no. 24, pp. 7721–35, Jun. 2008.

[82] K. Han, J. Huang, S. Chai, S. Wen, and W. Deng, “Anisotropic Mobilities in Organic Semiconductors,” *Protoc. Exch.*, p. doi:10.103/protex.2013.070, 2013.

[83] V. Stehr, J. Pfister, R. F. Fink, B. Engels, and C. Deibel, “First-principles calculations of anisotropic charge-carrier mobilities in organic semiconductor crystals,” *Phys. Rev. B*, vol. 83, no. 15, p. 155208, Apr. 2011.

[84] W. Hourani, K. Rahimi, I. Botiz, F. P. V. Koch, G. Reiter, P. Lienerth, T. Heiser, J.-L. Bubendorff, and L. Simon, “Anisotropic charge transport in large single crystals of π-conjugated organic molecules.,” *Nanoscale*, vol. 6, no. 9, pp. 4774–80, May 2014.

[85] B. Fraboni, R. DiPietro, A. Castaldini, A. Cavallini, A. Fraleoni-Morgera, L. Setti, I. Mencarelli, and C. Femoni, “Anisotropic charge transport in organic single crystals based on dipolar molecules,” *Org. Electron.*, vol. 9, no. 6, pp. 974–978, Dec. 2008.

[86] J. E. Anthony, “Small-Molecule, Nonfullerene Acceptors for Polymer Bulk Heterojunction Organic Photovoltaics,” *Chem. Mater.*, vol. 23, no. 3, pp. 583–590, Feb. 2011.

[87] W. S. Shin, H.-H. Jeong, M.-K. Kim, S.-H. Jin, M.-R. Kim, J.-K. Lee, J. W. Lee, and Y.-S. Gal, “Effects of functional groups at perylene diimide derivatives on organic photovoltaic device application,” *J. Mater. Chem.*, vol. 16, no. 4, pp. 384–390, Jan. 2006.

[88] P. R. Buseck, S. J. Tsipursky, and R. Hettich, “Fullerenes from the geological environment.,” *Science*, vol. 257, no. 5067, pp. 215–7, Jul. 1992.

[89] H. W. Kroto, J. R. Heath, S. C. O’Brien, R. F. Curl, and R. E. Smalley, “C_{60}: Buckminsterfullerene,” *Nature*, vol. 318, no. 6042, pp. 162–163, Nov. 1985.

[90] J. C. Hummelen, B. W. Knight, F. LePeq, F. Wudl, J. Yao, and C. L. Wilkins, "Preparation and Characterization of Fulleroid and Methanofullerene Derivatives," *J. Org. Chem.*, vol. 60, no. 3, pp. 532–538, Feb. 1995.

[91] T. B. Singh, N. Marjanović, G. J. Matt, S. Günes, N. S. Sariciftci, A. Montaigne Ramil, A. Andreev, H. Sitter, R. Schwödiauer, and S. Bauer, "High-mobility n-channel organic field-effect transistors based on epitaxially grown C_{60} films," *Org. Electron.*, vol. 6, no. 3, pp. 105–110, Jun. 2005.

[92] P. M. Allemand, A. Koch, F. Wudl, Y. Rubin, F. Diederich, M. M. Alvarez, S. J. Anz, and R. L. Whetten, "Two different fullerenes have the same cyclic voltammetry," *J. Am. Chem. Soc.*, vol. 113, no. 3, pp. 1050–1051, Jan. 1991.

[93] J. M. Ball, R. K. M. Bouwer, F. B. Kooistra, J. M. Frost, Y. Qi, E. B. Domingo, J. Smith, D. M. de Leeuw, J. C. Hummelen, J. Nelson, A. Kahn, N. Stingelin, D. D. C. Bradley, and T. D. Anthopoulos, "Soluble fullerene derivatives: The effect of electronic structure on transistor performance and air stability," *J. Appl. Phys.*, vol. 110, no. 1, p. 014506, Jul. 2011.

[94] H. Yoshida, "Low-Energy Inverse Photoemission Study on the Electron Affinities of Fullerene Derivatives for Organic Photovoltaic Cells," *J. Phys. Chem. C*, vol. 118, no. 42, pp. 24377–24382, Oct. 2014.

[95] C. J. Brabec, A. Cravino, D. Meissner, N. S. Sariciftci, T. Fromherz, M. T. Rispens, L. Sanchez, and J. C. Hummelen, "Origin of the Open Circuit Voltage of Plastic Solar Cells," *Adv. Funct. Mater.*, vol. 11, no. 5, pp. 374–380, Oct. 2001.

[96] M. Keshavarz-K, B. Knight, R. C. Haddon, and F. Wudl, "Linear free energy relation of methanofullerene C61-substituents with cyclic voltammetry: Strong electron withdrawal anomaly," *Tetrahedron*, vol. 52, no. 14, pp. 5149–5159, Apr. 1996.

[97] F. B. Kooistra, J. Knol, F. Kastenberg, L. M. Popescu, W. J. H. Verhees, J. M. Kroon, and J. C. Hummelen, "Increasing the open circuit voltage of bulk-heterojunction solar cells by raising the LUMO level of the acceptor.," *Org. Lett.*, vol. 9, no. 4, pp. 551–4, Feb. 2007.

[98] M. T. Rispens, A. Meetsma, R. Rittberger, C. J. Brabec, N. S. Sariciftci, and J. C. Hummelen, "Influence of the solvent on the crystal structure of PCBM and the efficiency of MDMO-PPV:PCBM 'plastic' solar cells," *Chem. Commun.*, no. 17, pp. 2116–2118, Aug. 2003.

[99] H. Hoppe and N. S. Sariciftci, “Morphology of polymer/fullerene bulk heterojunction solar cells,” *J. Mater. Chem.*, vol. 16, no. 1, pp. 45–61, Dec. 2006.

[100] G. Li, V. Shrotriya, J. Huang, Y. Yao, T. Moriarty, K. Emery, and Y. Yang, “High-efficiency solution processable polymer photovoltaic cells by self-organization of polymer blends,” *Nat. Mater.*, vol. 4, no. 11, pp. 864–868, Oct. 2005.

[101] W. Ma, C. Yang, X. Gong, K. Lee, and A. J. Heeger, “Thermally Stable, Efficient Polymer Solar Cells with Nanoscale Control of the Interpenetrating Network Morphology,” *Adv. Funct. Mater.*, vol. 15, no. 10, pp. 1617–1622, Oct. 2005.

[102] X. Yang and J. Loos, “Toward High-Performance Polymer Solar Cells: The Importance of Morphology Control,” *Macromolecules*, vol. 40, no. 5, pp. 1353–1362, Mar. 2007.

[103] N. Blouin, A. Michaud, and M. Leclerc, “A Low-Bandgap Poly(2,7-Carbazole) Derivative for Use in High-Performance Solar Cells,” *Adv. Mater.*, vol. 19, no. 17, pp. 2295–2300, Sep. 2007.

[104] Z. He, C. Zhong, S. Su, M. Xu, H. Wu, and Y. Cao, “Enhanced power-conversion efficiency in polymer solar cells using an inverted device structure,” *Nat. Photonics*, vol. 6, no. September, pp. 593–597, 2012.

[105] Y. Liang, Z. Xu, J. Xia, S.-T. Tsai, Y. Wu, G. Li, C. Ray, and L. Yu, “For the bright future-bulk heterojunction polymer solar cells with power conversion efficiency of 7.4%.,” *Adv. Mater.*, vol. 22, no. 20, pp. E135–8, May 2010.

[106] M. P. Paranthaman, W. Wong-Ng, and R. N. Bhattacharya, *Semiconductor Materials for Solar Photovoltaic Cells*. Springer, 2015.

[107] D. H. Wang, J. K. Kim, J. H. Seo, I. Park, B. H. Hong, J. H. Park, and A. J. Heeger, “Transferable graphene oxide by stamping nanotechnology: electron-transport layer for efficient bulk-heterojunction solar cells.,” *Angew. Chem. Int. Ed. Engl.*, vol. 52, no. 10, pp. 2874–80, Mar. 2013.

[108] L. Ye, S. Zhang, W. Zhao, H. Yao, and J. Hou, “Highly Efficient 2D-Conjugated Benzodithiophene-Based Photovoltaic Polymer with Linear Alkylthio Side Chain,” *Chem. Mater.*, vol. 26, no. 12, pp. 3603–3605, Jun. 2014.

[109] J. Zhao, Y. Li, G. Yang, K. Jiang, H. Lin, H. Ade, W. Ma, and H. Yan, “Efficient organic solar cells processed from hydrocarbon solvents,” *Nat. Energy*, vol. 1,

no. 2, p. 15027, Jan. 2016.

[110] X. Zhan and D. Zhu, “Conjugated polymers for high-efficiency organic photovoltaics,” *Polym. Chem.*, vol. 1, no. 4, p. 409, May 2010.

[111] O. Inganäs, F. Zhang, K. Tvingstedt, L. M. Andersson, S. Hellström, and M. R. Andersson, “Polymer photovoltaics with alternating copolymer/fullerene blends and novel device architectures.,” *Adv. Mater.*, vol. 22, no. 20, pp. E100–16, May 2010.

[112] R. Noriega, A. Salleo, and A. J. Spakowitz, “Chain conformations dictate multiscale charge transport phenomena in disordered semiconducting polymers.,” *Proc. Natl. Acad. Sci. U. S. A.*, vol. 110, no. 41, pp. 16315–20, Oct. 2013.

[113] V. Skrypnychuk, G.-J. A. H. Wetzelaer, P. I. Gordiichuk, S. C. B. Mannsfeld, A. Herrmann, M. F. Toney, and D. R. Barbero, “Ultrahigh Mobility in an Organic Semiconductor by Vertical Chain Alignment,” *Adv. Mater.*, vol. 28, no. 12, p. 10.1002/adma.201503422, Jan. 2016.

[114] D. Venkateshvaran, M. Nikolka, A. Sadhanala, V. Lemaur, M. Zelazny, M. Kepa, M. Hurhangee, A. J. Kronemeijer, V. Pecunia, I. Nasrallah, I. Romanov, K. Broch, I. McCulloch, D. Emin, Y. Olivier, J. Cornil, D. Beljonne, and H. Sirringhaus, “Approaching disorder-free transport in high-mobility conjugated polymers,” *Nature*, vol. 515, no. 7527, pp. 384–388, Nov. 2014.

[115] W. Zhang, Y. Han, X. Zhu, Z. Fei, Y. Feng, N. D. Treat, H. Faber, N. Stingelin, I. McCulloch, T. D. Anthopoulos, and M. Heeney, “A Novel Alkylated Indacenodithieno[3,2-b]thiophene-Based Polymer for High-Performance Field-Effect Transistors.,” *Adv. Mater.*, Oct. 2015.

[116] X. Zhang, H. Bronstein, A. J. Kronemeijer, J. Smith, Y. Kim, R. J. Kline, L. J. Richter, T. D. Anthopoulos, H. Sirringhaus, K. Song, M. Heeney, W. Zhang, I. McCulloch, and D. M. DeLongchamp, “Molecular origin of high field-effect mobility in an indacenodithiophene-benzothiadiazole copolymer.,” *Nat. Commun.*, vol. 4, p. 2238, Jan. 2013.

[117] K. Cnops, G. Zango, J. Genoe, P. Heremans, M. V. Martinez-Diaz, T. Torres, and D. Cheyns, “Energy Level Tuning of Non-Fullerene Acceptors in Organic Solar Cells,” *J. Am. Chem. Soc.*, vol. 137, no. 28, pp. 8991–8997, Jul. 2015.

[118] O. K. Kwon, M. A. Uddin, J.-H. Park, S. K. S. Y. Park, T. L. Nguyen, H. Y. Woo, and S. K. S. Y. Park, “A High Efficiency Nonfullerene Organic Solar Cell

with Optimized Crystalline Organizations.," *Adv. Mater.*, vol. 28, no. 5, pp. 910–6, Feb. 2016.

[119] Y. Lin and X. Zhan, "Non-fullerene acceptors for organic photovoltaics: an emerging horizon," *Mater. Horizons*, vol. 1, no. 5, p. 470, Apr. 2014.

[120] C. B. Nielsen, S. Holliday, H.-Y. Chen, S. J. Cryer, and I. McCulloch, "Non-fullerene electron acceptors for use in organic solar cells.," *Acc. Chem. Res.*, vol. 48, no. 11, pp. 2803–12, Nov. 2015.

[121] M. Reyes-Reyes, K. Kim, and D. L. Carroll, "High-efficiency photovoltaic devices based on annealed poly(3-hexylthiophene) and 1-(3-methoxycarbonyl)-propyl-1- phenyl-(6,6)C61 blends," *Appl. Phys. Lett.*, vol. 87, no. 8, p. 083506, Aug. 2005.

[122] S. E. Shaheen, C. J. Brabec, N. S. Sariciftci, F. Padinger, T. Fromherz, and J. C. Hummelen, "2.5% efficient organic plastic solar cells," *Appl. Phys. Lett.*, vol. 78, no. 6, p. 841, Feb. 2001.

[123] H. Hoppe, M. Niggemann, C. Winder, J. Kraut, R. Hiesgen, A. Hinsch, D. Meissner, and N. S. Sariciftci, "Nanoscale Morphology of Conjugated Polymer/Fullerene-Based Bulk-Heterojunction Solar Cells," *Adv. Funct. Mater.*, vol. 14, no. 10, pp. 1005–1011, Oct. 2004.

[124] F. Padinger, R. S. Rittberger, and N. S. Sariciftci, "Effects of Postproduction Treatment on Plastic Solar Cells," *Adv. Funct. Mater.*, vol. 13, no. 1, pp. 85–88, Jan. 2003.

[125] Y. Kim, S. A. Choulis, J. Nelson, D. D. C. Bradley, S. Cook, and J. R. Durrant, "Device annealing effect in organic solar cells with blends of regioregular poly(3-hexylthiophene) and soluble fullerene," *Appl. Phys. Lett.*, vol. 86, no. 6, p. 063502, Jan. 2005.

[126] X. Yang, J. Loos, S. C. Veenstra, W. J. H. Verhees, M. M. Wienk, J. M. Kroon, M. A. J. Michels, and R. A. J. Janssen, "Nanoscale morphology of high-performance polymer solar cells.," *Nano Lett.*, vol. 5, no. 4, pp. 579–83, Apr. 2005.

[127] V. Shrotriya, Y. Yao, G. Li, and Y. Yang, "Effect of self-organization in polymer/fullerene bulk heterojunctions on solar cell performance," *Appl. Phys. Lett.*, vol. 89, no. 6, p. 063505, Aug. 2006.

[128] Y. Chen, X. Wan, and G. Long, "High performance photovoltaic applications

using solution-processed small molecules.," *Acc. Chem. Res.*, vol. 46, no. 11, pp. 2645–55, Nov. 2013.

[129] C. V. Kumar, L. Cabau, A. Viterisi, S. Biswas, G. D. Sharma, and E. Palomares, "Solvent Annealing Control of Bulk Heterojunction Organic Solar Cells with 6.6% Efficiency Based on a Benzodithiophene Donor Core and Dicyano Acceptor Units," *J. Phys. Chem. C*, vol. 119, no. 36, pp. 20871–20879, Sep. 2015.

[130] Y. Zhao, Z. Xie, Y. Qu, Y. Geng, and L. Wang, "Solvent-vapor treatment induced performance enhancement of poly(3-hexylthiophene):methanofullerene bulk-heterojunction photovoltaic cells," *Appl. Phys. Lett.*, vol. 90, no. 4, p. 043504, Jan. 2007.

[131] C. J. Brabec, U. Scherf, and V. Dyakonov, Eds., *Organic Photovoltaics: Materials, Device Physics, and Manufacturing Technologies*. Wiley, 2014.

[132] J. Seok, T. J. Shin, S. Park, C. Cho, J.-Y. Lee, D. Yeol Ryu, M. H. Kim, and K. Kim, "Efficient organic photovoltaics utilizing nanoscale heterojunctions in sequentially deposited polymer/fullerene bilayer.," *Sci. Rep.*, vol. 5, p. 8373, Jan. 2015.

[133] T. K. An, I. Kang, H. Yun, H. Cha, J. Hwang, S. Park, J. Kim, Y. J. Kim, D. S. Chung, S.-K. Kwon, Y.-H. Kim, and C. E. Park, "Solvent additive to achieve highly ordered nanostructural semicrystalline DPP copolymers: toward a high charge carrier mobility.," *Adv. Mater.*, vol. 25, no. 48, pp. 7003–9, Dec. 2013.

[134] D. Khatiwada, S. Venkatesan, E. C. Ngo, and Q. Qiao, "Versatile Role of Solvent Additive for Tailoring Morphology in Polymer Solar Cells for Efficient Charge Transport.," *J. Nanosci. Nanotechnol.*, vol. 15, no. 9, pp. 7040–4, Sep. 2015.

[135] J. Y. Na, B. Kang, D. H. Sin, K. Cho, and Y. D. Park, "Understanding Solidification of Polythiophene Thin Films during Spin-Coating: Effects of Spin-Coating Time and Processing Additives.," *Sci. Rep.*, vol. 5, p. 13288, Jan. 2015.

[136] L. A. Perez, J. T. Rogers, M. A. Brady, Y. Sun, G. C. Welch, K. Schmidt, M. F. Toney, H. Jinnai, A. J. Heeger, M. L. Chabinyc, G. C. Bazan, and E. J. Kramer, "The Role of Solvent Additive Processing in High Performance Small Molecule Solar Cells," *Chem. Mater.*, vol. 26, no. 22, pp. 6531–6541, Nov. 2014.

[137] T. Salim, L. H. Wong, B. Bräuer, R. Kukreja, Y. L. Foo, Z. Bao, and Y. M. Lam, "Solvent additives and their effects on blend morphologies of bulk

heterojunctions," *J. Mater. Chem.*, vol. 21, no. 1, pp. 242–250, Dec. 2011.

[138] X. Zhu, F. Zhang, Q. An, H. Huang, Q. Sun, L. Li, F. Teng, and W. Tang, "Effect of solvent additive and ethanol treatment on the performance of PIDTDTQx:$PC_{71}BM$ polymer solar cells," *Sol. Energy Mater. Sol. Cells*, vol. 132, pp. 528–534, Jan. 2015.

[139] W. Kim, J. K. Kim, E. Kim, T. K. Ahn, D. H. Wang, and J. H. Park, "Conflicted Effects of a Solvent Additive on PTB7:PC 71 BM Bulk Heterojunction Solar Cells," *J. Phys. Chem. C*, vol. 119, no. 11, pp. 5954–5961, Mar. 2015.

[140] N. D. Treat, J. A. Nekuda Malik, O. Reid, L. Yu, C. G. Shuttle, G. Rumbles, C. J. Hawker, M. L. Chabinyc, P. Smith, and N. Stingelin, "Microstructure formation in molecular and polymer semiconductors assisted by nucleation agents.," *Nat. Mater.*, vol. 12, no. 7, pp. 628–33, Jul. 2013.

[141] K. R. Graham, J. Mei, R. Stalder, J. W. Shim, H. Cheun, F. Steffy, F. So, B. Kippelen, and J. R. Reynolds, "Polydimethylsiloxane as a macromolecular additive for enhanced performance of molecular bulk heterojunction organic solar cells.," *ACS Appl. Mater. Interfaces*, vol. 3, no. 4, pp. 1210–1215, Apr. 2011.

[142] G. J. Chae, S.-H. Jeong, J. H. Baek, B. Walker, C. K. Song, and J. H. Seo, "Improved performance in TIPS-pentacene field effect transistors using solvent additives," *J. Mater. Chem. C*, vol. 1, no. 27, pp. 4216–4221, Jun. 2013.

[143] K. Ellmer, "Past achievements and future challenges in the development of optically transparent electrodes," *Nat. Photonics*, vol. 6, no. 12, pp. 809–817, Nov. 2012.

[144] I. Hamberg and C. G. Granqvist, "Evaporated Sn-doped In_2O_3 films: Basic optical properties and applications to energy-efficient windows," *J. Appl. Phys.*, vol. 60, no. 11, p. R123, Dec. 1986.

[145] Y. Zhou, T. M. Khan, J. W. Shim, A. Dindar, C. Fuentes-Hernandez, and B. Kippelen, "All-plastic solar cells with a high photovoltaic dynamic range," *J. Mater. Chem. A*, vol. 2, no. 10, p. 3492, Feb. 2014.

[146] K. P. Loh, S. W. Tong, and J. Wu, "Graphene and Graphene-like Molecules: Prospects in Solar Cells.," *J. Am. Chem. Soc.*, vol. 138, no. 4, pp. 1095–102, Feb. 2016.

[147] K. Sugiyama, H. Ishii, Y. Ouchi, and K. Seki, "Dependence of indium–tin–oxide

work function on surface cleaning method as studied by ultraviolet and x-ray photoemission spectroscopies," *J. Appl. Phys.*, vol. 87, no. 1, p. 295, Jan. 2000.

[148] P.-R. Huang, Y. He, C. Cao, and Z.-H. Lu, "The origin of the high work function of chlorinated indium tin oxide," *NPG Asia Mater.*, vol. 5, no. 8, p. e57, Aug. 2013.

[149] A. Sharma, B. Kippelen, P. J. Hotchkiss, and S. R. Marder, "Stabilization of the work function of indium tin oxide using organic surface modifiers in organic light-emitting diodes," *Appl. Phys. Lett.*, vol. 93, no. 16, p. 163308, Oct. 2008.

[150] W. Tress, *Organic Solar Cells: Theory, Experiment, and Device Simulation*, vol. 22. Springer, 2014.

[151] Y. Zhou, J. W. Shim, C. Fuentes-Hernandez, A. Sharma, K. A. Knauer, A. J. Giordano, S. R. Marder, and B. Kippelen, "Direct correlation between work function of indium-tin-oxide electrodes and solar cell performance influenced by ultraviolet irradiation and air exposure.," *Phys. Chem. Chem. Phys.*, vol. 14, no. 34, pp. 12014–21, Sep. 2012.

[152] M. G. Helander, Z. B. Wang, J. Qiu, and Z. H. Lu, "Band alignment at metal/organic and metal/oxide/organic interfaces," *Appl. Phys. Lett.*, vol. 93, no. 19, p. 193310, Nov. 2008.

[153] T.-H. Lai, S.-W. Tsang, J. R. Manders, S. Chen, and F. So, "Properties of interlayer for organic photovoltaics," *Mater. Today*, vol. 16, no. 11, pp. 424–432, Nov. 2013.

[154] J. Meyer, S. Hamwi, M. Kröger, W. Kowalsky, T. Riedl, and A. Kahn, "Transition metal oxides for organic electronics: energetics, device physics and applications.," *Adv. Mater.*, vol. 24, no. 40, pp. 5408–27, Oct. 2012.

[155] S. Chen, J. R. Manders, S.-W. Tsang, and F. So, "Metal oxides for interface engineering in polymer solar cells," *J. Mater. Chem.*, vol. 22, no. 46, p. 24202, Nov. 2012.

[156] S. R. Hammond, J. Meyer, N. E. Widjonarko, P. F. Ndione, A. K. Sigdel, A. Garcia, A. Miedaner, M. T. Lloyd, A. Kahn, D. S. Ginley, J. J. Berry, and D. C. Olson, "Low-temperature, solution-processed molybdenum oxide hole-collection layer for organic photovoltaics," *J. Mater. Chem.*, vol. 22, no. 7, p. 3249, Jan. 2012.

[157] B. Mustafa, J. Griffin, A. S. Alsulami, D. G. Lidzey, and A. R. Buckley,

"Solution processed nickel oxide anodes for organic photovoltaic devices," *Appl. Phys. Lett.*, vol. 104, no. 6, p. 063302, Feb. 2014.

[158] J. R. Manders, S.-W. Tsang, M. J. Hartel, T.-H. Lai, S. Chen, C. M. Amb, J. R. Reynolds, and F. So, "Solution-Processed Nickel Oxide Hole Transport Layers in High Efficiency Polymer Photovoltaic Cells," *Adv. Funct. Mater.*, vol. 23, no. 23, pp. 2993–3001, Jun. 2013.

[159] B. Ecker, H.-J. Egelhaaf, R. Steim, J. Parisi, and E. von Hauff, "Understanding S-Shaped Current–Voltage Characteristics in Organic Solar Cells Containing a TiOx Interlayer with Impedance Spectroscopy and Equivalent Circuit Analysis," *J. Phys. Chem. C*, vol. 116, no. 31, pp. 16333–16337, Aug. 2012.

[160] T. Hirao, M. Furuta, H. Furuta, T. Matsuda, T. Hiramatsu, H. Hokari, M. Yoshida, H. Ishii, and M. Kakegawa, "Novel top-gate zinc oxide thin-film transistors (ZnO TFTs) for AMLCDs," *J. Soc. Inf. Disp.*, vol. 15, no. 1, p. 17, 2007.

[161] L. K. Jagadamma, M. Al-Senani, A. El-Labban, I. Gereige, G. O. Ngongang Ndjawa, J. C. D. Faria, T. Kim, K. Zhao, F. Cruciani, D. H. Anjum, M. A. McLachlan, P. M. Beaujuge, and A. Amassian, "Polymer Solar Cells with Efficiency >10% Enabled via a Facile Solution-Processed Al-Doped ZnO Electron Transporting Layer," *Adv. Energy Mater.*, vol. 5, no. 12, p. 1500204, Apr. 2015.

[162] J. Kong, J. Lee, Y. Jeong, M. Kim, S.-O. Kang, and K. Lee, "Biased internal potential distributions in a bulk-heterojunction organic solar cell incorporated with a TiOx interlayer," *Appl. Phys. Lett.*, vol. 100, no. 21, p. 213305, May 2012.

[163] D. Liu and T. L. Kelly, "Perovskite solar cells with a planar heterojunction structure prepared using room-temperature solution processing techniques," *Nat. Photonics*, vol. 8, no. 2, pp. 133–138, Dec. 2013.

[164] G. B. Murdoch, S. Hinds, E. H. Sargent, S. W. Tsang, L. Mordoukhovski, and Z. H. Lu, "Aluminum doped zinc oxide for organic photovoltaics," *Appl. Phys. Lett.*, vol. 94, no. 21, p. 213301, May 2009.

[165] B.-Y. Oh, M.-C. Jeong, T.-H. Moon, W. Lee, J.-M. Myoung, J.-Y. Hwang, and D.-S. Seo, "Transparent conductive Al-doped ZnO films for liquid crystal displays," *J. Appl. Phys.*, vol. 99, no. 12, p. 124505, Jun. 2006.

[166] L. K. Jagadamma, M. Abdelsamie, A. El Labban, E. Aresu, G. O. Ngongang Ndjawa, D. H. Anjum, D. Cha, P. M. Beaujuge, and A. Amassian, "Efficient

inverted bulk-heterojunction solar cells from low-temperature processing of amorphous ZnO buffer layers," *J. Mater. Chem. A*, vol. 2, no. 33, p. 13321, Jun. 2014.

[167] K. Kim, S. Y. Park, K.-H. Lim, C. Shin, J.-M. Myoung, and Y. S. Kim, "Low temperature and solution-processed Na-doped zinc oxide transparent thin film transistors with reliable electrical performance using methanol developing and surface engineering," *J. Mater. Chem.*, vol. 22, no. 43, p. 23120, Oct. 2012.

[168] Y. Zhou, C. Fuentes-Hernandez, J. Shim, J. Meyer, A. J. Giordano, H. Li, P. Winget, T. Papadopoulos, H. Cheun, J. Kim, M. Fenoll, A. Dindar, W. Haske, E. Najafabadi, T. M. Khan, H. Sojoudi, S. Barlow, S. Graham, J.-L. Brédas, S. R. Marder, A. Kahn, and B. Kippelen, "A universal method to produce low-work function electrodes for organic electronics.," *Science*, vol. 336, no. 6079, pp. 327–32, Apr. 2012.

[169] A. G. Emslie, F. T. Bonner, and L. G. Peck, "Flow of a Viscous Liquid on a Rotating Disk," *J. Appl. Phys.*, vol. 29, no. 5, p. 858, Jun. 1958.

[170] D. Meyerhofer, "Characteristics of resist films produced by spinning," *J. Appl. Phys.*, vol. 49, no. 7, p. 3993, Aug. 1978.

[171] F. C. Krebs, "Fabrication and processing of polymer solar cells: A review of printing and coating techniques," *Sol. Energy Mater. Sol. Cells*, vol. 93, no. 4, pp. 394–412, Apr. 2009.

[172] L. Wengeler, M. Schmitt, K. Peters, P. Scharfer, and W. Schabel, "Comparison of large scale coating techniques for organic and hybrid films in polymer based solar cells," *Chem. Eng. Process. Process Intensif.*, vol. 68, pp. 38–44, Jun. 2013.

[173] Y.-H. Chang, S.-R. Tseng, C.-Y. Chen, H.-F. Meng, E.-C. Chen, S.-F. Horng, and C.-S. Hsu, "Polymer solar cell by blade coating," *Org. Electron.*, vol. 10, no. 5, pp. 741–746, Aug. 2009.

[174] J. Krantz, M. Richter, S. Spallek, E. Spiecker, and C. J. Brabec, "Solution-Processed Metallic Nanowire Electrodes as Indium Tin Oxide Replacement for Thin-Film Solar Cells," *Adv. Funct. Mater.*, vol. 21, no. 24, pp. 4784–4787, Dec. 2011.

[175] C. Waldauf, M. Morana, P. Denk, P. Schilinsky, K. Coakley, S. A. Choulis, and C. J. Brabec, "Highly efficient inverted organic photovoltaics using solution based titanium oxide as electron selective contact," *Appl. Phys. Lett.*, vol. 89, no. 23, p. 233517, Dec. 2006.

[176] B.-K. Yu, D. Vak, J. Jo, S.-I. Na, S.-S. Kim, M.-K. Kim, and D.-Y. Kim, "Factors to be Considered in Bulk Heterojunction Polymer Solar Cells Fabricated by the Spray Process," *IEEE J. Sel. Top. Quantum Electron.*, vol. 16, no. 6, pp. 1838–1846, Nov. 2010.

[177] C. Girotto, D. Moia, B. P. Rand, and P. Heremans, "High-Performance Organic Solar Cells with Spray-Coated Hole-Transport and Active Layers," *Adv. Funct. Mater.*, vol. 21, no. 1, pp. 64–72, Jan. 2011.

[178] J.-W. Kang, Y.-J. Kang, S. Jung, M. Song, D.-G. Kim, C. Su Kim, and S. H. Kim, "Fully spray-coated inverted organic solar cells," *Sol. Energy Mater. Sol. Cells*, vol. 103, pp. 76–79, Aug. 2012.

[179] J. E. Lewis, E. Lafalce, P. Toglia, and X. Jiang, "Over 30% transparency large area inverted organic solar array by spray," *Sol. Energy Mater. Sol. Cells*, vol. 95, no. 10, pp. 2816–2822, Oct. 2011.

[180] D. Angmo, M. Hösel, and F. C. Krebs, "All solution processing of ITO-free organic solar cell modules directly on barrier foil," *Sol. Energy Mater. Sol. Cells*, vol. 107, pp. 329–336, Dec. 2012.

[181] F. Jakubka, M. Heyder, F. Machui, J. Kaschta, D. Eggerath, W. Lövenich, F. C. Krebs, and C. J. Brabec, "Determining the coating speed limitations for organic photovoltaic inks," *Sol. Energy Mater. Sol. Cells*, vol. 109, pp. 120–125, Feb. 2013.

[182] F. C. Krebs, "All solution roll-to-roll processed polymer solar cells free from indium-tin-oxide and vacuum coating steps," *Org. Electron.*, vol. 10, no. 5, pp. 761–768, Aug. 2009.

[183] L. Wengeler, K. Peters, M. Schmitt, T. Wenz, P. Scharfer, and W. Schabel, "Fluid-dynamic properties and wetting behavior of coating inks for roll-to-roll production of polymer-based solar cells," *J. Coatings Technol. Res.*, vol. 11, no. 1, pp. 65–73, Apr. 2013.

[184] N. Li, D. Baran, K. Forberich, F. Machui, T. Ameri, M. Turbiez, M. Carrasco-Orozco, M. Drees, A. Facchetti, F. C. Krebs, and C. J. Brabec, "Towards 15% energy conversion efficiency: a systematic study of the solution-processed organic tandem solar cells based on commercially available materials," *Energy Environ. Sci.*, vol. 6, no. 12, p. 3407, Nov. 2013.

[185] Z. Liu, X. Ouyang, R. Peng, Y. Bai, D. Mi, W. Jiang, A. Facchetti, and Z. Ge, "Efficient polymer solar cells based on the synergy effect of a novel non-

conjugated small-molecule electrolyte and polar solvent," *J. Mater. Chem. A*, vol. 4, no. 7, pp. 2530–2536, Feb. 2016.

[186] X. Ouyang, R. Peng, L. Ai, X. Zhang, and Z. Ge, "Efficient polymer solar cells employing a non-conjugated small-molecule electrolyte," *Nat. Photonics*, vol. 9, no. 8, pp. 520–524, Jul. 2015.

[187] P. Würfel, *Physics of Solar Cells: From Principles to New Concepts*. Wiley, 2008.

[188] R. H. Bube, *Photovoltaic Materials*. Imperial College Press, 1998.

[189] M. C. Scharber, D. Mühlbacher, M. Koppe, P. Denk, C. Waldauf, A. J. Heeger, and C. J. Brabec, "Design Rules for Donors in Bulk-Heterojunction Solar Cells—Towards 10 % Energy-Conversion Efficiency," *Adv. Mater.*, vol. 18, no. 6, pp. 789–794, Mar. 2006.

[190] N. K. Elumalai and A. Uddin, "Open circuit voltage of organic solar cells: an in-depth review," *Energy Environ. Sci.*, vol. 9, no. 2, pp. 391–410, Feb. 2016.

[191] C. Poelking, M. Tietze, C. Elschner, S. Olthof, D. Hertel, B. Baumeier, F. Würthner, K. Meerholz, K. Leo, and D. Andrienko, "Impact of mesoscale order on open-circuit voltage in organic solar cells.," *Nat. Mater.*, vol. 14, no. 4, pp. 434–9, Apr. 2015.

[192] Z. Wang, Y. Uemura, Y. Zhou, T. Miyadera, R. Azumi, Y. Yoshida, and M. Chikamatsu, "Understanding device-structure-induced variations in open-circuit voltage for organic photovoltaics.," *ACS Appl. Mater. Interfaces*, vol. 7, no. 20, pp. 10814–22, May 2015.

[193] P. Yang, M. Yuan, D. F. Zeigler, S. E. Watkins, J. A. Lee, and C. K. Luscombe, "Influence of fluorine substituents on the film dielectric constant and open-circuit voltage in organic photovoltaics," *J. Mater. Chem. C*, vol. 2, no. 17, pp. 3278–3284, Apr. 2014.

[194] M. A. Green, "Solar cell fill factors: General graph and empirical expressions," *Solid. State. Electron.*, vol. 24, no. 8, pp. 788–789, Aug. 1981.

[195] Y. Liu, J. Zhao, Z. Li, C. Mu, W. Ma, H. Hu, K. Jiang, H. Lin, H. Ade, and H. Yan, "Aggregation and morphology control enables multiple cases of high-efficiency polymer solar cells.," *Nat. Commun.*, vol. 5, p. 5293, Jan. 2014.

[196] L. Lu, M. A. Kelly, W. You, and L. Yu, “Status and prospects for ternary organic photovoltaics,” *Nat. Photonics*, vol. 9, no. 8, pp. 491–500, Jul. 2015.

[197] L. Lu, T. Xu, W. Chen, E. S. Landry, and L. Yu, “Ternary blend polymer solar cells with enhanced power conversion efficiency,” *Nat. Photonics*, vol. 8, no. 9, pp. 716–722, Aug. 2014.

[198] Y. (Michael) Yang, W. Chen, L. Dou, W.-H. Chang, H.-S. Duan, B. Bob, G. Li, and Y. Yang, “High-performance multiple-donor bulk heterojunction solar cells,” *Nat. Photonics*, vol. 9, no. 3, pp. 190–198, Feb. 2015.

[199] A. Dai, Y. Zhou, A. L. Shu, S. K. Mohapatra, H. Wang, C. Fuentes-Hernandez, Y. Zhang, S. Barlow, Y. L. Loo, S. R. Marder, B. Kippelen, and A. Kahn, “Enhanced charge-carrier injection and collection via lamination of doped polymer layers p-doped with a solution-processible molybdenum complex,” *Adv. Funct. Mater.*, vol. 24, pp. 2197–2204, 2014.

[200] A. Higgins, S. K. Mohapatra, S. Barlow, S. R. Marder, and A. Kahn, “Dopant controlled trap-filling and conductivity enhancement in an electron-transport polymer,” *Appl. Phys. Lett.*, vol. 106, no. 16, p. 163301, Apr. 2015.

[201] V. Palenskis, “Drift Mobility, Diffusion Coefficient of Randomly Moving Charge Carriers in Metals and Other Materials with Degenerated Electron Gas,” *World J. Condens. Matter Phys.*, vol. 03, no. 01, pp. 73–81, Feb. 2013.

[202] H. Li, B. C.-K. Tee, J. J. Cha, Y. Cui, J. W. Chung, S. Y. Lee, and Z. Bao, “High-mobility field-effect transistors from large-area solution-grown aligned C_{60} single crystals.,” *J. Am. Chem. Soc.*, vol. 134, no. 5, pp. 2760–5, Feb. 2012.

[203] Z. An, J. Yu, S. C. Jones, S. Barlow, S. Yoo, B. Domercq, P. Prins, L. D. A. Siebbeles, B. Kippelen, and S. R. Marder, “High Electron Mobility in Room-Temperature Discotic Liquid-Crystalline Perylene Diimides,” *Adv. Mater.*, vol. 17, no. 21, pp. 2580–2583, Nov. 2005.

[204] B. Domercq, J. Yu, B. R. Kaafarani*, T. Kondo, S. Yoo, J. N. Haddock, S. Barlow, S. R. Marder, and B. Kippelen, “A Comparative Study of Charge Mobility Measurements in a Diamine and in a Hexaazatrinaphthylene Using Different Techniques,” *Mol. Cryst. Liq. Cryst.*, vol. 481, no. 1, pp. 80–93, Feb. 2008.

[205] T. M. Burke and M. D. McGehee, “How high local charge carrier mobility and an energy cascade in a three-phase bulk heterojunction enable >90% quantum efficiency.,” *Adv. Mater.*, vol. 26, no. 12, pp. 1923–8, Mar. 2014.

[206] N. Vukmirović, C. S. Ponseca, H. Němec, A. Yartsev, and V. Sundström, “Insights into the Charge Carrier Terahertz Mobility in Polyfluorenes from Large-Scale Atomistic Simulations and Time-Resolved Terahertz Spectroscopy,” *J. Phys. Chem. C*, vol. 116, no. 37, pp. 19665–19672, Sep. 2012.

[207] J. E. Lilienfeld, “Method and apparatus for controlling electric currents,” US1745175 A, 28-Jan-1930.

[208] J. N. Shurkin, *Broken Genius: The Rise and Fall of William Shockley, Creator of the Electronic Age*. Palgrave Macmillan, 2006.

[209] J. C. Blakesley, F. A. Castro, W. Kylberg, G. F. A. Dibb, C. Arantes, R. Valaski, M. Cremona, J. S. Kim, and J.-S. Kim, “Towards reliable charge-mobility benchmark measurements for organic semiconductors,” *Org. Electron.*, vol. 15, no. 6, pp. 1263–1272, Jun. 2014.

[210] C. Lombardo, “Lateral mobility measurements in organic bulk heterojunctions: comparison of field-effect and space charge mobilities,” *J. Photonics Energy*, vol. 2, no. 1, p. 021007, Apr. 2012.

[211] T. Akasaka, A. Osuka, S. Fukuzumi, H. Kandori, and Y. Aso, Eds., *Chemical Science of π-Electron Systems*, vol. 29. Springer, 2015.

[212] V. Gold and I. U. of P. and A. Chemistry, *Compendium of Chemical Terminology: IUPAC Recommendations*. Blackwell Scientific Publications, 1987.

[213] D. M. Hercules and S. H. Hercules, “Analytical chemistry of surfaces. Part I. General aspects,” *J. Chem. Educ.*, vol. 61, no. 5, p. 402, May 1984.

[214] M. P. Seah and W. A. Dench, “Quantitative electron spectroscopy of surfaces: A standard data base for electron inelastic mean free paths in solids,” *Surf. Interface Anal.*, vol. 1, no. 1, pp. 2–11, Feb. 1979.

[215] C. Nordling, E. Sokolowski, and K. Siegbahn, “Precision Method for Obtaining Absolute Values of Atomic Binding Energies,” *Phys. Rev.*, vol. 105, no. 5, pp. 1676–1677, Mar. 1957.

[216] D. W. Turner, *Molecular Photoelectron Spectroscopy*, vol. 75, no. 2. Wiley, 1971.

[217] J. W. Rabalais, *Principles of ultraviolet photoelectron spectroscopy*. Wiley,

1977.

[218] M. A. Cranswick, *Gas-phase Photoelectron Spectroscopy and Computational Studies of Metal-thiolate Interactions: Implications to Biological Electron Transfer*. ProQuest, 2008.

[219] G. K. Benning, “Atomic force microscope and method for imaging surfaces with atomic resolution,” US4724318 A, 09-Feb-1988.

[220] G. Binnig and C. F. Quate, “Atomic Force Microscope,” *Phys. Rev. Lett.*, vol. 56, no. 9, pp. 930–933, Mar. 1986.

[221] F. J. Giessibl, “AFM’s path to atomic resolution,” *Mater. Today*, vol. 8, no. 5, pp. 32–41, May 2005.

[222] P. Hapala, G. Kichin, C. Wagner, F. S. Tautz, R. Temirov, and P. Jelínek, “Mechanism of high-resolution STM/AFM imaging with functionalized tips,” *Phys. Rev. B*, vol. 90, no. 8, p. 085421, Aug. 2014.

[223] N. R. Wilson and J. V Macpherson, “Carbon nanotube tips for atomic force microscopy.,” *Nat. Nanotechnol.*, vol. 4, no. 8, pp. 483–91, Aug. 2009.

[224] N. A. Geisse, “AFM and combined optical techniques,” *Mater. Today*, vol. 12, no. 7–8, pp. 40–45, Jul. 2009.

[225] F. J. Giessibl, “Advances in atomic force microscopy,” *Rev. Mod. Phys.*, vol. 75, no. 3, pp. 949–983, Jul. 2003.

[226] L. Gross, F. Mohn, N. Moll, P. Liljeroth, and G. Meyer, “The chemical structure of a molecule resolved by atomic force microscopy.,” *Science*, vol. 325, no. 5944, pp. 1110–4, Aug. 2009.

[227] Q. Zhong, D. Inniss, K. Kjoller, and V. B. Elings, “Fractured polymer/silica fiber surface studied by tapping mode atomic force microscopy,” *Surf. Sci. Lett.*, vol. 290, no. 1–2, pp. L688–L692, Jun. 1993.

[228] R. Berger, A. L. Domanski, and S. A. L. Weber, “Electrical characterization of organic solar cell materials based on scanning force microscopy,” *Eur. Polym. J.*, vol. 49, no. 8, pp. 1907–1915, Aug. 2013.

[229] B. Bhushan, *Scanning Probe Microscopy in Nanoscience and Nanotechnology*

3. Springer Science & Business Media, 2012.

[230] M. Guide, X.-D. Dang, and T.-Q. Nguyen, "Nanoscale characterization of tetrabenzoporphyrin and fullerene-based solar cells by photoconductive atomic force microscopy.," *Adv. Mater.*, vol. 23, no. 20, pp. 2313–9, May 2011.

[231] J. Chen, X. Yu, K. Hong, J. M. Messman, D. L. Pickel, K. Xiao, M. D. Dadmun, J. W. Mays, A. J. Rondinone, B. G. Sumpter, and S. M. Kilbey II, "Ternary behavior and systematic nanoscale manipulation of domain structures in P3HT/PCBM/P3HT-b-PEO films," *J. Mater. Chem.*, vol. 22, no. 26, p. 13013, Jun. 2012.

[232] M. Shao, J. Keum, J. Chen, Y. He, W. Chen, J. F. Browning, J. Jakowski, B. G. Sumpter, I. N. Ivanov, Y.-Z. Ma, C. M. Rouleau, S. C. Smith, D. B. Geohegan, K. Hong, and K. Xiao, "The isotopic effects of deuteration on optoelectronic properties of conducting polymers.," *Nat. Commun.*, vol. 5, p. 3180, Jan. 2014.

[233] N. D. Treat, M. A. Brady, G. Smith, M. F. Toney, E. J. Kramer, C. J. Hawker, and M. L. Chabinyc, "Interdiffusion of PCBM and P3HT Reveals Miscibility in a Photovoltaically Active Blend," *Adv. Energy Mater.*, vol. 1, no. 1, pp. 82–89, Jan. 2011.

[234] W. H. Bragg and W. L. Bragg, "The Reflection of X-rays by Crystals," *Proc. R. Soc. A Math. Phys. Eng. Sci.*, vol. 88, no. 605, pp. 428–438, Jul. 1913.

[235] W. D. Callister and D. G. Rethwisch, *Materials Science and Engineering: An Introduction, 8th Edition*. Wiley, 2009.

[236] H. P. Myers, *Introductory Solid State Physics, Second Edition*. Taylor & Francis, 1997.

[237] S. W. H. Bragg, "The Structure of Organic Crystals," *Proc. Phys. Soc. London*, vol. 34, no. 1, pp. 33–50, Dec. 1921.

[238] R. W. G. Wyckoff and E. Posnjak, "The Crystal Structure Of Ammonium Chloroplatinate," *J. Am. Chem. Soc.*, vol. 43, no. 11, pp. 2292–2309, Nov. 1921.

[239] K. Lonsdale, "The Structure of the Benzene Ring : Abstract : Nature," *Nature*, vol. 122, p. 810, 1928.

[240] L. Pauling, *The Nature of the Chemical Bond and the Structure of Molecules and Crystals: An Introduction to Modern Structural Chemistry*. Cornell University

Press, 1960.

[241] S. W. H. Bragg, “The Crystalline Structure of Anthracene,” *Proc. Phys. Soc. London*, vol. 35, no. 1, pp. 167–169, Jan. 1922.

[242] W. C. Marra, “X-ray total-external-reflection–Bragg diffraction: A structural study of the GaAs-Al interface,” *J. Appl. Phys.*, vol. 50, no. 11, p. 6927, Jul. 1979.

[243] S. G. Podorov, N. N. Faleev, K. M. Pavlov, D. M. Paganin, S. A. Stepanov, and E. Förster, “A new approach to wide-angle dynamical X-ray diffraction by deformed crystals,” *J. Appl. Crystallogr.*, vol. 39, no. 5, pp. 652–655, Sep. 2006.

[244] S. G. Podorov and A. Nazarkin, “Wide-angle x-ray diffraction theory versus classical dynamical theory,” p. 7, Nov. 2009.

CHAPTER 2 DUAL-ACCEPTOR PERYLENE DIIMIDE TERNARY BULK HETEROJUNCTIONS IN ORGANIC PHOTOVOLTAIC DEVICES

2.1 Introduction

2.1.1 Ternary Bulk Heterojunctions in Organic Photovoltaics

In the past few years the field of organic photovoltaic (OPV) devices has undergone dramatic improvements. With the continuingly advancing synthesis of 'push-pull' donor polymers and small molecules, the power conversion efficiencies of the latest cells are starting to show promise of being able to compete with inorganic solar cells. However, it at this point it is widely thought that substantial progress is most likely to come from increased control of the active layer morphology.[1–4]

As discussed in Chapter 1, the wide implementation of the bulk heterojunction, designed to maximize interfacial area between the donor and acceptor phase,[5,6] has introduced a complex set of variables to the charge generation and transport processes, depending upon domain sizes, purity, order, and distribution. For example, small domain sizes can decrease the probability of successful charge separation (leading to geminate recombination) by limiting the distance over which two opposing charges can be separated during the initial steps of the process.[2] Also after charge separation has occurred, bimolecular recombination can take place between independent charges, especially in systems where an inadequate pathway exists for the charges to leave the active layer.[7] Rough surfaces and the presence of voids can increase the series resistance and lead to the presence of short-circuits.[8] Lastly, different materials will

naturally have different morphologies, depending on a number of factors including structure, polarity, and miscibility with the other compound as well as the solvent, making morphology optimization trends difficult to predict.

An approach that has received some attention is the use of ternary blends to improve charge generation/extraction or increase current density by harvesting a greater portion of the solar irradiance. A number of publications have reported short-circuit current density (J_{SC}) maximization and open-circuit voltage (V_{OC}) modulation by carefully controlling the ratio of two donor materials.[9–11] Of course, it was found that incorporation of a third material also yielded new morphological effects. The addition of controlled portions of regio-random poly(3-hexylthiophene) (P3HT) added to regio-regular P3HT:phenyl-C_{61}-butyric acid methylester ($PC_{61}BM$) blends were found to exhibit a higher degree of crystallinity with smaller crystalline domains than use of the purely regio-regular donor polymer, as observed by Campoy-Quiles *et al.*[12] A higher V_{OC} is also observed and it attributed to a higher polymer ionization energy caused by the isolated random chains. Li *et al*. also observed that the addition of small portions of poly[hepta-decanyl-carbazole-(dithienyl-benzothiadiazole)] (PCPDTBT) to P3HT:$PC_{61}BM$ blends can slightly increase the V_{OC} values but further addition will disrupt the film crystallinity and cause drastic drops in the J_{SC}.[13] An additional study performed by Lim *et al*. demonstrated that the incorporation of low-bandgap benzothiadiazole and thiophene-based oligomers into a P3HT:$PC_{61}BM$ cell caused increased P3HT crystallinity resulting in a higher J_{SC}.[14] A more crystalline version of the oligomer, featuring longer alkyl chains, actually lowered device efficiency.

2.1.2 Dual-Acceptor Ternary Bulk Heterojunctions

Ternary systems with multiple acceptors have yet to achieve any improvements in device performance, besides the use of specific fullerene blends[15] with P3HT.

Perhaps the second most studied acceptor material, after the fullerenes, are perylene diimides (PDIs).[16–18] As observed by Shoaee *et al*., P3HT:PDI thin films demonstrate considerable photoluminescence quenching, indicative of a favored electron transfer from the excited P3HT to the PDI.[19] These blends also show very efficient polaron yields at low driving forces for charge separation, relative to polymer:$PC_{61}BM$ blends, as observed by transient absorption spectroscopy. This is typically a sign of an effective charge separation process. Unfortunately, devices prepared from these P3HT:PDI blends have generally poor power conversion efficiencies (PCEs).[16,19,20] The primary cause, supported by the decay rate and timescales of absorption transients, is believed to be bimolecular recombination brought about by poor pathways for electron extraction through the PDI crystallites.

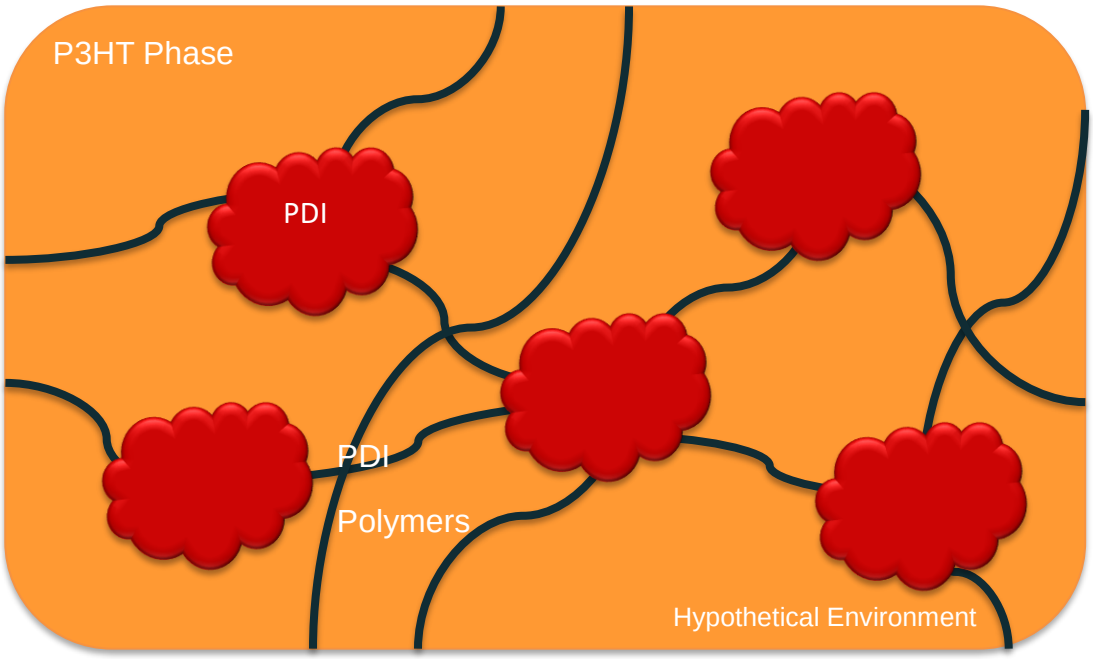

Figure 2.1**.** Hypothetical environment of the ternary P3HT/PDI/PDI polymer blend.

According to transmission electron microscopy and atomic force microscopy measurements, planar PDIs arrange into small crystalline phases on the order of tens of

nanometers within the larger P3HT phase.[19] This segregated morphology is considered to be detrimental to the ability of separated polarons to escape the active layer and be collected by the electrodes. However, previous research involving alternating PDI and dithienothiophene (DTT) polymers mixed with a branched polythiophene yielded successful OPV devices, with efficiencies up to 1.5%.[21] This work explores whether the incorporation of two PDI-derived acceptors into a ternary blend with P3HT could promote a morphology, involving interactions between PDI and PDI polymer phases (example in Figure 2.1), in which the separated charges will be provided with a suitable pathways to the electrode and thus have a higher probability of leaving the active layer and reaching their respective electrodes.

2.2 Methods & Results

2.2.1 Synthesis

A schematic representation of the synthesis work is shown in Figure 2.2. The small molecule *N,N'*-di(2-decyltetradecyl)perylene-3,4,9,10-tetracarboxylic diimide, referred to from this point on as PDI, was selected due to favorable electronic interactions with poly-3-hexylthiophene, indicated by strong photoluminescence quenching.[19] The side-chain precursor, 2-decyl-1-tetradecylamine, was synthesized by conversion from the alcohol by way of bromination followed by an Ing-Manske-modified Gabriel procedure as described by Guo *et al*.[22] PDI is formed upon condensation of this amine and perylene-3,4,9,10-tetracarboxylic acid anhydride.[23]

Poly{[*N*,*N*'-bis(2-decyl-tetradecyl)-3,4,9,10-perylene diimide-1,7-diyl]-*alt*-(dithieno[3,2-*b*:2',3'-*d*]thiophene-2,6-diyl)}, which will be referred to from this point as

the PDI polymer, shares the same side-chain as the small molecule and displays the highest electron mobility of PDI polymers to date.[24] The synthesis of the PDI polymer was achieved via Stille coupling of N,N'-bis(2-decyl-tetradecyl)-1,7-dibromo-3,4,9,10-perylene diimide, obtained by condensation of 2-decyl-1-tetradecylamine with 1,7-dibromoperylene-3,4,9,10-tetracarboxylic acid dianhydride (provided by Solvay), and 2,6-bis(tri-*n*-butylstannyl)dithieno[3,2-*b*:2',3'-*d*]thiophene, obtained by stannylation of 2,6-dibromodithieno[3,2-b:2',3'-d]thiophene (provided by Solvay) through bromine-lithium exchange followed by treatment with tri-*n*-butyltin chloride, as described by Zhan *et al.*[21] The PDI polymer was then purified by size-exclusion chromatography and Soxhlet extraction. All intermediates were characterized by ^{1}H nuclear magnetic resonance (NMR) spectroscopy, and final products were characterized additionally by ^{13}C NMR spectroscopy (not including Polymer PDI) and elemental analysis (at Atlantic Microlabs), with similar purity and yield to that being achieved in literature. As a note, 1,7-dibromoperylene-3,4,9,10-tetracarboxylic acid dianhydride will always contain some of the 1,6-dibrominated isomer that will persist through conversion to the diimide and polymerization, but only the former is shown for consistency.

The molecular weight distribution of the PDI polymer was determined using gel permeation chromatography (GPC). The weight average molecular weight (M_W), number average molecular weight (M_N) and polydispersity index (obtained by M_W/M_N) of the polymer were estimated on a PL-GPC Model 210 chromatograph at 35 °C, using THF as the eluent and polystyrene standards as calibrants. M_W, M_N, and the polydispersity index were determined to be ~ 25 kDa, ~ 11 kDa, and ~ 2.1 respectively, which are all slightly higher values than obtained by Zhan *et al.*;[21] the molecular weights might fall short of the actual value due to poor solubility of the higher molecular weight polymers in the given solvent.

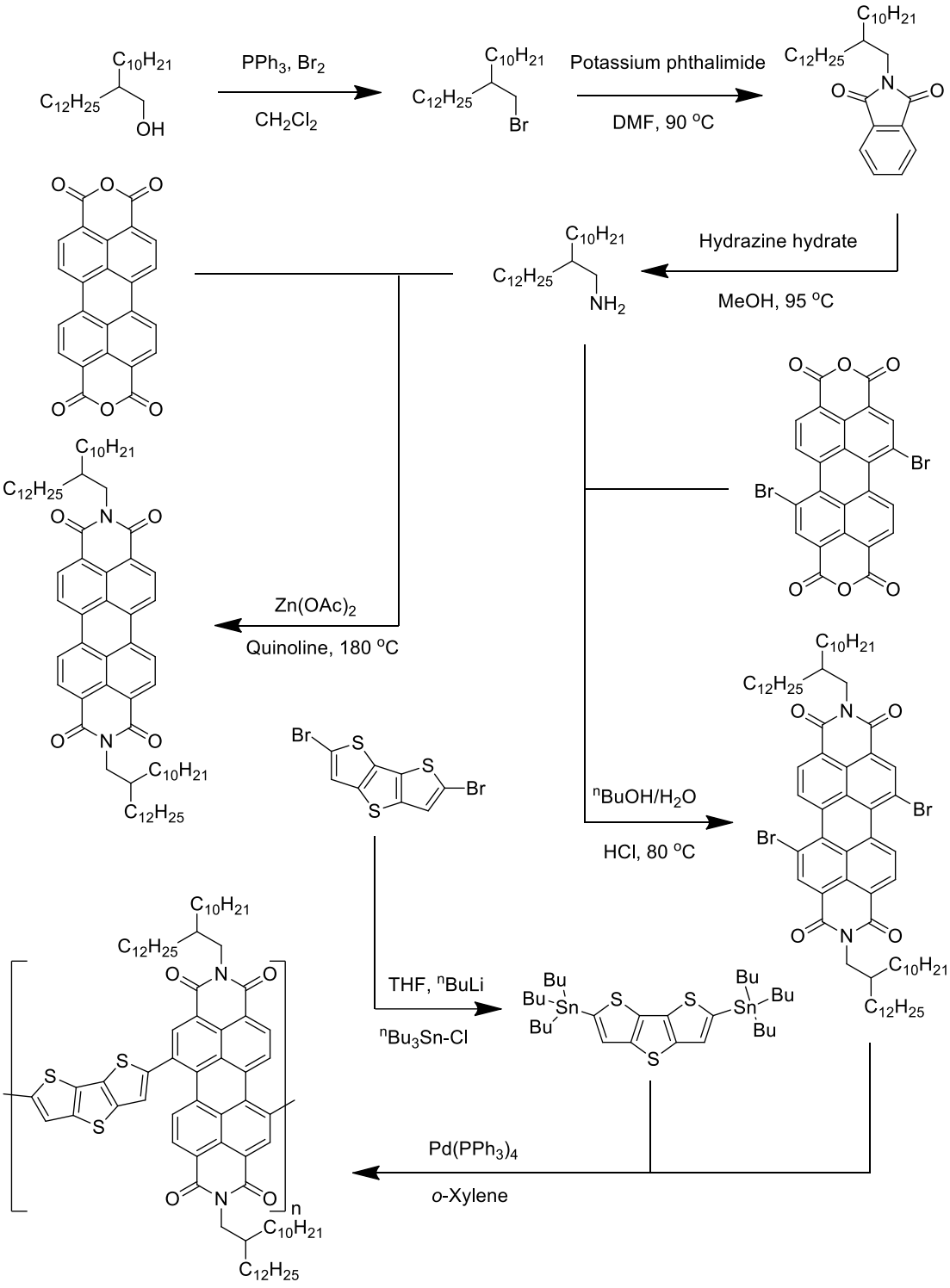

Figure 2.2. Reaction scheme outlining the formation of the two products, *N*,*N'*-di(2-decyl-tetradecyl)perylenetetracarboxylic-diimide and poly{[*N*,*N'*-bis(2-decyl-tetradecyl)-3,4,9,10-perylenediimide-1,7-diyl]-alt-(dithieno[3,2-*b*:2',3'-*d*]thiophene-2,6-diyl)}.

2.2.2 Differential Scanning Calorimetry

The thermal characteristics of these perylene derivatives, and their interactions with the donor polymer P3HT, were explored with differential scanning calorimetry (DSC). DSC thermoanalysis allows for the quantitative determination of phase transitions via the detected difference in thermal energy required to raise the temperature of a sample versus a reference material of known heat capacity. Data are plotted as the heat flow (given as power over sample mass) for a given temperature, and allow for the acquisition of transition points and enthalpies. Passing through endothermic/exothermic physical transitions, such as phase changes or glass transitions, will result in the absorption/release of a greater amount of heat per mass, and can manifest as peaks or depressions in the heat flow. The technique was invented by Michael J. O'Neill and Emmett S. Watson in 1962,[25] and commercialized the very next year. DSC has been employed quite extensively in the fields of organic electronics, used to probe the mixing and miscibilities of co-deposited materials such as those in bulk heterojunctions.[26–28]

DSC revealed several altered and/or new phase transitions depending on the donor:acceptor ratio in blended P3HT:PDI films, shown in Figure 2.3. Heterojunction films were drop-cast on solvent & UV-Ozone-cleaned glass substrates, then removed with a metal blade and sealed in a hermetic aluminum pan. An empty pan was used as the reference. Solutions were prepared with a total concentration of 10-15 mg/mL in chlorobenzene. All steps were performed in the inert environment of a glovebox. Drop-casting was implemented in lieu of spin-coating in order to collect sufficient sample required for an accurate measurement, ~ 3-5 mg. The second cooling cycle of samples is used to avoid solvent-related artifacts.

The enthalpy of PDI's melting transition is greatly suppressed by the presence of P3HT but the melting point does not strongly vary in temperature while it is visible (80-100 wt. % PDI), while the P3HT melting point is linearly lowered by the presence of PDI, but retains a reasonable enthalpy proportional to its concentration. Two new transitions are observed between these melting points, both appearing within the range of ~70-80 wt. % PDI (~50 mol. %). These data offer evidence that P3HT and PDI are expected to mix very well, rather than form neat, completely segregated, material phases. Blending the two materials and annealing results in very little of the pure ordered phase of PDI; likely the acceptor is distributed in the donor phase or forms a new ordered phase with the polymer, as evidenced by the depression of the P3HT melting point and the new transitions respectively.

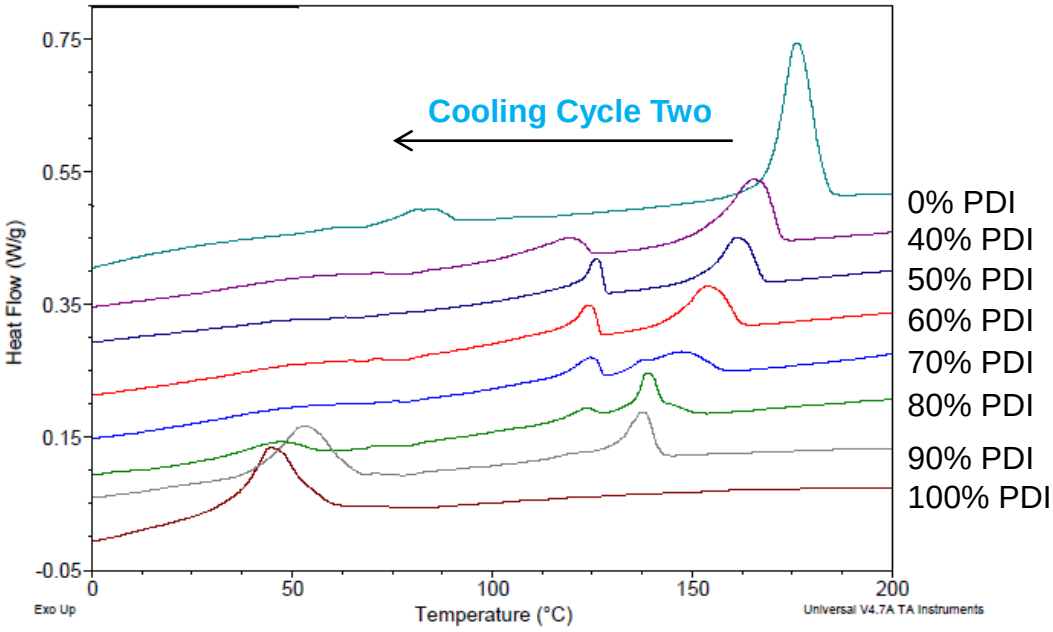

Figure 2.3. Differential scanning calorimetry of various blends of P3HT and PDI, given in wt. % of the PDI. The second cooling curve is shown to exclude solvent/processing effects.

Upon measuring DSC scans with a number of possible binary and ternary blends, exhibited in Figure 2.4, no thermal features were observed up to 400 ºC for neat Polymer PDI, but the incorporation of the polymer into films with P3HT and the small molecule PDI afforded some noticeable effects. The 1:1 by weight mixture of PDI with Polymer PDI caused a significant depression in the magnitude and area of the melting point of PDI, much greater than would be expected if the feature was simply reduced by half, accounting for dilution. It should also be noted that continued cycling of the temperature (heating to a maximum of 360 ºC and cooling down to -60 ºC) saw the complete disappearance of this thermal transition. A possible conclusion is the incorporation of the two materials into a single, poorly ordered phase, suggesting homogeneous blending of the two materials, a theory supported by the smooth films detected by atomic force microscopy to be seen in Figure 2.10. A 1:1:1 by weight mixtures of all three species results in a complicated curve, with certain characteristics resembling both the P3HT:PDI and the PDI:Polymer PDI binary blends. While drawing conclusions from this ternary mix is rather challenging, there seems to be evidence that PDI is interacting with both polymers, as revealed by the disappearance of the melting point of PDI and the depression of the melting point of P3HT.

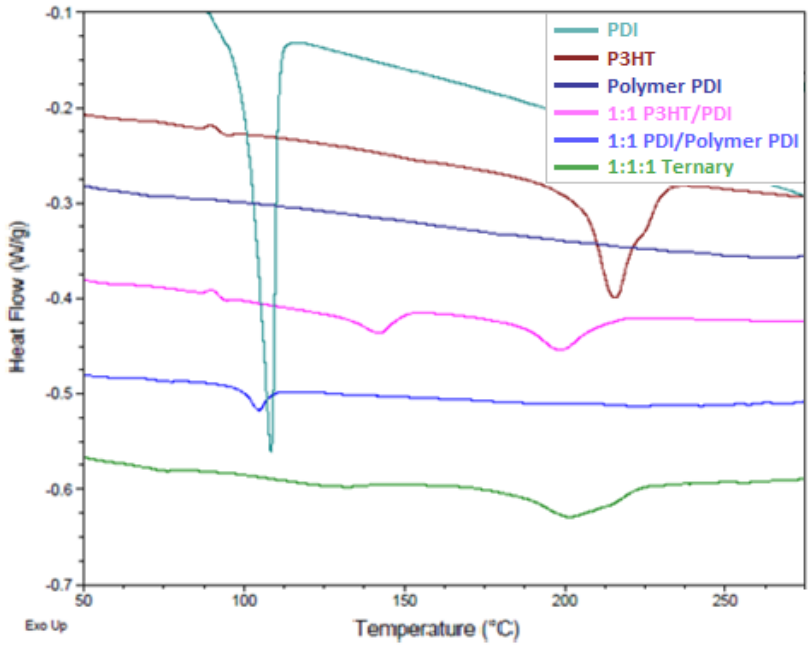

Figure 2.4. Differential scanning calorimetry (DSC) on neat P3HT, neat small molecule PDI, neat polymer PDI, and corresponding binary and ternary blends. The second heating curve is shown to remove solvent/processing effects.

2.2.3 Scanning Electron Microscopy

The film properties of P3HT:PDI heterojunctions were analyzed with scanning electron microscopy (SEM) in order to further explore the morphological characteristics of this blend. SEM is a surface measurement technique that can produce images as the result of various interactions between a focused electron beam and a sample, yielding information regarding surface composition and morphology with resolutions on the order of a nanometer. The invention of SEM is credited to Manfred von Ardenne, who in 1937 produced a high-magnification microscope with a minute raster scan of a beam of electrons, his work eventually leading to the construction of the first high-magnification SEM, and an expansion of SEM theory and detection modes.[29–31] SEM can be used in a number of modes, including for the detection of backscattering primary electrons, luminescence from relaxing electrons (which can be generated as valence electrons replenish secondary electron vacancies or by

cathodoluminescence), and, most commonly, ejected secondary electrons. SEM has been implemented in numerous organic electronic fields in order to study material microstructure, phase segregation, and layer interfaces.[26,32–34] Samples for SEM were prepared in the following manner: 200 nm-thick patterned ITO-on-glass substrates were sonicated in 5% vol/vol Triton X in water, water, acetone, and isopropanol, and then UV-ozone cleaned for 10 min. PEDOT:PSS (Clevios P VP Al 4083) was spin-cast at 4000 rpm for 45 s, then annealed at 120 °C for 10 min. 20 mg / mL chlorobenzene solutions of various ratios of P3HT:PDI were spun-cast at 1000 rpm for 60 s to give ~120 nm films. A thin layer (< 30 nm) of silver was then sputtered on top of the sample to combat charging effects. SEM was performed on an FEI Quanta microscope by Dr. Michael Clark at the Wright-Patterson Air Force Base.

As seen in Figure 2.5, SEM of P3HT:PDI films at various ratios revealed large features relative to those seen in P3HT:$PC_{61}BM$ films, with sizes of hundreds of nanometers in films containing larger concentrations of the perylene derivative. This appears to be in good agreement with the transmission electron microscopy results reported by Shoaee *et al.*,[19] who state that such morphologies lead to poor exciton dissociation as the excitons are unable to reach donor-acceptor interfaces. The DSC results from Section 2.2.2 also indicate that these large domains might be mixed phases of P3HT and PDI; specifically PDI could be incorporating into the P3HT phases, depressing the melting point of the polymer, as is observed for the 1:1 blend. The large features in the 1:4 P3HT:PDI blend could be a new blended phases, as the enthalpy for thermal transitions of the neat materials are pretty strongly suppressed.

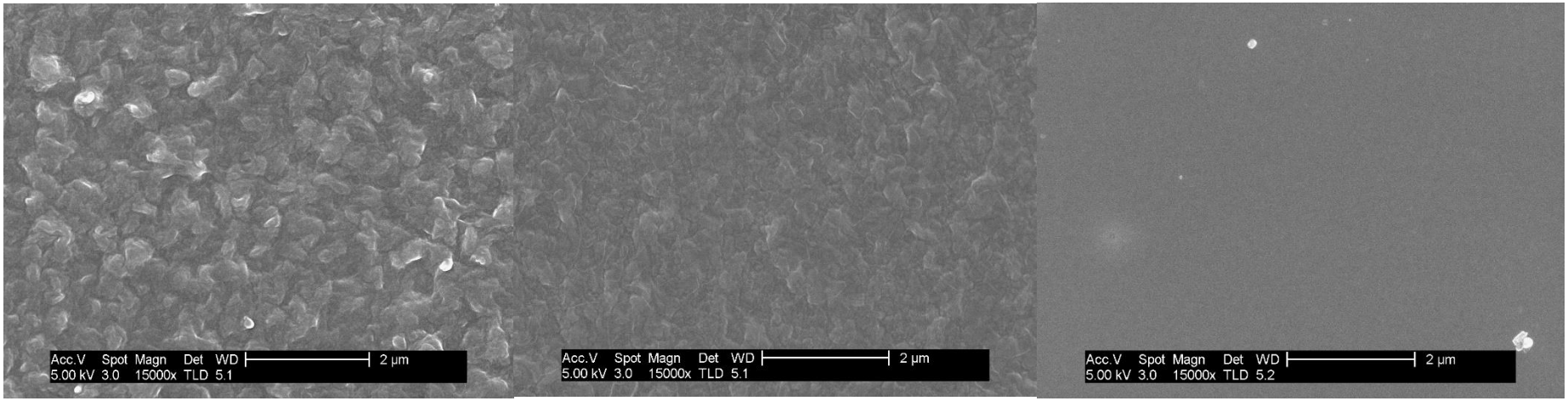

Figure 2.5. Scanning electron microscopy images of 1:4 P3HT:PDI (left), 1:1 P3HT:PDI (middle), and 1:1 P3HT:$PC_{61}BM$ (right) films spun-cast from *o*-dichlorobenzene, at 15000× magnification. SEM was performed on an FEI Quanta microscope by Dr. Michael Clark at the Wright-Patterson Air Force Base.

2.2.4 Grazing-Incidence Wide Angle X-ray Diffraction and Scattering

A detailed discussion of grazing-incidence X-ray diffraction (GIXRD) and grazing-incidence wide-angle X-ray scattering (GIWAXS) in BHJ OPV active layers was given in Chapter 1. GIWAXS and GIXRD of spin-cast films was performed at the Diamond Light Source (Beamline I07 – Surface and Interface Diffraction) at the Harwell Science and Innovation Campus in Oxfordshire, United Kingdom, and using a Rigaku ATX-G instrument at the Wright Patterson Air Force Base, respectively. The experimental parameters on Beamline I07 were established as a sample-to-detector distance of 33 cm, an X-ray wavelength of 1.378 Å, and the detector angles of 0.10-0.20°. Data were analyzed using Fit 2d. (http://www.esrf.eu/computing/scientific/FIT2D/) Samples were prepared in the following manner: 20 mg / mL chloroform solutions were for up to 1 hr in inert atmosphere. Solutions were spun-cast at 1500 rpm for 45 s on plasma-cleaned silicon substrates to achieve films ca. 120 nm in thickness, after which samples were annealed at 140 °C for 30 min. GIXRD patterns were recorded using a Smartlab system (Rigaku) with Cu Kα radiation (λ = 0.15418 nm) and measured in 2θ mode with an incidence angle of 0.1-0.2°. These samples were prepared in the following manner: 200 nm-thick patterned ITO-on-glass substrates were sonicated in 5% vol/vol Triton X in water, water, acetone, and isopropanol, and then UV-ozone cleaned for 10 min. PEDOT:PSS (Clevios P VP Al 4083) was spin-cast at 4000 rpm for 45 s, then annealed at 120 °C for 10 min. 20 mg / mL solutions of total material (binary or ternary blends) were prepared at various ratios, then spin-cast and annealed.

A comparison of the WAXS images of P3HT:PDI films is shown in Figure 2.6. The neat film of PDI displays a sharp intense (100) lamellar peak at q = 0.20 $Å^{-1}$ corresponding to distance of ca. 3.2 nm, with second and third order peaks at q = 0.40

Å^{-1} and q = 0.61 Å^{-1} respectively. Neat P3HT in turn has a somewhat broader (100) reflection at q = 0.40 Å^{-1}, corresponding a distance of ca. 1.6 nm, as is typically for the regio-regular polythiophene.[35–37] Upon blending, none of these features are specifically preserved, as would be expected for a complete lack of material miscibility. With increasing concentration of PDI, the P3HT feature normal to the plane fades in intensity, while the PDI feature appears to lose directionality and increases in q-value. The corresponding spacing decreases to 2.9 nm and 2.7 nm when the ratio of P3HT:PDI is changed to 1:4 and 1:1 respectively. These results seem indicate that indeed a mixed phase has formed between the two materials, as evidenced by the DSC data in Section 2.2.2.

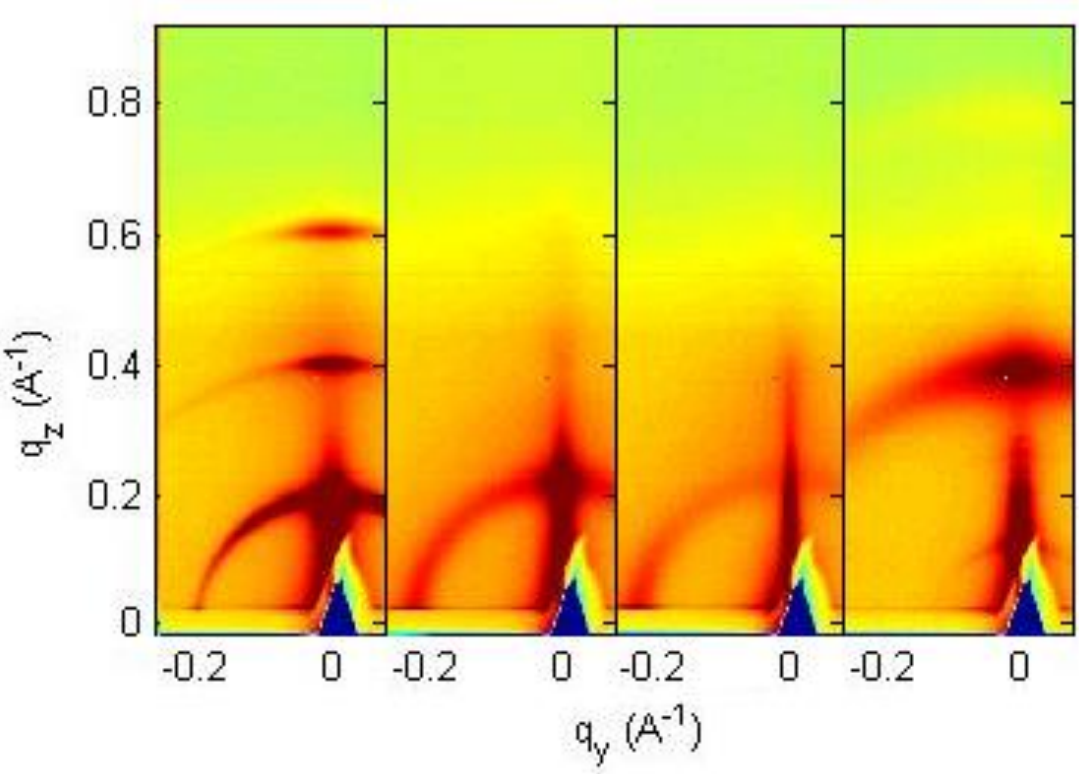

Figure 2.6. Comparison of observable features in grazing-incidence wide angle X-ray scattering images of films composed of neat small molecule PDI (left), a 1:4 by weight blend of P3HT and PDI (left middle), a 1:1 by weight blend of P3HT and PDI (right middle), and neat P3HT (right). Films were deposited from chloroform solutions at 1500 rpm for 45 seconds.

Grazing-incidence X-ray diffraction (GIXRD) of films processed in the same manner as the OPV devices in Figure 2.7 demonstrated consistent strong peaks related to the (100) lamellar packing of P3HT at 5.6º (ca. 1.6 nm) with second and third order diffraction peaks. However in P3HT:PDI films, the PDI (100) peak at ca. 3.0º (ca. 3.0 nm) however is much broader and weaker than as seen in neat films. Addition of Polymer PDI resulted in a further reduction of the small molecule crystallization peak, possibly indicating an interacting phase of the two acceptors that is more amorphous in nature. The neat polymer does not display a diffraction peak and, consistent with to its lack of thermal transitions as observed by differential scanning calorimetry, is most likely a rather amorphous material itself. Use of lower volatility solvents results in a disappearance of the P3HT stacking features, even with annealing, which is likely responsible for their poor performance (see Section 2.2.5). The lower order observed for the P3HT:PDI films in Figure 2.6 is related to this, as those films were prepared from chloroform.

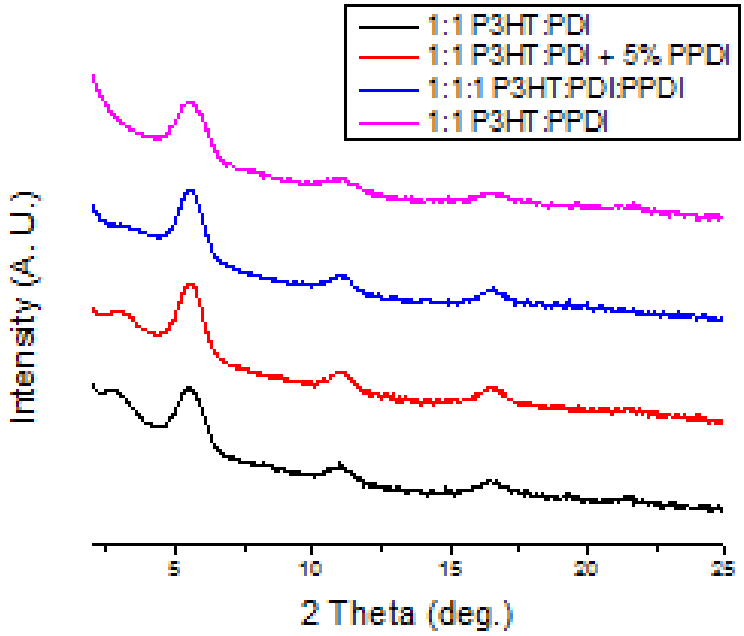

Figure 2.7. X-ray diffraction of organic photovoltaic cells prepared at the Wright Patterson Air Force Base with active layers deposited from *o*-dichlorobenzene. The diffraction peaks of PDI and P3HT appear at ca. 3.0º and 5.6º respectively; Polymer PDI does not exhibit any peaks in the region observed.

2.2.5 Organic Photovoltaic Devices

An in-depth discussion of organic photovoltaics theory and general processing procedures was given in Chapter 1. For the study in this chapter, photovoltaic devices were fabricated in the Solid State Device Laboratory at the Georgia Institute of Technology. 200 nm-thick patterned ITO-on-glass substrates were sonicated in 5% vol/vol Triton X in water, water, acetone, and isopropanol, and then UV-ozone cleaned for 10 min. PEDOT:PSS (Clevios P VP Al 4083) was spin-cast at 4000 rpm for 45 s, then annealed at 120 °C for 10 min. 20 mg / mL solutions of total material (binary or ternary blends) were prepared at various ratios, then spin-cast and annealed. 20 nm Ca and 100 nm Al were deposited above the active layer by thermal evaporation.

Devices prepared from P3HT:PDI blends gave performances consistently below 0.1% PCE, so the initial focus became to optimize P3HT:Polymer PDI OPVs. Previously, when blended with a bi(thienylenevinylene)-substituted polythiophene donor, Polymer PDI-based active layers gave OPV PCEs of over 1%.[21] Devices of ITO/PEDOT:PSS/P3HT:Polymer PDI/Ca/Al were optimized up to comparable values of ca. 0.7% PCE, with a 3:2 mass ratio, 120 nm thickness, *o*-dichlorobenzene solvent, and 140 ºC annealing for 45 min. Using this system as a reference, the polymer acceptor was gradually substituted with PDI, as a percentage of the total acceptor mass, shown in Figure 2.8. It was observed that the presence of the small molecule perylene derivative resulted in a rapid and steady decline of the V_{OC} and the fill factor, and began to adversely affect the current density at more substantial percentages. The open-circuit voltage decreases by 100, 220, and 250 mV for 5, 7.5 and 10 % incorporation of the small molecular into the total acceptor mass. The fill factor decreases from 55 to 38% overall. This large change is surprising, considering that it is a very small portion of the overall weight. Additionally, devices fabricated using a higher molecular weight P3HT and processed in the same way gave lower control PCEs and a short circuit current density increase at 5% and 10% addition of PDI, but still resulted in open-circuit voltage decreases simultaneously. This indicates that although the incorporation of PDI into the blend will have morphological effects on the polythiophene donor, these effects are likely not related to the drop in V_{OC}. A series of devices were also fabricated from chloroform or chlorobenzene but were much less efficient (<0.2% PCE) than those from *o*-dichlorobenzene, even with thermal annealing.

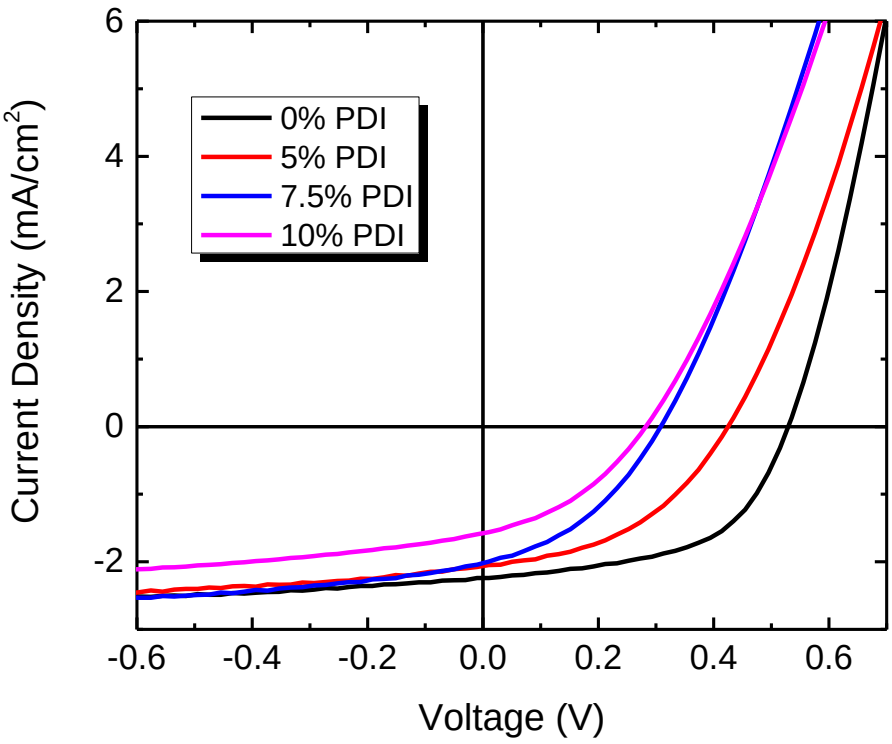

Figure 2.8. *J-V* curves demonstrating the decrease in performance due to PDI addition to photovoltaic devices of 3:2 P3HT:Polymer PDI.

Table 2.1. Device performance values of 3:2 P3HT:Polymer PDI devices with percentages of PDI addition by total acceptor mass.

Content PDI	J_{SC} **(mA/cm^2)**	V_{OC} **(V)**	***FF*** **(%)**	**PCE (%)**
0%	2.2 ± 0.1	0.53 ± 0.01	55 ± 1	0.65 ± 0.03
5%	2.1 ± 0.1	0.43 ± 0.02	44 ± 1	0.39 ± 0.01
7.5%	2.0 ± 0.1	0.31 ± 0.01	39 ± 1	0.24 ± 0.01
10%	1.6 ± 0.1	0.28 ± 0.01	38 ± 2	0.17 ± 0.01

2.2.6 Atomic Force Microscopy

An in-depth discussion of atomic force microscopy (AFM) relating to organic photovoltaic devices was given in Chapter 1. For the work in this chapter, AFM was

conducted on a Bruker Dimension Icon in tapping mode, using Bruker RTESP-150 antimony-doped silicon tips, and analyzed with Gwyddion SPM analysis software. 20 mg / mL o-dichlorobenzene solutions were spin-cast at 1000 rpm for 60 s on UV-ozone cleaned ITO substrates to give ca. 120 nm films. Samples were prepared under conditions similar to those used for OPV fabrication: 200 nm-thick patterned ITO-on-glass substrates were sonicated in 5% vol/vol Triton X in water, water, acetone, and isopropanol, and then UV-ozone cleaned for 10 min. PEDOT:PSS (Clevios P VP Al 4083) was spin-cast at 4000 rpm for 45 s, then annealed at 120 °C for 10 min. 20 mg / mL solutions of total material (binary or ternary blends) were prepared at various ratios, then spin-cast and annealed.

When observed by AFM, many of the binary and ternary blend films appear similar exhibiting lateral topographical features with dimensions of ca. 30 nm indicating a relatively smooth film, yet the phase scans, shown in Figure 2.9, are quite distinct. These images represent shifts in the oscillation of the cantilever caused by energy dissipation due to variations in mechanical compliance, which can be affected by the composition, friction, adhesiveness and viscoelasticity of the sample, where large differences can be interpreted as the presence of different materials or, at the very least, changes in a material's density. For blends of P3HT and PDI, large segregated phases are observed on the order of hundreds of nanometers, similar to the features noted in the SEM images in Figure 2.5. However the blends of P3HT:Polymer PDI display the familiar lamellar order of P3HT, indicating that the donor is pushed to the surface. Although this is counterintuitive to a good device structure, as the hole-extraction layer (PEDOT:PSS) is beneath the film, this is commonly seen on the surface of efficient P3HT/$PC_{61}BM$ films.[38–40] A 1:1:1 ternary blend of the three materials offers a picture unlike the other two, where the surface is not featureless, but there does not

seem to be a well-defined difference between donor and acceptor phases. There is also no lamellar pattern from P3HT, indicating that the presence of PDI is altering the vertical distribution of the donor and acceptor phases.

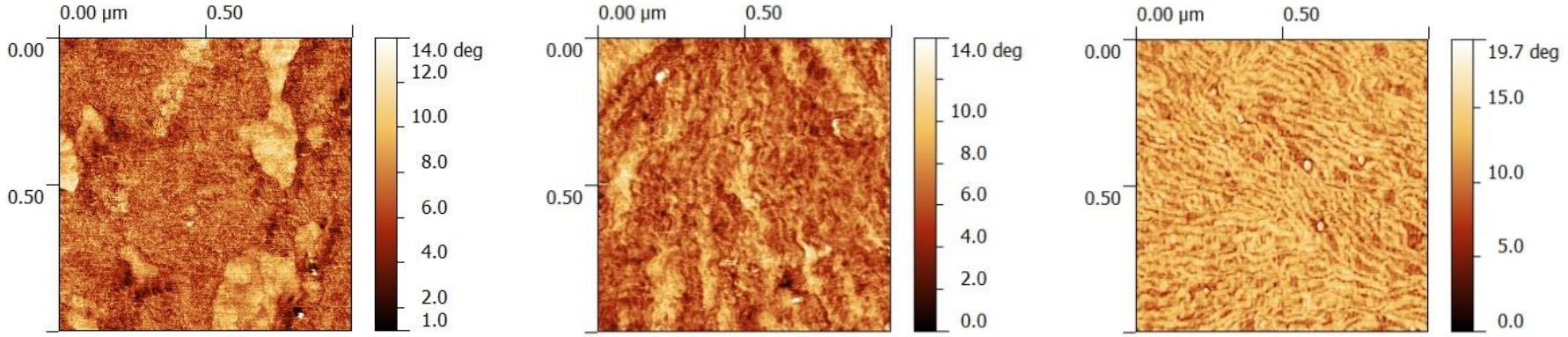

Figure 2.9. Phase atomic force microscopy images of films composed of a 1:1 by weight blend of P3HT and small molecule PDI (left), a 1:1:1 by weight ternary blend (middle), and a 1:1 by weight blend of P3HT and polymer PDI (right).

Taking a closer look at the interactions of the two acceptors together in Figure 2.10, AFM topographical scan displayed a transformation from rather smooth neat films (with slightly larger features in the PDI film) to an emergence of a rather rough surface, with what appear to be thin, sub-micron, plate-like features piled in levels. However, upon annealing the film at temperatures similar to those used in photovoltaic devices (140 ºC), a completely new image came into formation. The film now appeared very smooth, without discernible features, as though the materials had reached a very homogenous mixture. This could point to a thermal acceleration of the infusion of PDI into Polymer PDI to the point that the two form a new phase, as mentioned in Section 2.2.2. If this occurs inside the active layer upon annealing, it could lead to a drastic change in material properties. It is, however, also possible that the observations in the AFM originate from complete phase segregation, with one material sitting above the other due to electrostatic attraction/repulsion from the surface, which might also explain the pinholes in the annealed film. The small holes in the annealed film could be pinholes originating from dewetting at the substrate surface, though the AFM tip is unable to resolve the depth of such small features.

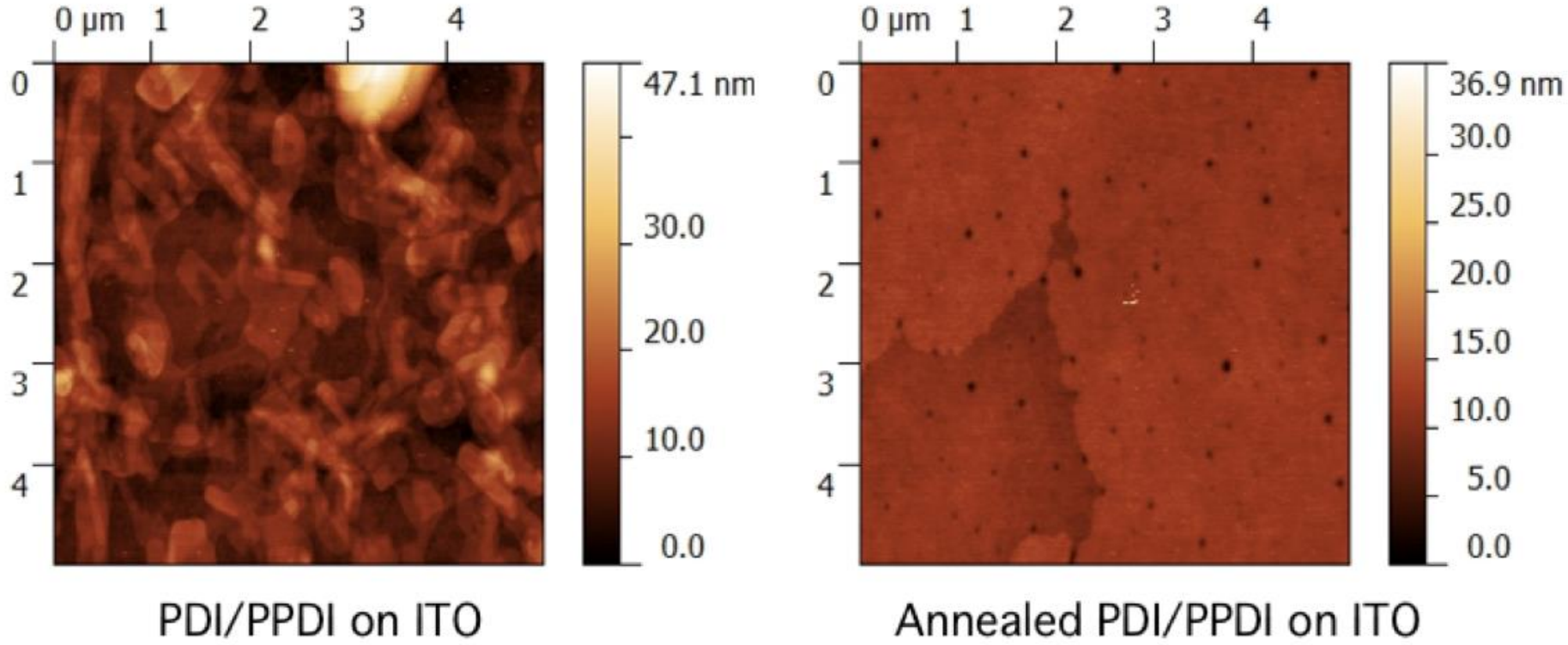

Figure 2.10. Atomic force microscopy images of a PDI:Polymer PDI film deposited from *o*-dichlorobenzene. Before annealing (left) the film is rough and stepped, but afterwards (right) it becomes much smoother.

This morphological perspective allows for a greater understanding of the ternary OPV film: after *o*-dichlorobenzene solvent and thermal annealing, P3HT has formed neat domains, though some of the material is possibly involved in amorphous regions with the other acceptors. The thermal treatment has resulted in well-blended acceptor phases that include both PDI and Polymer PDI, without any of the crystallinity or short-range order typical to the small molecule.

2.2.7 Electrochemical Thin Film Studies

In order to observe the effects of acceptor blending on the oxidation-reduction (redox) potentials of thin films, electrochemical measurements, more specifically cyclic and square-wave voltammetry, were performed on films cast on ITO/glass substrates. In general, electrochemistry describes the study of chemical reactions – which can be simple 1e-transfer reactions or more complex processes induced by electron-transfer – that occur on the interface between a biased electrode and an ionic conductor, which is often an electrolyte-populated solution. Determination of a material's electrochemical potentials relative to a given reference electrode, in solid-state or in solution, can be achieved with a potentiodynamic electrochemical measurement, such as cyclic voltammetry. The first oxidation and reduction potentials can then be used to estimate the solid-state ionization energies and electron affinities, respectively, relevant to organic electronics using the absolute potential of the reference system (although this is challenging to accurately determine) and making assumptions regarding the differences between solvation energies and solid-state polarization energies.

Attempts to understand the relationship between chemical reactions and electricity were first proposed by Luigi Galvani in 1791, when he sought to explain the effect of electricity on biological life forms, namely on nerves and muscles.[41] Soon after, the processes of electroplating and the electrolytic decomposition of water were

discovered by William Nicholson and Johann Wilhelm Ritter.[42] This work led to a number of developments over the next two centuries, including Michael Faraday's laws of electrochemistry, the development of the first fuel cell by William Grove in 1839, and the modern understanding of ionic disassociation and acid/base behavior from the work of Svante Arrhenius and Johannes Nicolaus Brønstead and Martin Lowry respectively.[43,44]

In cyclic voltammetry experiments, a cell will have three electrodes: the working electrode, at which the oxidation or reduction to be studied occurs at the appropriate bias, the counter electrode, which opposes the working electrode to maintain charge balance, and the reference electrode, of which the potential is known, but through which current does not flow. These electrodes are immersed in an electrolyte solution, ensuring conductivity, and the analyte, the material to be studied, is either co-dissolved in the solution or coated upon the working electrode. The bias between the working and reference electrodes is linearly scanned over time in a cyclical pattern, while the current between the working and counter electrodes is observed. For example, as a cathodic potential is applied, the reduction of the analyte will be evident in an increase of the current up to the reduction potential, after which the current will decrease as non-reduced species are fully consumed. Now sweeping the potential back in the opposite direction will result in an oxidation peak (with opposing current flow) assuming the reaction is reversible.

Electrochemical techniques on organic thin films to study solid-state redox potentials and electrochemical gaps has been applied extensively in work related to organic electronics, especially on blended materials.[45–48] Though electrolyte diffusion has the potential to distort I-V curve shapes, redox onsets can be compared qualitatively. In this work, electrochemistry was performed on thin films of the two

neat acceptors, and films of the two blended at 50:50 by weight, both pre- and post-annealing. The solutions containing polymer could be spin-cast on UV-ozone cleaned ITO without incident, but the solution of PDI in *o*-dichlorobenzene experienced substantial dewetting and had to be drop-cast. The films were vacuum dried and, with minimal atmospheric exposure, placed in an electrolyte solution of tetrabutylammonium hexafluorphosphate in propylene carbonate with a platinum flag as the counter electrode. The reference electrode used was Ag/AgCl, which was later calibrated against the ferrocenium / ferrocene couple, allowing determination of the plotted values. Cyclic voltammetry was performed on each of the films, after which the results in Figure 2.11 were recorded using squarewave voltammetry, where voltage is pulsed during each step of a linear sweep to reduce charging current, sweeping from 0 to -1.2 V and back versus the quasi-reference electrode.

An initial observation is that the *EA* (4.0 eV) of PDI, estimated from the onset relative to ferrocenium/ferrocene assuming a relation $EA = eE_{red} + 4.8$ eV, is clearly lower than that of the Polymer PDI (4.2 eV), so electron transfer from the 1e-reduced polymer to the PDI is anticipated to be endergonic. Accordingly, Polymer PDI to PDI electron transfer cannot explain the decrease in the V_{OC}. Exciton transfer between the two is also ruled out, as blended films of the two acceptors demonstrate photoluminescence quenching of both chromophores, which is enhanced with annealing. While the as-cast blended film exhibits an onset similar to the polymer, upon annealing the film the onset of the first reduction undergoes a cathodic shift by ~ 70 mV. Similar experiments with the pure films did not yield such shifts. This suggests that, as seen via AFM and DSC, Polymer PDI is being diluted into a more homogeneous mixture with PDI, in that the electronic interactions between polymers are weakening and, as such, the LUMO is destabilized. This destabilization of the acceptor LUMO

could account for the decrease in OPV performance if the charge transport is also being affected.

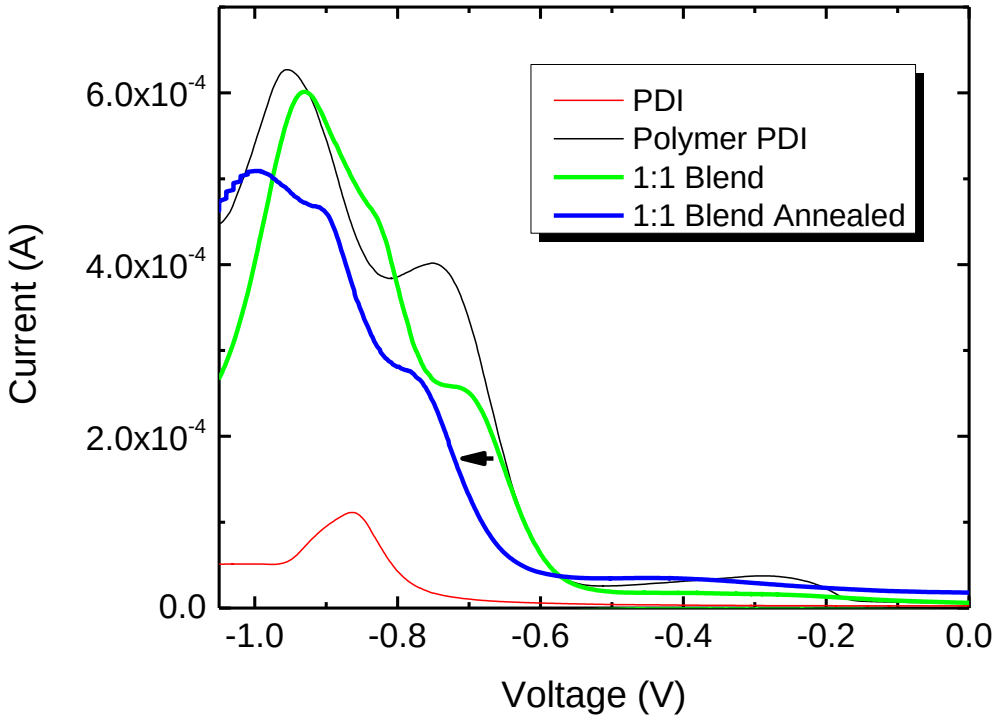

Figure 2.11. Square wave voltammetry of films of PDI, Polymer PDI, and a blend of the two prepared from *o*-dichlorobenzene, pre- and post-thermal annealing. The step size was 0.05 V with a current drop of 0.1 mA.

2.2.8 Time-Of-Flight Electron Mobility

The electron mobility in the neat and blended acceptor films was measured by time-of-flight (TOF) mobility. TOF-type measurements, used for a number of spectroscopic and spectrometric experiments, record the time required for a particle to travel a specific distance in a given medium. To determine electron mobility in this manner, a controlled laser pulse is directed through the transparent electrode of a metal-semiconductor-metal structure, typically at the absorbance peak of the semiconductor.

When a field is applied, charge carriers of one type, dictated by the applied bias direction, are swept immediately into the transparent electrode, whereas the charge carriers of opposite sign must traverse the bulk and are received at the opposing electrode. The mobility of the latter carriers is estimated as the velocity of the charge carrier (distance / time), divided by the applied electric field. This type of measurement has been implemented in organic materials as early as 1960, when the hole mobility of anthracene crystals was measured,[49] and has found extensive use with organic thin films for electronic applications.[50–53]

The TOF electron mobility was determined on thick (> 1 μm, exact thicknesses determined by profilometry) drop-cast films of neat Polymer PDI, and blended films of the two perylenediimide derivatives, on ITO, annealed under identical conditions to the OPV devices and capped with silver electrodes. The films were excited through the transparent electrode @ 600 nm under varying fields; the fit of mobility was extrapolated to a zero-field value. The hole mobilities of P3HT samples were also measured to ensure the integrity of the values. This TOF experiment was conducted by Dr. Christopher Bailey at the Wright Pattern Air Force Base.

The field-effect mobility of Polymer PDI has been reported previously to be 1.3×10^{-2} $cm^2/(Vs)$,[21] but these techniques differ substantially in terms of the region of charge transport (bulk vs. channel), the direction of charge transport to the surface (which will differ if the material is anisotropic) effects of contact resistance, and even film processing methods, diminishing the reliability of quantitative comparisons. FET mobility discussions were expanded in Chapter 1. Measured by TOF, neat Polymer PDI exhibits an impressive zero-field electron mobility of 1.4×10^{-1} $cm^2/(Vs)$, but this value is greatly diminished with very small additions of PDI, reduced by ~20 and 40 times when, respectively, 7.5% and 15% of the film's mass is composed of the small

molecule. Neat PDI was sufficiently not smooth at such thicknesses for meaningful measurement of TOF mobility. Fits of electron mobilities against electric field are shown in Figure 2.12. It is apparent that the introduction of PDI into Polymer PDI has greatly hampered the ability of the material to transport electrons. Consistent with the LUMO destabilization observed in electrochemical data in the previous section, the disruption of Polymer PDI interchain interactions by PDI has the potential to decrease interchain mobility; together this can account for the performance losses in OPV devices. As a note, negative mobility dependence on electric field has been explained in the past as the result of substantial spatial disorder in polythiophene films, and could perhaps be related to the drop-casting method of deposition.[54–56]

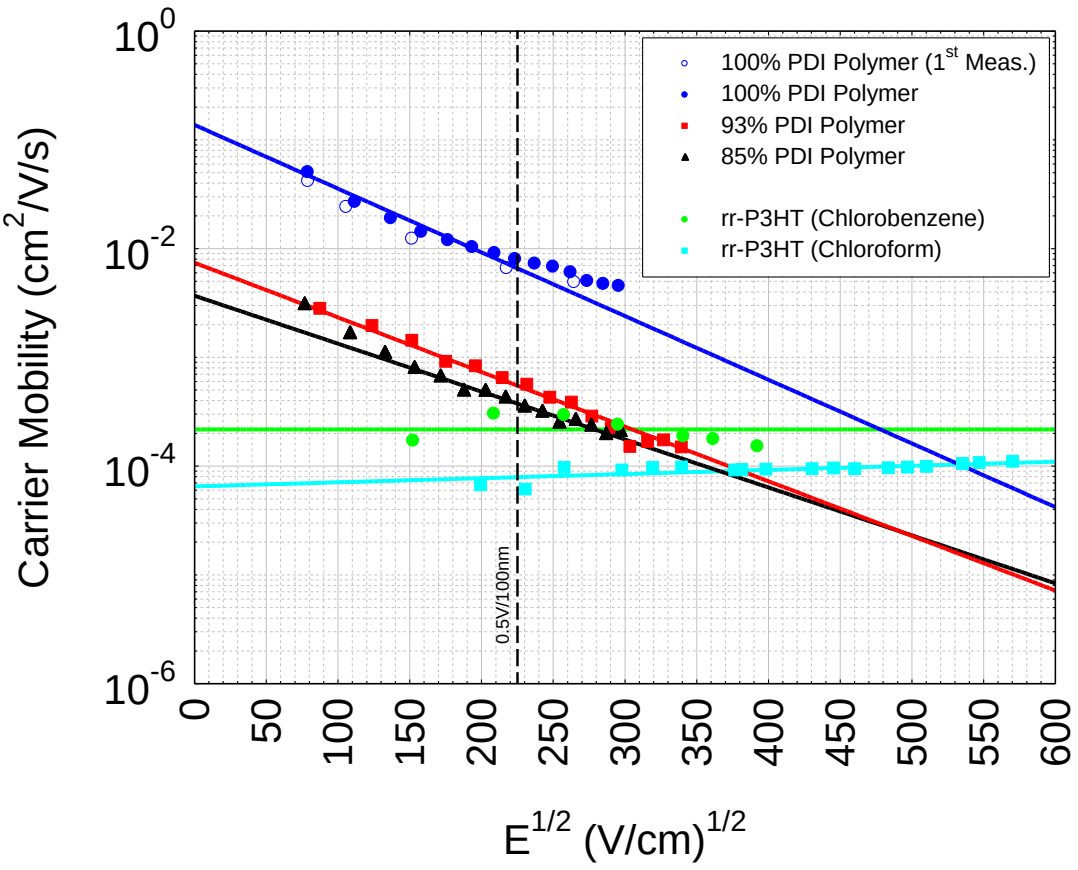

Figure 2.12. Time-of-flight carrier mobility of thick films of PDI, Polymer PDI, and P3HT, fitted to a zero-field value. This TOF experiment was conducted by Dr. Christopher Bailey at the Wright Pattern Air Force Base.

Table 2.2. Calculated charge mobilities of thick films of PDI, Polymer PDI, and P3HT, fitted to a zero-field value. P3HT films were cast from both chlorobenzene (a) and chloroform (b).

Material	**Film Thickness (μm)**	**Mobility (cm^2/(Vs)) @ 0 V/cm**
Polymer PDI	16	1.4×10^{-1}
Polymer PDI + 7.5% PDI	13	7.4×10^{-3}
Polymer PDI + 15% PDI	17	3.7×10^{-3}
P3HT[a]	0.69	2.2×10^{-4}
P3HT[b]	1.2	6.5×10^{-5}

2.3 Conclusion

Ternary organic photovoltaic devices were prepared using P3HT, small-molecule PDI, and Polymer PDI. Incorporation of PDI into optimized P3HT:Polymer PDI devices leads to reduction in device performance via open-circuit voltage and fill factor. In order to better understand the reason for the drop in V_{OC} observed in these ternary blends, a morphological study was conducted with atomic force microscopy, differential scanning calorimetry, and X-ray diffraction. These studies offered evidence that PDI and Polymer PDI, originally chosen for their miscibility, were blending together to form a new phase. Square wave voltammetry demonstrated that the electron affinity of the polymer is greater than that of the small molecule, ruling out a cascading electron transfer to the small molecule. Also observed was that the blend shared a first reduction onset with the pure polymer, but annealing the film resulted in a cathodic shift of this onset, which could be due to the interruption of Polymer PDI's intermolecular electronic coupling. This is difficult to confirm due to the lack of thermal and diffractive features in the blended films and films of the pure polymer, but a significant drop in the charge mobility of the acceptor phase was confirmed using TOF mobility. While it also might be possible that the materials phase segregate upon annealing, this would not coincide with the TOF trends. A possible representation of the blended environment, based on the AFM, DSC and WAXS results, is shown in Figure 2.13.

Figure 2.13. Hypothetical representation of the blended PDI and Polymer PDI phases surrounded by P3HT domains.

These findings can account for the drop in the open-circuit voltage observed in the ternary blends, as V_{OC} is affected not only by the *EA* of the acceptor and the *IE* of the donor, but on a number of properties that determine the carrier generation/recombination rate at the donor/acceptor interface, as discussed in Chapter 1. While efficient charge separation in P3HT:PDI blends has been established by Shoaee et al.,[19] similar experiments have not been performed for the other materials in this series, and the blending of acceptors could have an unforeseen effect on charge transport, facilitating a recombination process. As many materials applied in organic photovoltaics today have very limited short-range order, an understanding of the properties of blended amorphous phases could eventually lead to enhancements in material properties.

Greater morphological control of bulk heterojunction films through the use of ternary blend systems could open up the idea of multi-acceptor systems. This approach

could be carried over to other blends that are known to suffer from bimolecular recombination due to insufficient electron transport or to morphological complications. With newly accessible materials, some with possibly superior light-harvesting or charge-separating qualities, OPV cells with greater power conversion efficiencies can be manufactured. Exploration of these systems could also possibly provide a channel by which to lower our reliance on the morphological crutch provided by the expensive fullerene derivatives. Going further, different materials with alternative properties could be used to maximize the efficiency of separate processes: for example one acceptor species that interacts well with the donor and is effective at charge separation transfers the electron to another acceptor species with larger phase domains, higher electron mobility, and a lesser interaction with the donor.

2.4 Works Cited

[1] J.-L. Brédas, J. E. Norton, J. Cornil, and V. Coropceanu, "Molecular understanding of organic solar cells: the challenges.," *Acc. Chem. Res.*, vol. 42, no. 11, pp. 1691–9, Nov. 2009.

[2] T. M. Clarke and J. R. Durrant, "Charge photogeneration in organic solar cells.," *Chem. Rev.*, vol. 110, no. 11, pp. 6736–67, Nov. 2010.

[3] B. Kippelen and J.-L. Brédas, "Organic Photovoltaics," *Energy Environ. Sci.*, vol. 2, no. 3, p. 251, Mar. 2009.

[4] T. L. Benanti and D. Venkataraman, "Organic solar cells: an overview focusing on active layer morphology.," *Photosynth. Res.*, vol. 87, no. 1, pp. 73–81, Jan. 2006.

[5] J. Nelson, "Organic photovoltaic films," *Curr. Opin. Solid State Mater. Sci.*, vol. 6, no. 1, pp. 87–95, Feb. 2002.

[6] D. Kearns and M. Calvin, "Photovoltaic Effect and Photoconductivity in Laminated Organic Systems," *J. Chem. Phys.*, vol. 29, no. 4, p. 950, Aug. 1958.

[7] F. Yang, M. Shtein, and S. R. Forrest, "Controlled growth of a molecular bulk heterojunction photovoltaic cell," *Nat. Mater.*, vol. 4, no. 1, pp. 37–41, Dec. 2004.

[8] P. Peumans, S. Uchida, and S. R. Forrest, "Efficient bulk heterojunction photovoltaic cells using small-molecular-weight organic thin films.," *Nature*, vol. 425, no. 6954, pp. 158–62, Sep. 2003.

[9] P. P. Khlyabich, B. Burkhart, A. E. Rudenko, and B. C. Thompson, "Optimization and simplification of polymer–fullerene solar cells through polymer and active layer design," *Polymer (Guildf).*, vol. 54, no. 20, pp. 5267–5298, Sep. 2013.

[10] L. Lu, T. Xu, W. Chen, E. S. Landry, and L. Yu, "Ternary blend polymer solar cells with enhanced power conversion efficiency," *Nat. Photonics*, vol. 8, no. 9, pp. 716–722, Aug. 2014.

[11] L. Lu, M. A. Kelly, W. You, and L. Yu, "Status and prospects for ternary organic photovoltaics," *Nat. Photonics*, vol. 9, no. 8, pp. 491–500, Jul. 2015.

[12] M. Campoy-Quiles, Y. Kanai, A. El-Basaty, H. Sakai, and H. Murata, “Ternary mixing: A simple method to tailor the morphology of organic solar cells,” *Org. Electron.*, vol. 10, no. 6, pp. 1120–1132, Sep. 2009.

[13] N. Li, F. Machui, D. Waller, M. Koppe, and C. J. Brabec, “Determination of phase diagrams of binary and ternary organic semiconductor blends for organic photovoltaic devices,” *Sol. Energy Mater. Sol. Cells*, vol. 95, no. 12, pp. 3465–3471, Dec. 2011.

[14] E. Lim, S. Lee, and K. K. Lee, “Improved photovoltaic performance of P3HT:PCBM cells by addition of a low band-gap oligomer.,” *Chem. Commun. (Camb).*, vol. 47, no. 3, pp. 914–6, Jan. 2011.

[15] P. P. Khlyabich, B. Burkhart, and B. C. Thompson, “Efficient ternary blend bulk heterojunction solar cells with tunable open-circuit voltage.,” *J. Am. Chem. Soc.*, vol. 133, no. 37, pp. 14534–7, Sep. 2011.

[16] J. E. Anthony, “Small-Molecule, Nonfullerene Acceptors for Polymer Bulk Heterojunction Organic Photovoltaics,” *Chem. Mater.*, vol. 23, no. 3, pp. 583–590, Feb. 2011.

[17] M. C. R. Delgado, E.-G. Kim, D. A. da Silva Filho, and J.-L. Bredas, “Tuning the charge-transport parameters of perylene diimide single crystals via end and/or core functionalization: a density functional theory investigation.,” *J. Am. Chem. Soc.*, vol. 132, no. 10, pp. 3375–87, Mar. 2010.

[18] J. Li, F. Dierschke, J. Wu, A. C. Grimsdale, and K. Müllen, “Poly(2,7-carbazole) and perylene tetracarboxydiimide: a promising donor/acceptor pair for polymer solar cells,” *J. Mater. Chem.*, vol. 16, no. 1, pp. 96–100, Dec. 2006.

[19] S. Shoaee, T. M. Clarke, C. Huang, S. Barlow, S. R. Marder, M. Heeney, I. McCulloch, and J. R. Durrant, “Acceptor energy level control of charge photogeneration in organic donor/acceptor blends.,” *J. Am. Chem. Soc.*, vol. 132, no. 37, pp. 12919–26, Sep. 2010.

[20] W. S. Shin, H.-H. Jeong, M.-K. Kim, S.-H. Jin, M.-R. Kim, J.-K. Lee, J. W. Lee, and Y.-S. Gal, “Effects of functional groups at perylene diimide derivatives on organic photovoltaic device application,” *J. Mater. Chem.*, vol. 16, no. 4, pp. 384–390, Jan. 2006.

[21] X. Zhan, Z. Tan, B. Domercq, Z. An, X. Zhang, S. Barlow, Y. Li, D. Zhu, B. Kippelen, and S. R. Marder, “A high-mobility electron-transport polymer with broad absorption and its use in field-effect transistors and all-polymer solar

cells.," *J. Am. Chem. Soc.*, vol. 129, no. 23, pp. 7246–7, Jun. 2007.

[22] X. Guo and M. D. Watson, "Conjugated polymers from naphthalene bisimide.," *Org. Lett.*, vol. 10, no. 23, pp. 5333–6, Dec. 2008.

[23] M.-C. Yuan, M.-H. Su, M.-Y. Chiu, and K.-H. Wei, "Synthesis and characterization of donor-bridge-acceptor alternating copolymers containing perylene diimide units and their application to photovoltaic cells," *J. Polym. Sci. Part A Polym. Chem.*, vol. 48, no. 6, pp. 1298–1309, Mar. 2010.

[24] X. Zhan, A. Facchetti, S. Barlow, T. J. Marks, M. A. Ratner, M. R. Wasielewski, and S. R. Marder, "Rylene and related diimides for organic electronics.," *Adv. Mater.*, vol. 23, no. 2, pp. 268–84, Jan. 2011.

[25] M. J. O'Neill and E. S. Watson, "Differential microcalorimeter," US3263484 A, 04-Apr-1962.

[26] G. J. Hedley, A. J. Ward, A. Alekseev, C. T. Howells, E. R. Martins, L. A. Serrano, G. Cooke, A. Ruseckas, and I. D. W. Samuel, "Determining the optimum morphology in high-performance polymer-fullerene organic photovoltaic cells.," *Nat. Commun.*, vol. 4, p. 2867, Jan. 2013.

[27] K. Tremel and S. Ludwigs, *P3HT Revisited – From Molecular Scale to Solar Cell Devices*, vol. 13. Berlin, Heidelberg: Springer, 2014.

[28] B. C. Schroeder, Z. Li, M. A. Brady, G. C. Faria, R. S. Ashraf, C. J. Takacs, J. S. Cowart, D. T. Duong, K. H. Chiu, C.-H. Tan, J. T. Cabral, A. Salleo, M. L. Chabinyc, J. R. Durrant, and I. McCulloch, "Enhancing fullerene-based solar cell lifetimes by addition of a fullerene dumbbell.," *Angew. Chem. Int. Ed. Engl.*, vol. 53, no. 47, pp. 12870–5, Nov. 2014.

[29] D. McMullan, "Scanning electron microscopy 1928-1965," *Scanning*, vol. 17, no. 3, pp. 175–185, Dec. 2006.

[30] M. von Ardenne, "Das Elektronen-Rastermikroskop," *Zeitschrift für Phys.*, vol. 109, no. 9–10, pp. 553–572, Sep. 1938.

[31] M. B. von Ardenne, *Elektronen-Übermikroskopie*. Berlin, Heidelberg: Springer Berlin Heidelberg, 1940.

[32] F. C. Krebs, Ed., *Stability and Degradation of Organic and Polymer Solar Cells*. John Wiley & Sons, 2012.

[33] M.-H. Yoon, C. Kim, A. Facchetti, and T. J. Marks, “Gate dielectric chemical structure-organic field-effect transistor performance correlations for electron, hole, and ambipolar organic semiconductors.,” *J. Am. Chem. Soc.*, vol. 128, no. 39, pp. 12851–69, Oct. 2006.

[34] F. So, Ed., *Organic Electronics: Materials, Processing, Devices and Applications*, vol. 24. CRC Press, 2009.

[35] S. Kwon, K. Yu, K. Kweon, G. Kim, J. Kim, H. Kim, Y.-R. Jo, B.-J. Kim, J. Kim, S. H. Lee, and K. Lee, “Template-mediated nano-crystallite networks in semiconducting polymers.,” *Nat. Commun.*, vol. 5, p. 4183, Jan. 2014.

[36] N. D. Treat, M. A. Brady, G. Smith, M. F. Toney, E. J. Kramer, C. J. Hawker, and M. L. Chabinyc, “Interdiffusion of PCBM and P3HT Reveals Miscibility in a Photovoltaically Active Blend,” *Adv. Energy Mater.*, vol. 1, no. 1, pp. 82–89, Jan. 2011.

[37] M. Shao, J. Keum, J. Chen, Y. He, W. Chen, J. F. Browning, J. Jakowski, B. G. Sumpter, I. N. Ivanov, Y.-Z. Ma, C. M. Rouleau, S. C. Smith, D. B. Geohegan, K. Hong, and K. Xiao, “The isotopic effects of deuteration on optoelectronic properties of conducting polymers.,” *Nat. Commun.*, vol. 5, p. 3180, Jan. 2014.

[38] J. Chen, X. Yu, K. Hong, J. M. Messman, D. L. Pickel, K. Xiao, M. D. Dadmun, J. W. Mays, A. J. Rondinone, B. G. Sumpter, and S. M. Kilbey II, “Ternary behavior and systematic nanoscale manipulation of domain structures in P3HT/PCBM/P3HT-b-PEO films,” *J. Mater. Chem.*, vol. 22, no. 26, p. 13013, Jun. 2012.

[39] G. Li, R. Zhu, and Y. Yang, “Polymer solar cells,” *Nat. Photonics*, vol. 6, no. 3, pp. 153–161, Feb. 2012.

[40] H. Yan, D. Li, K. Lu, X. Zhu, Y. Zhang, Y. Yang, and Z. Wei, “Evolution of polymer photovoltaic performances from subtle chemical structure variations.,” *Phys. Chem. Chem. Phys.*, vol. 14, no. 43, pp. 15127–34, Nov. 2012.

[41] J. R. Norris and D. W. Ribbons, Eds., *Methods in Microbiology, Volume 6B*. London: Academic Press, 1972.

[42] K. J. Laidler, *The World of Physical Chemistry*. Oxford University Press, 1995.

[43] W. H. Harris, J. S. Levey, and C. University, *The New Columbia Encyclopedia*. Columbia University Press, 1975.

[44] W. L. Masterton and C. N. Hurley, *Chemistry: Principles and Reactions*. Cengage Learning, 2008.

[45] K. Colladet, S. Fourier, T. J. Cleij, L. Lutsen, J. Gelan, D. Vanderzande, L. Huong Nguyen, H. Neugebauer, S. Sariciftci, A. Aguirre, G. Janssen, and E. Goovaerts, "Low Band Gap Donor−Acceptor Conjugated Polymers toward Organic Solar Cells Applications," *Macromolecules*, vol. 40, no. 1, pp. 65–72, Jan. 2007.

[46] K. Kawashima, Y. Tamai, H. Ohkita, I. Osaka, and K. Takimiya, "High-efficiency polymer solar cells with small photon energy loss.," *Nat. Commun.*, vol. 6, p. 10085, Jan. 2015.

[47] C. K. Song, A. C. White, L. Zeng, B. J. Leever, M. D. Clark, J. D. Emery, S. J. Lou, A. Timalsina, L. X. Chen, M. J. Bedzyk, and T. J. Marks, "Systematic investigation of organic photovoltaic cell charge injection/performance modulation by dipolar organosilane interfacial layers.," *ACS Appl. Mater. Interfaces*, vol. 5, no. 18, pp. 9224–40, Sep. 2013.

[48] J. Zhao, Y. Li, H. Lin, Y. Liu, K. Jiang, C. Mu, T. Ma, J. Y. Lin Lai, H. Hu, D. Yu, and H. Yan, "High-efficiency non-fullerene organic solar cells enabled by a difluorobenzothiadiazole-based donor polymer combined with a properly matched small molecule acceptor," *Energy Environ. Sci.*, vol. 8, no. 2, pp. 520–525, Feb. 2015.

[49] R. G. Kepler, "Charge Carrier Production and Mobility in Anthracene Crystals," *Phys. Rev.*, vol. 119, no. 4, pp. 1226–1229, Aug. 1960.

[50] S.-W. Liu, C.-C. Lee, W.-C. Su, C.-H. Yuan, C.-F. Lin, K.-T. Chen, Y.-S. Shu, Y.-Z. Li, T.-H. Su, B.-Y. Huang, W.-C. Chang, and Y.-H. Liu, "Downscaling the Sample Thickness to Sub-Micrometers by Employing Organic Photovoltaic Materials as a Charge-Generation Layer in the Time-of-Flight Measurement.," *Sci. Rep.*, vol. 5, p. 10384, Jan. 2015.

[51] B. Philippa, M. Stolterfoht, P. L. Burn, G. Juška, P. Meredith, R. D. White, and A. Pivrikas, "The impact of hot charge carrier mobility on photocurrent losses in polymer-based solar cells.," *Sci. Rep.*, vol. 4, p. 5695, Jan. 2014.

[52] S. Tiwari and N. C. Greenham, "Charge mobility measurement techniques in organic semiconductors," *Opt. Quantum Electron.*, vol. 41, no. 2, pp. 69–89, Aug. 2009.

[53] V. Coropceanu, J. Cornil, D. A. da Silva Filho, Y. Olivier, R. Silbey, and J.-L.

Brédas, “Charge transport in organic semiconductors.,” *Chem. Rev.*, vol. 107, no. 4, pp. 926–52, Apr. 2007.

[54] V. Kažukauskas, M. Pranaitis, V. Čyras, L. Sicot, and F. Kajzar, “Negative mobility dependence on electric field in poly(3-alkylthiophenes) evidenced by the charge extraction by linearly increasing voltage method,” *Thin Solid Films*, vol. 516, no. 24, pp. 8988–8992, Oct. 2008.

[55] A. J. Mozer and N. S. Sariciftci, “Negative electric field dependence of charge carrier drift mobility in conjugated, semiconducting polymers,” *Chem. Phys. Lett.*, vol. 389, no. 4–6, pp. 438–442, May 2004.

[56] A. J. Mozer, N. S. Sariciftci, A. Pivrikas, R. Österbacka, G. Juška, L. Brassat, and H. Bässler, “Charge carrier mobility in regioregular poly(3-hexylthiophene) probed by transient conductivity techniques: A comparative study,” *Phys. Rev. B*, vol. 71, no. 3, p. 035214, Jan. 2005.

CHAPTER 3 ULTRA-LOW P-DOPING OF POLY(3-HEXYLTHIOPHENE) AND ITS IMPACT ON POLYMER AGGREGATION AND PHOTOVOLTAIC PERFORMANCE

3.1 Introduction

3.1.1 Origins of Electrical Doping

The effects of electrical dopants in semiconducting materials have been studied since the late 19th century, when photoconductivity was first observed in selenium wires by Willoughby Smith,[1] after which it was speculated by Shelford Bidwell that the semiconductor's properties may be due to impurities introduced during material processing, rather than intrinsic behavior of the selenium.[2] Following this claim he constructed cells of sulfur with intentionally added silver and observed a similar photoconductivity effect, demonstrating that this concept of impurity inclusion had the potential to be applied to multiple material systems.

The process of doping was not effectively developed until 1950, when John R. Woodyard filed a patent regarding the preparation of a unidirectionally conducting germanium alloy containing up to 1% of phosphorus.[3] At around the same time, Sparks *et al.* at Bell Laboratories described the immersion of n-type germanium single crystals in a gallium-doped, p-type germanium melt to create a junction.[4] From here originates the classic example of semiconductor doping that is a silicon p-n junction: a boundary at the interface of p-type, where electron acceptors such as boron are included in the silicon lattice to form positive holes in the valence band, and n-type silicon, where electron donors such as phosphorus are introduced that contribute negative electrons to

the conduction band, inside a semiconductor, a discovery credited to Russell Ohl.[5,6] The formed junction is an essential component of many classes of semiconductor electronic devices including diodes, transistors, and solar cells.

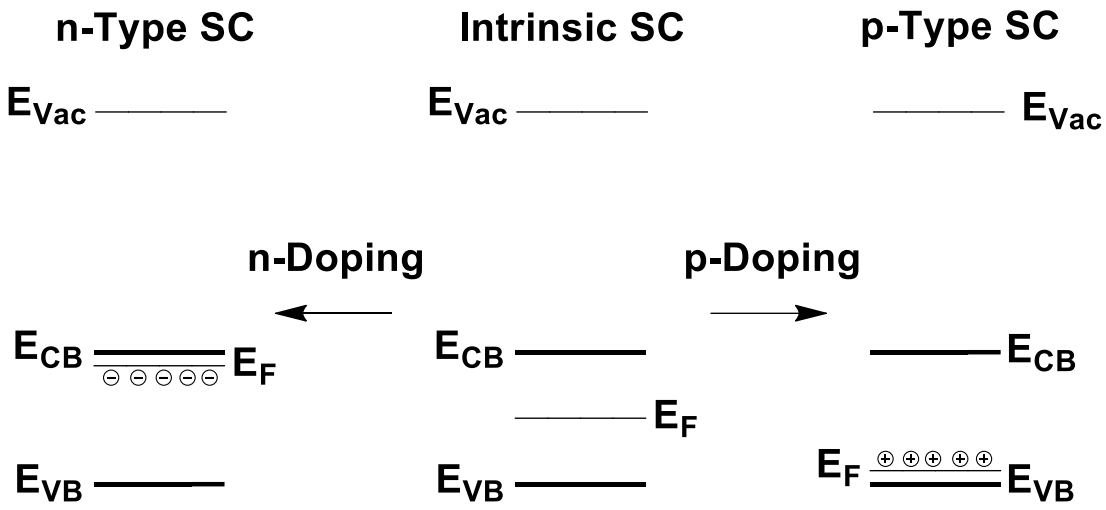

Figure 3.1. The introduction of dopants into a semiconductor can result in a shift in the Fermi level energy and the contribution of carriers to a charge transport band, the carrier sign and specific band dependent upon the type of dopant used.

3.1.2 Electrical Doping in Organic Semiconductors

Electrical doping can also be extended to organic semiconductors, albeit through different processes. Two primary methods, electrochemical and chemical doping, both involve redox processes. In electrochemical doping, the organic material is coated on an electrode and suspended in an electrolyte solution, along with discrete counter and reference electrodes, where an applied potential difference causes oxidation or reduction of the material balanced by counter ion diffusion, achieving n- or p-doping.[7,8] Chemical doping involves exposing the semiconductor to oxidants or reductants, which can be elemental molecules, such as oxygen or bromine, alkali metals or, more recently, redox-active small molecules. As opposed to pure inorganic

semiconductors, where dopant loading is typically rather low (ca. 10^{-2}-10^{-3} at. %), organic semiconductor doping generally must carried out with moderate to high dopant loadings (> ca. 1 mol. or wt. %) due to higher impurity concentrations and structural disorder in order to significantly shift the Fermi level and thus reduce carrier-injection barriers, and/or to improve conductivity (σ) by adding "free" carriers to the transport levels. Although these effects are useful for applications such as hole-extraction layers for OPVs and for reducing contact resistance in OFETs,[9,10] high levels of doping are unsuitable for the channel of OFETs, where they can reduce the current on/off ratio and for the active layer of OPVs, where high conductivity materials can decrease shunt resistance and eventually result in shorting between electrodes.[11–13]

3.1.3 Electrical Doping for Trap Passivation

As was discussed in Chapter 1, organic semiconductors have inherent trap, or gap, states due to structural/morphological imperfections and irregularities[14–16] or to impurities originating from synthetic or material processing.[17–19] Doping with very low loading of dopants (or use of dopants that are insufficiently strong reductants or oxidants to introduce free carriers), akin to the concentrations used in inorganic semiconductors, can potentially also be used to passivate gap states[20,21] in organic semiconductors, i.e. filling electron traps or hole traps with their respective carriers, without introducing excessive conductivity. Low molecular dopant loading (generally < ca. 1 wt. %) has been shown to passivate gap states in organic semiconductor films.[22–24] In studies of vacuum co-deposition of C_{60}, the conductivity initially increases in a superlinear fashion with the loading of n-dopant, but at higher concentrations approaches a linear dependence; these two regimes of dopant loading dependence have been assigned to filling of trap states and free carrier contribution to the conduction band, respectively, and suggest a trap density of 10^{18}-10^{19} cm^{-3}.[22] Channel doping of

C_{60}-based OFETs in the trap-filling regime of dopant concentration can be used to increase the mobility and decrease the threshold voltage without significantly impairing the current on/off ratio.[25] Low loadings of p-dopants have also been applied in the active layers of bulk heterojunction (BHJ) polymer/fullerene solar cells. p-Doping of PCPDTBT/$PC_{61}BM$ with 2,3,5,6-tetrafluoro-7,7,8,8-tetracyano-quinodimethane (F_4-TCNQ) was found to increase the power conversion efficiency (PCE), mostly due to an increase in the short-circuit current (J_{SC}), from 3.3% to a maximum value of 3.6% at a loading of 0.5 wt% with respect to the polymer, with further increases in the dopant loading leading to a decrease in PCE.[26] Low loadings of F_4-TCNQ have also been found to improve the PCE of a variety of other polymer/fullerene blends including PCDTBT/$PC_{71}BM$ cells, for which the PCE was increased from 6.4 to 7.9%, again largely as a result of increasing J_{SC}, by use of 0.4 wt. % of the dopant.[27]

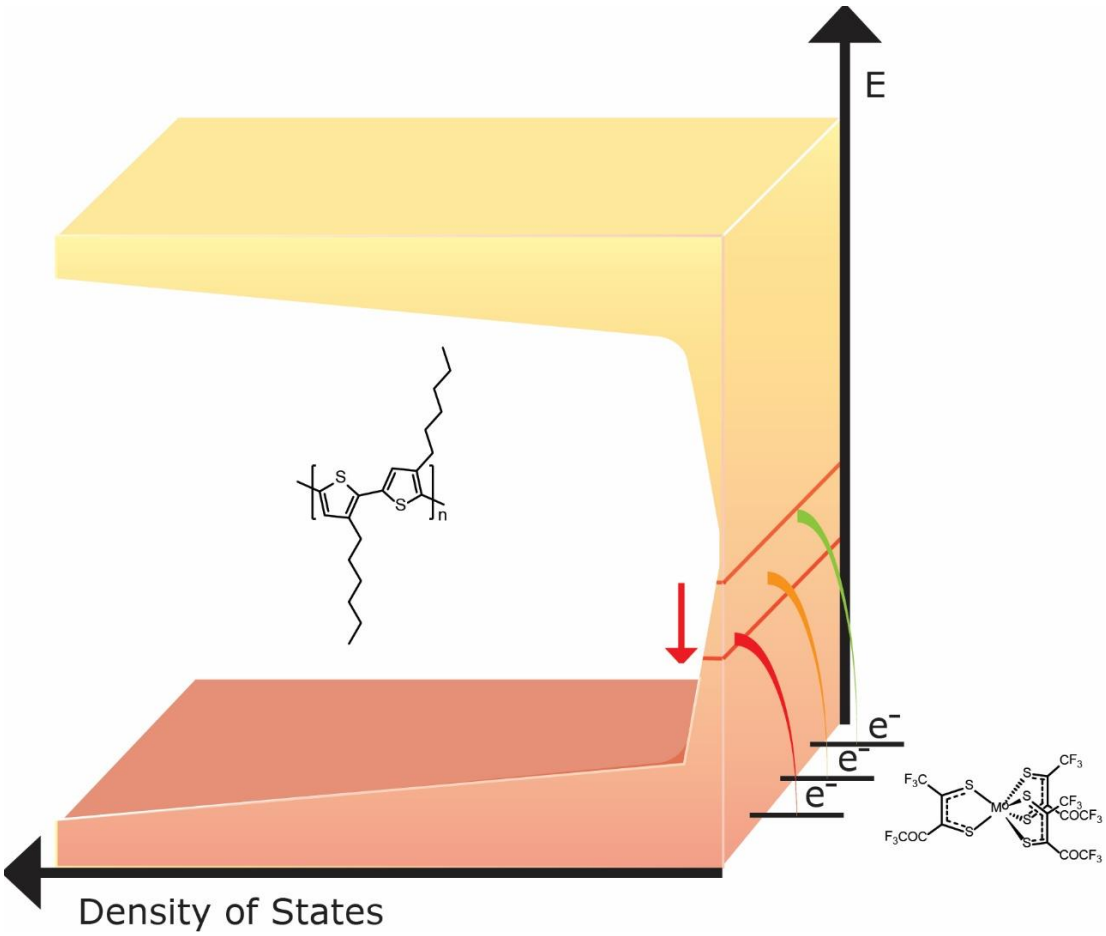

Figure 3.2. Structures of poly(3-hexylthiophene) and molybdenum tris[1-(trifluoromethylcarbonyl)-2-(trifluoromethyl)-ethane-1,2-dithiolene], and a schematic illustrating passivation of low-density gap states by electron transfer to a p-dopant.

There have been several studies of the effects of low levels of p-doping on BHJ OPV devices[26,27] based on donor-acceptor polymers, yet to our knowledge there are no studies incorporating solar cells that employ the widely studied OPV material, poly(3-hexylthiophene) (P3HT), an important benchmark conjugated polymer widely used in organic electronics and photovoltaics, in the active layer. In this chapter the effects of low dopant loading on the electronic and morphological characteristics of P3HT films and on the device performance of P3HT/$PC_{61}BM$ solar cells are investigated. These studies principally employ the molecular p-dopant molybdenum tris[1-(trifluoromethylcarbonyl)-2-(trifluoromethyl)-ethane-1,2-dithiolene], Mo(tfd-

$COCF_3)_3$, with a reduction potential of +0.39 V vs. $FeCp_2^{+/0}$ (estimated *EA* of ca. 5.7 eV based on photoelectron spectroscopy of a similar dopant),[28,29] that has been shown to p-dope graphene and small-molecule organic semiconductors,[30,31] and has sufficient miscibility with organic solvents and many semiconductor materials to allow for solution processing.*

To discuss the effects of trap passivation by p-dopants, it is important to differentiate between 'trap-filling' and 'band-filling' with respect to charge carriers. An undoped semiconductor typically has its Fermi level energy near the mid-point between its valence band and conduction band.[32,33] With certain material systems, this level can be found closer to either valence or conduction band, depending on the distribution of trap states within the transport gap, as well as the various details of the band structure.[34–37] The density of these states will vary across materials, and for organic polymers, such as the material in this study, the density of states can be dependent on molecular weight, crystallinity, and morphology. For a hole-transporting material, the initial addition of

---

* $Mo(tfd\text{-}COCF_3)_3$ exhibits good solubility in various organic solvents; for example, 25 mg mL^{-1} in chlorobenzene.[28] Hansen solubility parameters (HSP) have been used to predict material miscibility in OPVs;[61] values have previously been reported for P3HT (δ_D = 18.7 $MPa^{1/2}$, δ_P = 1.4 $MPa^{1/2}$, and δ_H = 4.5 $MPa^{1/2}$) and $PC_{61}BM$ (δ_D = 18.7 $MPa^{1/2}$, δ_P = 4.0 $MPa^{1/2}$, and δ_H = 6.1 $MPa^{1/2}$). Using second-order estimates of the HSP for $Mo(tfd\text{-}COCF_3)_3$, with approximations for the molybdenum core as well as the charge distribution in the dithienolene rings, parameters of δ_D = 26.1 $MPa^{1/2}$, δ_P = 4.0 $MPa^{1/2}$, and δ_H = 6.1 $MPa^{1/2}$ were obtained.[62] Beyond the rather poor overlap of the dispersion solubility parameters of the dopant with the semiconducting materials, these HSP suggest better dopant miscibility with the fullerene than with the polymer. An important limitation of these predictions is that they assume neutral molecules and do not account for the coulombic attraction between the dopant anions and the doped material.

p-dopants can extract electrons from the low-density states above the valence band, moving the Fermi level towards the valence-band edge.[20,21] As the dopant loading increases and localized states have largely been passivated, additional p-dopants will begin to remove electrons from the hole transport states. As the density of states in a charge transport band is much higher than that within the gap, a substantially greater amount of dopant is required to shift the Fermi level or increase the conductivity by a given magnitude.

3.2 Methods & Results

3.2.1 Conductivity & Mobility Measurements

An in-depth discussion regarding the methodology of conductivity and mobility (μ) measurements of organic semiconductors was given in Chapter 1. For this chapter, both σ and μ were measured at the King Abdullah University of Science and Technology on spun-cast P3HT films containing various loadings of $Mo(tfd\text{-}COCF_3)_3$, deposited over plasma-cleaned pre-patterned electrodes (45 nm Au/5 nm ITO) on 230 nm silica over silicon (3×10^{17} cm^{-3} n-doped) substrates. The conductivity was estimated using the ohmic (linear) region of the I-V curves between the source and drain electrodes, converting current to current density using film thickness and channel width, which in all cases were 50-100 nm and 2 mm respectively, and voltage to field using channel length, which were 2, 5, 10 or 20 μm. Conductivities measured at all four channel lengths gave similar values, indicating that contact resistance is negligible relative to film resistance. σ values are average across at least 8 pixels from all four channel lengths. Mobility values were measured in a field-effect transistor (FET)

format using an EP4 cascade microtech probe station & a Keithley 2400 source meter. Mobilities were determined by fitting the slope (m) of $I_D^{1/2}$-V_{GS} in the saturation regime by the expression $\mu = 2Lm^2/WC_i$, where L and W are the length and width of the channel, and C_i is the geometric capacitance of the gate dielectric, which is ca. 15 nF/cm^2 for the 230 nm silica over silicon (3×10^{17} cm^{-3} n-doped) substrates used in this work.[38] Thicknesses were determined using a Dektak 150 profilometer. Doped solutions were pre-mixed by adding small volumes of 0.1 or 1 mg / mL Mo(tfd-$COCF_3$)$_3$ solutions to 15-25 mg / mL P3HT chlorobenzene solutions and stirring for up to an hour in inert atmosphere. Solutions were spun-cast at 1000-1500 rpm for 60 s to achieve films between 50-100 nm in thickness, after which samples were dried in vacuum (~10^{-6} Torr) and then possibly annealed at 120 °C for 30 min. Besides substrate cleaning, all processing steps and device testing were performed in an inert atmosphere.

The fitted σ values for pristine & annealed films are plotted in Figure 3.3 against their wt. % dopant. Weight percent has been used in previous studies with polymers, which is preferred over mol. % due to variations in polymer molecular weight and polydispersity. For means of conversion, 1 wt. % dopant is equivalent to 1 dopant molecule for every 511 P3HT monomer units.

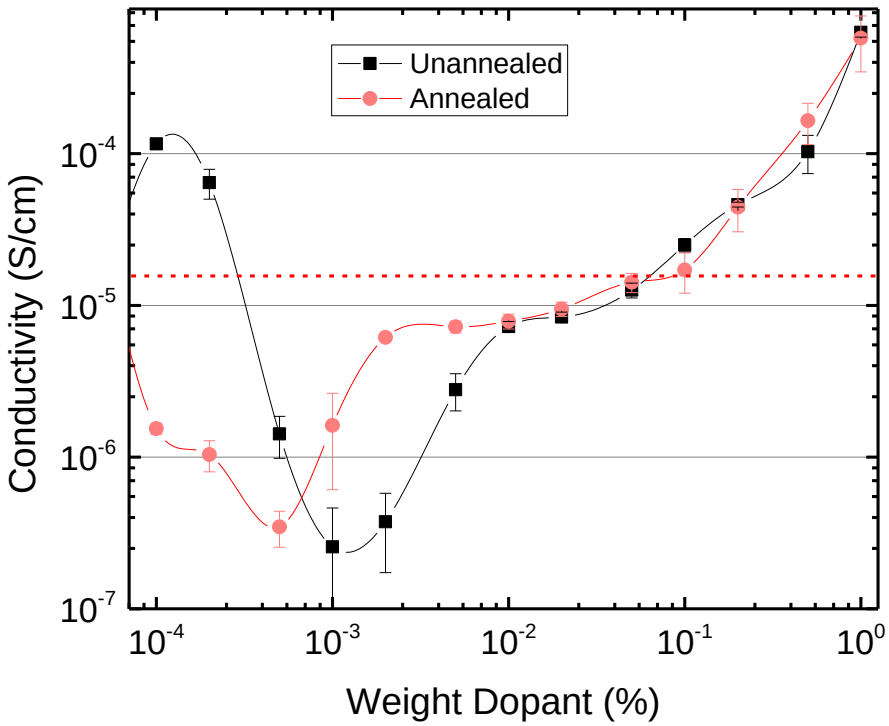

Figure 3.3. Conductivity trends of P3HT thin films doped with 0.0001 to 1% Mo(tfd-$COCF_3)_3$. The undoped value is shown as a dotted line.

The evolution of the conductivity with increasing dopant concentration reveals a more complex progression for this material system than was observed in fullerene[22] or N-2200[39] systems n-doped over many orders of magnitude. The measured σ value of the undoped P3HT thin film was 1.4×10^{-5} S cm^{-1}, in good agreement with literature values.[9] This is generally reduced for very low concentrations of p-dopant, decreasing to 2.6×10^{-7} S cm^{-1} at 10^{-3} wt. % dopant. This change is attributed to alterations in the P3HT order upon the introduction of the small molecules into the film (*vide infra*). Similar trends have been seen for the lowest doping concentrations of F_4-TCNQ in P3HT.[40] This regime of reduced conductivity is followed by a sharp increase in σ as the doping level is increased to ca. 0.01 wt. %; this effect is attributed to the ultra-low doping, trap-filling regime, although this increase is largely the recovery of

conductivities comparable with those of undoped films. The further increase at higher levels is more gradual, suggesting valence-band filling.

Though they exhibit reasonable hole mobilities, P3HT OFETs prepared from chlorobenzene exhibit hysteresis, which manifests in poor overlap in forward and reverse traces as well as unreliable threshold voltages (V_{Th}) and poor on/off ratios, as shown in Figure 3.4. These effects may be particular to the solvent chosen and the processing methods, as has been explored by Cheng *et al.*[41] Chlorobenzene is not popularly used in P3HT FETs, but was nevertheless used here for consistency with the bulk heterojunction solar cell work, which is the central theme of this study.

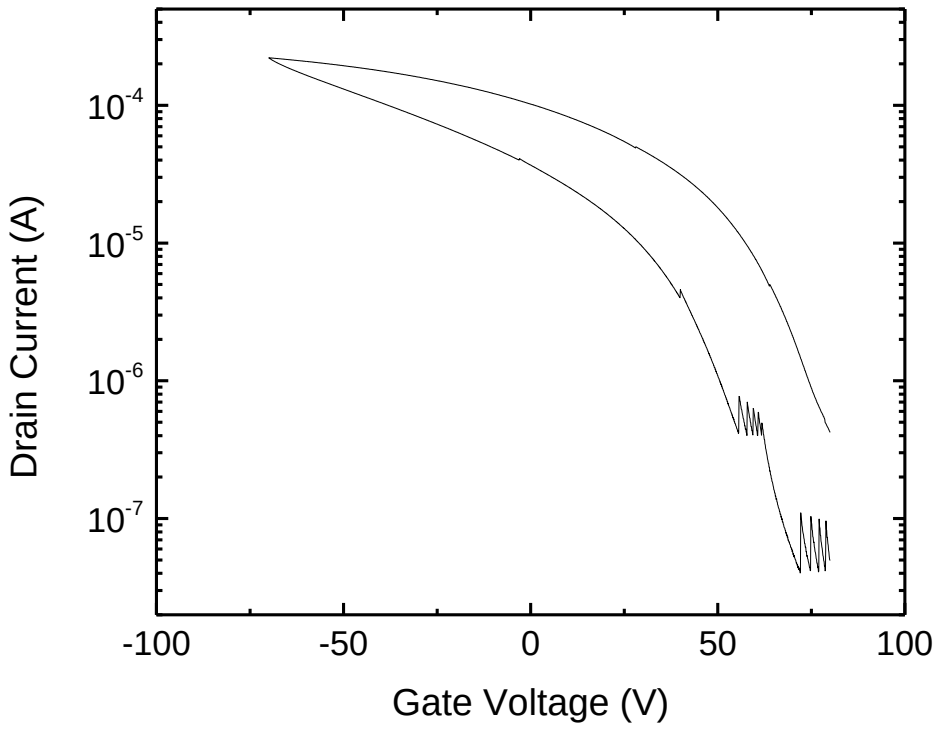

Figure 3.4. An example of hysteresis in P3HT FETs deposited from chlorobenzene.

FET hole mobilities calculated from forward gate sweeps (+ to -) are given in Figure 3.5 and Table 3.1. From the μ data, the improvements in the conductivity are

presumably largely attributable to an increase in the number of charge carriers. Certainly the field-effect mobility is rather invariant with doping level, as has been similarly observed for other doped materials;[31] however, the mobility under saturation conditions is likely to be very different to that relevant to the conductivity measurements since in the former the number of injected carriers, and, therefore, potentially the extent of trap-filling, greatly exceeds the number of carriers contributed by the dopants. Changes in the number of free carriers could possibly be resolved in the behavior of the V_{Th}, but unfortunately these values are not reliable due to hysteresis. The reduction in on/off ratio observed above 0.01 wt. % is consistent with the increase in conductivity associated with the band-filling regime of doping. The trends are similar for pristine and annealed samples.

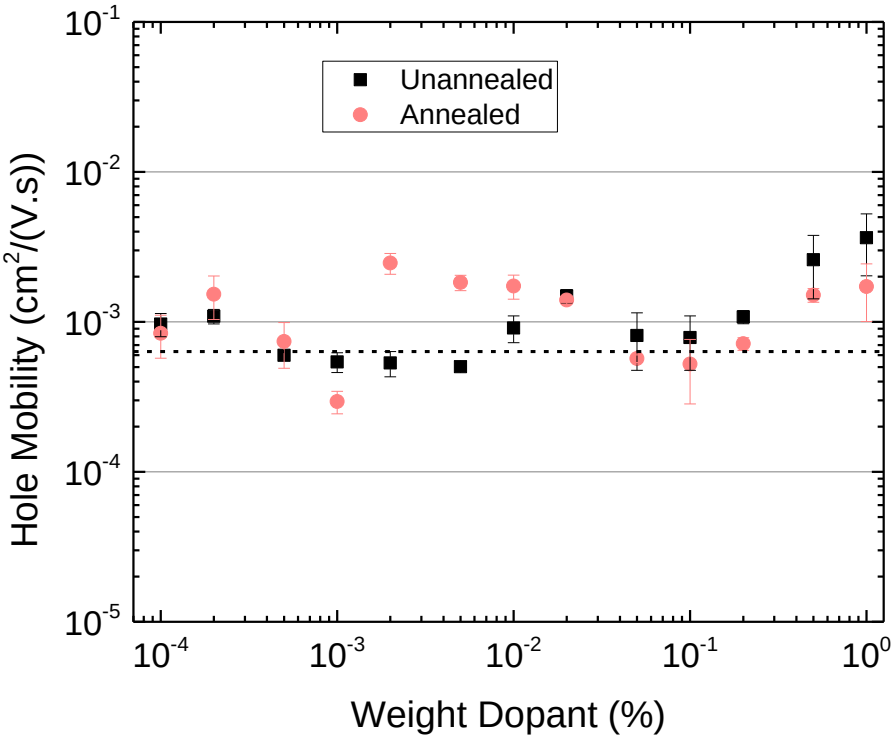

Figure 3.5. OFET hole mobility trends of P3HT thin films doped with 0.0001 to 1% Mo(tfd-$COCF_3$)$_3$, pristine and annealed. The undoped value is indicated by the dotted line.

Table 3.1. OFET hole mobility values of P3HT thin films doped with 0.0001 to 1% Mo(tfd-$COCF_3$)$_3$, pristine and annealed. V_{Th} is unreliable due to hysteresis and was not compared to avoid confusion.

Dopant Concentration	**$\mu \times 10^4$ (cm^2 V^{-1} s^{-1})**	**On/Off**
Pristine		
Undoped	6.2 ± 0.9	10^3
0.0001%	9.7 ± 1.7	10^3
0.0002%	10.9 ± 1.2	10^3
0.0005%	6.0 ± 0.3	10^4
0.001%	5.4 ± 0.8	10^4
0.002%	5.3 ± 1.0	10^5

0.005%	5.0 ± 0.7	10^5
0.01%	9.1 ± 1.8	10^3
0.02%	14.9 ± 1.5	10^2
0.05%	8.1 ± 3.4	10^2
0.1%	7.9 ± 3.1	10^1
0.2%	10.8 ± 1.1	10^2
0.5%	26.0 ± 11.7	10^2
1.0%	36.4 ± 16.1	10^1
Annealed		
Undoped	6.8 ± 1.1	10^3
0.0001%	8.4 ± 2.8	10^4
0.0002%	15.3 ± 4.9	10^4
0.0005%	7.4 ± 2.5	10^4
0.001%	2.9 ± 0.5	10^4
0.002%	24.7 ± 3.9	10^5
0.005%	18.3 ± 2.1	10^5
0.01%	17.3 ± 3.2	10^3
0.02%	14.0 ± 0.5	10^3
0.05%	5.7 ± 0.3	10^3
0.1%	5.2 ± 2.4	10^3
0.2%	7.2 ± 0.7	10^2
0.5%	15.1 ± 1.6	10^1
1.0%	17.2 ± 0.7	10^1

A series of devices were also prepared using toluene as the solvent, as is more common used in P3HT transistors, μ data for which are shown in Figure 3.6. Although

the values are in agreement with literature at 1.0×10^{-2} cm^2 V^{-1} s^{-1} for the undoped P3HT film,[41] there is no significant change or discernable trend across a reasonable range of dopant loadings.

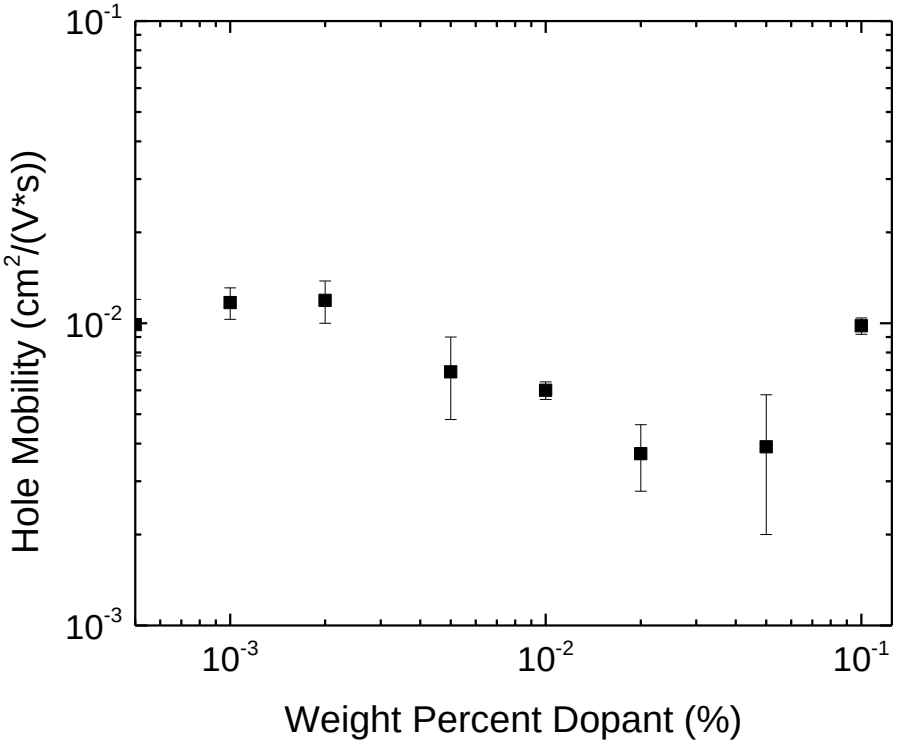

Figure 3.6. OFET hole mobility trends of P3HT thin films prepared from toluene, doped with 0.001 to 0.1% Mo(tfd-$COCF_3$)$_3$.

3.2.2 Ultra-violet Photoelectron Spectroscopy

A detailed discussion of photoelectron spectroscopy was given in Chapter 1. For this chapter, ultra-violet photoelectron spectroscopy was performed at the King Abdullah University of Science and Technology in an ultra-high vacuum environment with a SPHERA U7 hemispherical energy analyzer (Omicron Nanotechnology), employing a 5 eV pass energy and 0.05 eV step size. Doped solutions were pre-mixed

by adding small volumes of 0.01 or 0.1 mg / mL $Mo(tfd\text{-}COCF_3)_3$ solutions to 5 mg / mL P3HT chlorobenzene solutions and stirring for up to 1 h in inert atmosphere. Solutions were spin-cast at 1000 rpm for 60 s to achieve films ca. 20 nm in thickness, after which samples were dried in vacuum (~10^{-6} Torr) and then annealed at 120 °C for 30 min. Besides substrate cleaning, all processing steps and device testing were performed in an inert atmosphere or vacuum, including transfer from the glovebox to the ultra-high vacuum system in a vacuum tube.

The work function (Φ) and ionization energies (*IE*) of doped P3HT films show evidence of trends that can be related to those in conductivity, as seen in Figure 3.7. The undoped P3HT film exhibited a Φ and *IE* of 3.83 ± 0.02 eV and 4.54 ± 0.03 eV respectively, indicating that the onset of the valence band lies ca. 0.71 eV below the Fermi level, in agreement with literature values.[42,43] The lowest doping concentrations result in a lower Φ than undoped P3HT, so that the valence band lies up to ca. 0.83 eV away from the Fermi level, in contrast to the expected effect of p-doping, but consistent with the decrease in conductivity seen in this doping regime, which could be due to morphological effects. It can be considered that the lowest concentrations of p-dopants might not effectively lead to a shift in the Fermi level due to a high population of deep trap states as observed by Tietze *et al.*[44] Then as the dopant loading is increased further, the Φ steadily increases until about 0.01 wt. % dopant after which it increases more gradually, the difference between the *IE* and Φ decreasing in much the same way.

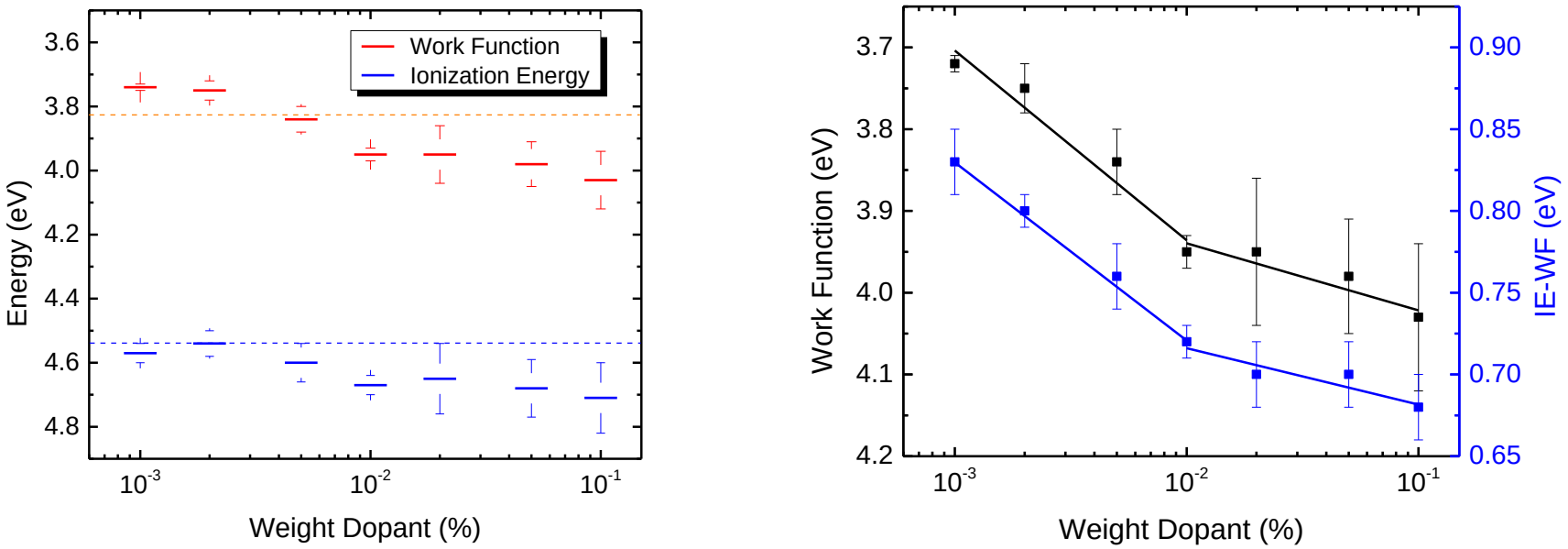

Figure 3.7. (left) Tabulated work functions and ionization energies of P3HT films doped at ultra-low concentrations. Undoped values are indicated by dotted lines. (right) Semi-logarithmic plots of the evolution of the work function and the valence band/Fermi level difference at ultra-low doping concentrations. The linear plots are guides to highlight the presence of two doping regimes.

Figure 3.8 displays a high-resolution scan of the area between the valence band and the Fermi level acquired using decreased step size and lengthened exposure periods. These spectra were adjusted to remove higher kinetic energy satellite features, baseline subtracted, intensity normalized to the main valence-band feature, and smoothed. The corrected spectra reveal the presence of a low, but non-zero, density-of-states extending across the energy range between the Fermi level and the valence band maximum. In the region corresponding to ultra-low doping, 0.001 to 0.1% dopant by weight, this feature undergoes a reduction in intensity, which could be indicative of trap-state passivation and changes in the energy distribution of the remaining traps.

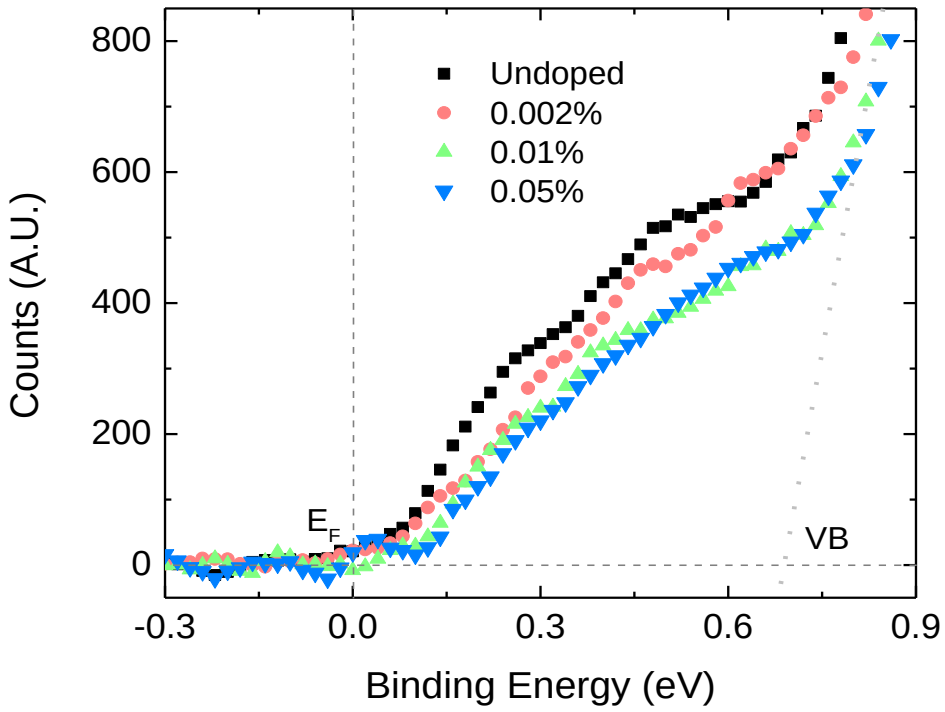

Figure 3.8. He(I) UPS spectra showing the region between the valence-band onset and the Fermi level.

3.2.3 Organic Photovoltaic Devices

An in-depth discussion of organic photovoltaics theory and general processing procedures was given in Chapter 1. For the study in this chapter, photovoltaic devices were fabricated at the King Abdullah University of Science and Technology. 200 nm-thick patterned ITO-on-glass substrates were sonicated in sodium dodecyl sulfate solution, water, acetone, and isopropanol, and then UV-ozone cleaned for 10 min. An 80% ethoxylated polyethylenimine (PEIE) solution (0.4 wt. % in ethanolamine; Sigma Aldrich) was spin-cast at 4000 rpm for 30 s, then annealed at 120 °C for 10 min. 20 mg / mL chlorobenzene solutions (5:4 wt/wt P3HT/$PC_{61}BM$) were spun-cast at 1000 rpm for 60 s to give ~120 nm films. Doped solutions were made by adding small volumes of 0.1 or 1 mg / mL Mo(tfd-$COCF_3)_3$ solutions to 20 mg/mL P3HT solutions and stirring for up to 1 h, before adding $PC_{61}BM$ solutions. Films were thermally annealed at 120 °C for 30 min. 15 nm MoO_3 and 80 nm Ag were deposited above the active layer by thermal evaporation.

In previous studies in which BHJ polymer/fullerene solar cells have been p-doped, PCEs have been increased at dopant levels of up to 0.4-0.5 wt%.[26,27] In the present system, however, doping of the active layer of ITO/PEIE/P3HT:$PC_{61}BM$/MoO_3/Ag OPVs with Mo(tfd-$COCF_3)_3$ results in a decrease in performance for all doping levels examined, largely through a drop in the fill factor as displayed in Figure 3.9 and Table 3.2. Even for the lowest concentrations at which we anticipate gap-state passivation, the values of J_{SC}, V_{OC}, and *FF* decrease sharply relative to the pristine sample. Such drops in *FF* and V_{OC} may be an indication of increased recombination. At dopant concentrations of 0.005 to 0.01 wt. %, at which we anticipate the most efficient trap passivation, without significant contribution of charge carriers, there is a slight increase in J_{SC}, although this effect cannot be

unambiguously attributed to trap passivation and at no point do efficiencies exceed the values for pristine samples. The fill factor proceeds to drop at higher doping levels, as charges are extracted from the valence band, and the curves develop S-shapes indicative of poor charge extraction.

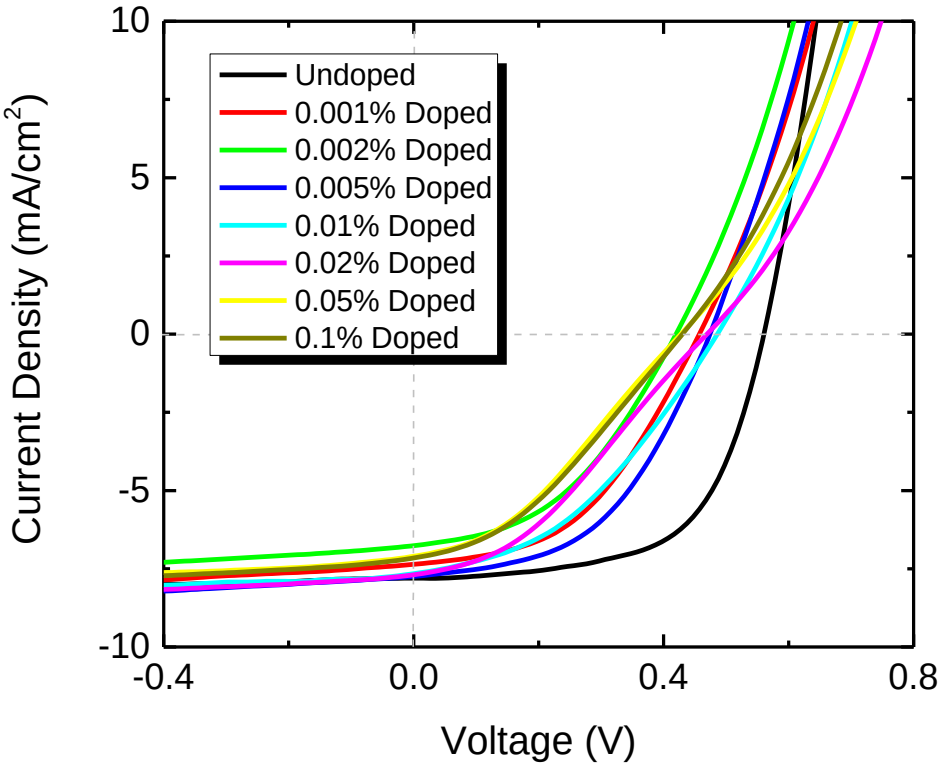

Figure 3.9. *J-V* curves for ITO/PEIE/P3HT/$PC_{61}BM$/MoO_3/Ag devices p-doped with Mo(tfd-$COCF_3$)$_3$ at concentrations corresponding to the sub-band-emptying regime.

Table 3.2. OPV performance values for ITO/PEIE/P3HT/$PC_{61}BM$/MoO_3/Ag devices p-doped with Mo(tfd-$COCF_3$)$_3$ at concentrations corresponding to the sub-band-emptying regime.

Dopant Concentration	***J*SC (mA/cm²)**	***V*OC (V)**	***FF* (%)**	**PCE (%)**
Undoped	7.6 ± 0.1	0.56 ± 0.02	61 ± 1	2.7 ± 0.1
0.001%	7.4 ± 0.1	0.46 ± 0.02	46 ± 1	1.6 ± 0.1

0.002%	6.8 ± 0.2	0.41 ± 0.02	43 ± 3	1.2 ± 0.1
0.005%	7.8 ± 0.1	0.47 ± 0.02	49 ± 3	1.8 ± 0.1
0.01%	7.7 ± 0.3	0.47 ± 0.02	39 ± 1	1.4 ± 0.1
0.02%	7.7 ± 0.1	0.47 ± 0.01	35 ± 2	1.3 ± 0.1
0.05%	7.1 ± 0.1	0.43 ± 0.01	35 ± 0	1.1 ± 0.0
0.1%	7.1 ± 0.1	0.43 ± 0.01	34 ± 3	1.0 ± 0.1

3.2.4 Transmission Electron Microscopy

Similar to scanning electron microscopy, which was discussed in Chapter 2, transmission electron microscopy (TEM), developed by Max Knoll and Ernst Ruska in 1931, is a technique by which a focused stream of electrons is transmitted through a thin film or sample, allowing for microscopy images at a considerably higher resolution than microscopes employing light due to the small de Broglie wavelength of electrons.[45] The maximum resolution achievable for a typical optical microscope, *d*, is given by:

$$d = \frac{\lambda}{2n \sin \theta} \qquad \text{Equation 3.1}$$

λ is the photon wavelength, n is the index of refraction of the lens, and θ is half of the angle of the incoming cone of light. In TEM, the wave-like properties of electrons allow their use in an analogous manner to a beam of electromagnetic radiation, where the de Broglie wavelength is dependent on the kinetic energy of the electrons. Accounting for relativistic effects as the electrons approach the speed of light (c), the wavelength of the electrons (λ_e) is given by:

$$\lambda_e \approx \frac{h}{\sqrt{2m_0E\left(1+\frac{E}{2m_0c^2}\right)}}$$ Equation 3.2

where h is Planck's constant, m_0 is an electron's invariant mass, and E is the kinetic energy of the electrons.[45] Electrons are generated by thermonic or field electron emission, accelerated by an electric field, and focused onto the sample by electromagnetic or electrostatic lenses. The resulting image, typically recorded on a ZnS phosphor screen, can contain information relating to electron density and material phases within the sample.

TEM has been used extensively as a tool to study D/A distribution in P3HT/fullerene blends, and for shorter polymers chains has been able to identify lamellar crystallinity.[46,47] Samples were prepared in the following manner: Doped solutions were pre-mixed by adding small volumes of 0.01 or 0.1 mg / mL Mo(tfd-$COCF_3)_3$ solutions to 5 mg / mL P3HT chlorobenzene solutions and stirring for up to 1 hr in inert atmosphere. Solutions were spin-cast at 1000 rpm for 60 s on UV ozone-cleaned glass substrates (without ITO layer) to achieve films of ca. 20 nm in thickness, after which samples were dried in vacuum (~10^{-6} Torr) and then annealed at 120 °C for 30 min. P3HT films were transferred to 3 mm Ni or Cu TEM grids by dipping, delaminating, and floating the films to the surface of DI water. The grids had a mesh size of 50 μm. After TEM sample preparation, they were given to Dr. Dalaver Anjum who performed the experiment on a FEI Titan at the King Abdullah University of Science and Technology.

Figure 3.10 displays TEM images of P3HT films, which identify the distribution of the molybdenum atoms of the dopants within the organic phase in more heavily loaded samples (≥ ca. 1 wt. %), due to observable scattering from high atomic number elements. At 1% dopant by weight, the lighter features indicate a non-uniform

distribution of dopants with clusters up to a few nanometers in size. As the loading is increased to 5 wt. % the dopants are found to have further segregated, clustered into areas with dimensions of ca. 10 nm.

Energy-dispersive X-ray spectroscopy (EDS) is an analytical measurement that can be performed simultaneously with TEM in the FEI Titan. Upon contact with the sample, high kinetic energy electrons from the focused beam can displace electrons from core levels, forming an electron hole upon ejection. This hole is quickly filled by an outer shell electron, which can release the excess potential energy in the form of an X-ray. X-ray energy and intensity are measured by a spectrometer, allowing for elemental characterization due to the unique X-ray emission spectrum fundamentally allowed for different atomic structures.[48] Figure 3.11 shows EDS obtained when focusing the electron beam on one of these clusters, identifying the molybdenum Kα relaxation at 17.4 keV. The uneven distribution at lower doping concentrations could indicate that the dopants are largely forced out of the crystalline regions of the polymer, interacting only at phase edges and in the amorphous region. This is in contrast to the doping of P3HT with the planar dopant F_4-TCNQ, where well-blended phases can be observed at similar dopant loadings.[49] The observation of dopant clusters can also suggest that not all of the dopants inside the cluster are interacting with the polymer, which could lower doping efficiency and possibly explain the unusual trends in conductivity and mobility. These clusters may instead be acting as quenching or recombination sites in the BHJ, explaining the drop in *FF*.

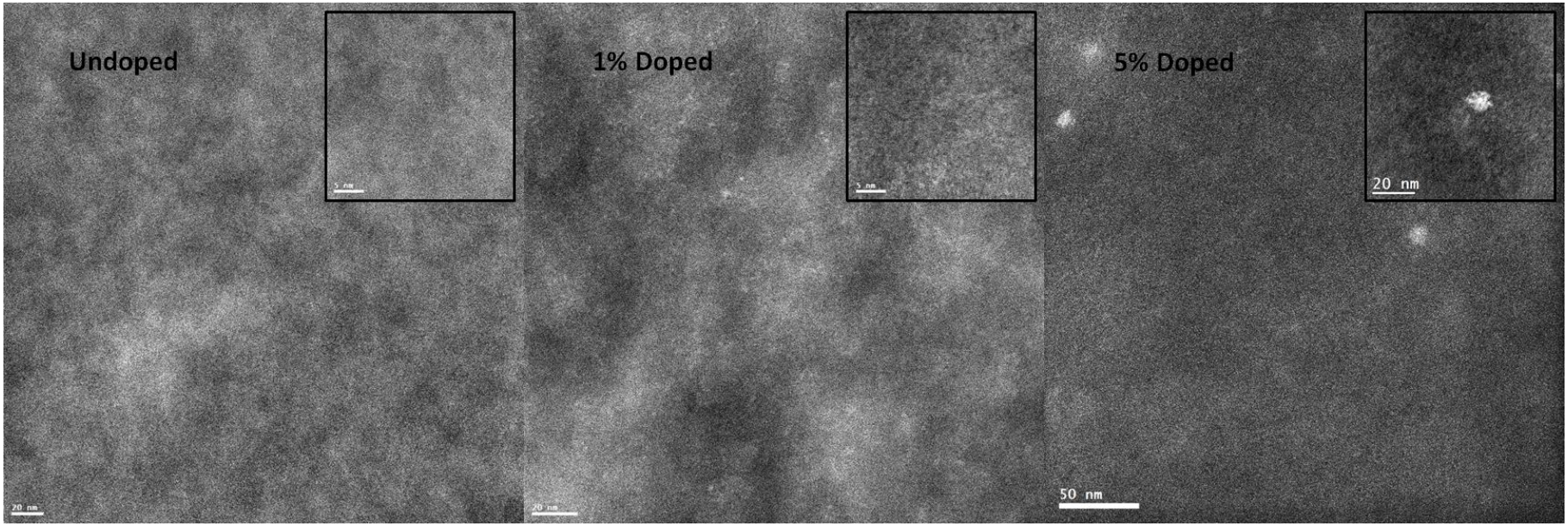

Figure 3.10. Transmission electron microscopy scans of undoped, 1%, and 5% doped P3HT films, spun-cast on UV ozone-cleaned glass then floated on water and collected on a Ni TEM grid.

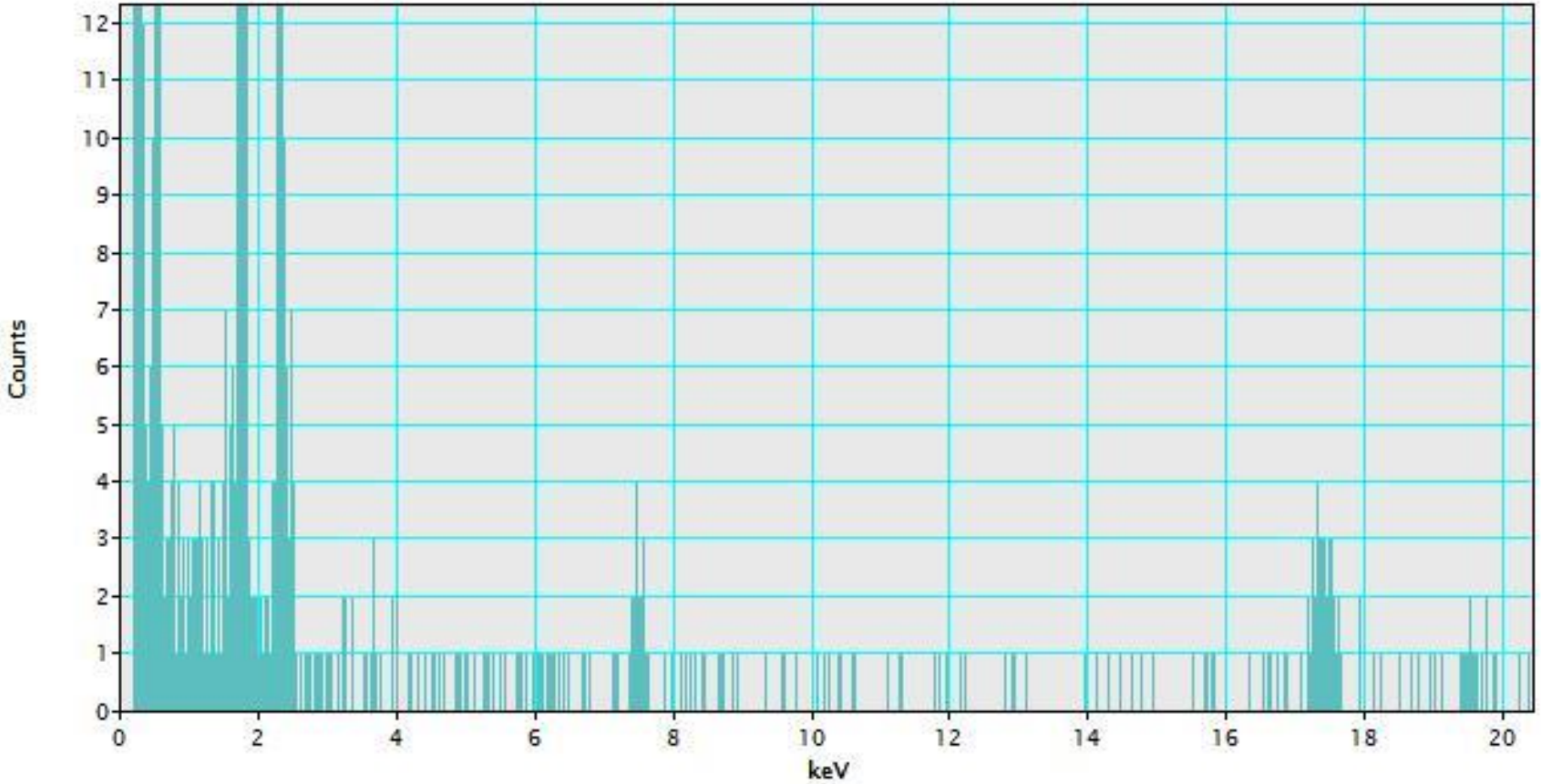

Figure 3.11. Energy dispersive spectrum during transmission electron microscopy, focused on a dopant aggregate inside a 5% p-doped P3HT film. The molybdenum Kα relaxation is observed at ca. 17.4 keV, the signal from the nickel grid is seen at ca. 7.5 keV, and the remaining elements have primary relaxation energies at ca. 3.0 eV and below.

3.2.5 Atomic Force Microscopy

An in-depth discussion of atomic force microscopy (AFM) relating to organic photovoltaic devices was given in Chapter 1. For the work in this chapter, AFM was conducted on a Bruker Dimension Icon in tapping mode, using Bruker RTESP-150 antimony-doped silicon tips, and analyzed with Gwyddion SPM analysis software. 20 mg / mL chlorobenzene solutions (5:4 P3HT/$PC_{61}BM$) were spin-cast at 1000 rpm for 60 s on UV-ozone cleaned ITO substrates to give ca. 120 nm films. Doped solutions were made by adding small volumes of 0.1 or 1 mg / mL $Mo(tfd\text{-}COCF_3)_3$ solutions to 20 mg/mL P3HT solutions and stirring for up to 1 hr, before adding $PC_{61}BM$ solutions. Films were thermally annealed at 120 °C for 30 min.

The surface morphology, as shown in Figure 3.12, while not indicating a substantial change in the topography, reveals a disruption of the fibrillar morphology, often observed in the phase scan for P3HT blends[47,50], at the surface of the BHJ film in the presence of the dopant, offering compelling evidence of a dopant-originated effect on polymer organization. After the inclusion of the p-dopant, the short fibrillar morphology seen in the undoped material becomes patchy and irregular, suggesting that the dopant may disrupt the fibril formation near the surface, with dopants either blocking phase formation or acting as nucleation sites. The surface roughness is relatively unaffected; root mean squared (RMS) values were 0.47 and 0.40 nm for the pristine and 0.1 wt. % doped films, respectively.

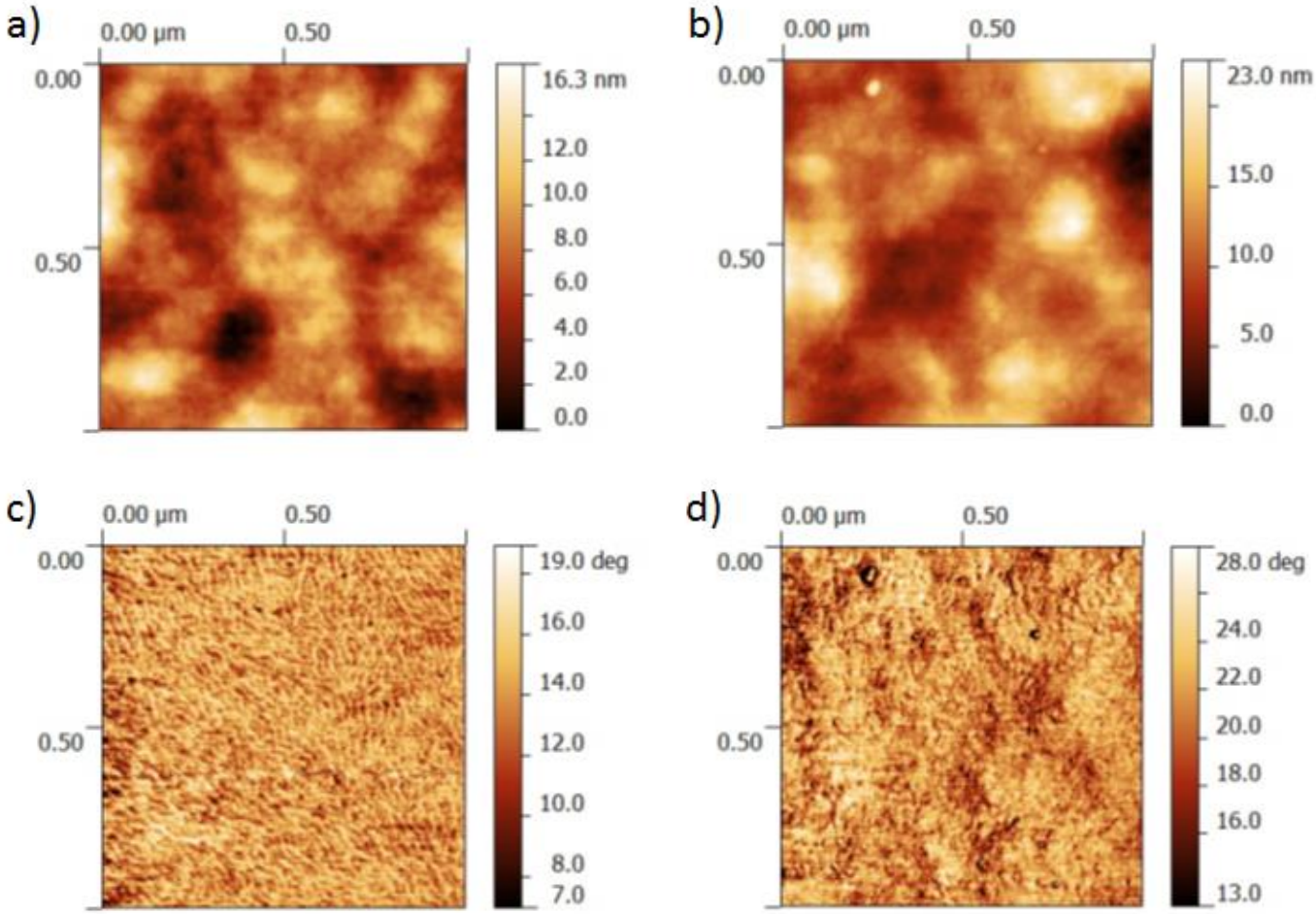

Figure 3.12**.** Atomic force microscopy height scans for pristine and 0.1 wt% Mo(tfd-$COCF_3$)$_3$-doped P3HT thin films, a) and b) respectively. The phase scans for the same regions are given in c) and d).

3.2.6 H-Aggregate Modelling of Absorbance Spectra

The UV-vis absorption spectra of P3HT films have been analyzed quantitatively to look for subtle changes in the local order upon doping. Applying a weakly interacting H-aggregate model to the absorbance of p-doped P3HT films, the fraction of aggregated P3HT and the free-exciton bandwidth (W) were estimated at various dopant concentrations.[51] W is related to conjugation length and intrachain order within the aggregates and can be estimated from the ratio of the 0-0 and 0-1 peak absorbance using the expression:

$$\frac{A_{0-0}}{A_{0-1}} = \left(\frac{1 - 0.24W/E_p}{1 + 0.073W/E_p}\right)^2 \qquad \text{Equation 3.3}$$

In this case the main intramolecular vibration, E_p, coupled to the electron transition is assumed to be a C=C symmetric stretch with an energy of ca. 0.18 eV. Calculated intrachain order and fraction aggregate can be affected by processing methods such as solvent choice and annealing conditions[52,53], and as such can plausibly be affected by the presence of impurities in the film. Samples were prepared in the following manner: Doped solutions were pre-mixed by adding small volumes of 0.1 or 1.0 mg / mL Mo(tfd-$COCF_3$)$_3$ solutions to 15 mg / mL P3HT chlorobenzene solutions and stirring for up to 1 hr in inert atmosphere. Solutions were spin-cast at 1000 rpm for 60 s on UV ozone-cleaned glass substrates (without ITO layer) to achieve films ca. 100 nm in thickness, which were then dried in vacuum (~10^{-6} Torr) and annealed at 120 °C for 30 min. Figure 3.13 demonstrates the fitting of the 0-0 to 0-4 absorbance peaks to the low energy region of the undoped film, up to ~ 2.3 eV, where no contribution from amorphous polymer is expected, using Gaussian curves to represent each transition.

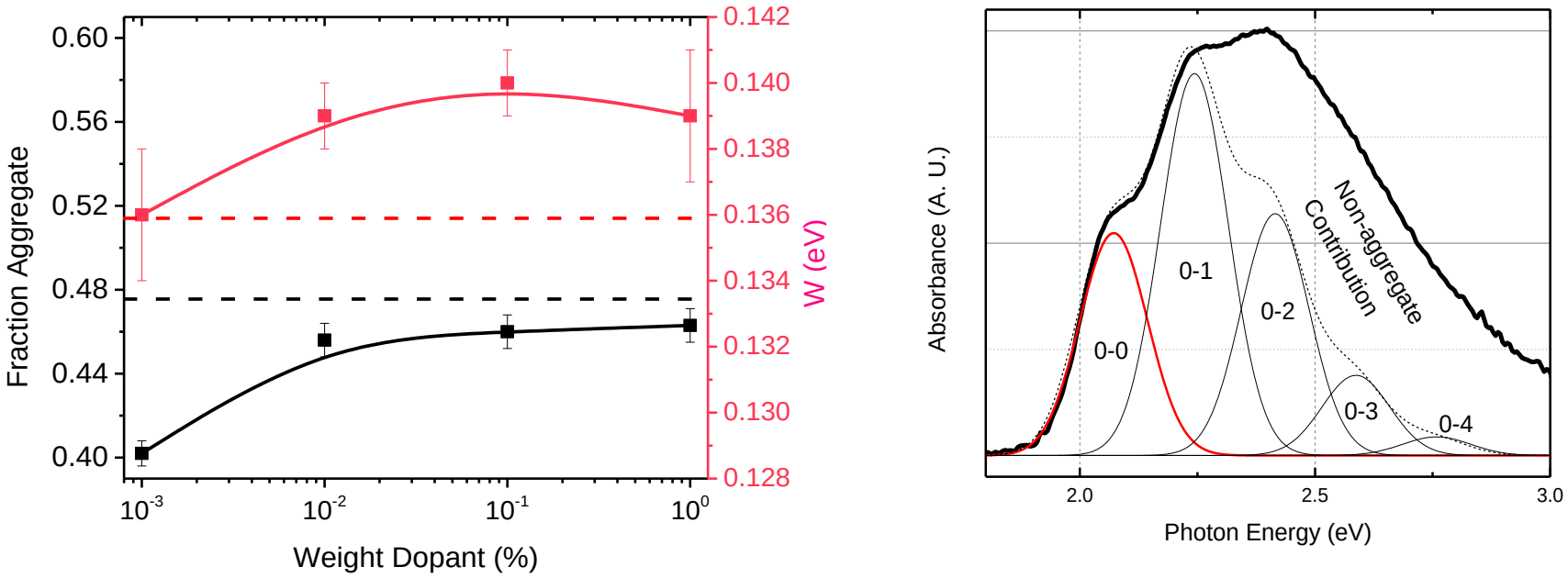

Figure 3.13. (left) Free-exciton bandwidth and fraction of aggregates estimated from UV-vis spectra for p-doped films of P3HT. Values for pristine films are displayed with dotted lines. (right) An example of H-aggregate fitting of the absorption spectrum of an undoped P3HT film.

To account for spatially correlated disorder in the film, the 0-0 and 0-1 peaks are fit to the absorption spectrum and, based on their ratio, the expected intensities of 0-2, 0-3, 0-4 peaks can be predicted in accordance with the Frank-Condon principle. Fitted values for the fraction of photophysical aggregates, determined by the ratio of the fitted peaks attributable to aggregated polythiophene over the full integrated spectrum, and W are given for doped P3HT films in Figure 3.13. Assuming the validity of the H-aggregate model and that no other factors affect the absorption spectrum, analysis of the spectra suggests that for low dopant concentration there is a drop in the aggregate fraction relative to undoped polymer, with the amorphous portion weighted for its lower oscillator strength. The total aggregated fraction drops by almost 7% at 10^{-3} wt. %, coinciding with the decrease in conductivity observed in Figure 3.3, though the exciton bandwidth of the aggregated portion experiences minimal changes. This can be attributable to the hypothesis that the interactions of the dopant only take place within the amorphous regions of the polymer and, at this concentration, the mixing of the materials results in a decrease of the proportion of ordered phase present. In blends with F_4-TCNQ, incorporation of the dopant into the aggregated P3HT phase has resulted in an increase in $A_{0\text{-}0}/A_{0\text{-}1}$, attributed to longer interaction lengths,[54] which is not observed in our system. At higher concentrations the fraction of aggregate returns to typical values, while the exciton bandwidth also grows slightly larger than for pristine values, indicating that it is possible that dopant presence is affecting aggregates and resulting in a slight decrease in intrachain order, yet it is most likely that most of the dopant has been pushed out of the polymer phase. A similar trend for annealed samples is shown in Figure 3.14.

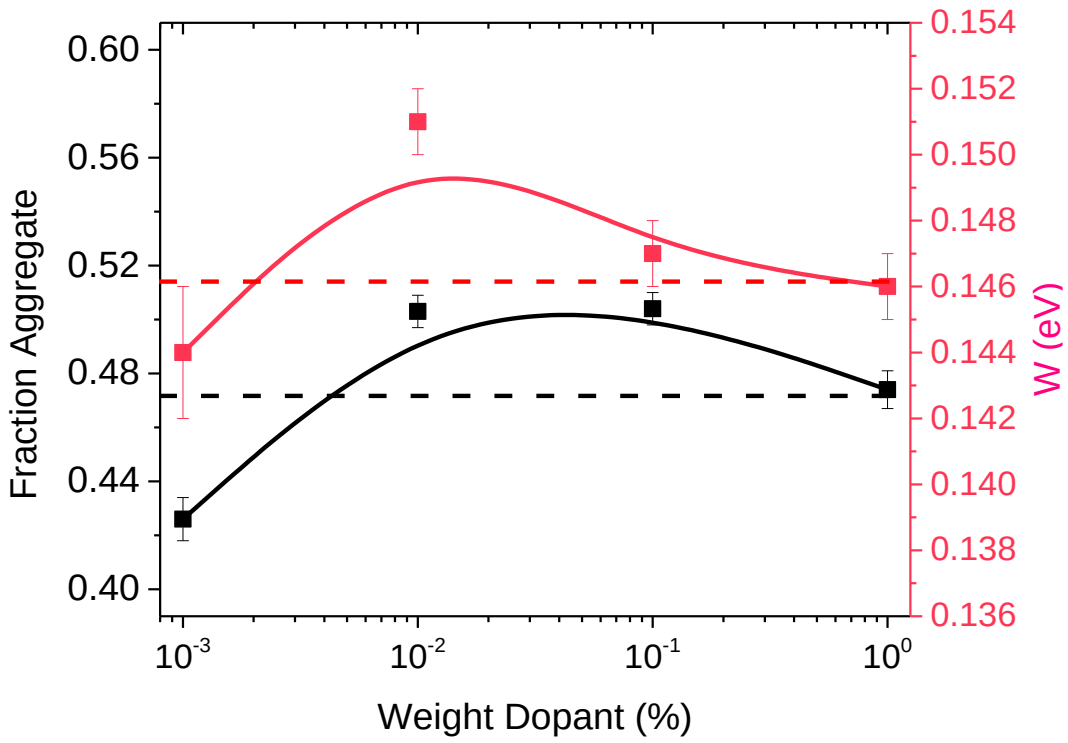

Figure 3.14. Free-exciton bandwidth and fraction of aggregates estimated from UV-vis spectra for annealed p-doped films of P3HT. Values for undoped films are indicated with dotted lines.

3.2.7 Grazing-Incidence Wide Angle X-Ray Scattering

A detailed discussion of grazing-incidence wide angle x-ray scattering (GIWAXS) in BHJ OPV active layers was given in Chapter 1. GIWAXS was conducted at the EAST – D1 beamline (http://www.chess.cornell.edu/chess/east/D1.htm) at the Cornell High Energy Synchrotron Source (CHESS) at Cornell University by Dr. Liyang Yu. The experimental parameters define the sample to detector distance as 100.25 mm, the X-ray wavelength as 1.155 Å, and the detector angle 0.15°. Data were analyzed using Fit 2d. (http://www.esrf.eu/computing/scientific/FIT2D/) Samples were prepared in the following manner: Doped solutions were pre-mixed by adding small volumes of 0.1 or 1.0 mg / mL Mo(tfd-$COCF_3$)$_3$ solutions to 15 mg / mL P3HT chlorobenzene

solutions and stirring for up to 1 hr in inert atmosphere. Solutions were spun-cast at 1000 rpm for 60 s on plasma-cleaned silicon substrates to achieve films ca. 100 nm in thickness, after which samples were dried in vacuum (~10^{-6} Torr) and then annealed at 120 °C for 30 min.

GIWAXS, displayed in Figure 3.15 as 1D q-plots summed across 90° of a 2D diffraction pattern, supports the absorbance modelling in that, while there appears to be a general trend of slight lamellar disorder induced by doping apparent in an increase of d-spacing in diffraction peaks, there is no compelling evidence of interruptions in short-range order, such as a decrease in integrated peak intensity, that might be expected from the dopant's presence primarily in crystalline portions of the polymer. From the pristine film, the π-stacking peak (010) shifts very slightly from 16.78 to 16.22 nm^{-1}, corresponding to an increase in d-spacing from 3.74 to 3.87 Å. The lamellar feature (100) also exhibits a shift from 15.6 to 16.2 Å. These increases in spacing are minor compared to the disruptions reported upon the incorporation of F_4-TCNQ into P3HT ordered phases, where d-spacings for (010) and (100) reach 4.11 Å and 18.0 Å respectively.[55] The successful blending of F_4-TCNQ into the P3HT phase is possibly due to its planar structure, as opposed to the 3-dimensional structure of Mo(tfd-$COCF_3)_3$. An increasing loading of the p-dopant also coincides with a slight decrease in the intensity of the P3HT (100) peak. As film thicknesses are comparable, this may indicate a decrease in the lamellar order of P3HT chain packing upon the inclusion of dopants.

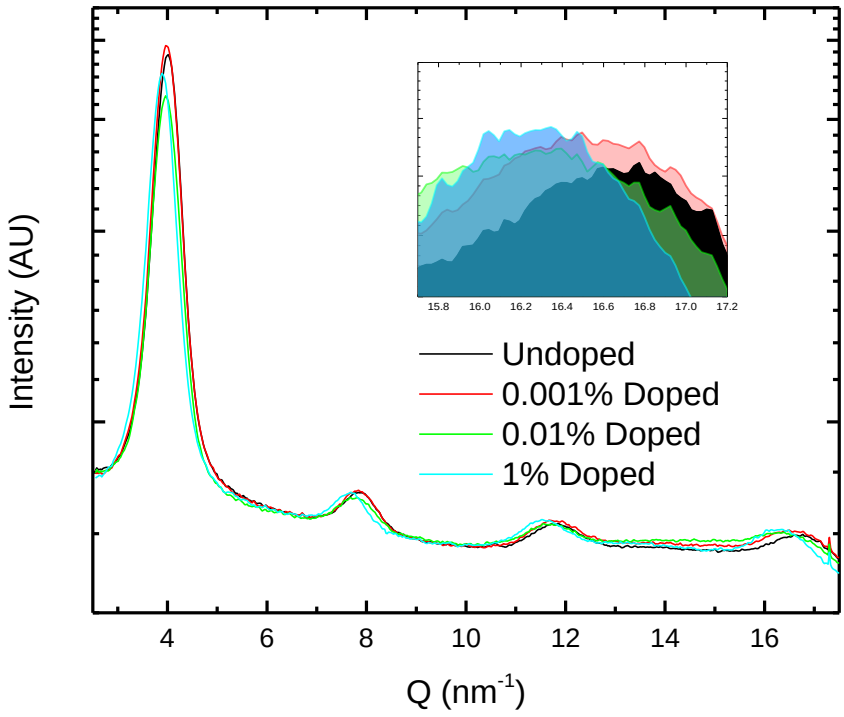

Figure 3.15. 1D GIWAXS patterns for P3HT doped with various wt. % of Mo(tfd-$COCF_3)_3$. The region near the (010) feature is shown in the inset. These patterns are integrated from 2D GIWAXS pseudocolor plot, such as that shown in Figure 1.16.

3.2.8 Rutherford Backscattering

Rutherford backscattering (RBS) spectroscopy is a technique in which backscattered high-energy ions are analyzed in order to determine elemental concentration and distribution in solid and gaseous samples, and is so named after Lord Ernest Rutherford's contribution to the well-known Geiger-Marsden "gold foil" experiment which, in 1913, led to a new understanding of atomic structure incorporating a positively charged nucleus.[56,57] RBS of solids involves elastic collisions between high kinetic energy ions, typically alpha particles, and the stationary nuclei in the sample. The energy of the backscattered particle (E) is given by:

$$E = E_0 \left(\frac{m_1 \cos\theta + \sqrt{m_2^2 - m_1^2 (\sin\theta)^2}}{m_1 + m_2} \right)^2 \qquad \text{Equation 3.4}$$

where E_0 is the kinetic energy of the incoming alpha particle, m_1 and m_2 are the masses of the alpha particle and the stationary nucleus respectively, and θ is the angle of the scattered alpha particle relative to its incoming path.[58] The energy is also lowered as the ion traverses through a material due to inelastic small-angle scattering off of electrons, referred to as the *stopping power* of the material and is typically proportional to the atomic number of the elements in the sample.[58] This allows for depth determination of elements in a solid sample.

An HRBS-V500 instrument, from Kobel Steel, was operated at the King Abdullah University of Science & Technology, using a 400 keV alpha-particle beam in order to move the molybdenum feature into the instrument detector's range. Samples were prepared in the following manner: Doped solutions were pre-mixed by adding a small volume of a 1.0 mg / mL Mo(tfd-$COCF_3$)$_3$ solution to a 15 mg / mL P3HT chlorobenzene solution and stirring for up to 1 hr in inert atmosphere. Solutions were spin-cast at 1000 rpm for 60 s on UV-ozone cleaned glass substrates to achieve films ~100 nm in thickness, after which samples were dried in vacuum (~10^{-6} Torr) and then annealed at 120 °C for 30 min.

The dopant distribution as a function of depth in a 5 wt % doped film was investigated with RBS. The heavy molybdenum nucleus allows facile differentiation of the dopant distribution inside the organic film, as carbon, silicon, oxygen, and even sulfur scatter at much lower energies, as demonstrated previously by Qi *et al*, who used RBS to investigate Mo(tfd)$_3$ as a dopant for α-NPD.[59] With an incoming helium particle beam at 400 keV, the calculated onset of particles scattered from molybdenum at the surface of the film, at ~ 360 keV, has a very low intensity as seen in Figure 3.16. As

particles penetrate the depth of a film, they lose energy due to glancing nuclei collisions (nuclear stopping) and interactions with electrons (electronic stopping) depending on their velocity and on the density and elemental composition of the film. The energy loss by unit of depth can be obtained as a product of density and scattering cross-section, $\rho\left(Z_1 Z_2 q^2/4Esin^2(\frac{\theta}{2})\right)^2$, where Z_1 and Z_2 are the atomic numbers of the projectile and scattering nucleus respectively. For the Molybdenum feature, with decreasing energy and increasing depth, the feature grows roughly until the calculated organic/glass interface at ~ 316 keV, suggesting that the dopants are unevenly distributed through the thickness of the film, with a tendency to settle away from the surface (although apparently still disrupting the P3HT surface fibril formation, as evidenced by the AFM phase images in Figure 3.12). Employing a film thickness of 100 nm, the energy of particles scattered from molybdenum atoms at any depth is calculated to have zero overlap with other elements in the film, indicating that the present signal intensity is originating entirely from the presence of the dopant. The build-up at the bottom of the film could be responsible for the lower fill factors at higher doping concentrations, arising from surface dipoles between the PEIE and the aggregating p-dopants. The distribution of fluorine, the other identifying element of the dopant, could not be as readily established given overlap with the signals from organic/substrate elements.

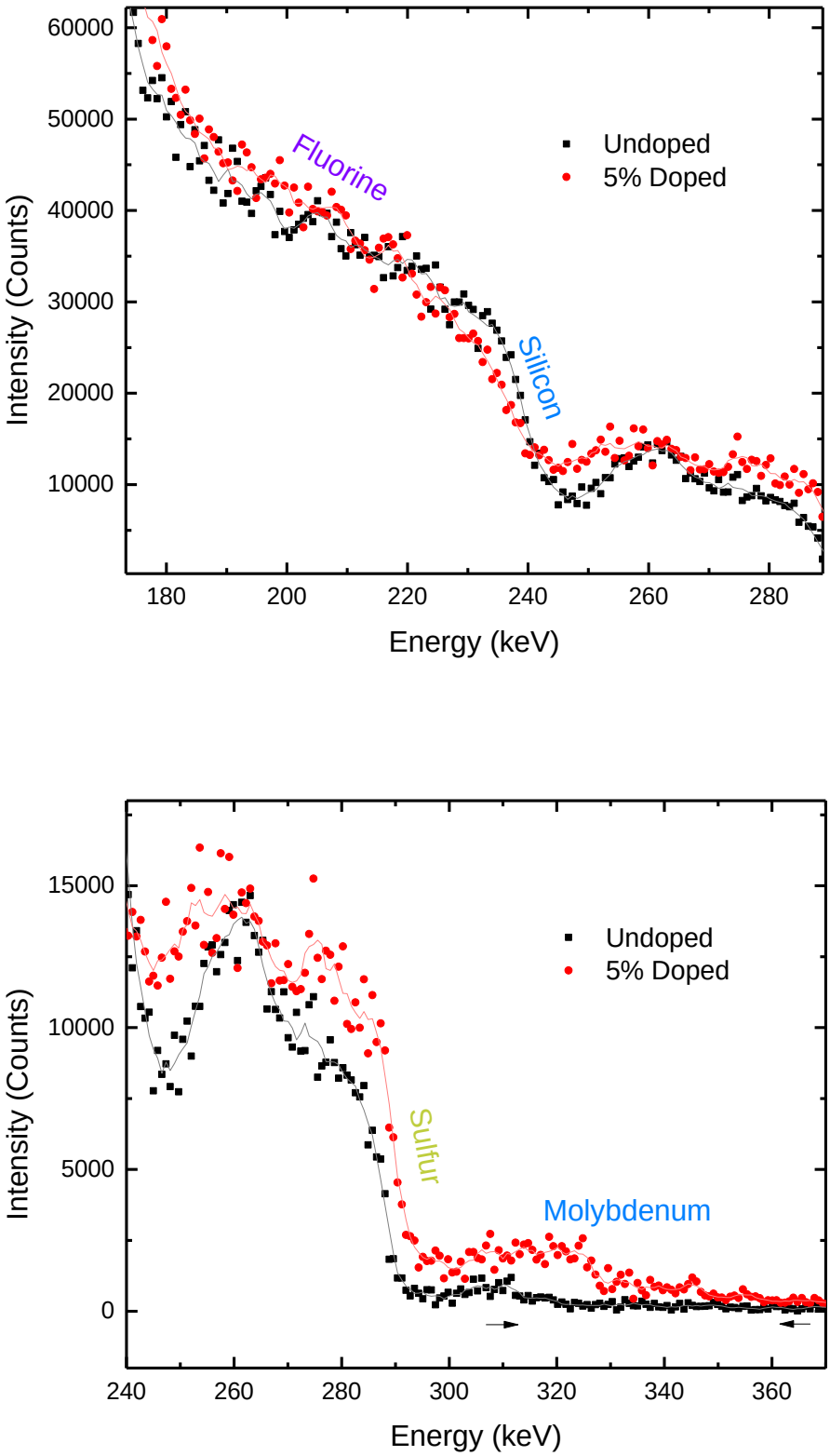

Figure 3.16. Rutherford backscattering spectra focusing on the Fluorine, Sulfur, and Molybdenum regions of undoped and doped P3HT films on glass. Lines are a smoothed average of values.

3.2.9 Organic Photovoltaic Devices with a Planar Dopant

p-Doping was also carried out with another oxidant, $Ni(tfd)_2$, exhibiting a comparable reduction potential to $Mo(tfd\text{-}COCF_3)_3$, the near-planar molecular structure of which might be anticipated to lead to less disruption of the P3HT film morphology than occurs with the bulky 3-dimensional molybdenum-based oxidant. $Ni(tfd)_2$ was introduced in the same manner to P3HT/$PC_{61}BM$ solar cells (see Section 3.2.3). The resulting trend in Figure 3.17 & Table 3.3 is very similar to that seen using the non-planar $Mo(tfd\text{-}COCF_3)_3$ dopant: after an initial drop in *FF* and J_{SC}, values of these parameters increase with increasing dopant concentration to reach maxima (still lower than the values seen for undoped films), as was seen when using the molybdenum dopant. However, the doping loading at which the *FF* and J_{SC} appear to recover is around one order of magnitude lower for $Ni(tfd)_2$ than for the Mo dopant. Though this dopant has a planar structure, the central Ni atom and tetrahedral $–CF_3$ groups result in a slightly increased thickness orthogonal to the plane relative to that of F_4-TCNQ, which can possibly prevent their incorporation into P3HT aggregates.

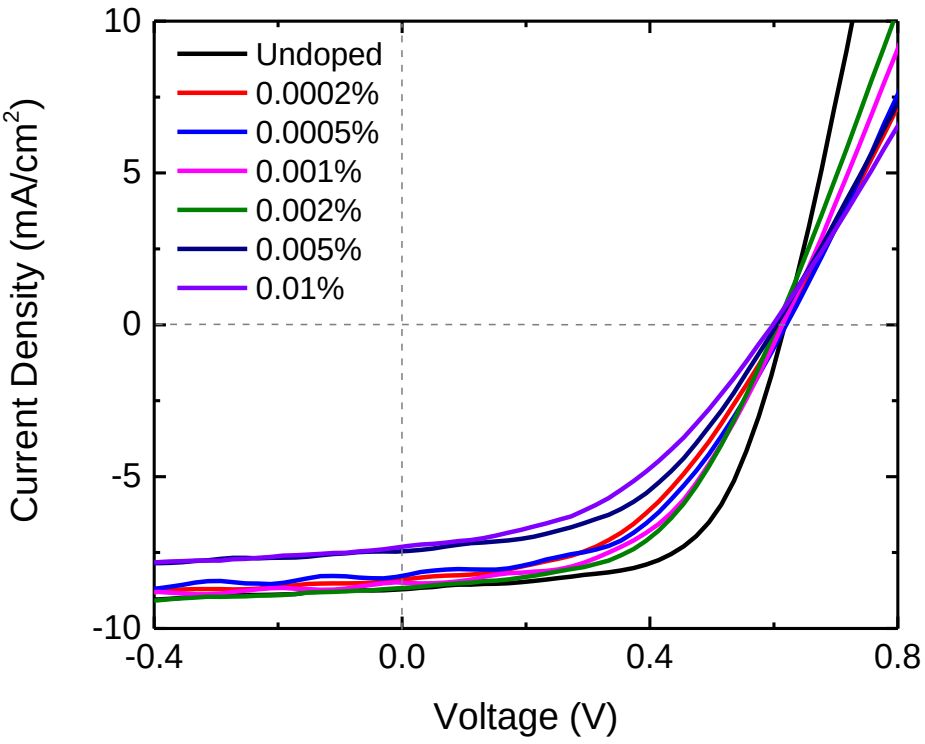

Figure 3.17. *J-V* curves of P3HT/$PC_{61}BM$ devices p-doped with $Ni(tfd)_2$.

Table 3.3. OPV performance values of P3HT/$PC_{61}BM$ devices p-doped with $Ni(tfd)_2$.

Dopant Concentration	***J*SC (mA/cm^2)**	***V*OC (V)**	***FF* (%)**	**PCE (%)**
Undoped	8.7 ± 0.3	0.62 ± 0.01	62 ± 2	3.3 ± 0.2
0.0002%	8.4 ± 0.3	0.62 ± 0.00	48 ± 4	2.5 ± 0.2
0.0005%	8.3 ± 0.3	0.62 ± 0.01	50 ± 2	2.6 ± 0.2
0.001%	8.5 ± 0.4	0.62 ± 0.00	52 ± 4	2.7 ± 0.2
0.002%	8.7 ± 0.4	0.61 ± 0.01	53 ± 1	2.8 ± 0.1
0.005%	8.5 ± 0.2	0.60 ± 0.01	49 ± 2	2.5 ± 0.1
0.01%	7.3 ± 0.6	0.60 ± 0.01	44 ± 4	2.0 ± 0.3

3.3 Conclusion

The effects of ultra-low p-dopant loading in P3HT thin films were examined by conductivity & photoelectron spectroscopy experiments; this doping did not lead to an improvement in the OPV performance of BHJ active layers with $PC_{61}BM$. TEM, AFM, UV-vis. absorbance modelling, GIWAXS, and RBS data suggest that the dopant is not evenly dispersed in the active layer, but is aggregating in amorphous regions with increasingly large and well-separated aggregates with increasing dopant loading. Although there appears to be a minor change in the long-range ordering of the P3HT phase upon introduction of the dopant, as observed by AFM, there is no compelling evidence of dopant inclusion within the crystalline phase. The non-uniform in-plane and out-of-plane distribution of the dopants, which results in interruptions in the long-range order of the P3HT phases and possibly manifests itself in over-doped pockets that increase energetic disorder inside the active layer, have a detrimental effect on the device performance that overshadows any possible benefit from passivation of the polymer trap states. In the complex morphologies that occur in OPV bulk heterojunctions, the use of dopants will lead to additional complications, especially in well-ordered systems; for this reason, p-doping might be more successful with materials that have less intricate short-range order than polythiophenes. Such systems are studied in the next chapter.

3.4 Additional Experimental Information

Poly(3-hexylthiophene-2,5-diyl) (regioregular, Electronic grade 4002-EE) was purchased from Rieke Metals Inc. $PC_{61}BM$ (ADS61BFA) was purchased from

American Dye Source Inc. Molybdenum tris[1-(trifluoromethylcarbonyl)-2-(trifluoromethyl)-ethane-1,2-dithiolene][30] and nickel bis[1,2-(trifluoromethyl)-ethane-1,2-dithiolene][60] were prepared according to the literature by Yadong Zhang and Raghunath R. Dasari, respectively.

3.5 Works Cited

[1] W. Smith, “Effect of Light on Selenium During the Passage of An Electric Current,” *Nature*, vol. 7, no. 173, pp. 303–303, Feb. 1873.

[2] S. Bidwell, “On the Sensitiveness of Selenium to Light, and the Development of a similar Property in Sulphur,” *Proc. Phys. Soc. London*, vol. 7, no. 1, pp. 129–145, Feb. 1885.

[3] J. R. Woodyard, “Nonlinear circuit device utilizing germanium,” 14-Nov-1950.

[4] M. Sparks and G. K. Teal, “Method of making p-n junctions.” p. US2631356 A, 17-Mar-1953.

[5] M. Riordan and L. Hoddeson, “The origins of the pn junction,” *IEEE Spectr.*, vol. 34, no. 6, pp. 46–51, Jun. 1997.

[6] M. Riordan and L. Hoddeson, *Crystal Fire: The Invention of the Transistor and the Birth of the Information Age*. W. W. Norton & Company, 1988.

[7] P. Kar, *Doping in Conjugated Polymers*. John Wiley & Sons, 2013.

[8] K. . Aasmundtveit, E. . Samuelsen, O. Inganäs, L. A. . Pettersson, T. Johansson, and S. Ferrer, “Structural aspects of electrochemical doping and dedoping of poly(3,4-ethylenedioxythiophene),” *Synth. Met.*, vol. 113, no. 1–2, pp. 93–97, Jun. 2000.

[9] A. Dai, Y. Zhou, A. L. Shu, S. K. Mohapatra, H. Wang, C. Fuentes-Hernandez, Y. Zhang, S. Barlow, Y. L. Loo, S. R. Marder, B. Kippelen, and A. Kahn, “Enhanced charge-carrier injection and collection via lamination of doped polymer layers p-doped with a solution-processible molybdenum complex,” *Adv. Funct. Mater.*, vol. 24, pp. 2197–2204, 2014.

[10] S. P. Tiwari, W. J. Potscavage, T. Sajoto, S. Barlow, S. R. Marder, and B. Kippelen, “Pentacene organic field-effect transistors with doped electrode-semiconductor contacts,” *Org. Electron.*, vol. 11, no. 5, pp. 860–863, May 2010.

[11] W. Gao and A. Kahn, “Electrical doping: the impact on interfaces of pi-conjugated molecular films,” *J. Phys. Condens. Matter*, vol. 15, pp. S2757–S2770, 2003.

[12] W. Gao and A. Kahn, “Electronic structure and current injection in zinc phthalocyanine doped with tetrafluorotetracyanoquinodimethane: Interface versus bulk effects,” *Org. Electron.*, vol. 3, no. 2, pp. 53–63, 2002.

[13] W. Gao and A. Kahn, “Controlled p doping of the hole-transport molecular material N,N-diphenyl-N,N-bis(1-naphthyl)-1,1-biphenyl-4,4-di amine with tetrafluorotetracyanoquinodimethane,” *J. Appl. Phys.*, vol. 94, pp. 359–366, 2003.

[14] D. V. Lang, X. Chi, T. Siegrist, A. M. Sergent, and A. P. Ramirez, “Amorphouslike density of gap states in single-crystal pentacene,” *Phys. Rev. Lett.*, vol. 93, no. 8, p. 086802, 2004.

[15] J. Rivnay, R. Noriega, J. E. Northrup, R. J. Kline, M. F. Toney, and A. Salleo, “Structural origin of gap states in semicrystalline polymers and the implications for charge transport,” *Phys. Rev. B - Condens. Matter Mater. Phys.*, vol. 83, no. 12, p. 121306, 2011.

[16] F. Bussolotti, S. Kera, K. Kudo, A. Kahn, and N. Ueno, “Gap states in Pentacene Thin Film Induced by Inert Gas Exposure,” *Phys. Rev. Lett.*, vol. 110, no. 26, p. 267602, Jun. 2013.

[17] W. L. Kalb, K. Mattenberger, and B. Batlogg, “Oxygen-related traps in pentacene thin films: Energetic position and implications for transistor performance,” *Phys. Rev. B - Condens. Matter Mater. Phys.*, vol. 78, p. 035334, 2008.

[18] C. Krellner, S. Haas, C. Goldmann, K. P. Pernstich, D. J. Gundlach, and B. Batlogg, “Density of bulk trap states in organic semiconductor crystals: Discrete levels induced by oxygen in rubrene,” *Phys. Rev. B - Condens. Matter Mater. Phys.*, vol. 75, no. 24, p. 245115, 2007.

[19] H. T. Nicolai, M. Kuik, G. A. H. Wetzelaer, B. de Boer, C. Campbell, C. Risko, J. L. Brédas, and P. W. M. Blom, “Unification of trap-limited electron transport in semiconducting polymers,” *Nat. Mater.*, vol. 11, pp. 882–887, 2012.

[20] Y. Qi, S. K. Mohapatra, S. Bok Kim, S. Barlow, S. R. Marder, and A. Kahn, “Solution doping of organic semiconductors using air-stable n-dopants,” *Appl. Phys. Lett.*, vol. 100, p. 083305, 2012.

[21] Y. Zhang, B. de Boer, and P. W. M. Blom, “Trap-free electron transport in poly(p -phenylene vinylene) by deactivation of traps with n -type doping,” *Phys. Rev. B*, vol. 81, no. 8, p. 085201, Feb. 2010.

[22] S. Olthof, S. Mehraeen, S. K. Mohapatra, S. Barlow, V. Coropceanu, J. L. Brédas, S. R. Marder, and A. Kahn, "Ultralow doping in organic semiconductors: Evidence of trap filling," *Phys. Rev. Lett.*, vol. 109, no. 17, p. 176601, 2012.

[23] S. Guo, S. B. Kim, S. K. Mohapatra, Y. Qi, T. Sajoto, A. Kahn, S. R. Marder, and S. Barlow, "N-doping of organic electronic materials using air-stable organometallics," *Adv. Mater.*, vol. 24, pp. 699–703, 2012.

[24] V. Coropceanu, J. Cornil, D. A. da Silva Filho, Y. Olivier, R. Silbey, and J.-L. Brédas, "Charge transport in organic semiconductors.," *Chem. Rev.*, vol. 107, no. 4, pp. 926–52, Apr. 2007.

[25] S. Olthof, S. Singh, S. K. Mohapatra, S. Barlow, S. R. Marder, B. Kippelen, and A. Kahn, "Passivation of trap states in unpurified and purified C_{60} and the influence on organic field-effect transistor performance," *Appl. Phys. Lett.*, vol. 101, 2012.

[26] A. Veysel Tunc, A. De Sio, D. Riedel, F. Deschler, E. Da Como, J. Parisi, and E. von Hauff, "Molecular doping of low-bandgap-polymer:fullerene solar cells: Effects on transport and solar cells," *Org. Electron.*, vol. 13, no. 2, pp. 290–296, Feb. 2012.

[27] Y. Zhang, H. Zhou, J. Seifter, L. Ying, A. Mikhailovsky, A. J. Heeger, G. C. Bazan, and T. Q. Nguyen, "Molecular doping enhances photoconductivity in polymer bulk heterojunction solar cells," *Adv. Mater.*, vol. 25, pp. 7038–7044, 2013.

[28] S. K. Mohapatra, Y. Zhang, B. Sandhu, M. S. Fonari, T. V. Timofeeva, S. R. Marder, and S. Barlow, "Synthesis, Characterization, and Crystal Structure of Molybdenum Complexes of Unsymmetrical Electron-Poor Dithiolene Ligands," *Submitted.*

[29] Y. Qi, T. Sajoto, S. Barlow, E.-G. Kim, J.-L. Brédas, S. R. Marder, and A. Kahn, "Use of a high electron-affinity molybdenum dithiolene complex to p-dope hole-transport layers.," *J. Am. Chem. Soc.*, vol. 131, no. 35, pp. 12530–1, Sep. 2009.

[30] S. A. Paniagua, J. Baltazar, H. Sojoudi, S. K. Mohapatra, S. Zhang, C. L. Henderson, S. Graham, S. Barlow, and S. R. Marder, "Production of heavily n- and p-doped CVD graphene with solution-processed redox-active metal–organic species," *Mater. Horiz.*, vol. 1, no. 1, pp. 111–115, Nov. 2014.

[31] J. Belasco, S. K. Mohapatra, Y. Zhang, S. Barlow, S. R. Marder, and A. Kahn,

"Molecular doping and tuning threshold voltage in 6,13-bis(triisopropylsilylethynyl)pentacene/polymer blend transistors," *Appl. Phys. Lett.*, vol. 105, no. 6, p. 063301, Aug. 2014.

[32] D. Cahen and A. Kahn, "Electron Energetics at Surfaces and Interfaces: Concepts and Experiments," *Adv. Mater.*, vol. 15, no. 4, pp. 271–277, Feb. 2003.

[33] N. Koch, "Organic electronic devices and their functional interfaces.," *Chemphyschem*, vol. 8, no. 10, pp. 1438–55, Jul. 2007.

[34] I. N. Hulea, H. B. Brom, A. J. Houtepen, D. Vanmaekelbergh, J. J. Kelly, and E. A. Meulenkamp, "Wide Energy-WindowView on the Density of States\rand Hole Mobility in Poly(p-Phenylene Vinylene)," *Phys. Rev. Lett.*, vol. 93, p. 166601, 2004.

[35] J. Hwang, E. G. Kim, J. Liu, J. L. Bredas, A. Duggal, and A. Kahn, "Photoelectron spectroscopic study of the electronic band structure of polyfluorene and fluorene-arylamine copolymers at interfaces," *J. Phys. Chem. C*, vol. 111, pp. 1378–1384, 2007.

[36] S. V Novikov, D. H. Dunlap, V. M. Kenkre, P. E. Parris, and A. V Vannikov, "Essential role of correlations in governing charge transport in disordered organic materials," *Phys. Rev. Lett.*, vol. 81, pp. 4472–4475, 1998.

[37] O. Tal, Y. Rosenwaks, Y. Preezant, N. Tessler, C. K. Chan, and A. Kahn, "Direct determination of the hole density of states in undoped and doped amorphous organic films with high lateral resolution," *Phys. Rev. Lett.*, vol. 95, no. 25, p. 256405, 2005.

[38] A. F. Stassen, R. W. I. de Boer, N. N. Iosad, and A. F. Morpurgo, "Influence of the gate dielectric on the mobility of rubrene single-crystal field-effect transistors," *Appl. Phys. Lett.*, vol. 85, no. 17, p. 3899, Oct. 2004.

[39] A. Higgins, S. K. Mohapatra, S. Barlow, S. R. Marder, and A. Kahn, "Dopant controlled trap-filling and conductivity enhancement in an electron-transport polymer," *Appl. Phys. Lett.*, vol. 106, no. 16, p. 163301, Apr. 2015.

[40] P. Pingel and D. Neher, "Comprehensive picture of p -type doping of P3HT with the molecular acceptor F_4TCNQ," *Phys. Rev. B*, vol. 87, no. 11, p. 115209, Mar. 2013.

[41] H.-L. Cheng, W.-Q. Lin, and F.-C. Wu, "Effects of solvents and vacancies on the electrical hysteresis characteristics in regioregular poly(3-hexylthiophene)

organic thin-film transistors," *Appl. Phys. Lett.*, vol. 94, no. 22, p. 223302, Jun. 2009.

[42] Z. Xu, L.-M. Chen, M.-H. Chen, G. Li, and Y. Yang, "Energy level alignment of poly(3-hexylthiophene): [6,6]-phenyl C_{61} butyric acid methyl ester bulk heterojunction," *Appl. Phys. Lett.*, vol. 95, no. 1, p. 013301, Jul. 2009.

[43] Y. Yi, J. E. Lyon, M. M. Beerbom, and R. Schlaf, "Characterization of indium tin oxide surfaces and interfaces using low intensity x-ray photoemission spectroscopy," *J. Appl. Phys.*, vol. 100, no. 9, p. 093719, Nov. 2006.

[44] M. L. Tietze, P. Pahner, K. Schmidt, K. Leo, and B. Lüssem, "Doped Organic Semiconductors: Trap-Filling, Impurity Saturation, and Reserve Regimes," *Adv. Funct. Mater.*, vol. 25, no. 18, pp. 2701–2707, May 2015.

[45] P. Champness, *An Introduction to Electron Diffraction in the Transmission Electron Microscope*. BIOS Scientific Publishers, 2001.

[46] T. J. Savenije, J. E. Kroeze, X. Yang, and J. Loos, "The formation of crystalline P3HT fibrils upon annealing of a PCBM:P3HT bulk heterojunction," *Thin Solid Films*, vol. 511–512, pp. 2–6, Jul. 2006.

[47] K. Tremel and S. Ludwigs, *P3HT Revisited – From Molecular Scale to Solar Cell Devices*, vol. 13. Berlin, Heidelberg: Springer, 2014.

[48] J. Goldstein, *Scanning Electron Microscopy and X-ray Microanalysis: Third Edition*. Plenum, 2003.

[49] F. Deschler, E. Da Como, T. Limmer, R. Tautz, T. Godde, M. Bayer, E. von Hauff, S. Yilmaz, S. Allard, U. Scherf, and J. Feldmann, "Reduced Charge Transfer Exciton Recombination in Organic Semiconductor Heterojunctions by Molecular Doping," *Phys. Rev. Lett.*, vol. 107, no. 12, p. 127402, Sep. 2011.

[50] R. C. Hiorns, P. Iratçabal, D. Bégué, A. Khoukh, R. De Bettignies, J. Leroy, M. Firon, C. Sentein, H. Martinez, H. Preud'homme, and C. Dagron-Lartigau, "Alternatively linking fullerene and conjugated polymers," *J. Polym. Sci. Part A Polym. Chem.*, vol. 47, no. 9, pp. 2304–2317, May 2009.

[51] F. C. Spano, "Modeling disorder in polymer aggregates: the optical spectroscopy of regioregular poly(3-hexylthiophene) thin films.," *J. Chem. Phys.*, vol. 122, no. 23, p. 234701, Jun. 2005.

[52] J. Clark, C. Silva, R. Friend, and F. Spano, “Role of Intermolecular Coupling in the Photophysics of Disordered Organic Semiconductors: Aggregate Emission in Regioregular Polythiophene,” *Phys. Rev. Lett.*, vol. 98, no. 20, p. 206406, May 2007.

[53] J. Clark, J.-F. Chang, F. C. Spano, R. H. Friend, and C. Silva, “Determining exciton bandwidth and film microstructure in polythiophene films using linear absorption spectroscopy,” *Appl. Phys. Lett.*, vol. 94, no. 16, p. 163306, Apr. 2009.

[54] C. Wang, D. T. Duong, K. Vandewal, J. Rivnay, and A. Salleo, “Optical measurement of doping efficiency in poly(3-hexylthiophene) solutions and thin films,” *Phys. Rev. B*, vol. 91, no. 8, p. 085205, Feb. 2015.

[55] H. Méndez, G. Heimel, S. Winkler, J. Frisch, A. Opitz, K. Sauer, B. Wegner, M. Oehzelt, C. Röthel, S. Duhm, D. Többens, N. Koch, and I. Salzmann, “Charge-transfer crystallites as molecular electrical dopants,” *Nat. Commun.*, vol. 6, p. 8560, Oct. 2015.

[56] R. Rhodes, *The making of the atomic bomb*. New York : Simon & Schuster, 1986.

[57] E. Rutherford and J. M. Nuttall, “LVII. Scattering of α particles by gases,” *Philos. Mag. Ser. 6*, vol. 26, no. 154, pp. 702–712, Oct. 1913.

[58] K. Oura, *Surface Science : an Introduction*. Berlin ; Springer-Verlag, 2003.

[59] Y. Qi, T. Sajoto, M. Kröger, A. M. Kandabarow, W. Park, S. Barlow, E.-G. Kim, L. Wielunski, L. C. Feldman, R. A. Bartynski, J.-L. Brédas, S. R. Marder, and A. Kahn, “A Molybdenum Dithiolene Complex as p -Dopant for Hole-Transport Materials: A Multitechnique Experimental and Theoretical Investigation,” *Chem. Mater.*, vol. 22, no. 2, pp. 524–531, Jan. 2010.

[60] D. J. Harrison, N. Nguyen, A. J. Lough, and U. Fekl, “New insight into reactions of Ni(S2C2(CF3)2)2 with simple alkenes: alkene adduct versus dihydrodithiin product selectivity is controlled by [Ni(S2C2(CF3)2)2]- anion.,” *J. Am. Chem. Soc.*, vol. 128, no. 34, pp. 11026–7, Aug. 2006.

[61] F. Machui and C. J. Brabec, *Semiconducting Polymer Composites: Principles, Morphologies, Properties and Applications*. Wiley, 2012.

[62] E. Stefanis and C. Panayiotou, “Prediction of Hansen Solubility Parameters with a New Group-Contribution Method,” *Int. J. Thermophys.*, vol. 29, no. 2, pp. 568–

585, May 2008.

CHAPTER 4 ULTRA-LOW P-DOPING OF LOW SHORT-RANGE ORDER POLYMERS IN EFFICIENT ORGANIC PHOTOVOLTAICS

4.1 Introduction

4.1.1 Additives in Organic Thin Film Processing

The deposition of organic thin films can be accomplished with a multitude of different techniques, even when limiting the discussion to solution-processing. The variation from technique to technique, such as blade-coating, spray-coating, spin-coating, etc., as well as the conditions applied has a powerful effect on the drying dynamics, and ultimately the phase growth and blending, of the dissolved or suspended materials.[1–5] To gain further control over the morphological outcome of these solution-processing methods, the use of additive molecules has become common practice.

In the fields of organic electronics, solvent additives have typically been classified as high-boiling point solvents that are added in small quantities to solutions, with the ability to alter material miscibility in solution as well as in the solid state, where the additive remains for a finite duration post-process, depending upon its volatility.[6–10] In organic photovoltaics, additives of this class, such as diiodooctane, have enabled enhanced customization of domain size and aggregate order in bulk heterojunctions employing small molecules or polymers, with the goal of optimizing exciton harvesting and separation.[9–12] Other, non-volatile agents, such as insulating polymers and hydrogen-bonding small molecules, can act as nucleation sites within a film, directing phase growth.[13–15] Ternary blends where one component is added at low

concentrations can also be considered a method of additive-based morphological control, as discussed in Chapter 2. The introduction of new materials into a film, even in very small amounts, has, more often than not, resulted in a morphological and/or microstructural change, regardless of intent.

4.1.2 Dopants Acting as Additives in Organic Photovoltaics

Trap states, as discussed in Chapter 3, can result from irregularities in the morphology that form during material processing[16,17] or from impurities introduced in the processing environment,[18–20] and can impede charge transport and increase recombination in OPV systems. To correct this, low levels of the molecular p-dopant 2,3,5,6-tetrafluoro-7,7,8,8-tetracyano-quinodimethane (F_4TCNQ) have been used to passivate trap states affecting donor polymers in the active layers of solution-processed polymer/fullerene bulk heterojunctions, observable through an increase in the short-circuit current density (J_{SC}). p-Doping of PCPDTBT/PC_{61}BM with F_4TCNQ was found to increase the power conversion efficiency from 3.3% to a maximum value of 3.6% at a loading of 0.5 wt. % with respect to the polymer, via an increase in the J_{SC} from 9.4 to 10.3 mA/cm^2, with further increases in the doping level leading to a decrease in PCE.[21] Low levels of F_4TCNQ doping have also led to an improvement in the performance of PCDTBT/PC_{71}BM cells, for which the PCE was increased from 6.4 to 7.9%, again largely as a result of increasing the J_{SC} from 11.0 to 14.0 mA/cm^2, by use of 0.4 wt% of the dopant.[22] No drastic effect on the BHJ nanostructure was seen upon dopant introduction, according to atomic force microscopy and X-ray scattering experiments.

Despite the publication of these studies regarding the effects of p-doping in bulk heterojunctions based on donor-acceptor copolymers,[21,22] molecular dopants have been unsuccessful in improving the performance of OPVs employing the widely studied

homopolymer, poly(3-hexylthiophene) (P3HT), when introduced into the bulk heterojunction. Studies with F_4TNCQ/P3HT blends in literature have shown a distinct change in P3HT order upon dopant incorporation, including evidence of co-phases of the two materials.[23–26] The work of the previous chapter, employing a non-planar molybdenum dithiolene derivative as the p-dopant, has also been unsuccessful in producing improvements in P3HT:PC_{61}BM OPVs due to inhomogeneous distributions of the dopants in the film, likely resulting from exclusion from the well-ordered domains during their formation.[27] This chapter presents a study of the effects of low doping levels, using similar dopants, on the electronic and morphological characteristics of the less-ordered, high-performance copolymers poly(thienothiophene-benzodithiophene) (PTB7) and poly[hepta-decanyl-carbazole-(dithienyl-benzothiadiazole)] (PCDTBT), and on the OPV performance of their respective solar cells with PC_{71}BM, with the goal of completing our understanding of the activity of these dopants in diverse bulk heterojunction films. We employ the molecular p-dopants molybdenum tris[1-(methoxycarbonyl)-2-(trifluoromethyl)-ethane-1,2-dithiolene], Mo(tfd-CO_2Me)$_3$,[28] and molybdenum tris[1-(trifluoromethylcarbonyl)-2-(trifluoromethyl)-ethane-1,2-dithiolene], Mo(tfd-$COCF_3$)$_3$,[29] which have high electron affinities (*EA*) of 5.2 and 5.4 eV respectively,‡

---

‡ Mo(tfd-CO_2Me)$_3$ and Mo(tfd-$COCF_3$)$_3$ oxidation potentials have estimated in the solution state by electrochemistry to be + 0.16 V and + 0.39 V vs. ferrocene respectively. As the *EA* of Mo(tfd-CO_2Me)$_3$ has been determined by inverse photoelectron spectroscopy to be 5.2 eV in the solid state, we estimate the *EA* of Mo(tfd-$COCF_3$)$_3$ by adding the difference in the oxidation potentials to the value.[52]

have been shown to p-dope graphene and small-molecule organic semiconductors,[29,30] and have sufficient miscibility with organic solvents and many semiconductors materials to allow for solution processing.

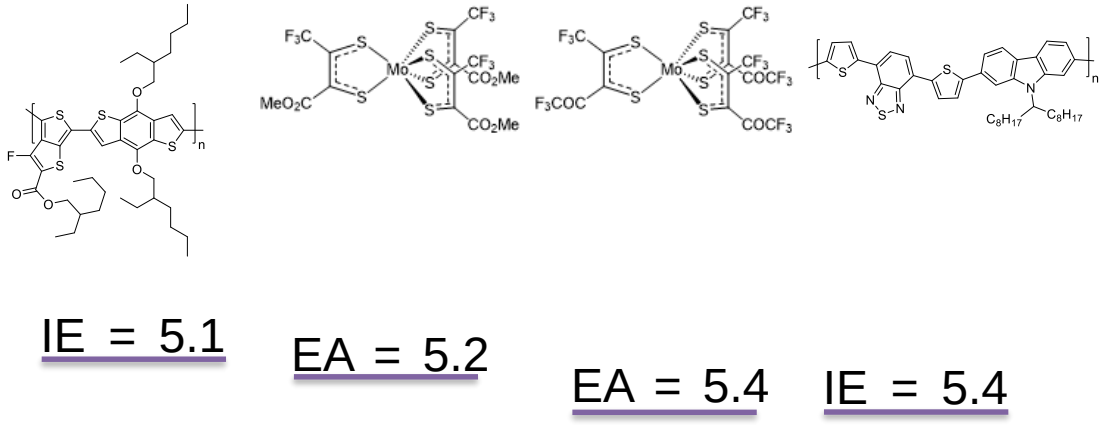

Figure 4.1. Structures and relevant energy levels of PTB7 (far left), Mo(tfd-CO_2Me)$_3$ (middle left), Mo(tfd-$COCF_3$)$_3$ (middle right), and PCDTBT (far right).

4.2 Methods & Results

4.2.1 Conductivity & Mobility Measurements

An in-depth discussion of the methods of conductivity and mobility (μ) measurements of organic semiconductors was given in Chapter 1. For this chapter, both σ and μ were measured at the King Abdullah University of Science and Technology on spun-cast PTB7 and PCDTBT films containing various loadings of Mo(tfd-CO_2Me)$_3$ and Mo(tfd-$COCF_3$)$_3$, respectively, deposited over plasma-cleaned pre-patterned electrodes (45 nm Au/5 nm ITO) on 230 nm silica over silicon (3×10^{17} cm^{-3} n-doped) substrates. The conductivity was estimated using the ohmic (linear) region of the *I-V* curves between the source and drain electrodes, converting current to current density using film thickness and channel width, which in all cases were 50-100 nm and 2 mm

respectively, and voltage to field using channel length, which were 2, 5, 10 or 20 μm. Conductivities measured at all four channel lengths gave similar values, indicating that contact resistance is negligible relative to film resistance. σ values are averaged across at least 8 pixels from all four channel lengths. Thicknesses were determined using a Dektak 150 profilometer. Doped solutions were pre-mixed by adding small volumes of 0.1 or 1 mg / mL Mo(tfd-$CO_2Me)_3$ or Mo(tfd-$COCF_3)_3$ solutions to 5 mg / mL PTB7 or PCDTBT chlorobenzene solutions and stirring for up to an hour in inert atmosphere. Solutions were spun-cast at 1000-1500 rpm for 60 s to achieve films between ca. 50 nm in thickness, after which samples were dried in vacuum (~10^{-6} Torr). Besides substrate cleaning, all processing steps and device testing were performed in an inert atmosphere.

OFET hole mobility was measured with the same devices, but generally displayed very minor decreases with increasing dopant concentration until 1%, above which no transistor activity was identified for any of the material/dopant systems. Mobility values were measured in a bottom-gate field-effect transistor (FET) format using an EP4 cascade microtech probe station & a Keithley 2400 source meter. Mobilities were determined by fitting the slope (m) of $I_D^{1/2}$-V_{GS} in the saturation regime by the expression $\mu = 2Lm^2/WC_i$, where L and W are the length and width of the channel, and C_i is the geometric capacitance of the gate dielectric, which is ca. 15 nF/cm^2 for the 230 nm silica over silicon (3×10^{17} cm^{-3} n-doped) substrates used in this work.[31] FET hole mobilities for PTB7 are displayed in Figure 4.1 by dopant concentration.

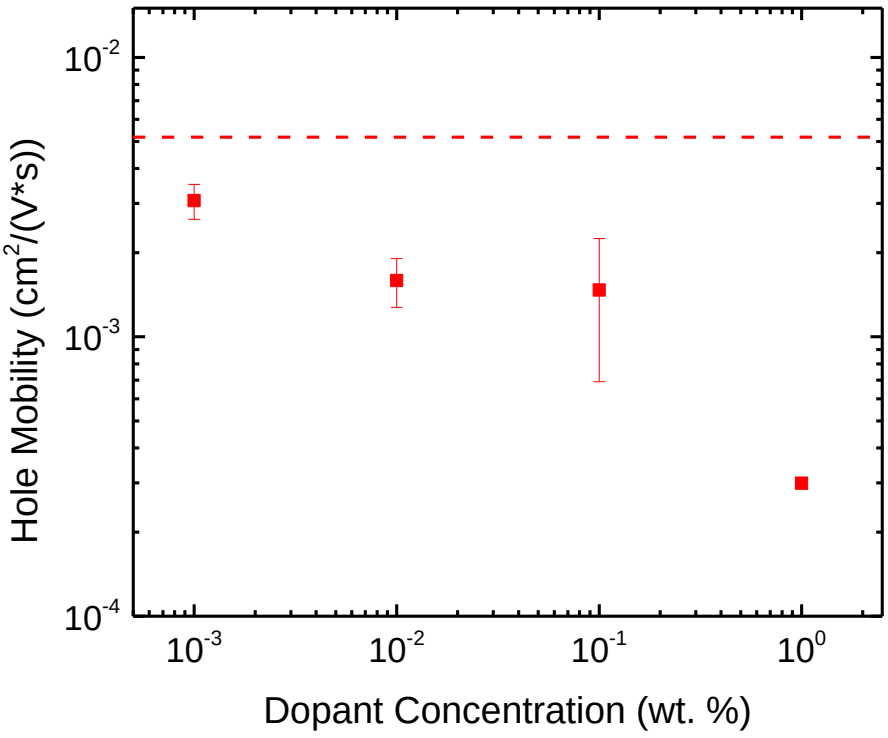

Figure 4.2. Hole mobility values of Mo(tfd-$CO_2Me)_3$-doped PTB7 upon the introduction of the p-dopant from concentrations of ca. 0.001 to 1 wt. %. The undoped value is indicated by the dotted line.

The fitted σ values for PTB7 and PCDTBT films are plotted in Figure 4.2 against their wt. % dopant. Larger increases in conductivity were observed with different p-dopants for each polymer: Mo(tfd-$CO_2Me)_3$ for PTB7 & Mo(tfd-$COCF_3)_3$ for PCDTBT. These dopants exhibit estimated electron affinities of 5.2 eV and 5.4 eV respectively determined electrochemically, which happen to line up well with the ionization energies of their respective polymers. Doping was implemented in solutions of the given dopant in chlorobenzene at percentages determined by weight %, as is convention with polymer doping. 1 wt. % Mo(tfd-$CO_2Me)_3$ in PTB7 corresponds to 1 dopant per ca. 98 monomers, and 1 wt. % Mo(tfd-$COCF_3)_3$ in PCDTBT corresponds to 1 dopant per ca. 122 monomers.

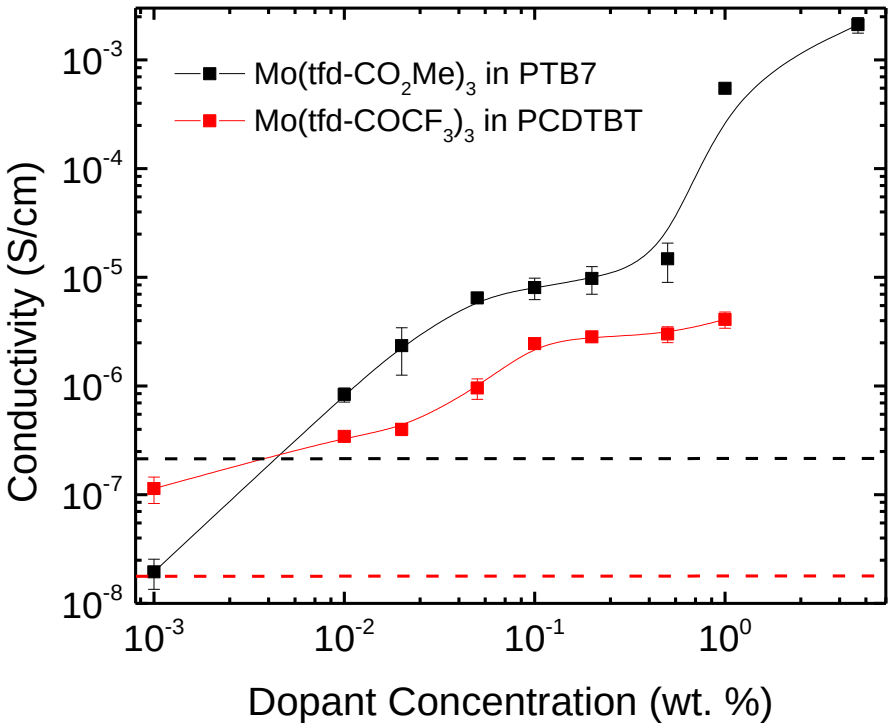

Figure 4.3. Conductivity evolutions of Mo(tfd-$CO_2Me)_3$-doped PTB7 and Mo(tfd-$COCF_3)_3$ PCDTBT upon the introduction of the respective p-dopants down to concentrations of ca. 0.001 wt. %. The lines are included as a visual guide. The undoped values are given by dotted lines.

The trends displayed above ca. 0.01 wt. % dopant concentration for both polymer/dopant systems are different from those that have been observed in other doped systems, and indicate varied collections of deep and shallow trap states among the two materials. For the PTB7/Mo(tfd-$CO_2Me)_3$ system, following the slight decrease in conductivity from 1.9×10^{-7} S/cm in the undoped case, in reasonable agreement with literature,[32] to 2.0×10^{-8} S/cm with 0.001 wt. % dopant, there is a gradual increase in σ with wt. %. This is interrupted by a depression in the slope at loadings between 0.05 to 0.5 wt. %. It is possible that this regime is due to an energetically localized distribution of trap states above the valence band, which is discussed further below. Following this

point there is a sharp jump in σ up to 5.5×10^{-4} S/cm at 1 wt. % dopant, leading to a more gradual increase.

The PCDTBT/Mo(tfd-$COCF_3$)$_3$ system displays a somewhat simpler trend, with increases in σ from the undoped value of 1.6×10^{-8} S/cm, again in reasonable agreement with literature,[33] up to 0.02 wt. % dopant where a sharper increase to 2.5×10^{-6} S/cm at 0.1 wt. % occurs. From this point there is less pronounced increase in conductivity growth up to 1 wt. % dopant, with the conductivity increasing to 4.1×10^{-6} S/cm. The stronger dopant Mo(tfd-$COCF_3$)$_3$ results in much higher conductivities with this polymer than its lower *EA* cousin, Mo(tfd-CO_2Me)$_3$, when doped to the same content by weight (see Figure 4.3). This is most likely due to the inability of the weaker dopant to passivate states or add carriers close to the valence band edge, occurring at ca. 5.4 eV for PCDTBT (Section 4.2.2).

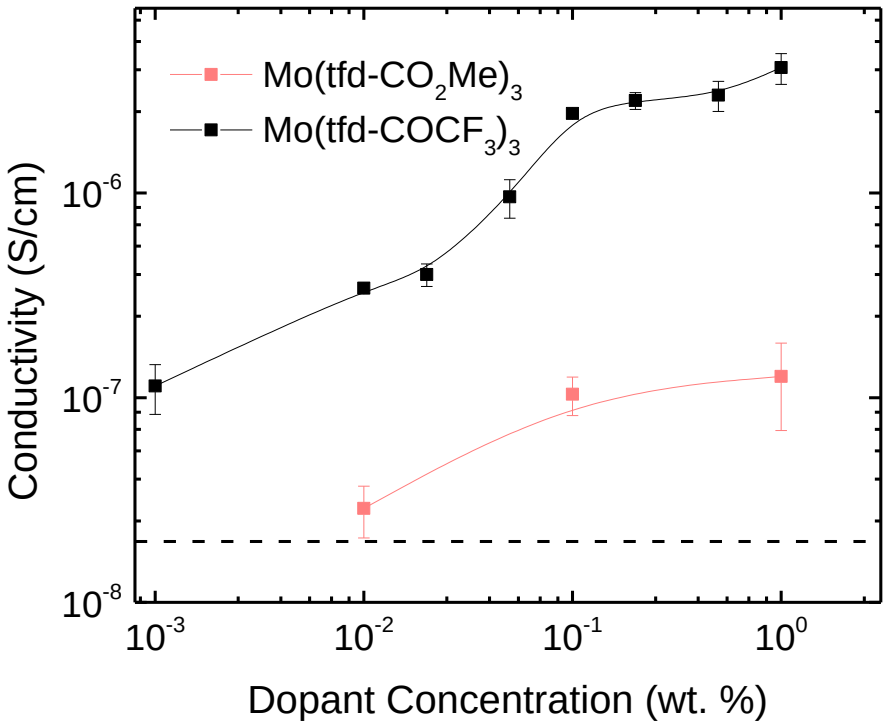

Figure 4.4. Comparison of the conductivity evolutions of PCDTBT with the p-dopants Mo(tfd-CO_2Me)$_3$ and Mo(tfd-$COCF_3$)$_3$. The lower *EA* of Mo(tfd-CO_2Me)$_3$ restricts its ability to passivate the traps of the high *IE* polymer, observable from the very slight improvement in conductivity. The lines are included as a visual guide. The undoped value is indicated by the dotted line.

Due to the amorphous nature of these materials, large percentages of dopant could be added to the film without processability issues (i.e. changes in morphology). For the PTB7/Mo(tfd-CO_2Me)$_3$ system the increase in the conductivity is consistent up to 30% (see Figure 4.4); its seems possible that doping could continue at higher concentrations before a drop in performance is observed, although quick inspection of the 30% film by optical microscopy shows a very small amount of aggregate-like features beginning to build up, scattered randomly across the film. The average conductivity for this sample, determined from the Ohmic region of the I-V curve, is 0.015 S/cm, and was checked with 4-point probe to a value of 0.025 S/cm. Note that this value is not as high as the conductivity observed from a P3HT film doped to 10%

by weight with the same dopant by Dai *et al.*[28], however PTB7 displays a greater versatility, with conductivities ranging across 6 orders of magnitude as the dopant concentration increases, due to the lower conductivity of the pristine polymer.

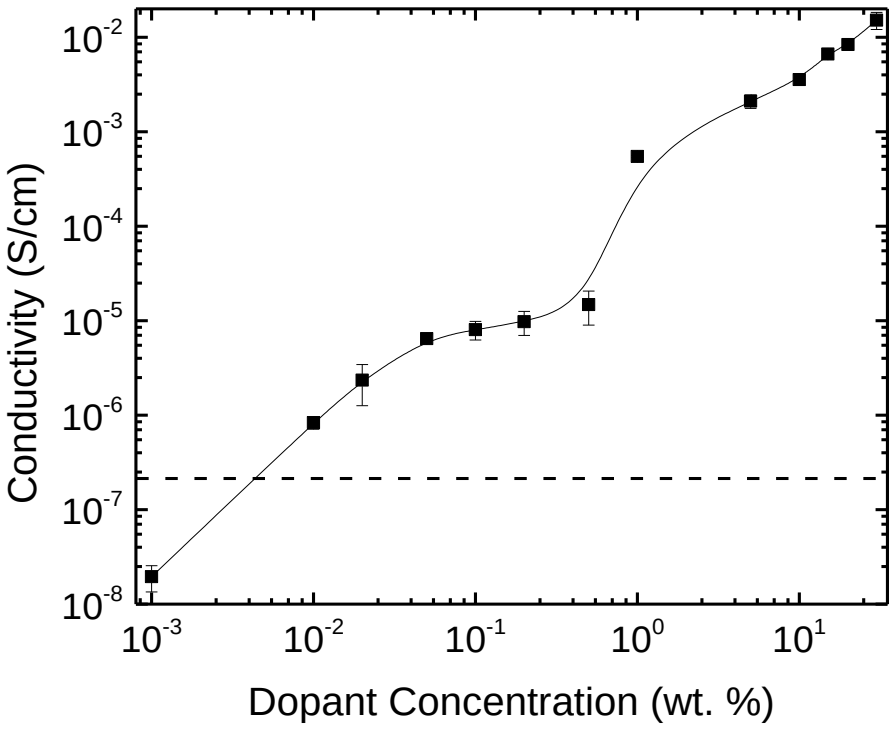

Figure 4.5. Conductivity values of Mo(tfd-$CO_2Me)_3$-doped PTB7 upon the introduction of the p-dopant from concentrations of ca. 0.001 to 30 wt. %. The line is included as a visual guide. The undoped value is given by a dotted line.

4.2.2 Ultra-violet Photoelectron Spectroscopy

A detailed discussion of photoelectron spectroscopy was given in Chapter 1. For this chapter, ultra-violet photoelectron spectroscopy (UPS) was performed in the ultra-high vacuum environment of a Kratos Axis Ultra^{DLD} XPS/UPS system at the Georgia Institute of Technology. All samples were in contact with the detector by a metallic clip and characterizations were performed at a take-off angle normal to the

film. Spot size was ca. 110 μm. UPS was acquired at 5 eV pass energy and 0.05 eV step size. Doped solutions were pre-mixed by adding small volumes of 0.1 or 1 mg / mL Mo(tfd-$CO_2Me)_3$ or Mo(tfd-$COCF_3)_3$ solutions to 5 mg / mL PTB7 or PCDTBT chlorobenzene solutions and stirring for up to an hour in inert atmosphere. ITO-on-glass substrates were solvent and plasma-cleaned; solutions were cast at 1500 rpm and dried in vacuum. Besides substrate cleaning, all processing steps and film testing were performed in an inert atmosphere or vacuum. The work function is determined by $WF = hv - BE_{SEE}$, where BE_{SEE} is binding energy of the secondary electron edge and hv is the He(I) photon energy (21.22 eV). The ionization energy is determined by $IE = WF + BE_{VBM}$, where BE_{VBM} is the cutoff of the valence band emission.

The Fermi level energy of an organic semiconductor lies between the valence band and conduction bands,[34,35] but its precise energy with the transport gap has a strong relationship to the distribution of trap states within this gap.[36–39] For polymers, the densities of such states can be dependent on molecular weight, crystallinity, and morphology. In hole-transporting materials, p-dopants remove electrons from these states of varying density above the valence band, which at a certain point can be observed in the shift of the Fermi level towards the valence-band edge.[40,41] Once local gap states have been passivated, dopants will remove electrons from the band itself. As the density of states is much higher than that within the gap, a much greater amount of dopant is required to shift the Fermi level or increase the conductivity by a given amount.

The work function (Φ) and ionization energy (*IE*) evolution of doped polymer films was determined by ultra-violet photoelectron spectroscopy, shown in Figure 4.5. Pristine PTB7 & PCDTBT, 20 nm films spin-cast from chlorobenzene on UV-Ozone cleaned ITO, exhibited Φs of 4.31 ± 0.01 eV and 4.39 ± 0.03 eV and *IE*s of 5.03 ± 0.02

eV and 5.39 ± 0.02 eV respectively, indicating differing valence band onset energies of ca. 0.72 eV and 1.00 eV relative to the Fermi level for the two polymers. Doping up to ca. 0.1 wt. % results in very minor changes in these values for either material system. However, at higher dopant concentrations the Φ begins to increase rapidly, corresponding to the features that may be related to trap passivation activity in the conductivity trends.

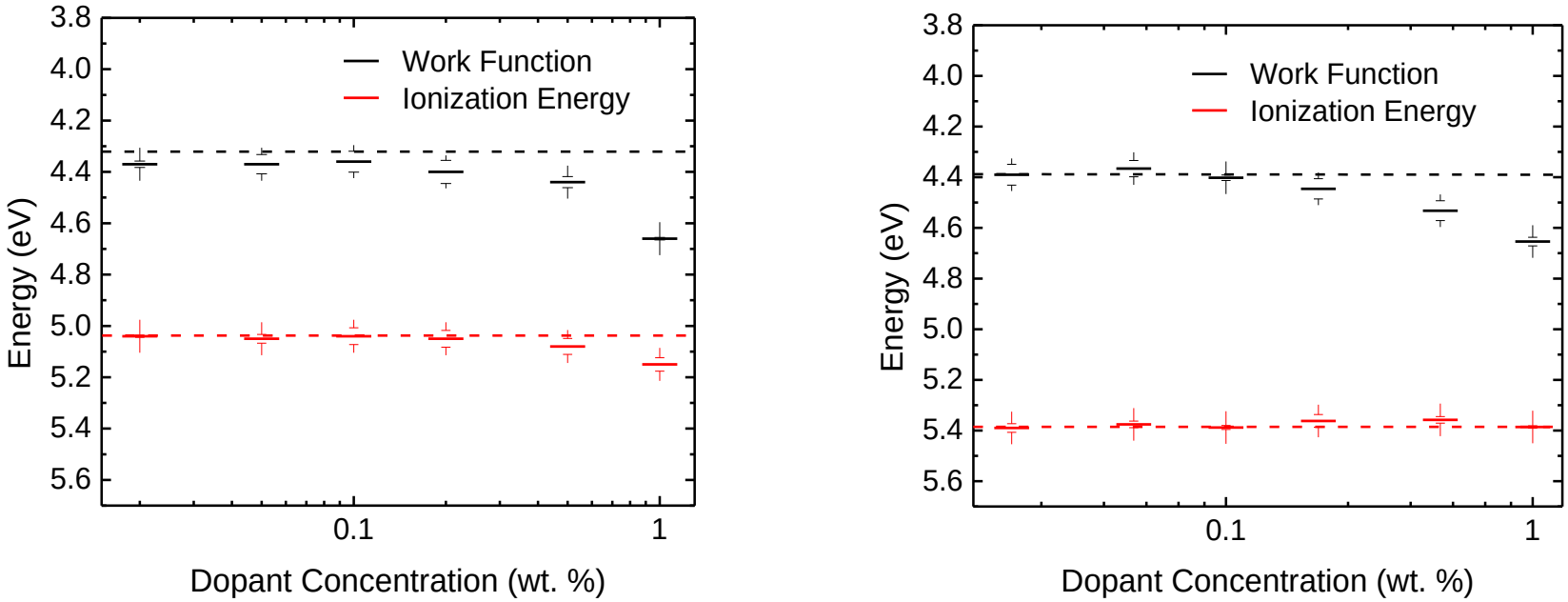

Figure 4.6. Work function and ionization energy evolution of PTB7 (left) and PCDTBT (right) upon the introduction of p-dopants Mo(tfd-$CO_2Me)_3$ and Mo(tfd-$COCF_3)_3$, respectively, from concentrations of ca. 0.02 to 1 wt. %, determined by UPS. Undoped values are represented by dotted lines.

The unchanging Φ at lower dopant concentrations is not necessarily an indication that no trap passivation is occurring in the regimes below 0.1 wt. %. At these ultra-low concentrations, the number holes added is presumably very small vs. the density of allowed states. Tietze *et al.* have demonstrated, in doped films of pentacene and ZnPc, that Fermi level energy modulation may only occur once the dopant concentration has approached the concentration of deep trap states.[42] After this point is reached, there is a transition to a dopant saturation regime, which proceeds with the passivation of shallow trap states and a rapid increase in Φ. For the present systems, this regime transition can be related to the depression in the PTB7 conductivity evolution, where it is possible that a large population of deep traps has been filled, as well as to the region of higher slope in that of PCDTBT. The difference between the two material systems could be the result of vastly differing impurities or morphologically-induced electronic variation.

4.2.3 Organic Photovoltaic Devices

An in-depth discussion of organic photovoltaics theory and general processing procedures was given in Chapter 1. For the study in this chapter, photovoltaic devices were fabricated at the King Abdullah University of Science and Technology. 200 nm-thick patterned ITO-on-glass substrates were sonicated in sodium dodecyl sulfate solution, water, acetone, and isopropanol, and then UV-ozone cleaned for 10 min. ZnO sol-gel was prepared by dissolving zinc acetate dihydrate (Sigma-Aldrich 379786) and ethanolamine (Sigma-Aldrich 411000) in 2-methoxyethanol (Sigma-Aldrich 284467) to a concentration of 0.75 M. After hydrolysis in air for ca. 24 h, the solution was spin-cast onto cleaned ITO surfaces in inert atmosphere, at 3000 rpm for 30 s, then annealed at 150 °C for 10 min before cooling down to room temperature, yielding a-ZnO films. The active layer blend solutions were stirred at 60 °C overnight and filtered using PTFE

0.45 µm filters before spin casting (800 rpm, 45 s and 1000 rpm, 45 s for PTB7 and PCDTBT donor polymers respectively). For PTB7:$PC_{71}BM$, BHJs active-layer blend solutions were obtained by mixing 1:1.5 w/w donor to acceptor ratios in chlorobenzene (concentration 25 mg/mL) with a 3% volume ratio of DIO. For PCDTBT:$PC_{71}BM$, BHJs active-layer blend solutions were obtained by mixing 1:4 w/w donor to acceptor ratios in 1:3 chlorobenzene/*o*-dichlorobenzene (concentration 15 mg/mL). Doped solutions were made by adding small volumes of 0.1 or 1 mg / mL $Mo(tfd\text{-}CO_2Me)_3$ or $Mo(tfd\text{-}COCF_3)_3$ solutions to the respective donor solutions and stirring for up to 1 h, before blending with $PC_{71}BM$ solutions. Samples were kept in a closed Petri dish for 20 min of solvent annealing after coating the active layer, then transferred into vacuum chamber (10^{-7} Torr) for thermal evaporation of MoO_x (15 nm) and silver (Ag) (100 nm). To ensure consistent results, each series of devices were fabricated simultaneously. The active area of the devices was 0.1 cm^2. The current density-voltage characteristics of the photovoltaic cells were measured using a Keithley 2400 under a simulated AM 1.5G solar irradiation at 100 mW/cm^2. The external quantum efficiency (EQE) was recorded by Oriel Quantum Efficiency Measurement Kit (Newport).

As noted in the previous paragraph, OPV devices incorporating PTB7 & PCDTBT active layers with $PC_{71}BM$ were doped by adding $Mo(tfd\text{-}CO_2Me)_3$ and $Mo(tfd\text{-}COCF_3)_3$ respectively to the active layer solutions, using polymer:dopant ratios in proximity to the trap passivation region observed in the conductivity and photoelectron spectroscopy experiments; results are shown in Figure 4.6 and Table 4.1. Cells constructed in a typical inverted format, with a layer-by-layer composition of ITO/a-ZnO/Active Layer/MoO_3/Ag, gave efficiencies of 7.7 ± 0.1 and 5.5 ± 0.2 % for PTB7/$PC_{71}BM$ and PCDTBT/$PC_{71}BM$ devices respectively, which are consistent with literature values for cells of this type.[43,44] Results were taken from over 25 cells from

multiple substrates in order to ensure the reliability of the observed trends. With both polymer systems, an indication of reduced recombination is observed as an increase in the current density, peaking at the point just before the Φ begins to increase rapidly, which corresponds to the passivation of deep traps and the transition to a dopant-saturated regime, as discussed previously. The greatest increase in J_{SC} is seen with 0.2 wt. % Mo(tfd-$CO_2Me)_3$ in PTB7/$PC_{71}BM$, from 16.4 to 19.9 (20.3 max) mA/cm^2, a ~21% boost and the highest J_{SC} value reported for an OPV to date. The J_{SC} of the PCDTBT/$PC_{71}BM$ also increases, peaking with 0.1 wt. % Mo(tfd-$COCF_3)_3$ at 11.1 mA/cm^2 from 10.2 mA/cm^2. The dopant concentrations for which peak performance is observed are similar to those seen for F_4TCNQ,[21,22] and similarly the fill factor (and measured shunt resistance) decrease quickly at higher dopant concentrations. There also appears to be a slight decrease in open-circuit voltage as dopant content increases, around 20 to 30 mV. These decreases in *FF* and V_{OC} could be due to increased charge-carrier density, which can lead to increased recombination via electron-hole annihilation and exciton quenching.[45] It is clear that while a benefit to the J_{SC} and PCE was realized, as hole-trapping is reduced and the effective charge transport in the system is improved, it is balanced with other detrimental recombinative pathways that are aided by the increased carrier density. It is for this reason that the final increase in power-conversion efficiency is on the order of ~10% for either system. Another possibility is that the presence of the dopants has changed the thickness or refractive index of the film, which could serve to optimize the absorbance of the active layer, leading to the improvement in the J_{SC}. The thickness changes were determined to be minimal by profilometry, but refractive indices have not been determined.

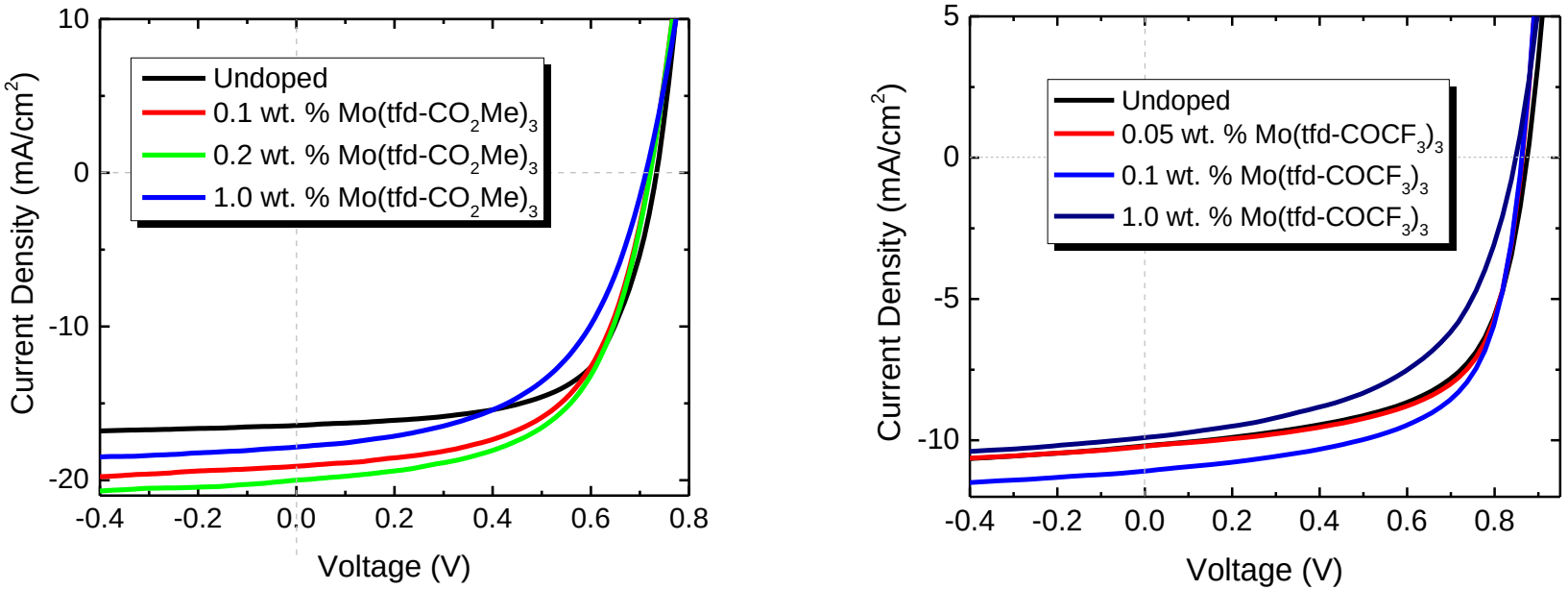

Figure 4.7. *J-V* curves of p-doped PTB7 (left) and PCDTBT (right) OPV cells with the acceptor $PC_{71}BM$ doped with $Mo(tfd\text{-}CO_2Me)_3$ and $Mo(tfd\text{-}COCF_3)_3$, respectively.

Table 4.1. OPV performance values of p-doped PTB7 (top) and PCDTBT (bottom) cells with the acceptor $PC_{71}BM$ doped with $Mo(tfd\text{-}CO_2Me)_3$ and $Mo(tfd\text{-}COCF_3)_3$, respectively. Averages are from over 25 cells.

Dopant Concentration	J_{SC} **(mA/cm^2)**	V_{OC} **(V)**	***FF* (%)**	**PCE (%)**
PTB7/$PC_{71}BM$ Doping with $Mo(tfd\text{-}CO_2Me)_3$				
Undoped	16.4 ± 0.1	0.73 ± 0.01	64 ± 1	7.7 ± 0.1
0.1 wt. %	18.8 ± 0.4	0.72 ± 0.01	59 ± 0	8.0 ± 0.1
0.2 wt. %	19.9 ± 0.4	0.72 ± 0.00	58 ± 1	8.4 ± 0.1
1.0 wt. %	18.0 ± 0.6	0.71 ± 0.01	53 ± 1	6.9 ± 0.2
PCDTBT/$PC_{71}BM$ Doping with $Mo(tfd\text{-}COCF_3)_3$				
Undoped	10.2 ± 0.2	0.88 ± 0.01	61 ± 1	5.5 ± 0.2
0.05 wt. %	10.2 ± 0.2	0.86 ± 0.00	64 ± 0	5.6 ± 0.1
0.1 wt. %	11.1 ± 0.3	0.86 ± 0.01	62 ± 1	6.0 ± 0.2
1.0 wt. %	9.9 ± 0.4	0.85 ± 0.01	55 ± 6	4.6 ± 0.7

The improvement in current density is supported by incident photon-to-electron conversion efficiency (IPCE) measurements. These curves feature a growth and subtle change in shape, specifically an increase in external quantum efficiency for lower energy photons and a red shift in the low-energy onset of ca. 40 meV for either system, observable in Figure 4.7. The integrated external quantum efficiencies are in agreement with the measured OPV short-circuit currents to 10% accuracy. This increased overall current generation is consistent with trap passivation and improved hole transport in the polymer phase, which can result in decreased bimolecular recombination; the red-shift can be an indication of improved exciton dissociation for lower energy excitons, as trap sites have been linked to geminate recombination.[46,47] In addition, Schwarz *et al.* have proposed dopant-assisted carrier photogeneration, where interactions of excitons and isolated neutral dopants can result in additional photocurrent, as an additional mechanism to explain the photocurrent increase.[48]

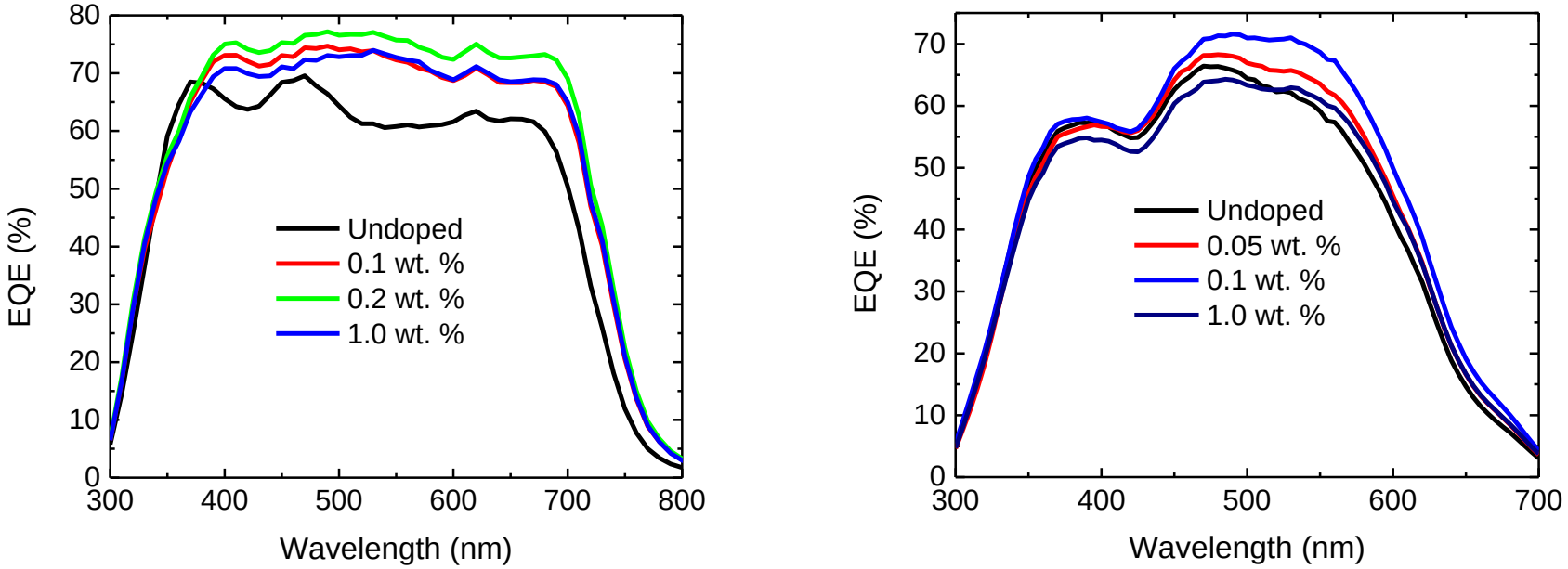

Figure 4.8. IPCE spectra of PTB7 (left) and PCDTBT (right) OPV cells with the acceptor $PC_{71}BM$, doped with varied concentrations of Mo(tfd-$CO_2Me)_3$ and Mo(tfd-$COCF_3)_3$ respectively.

Doping of PCDTBT was also attempted with the lower *EA* dopant Mo(tfd-$CO_2Me)_3$ in an attempt to selectively dope trap states without depleting the valence band. However, no improvement in performance is observed (see Figure 4.8); the electron affinity of the dopant is presumably not sufficiently high to passivate the trap states that reduce device performance. Consistent with the other material systems, *FF* and V_{OC} are reduced up to 1 wt. % dopant, and a slight red-shift is observed in the IPCE, but does not result in improved J_{SC}, which declined at 1 wt. % as well. It is possible that the dopant, while unable to fill necessary trap states to improve performance is still able to increase the carrier density, ultimately lowering performance at higher concentrations.

Coinciding with the decrease in the *FF*, the change of shape in the IPCE for the attempted devices can possibly be related to a slight change in thickness or refractive index of the active layer film, as these properties will have an effect on the optical interference and absorbance at various depths in the film. However, the difference in the behavior of the two dopants with PCDTBT indicates the likelihood of trap passivation as a possible contributor to the increase in photocurrent in addition to the optical effects.

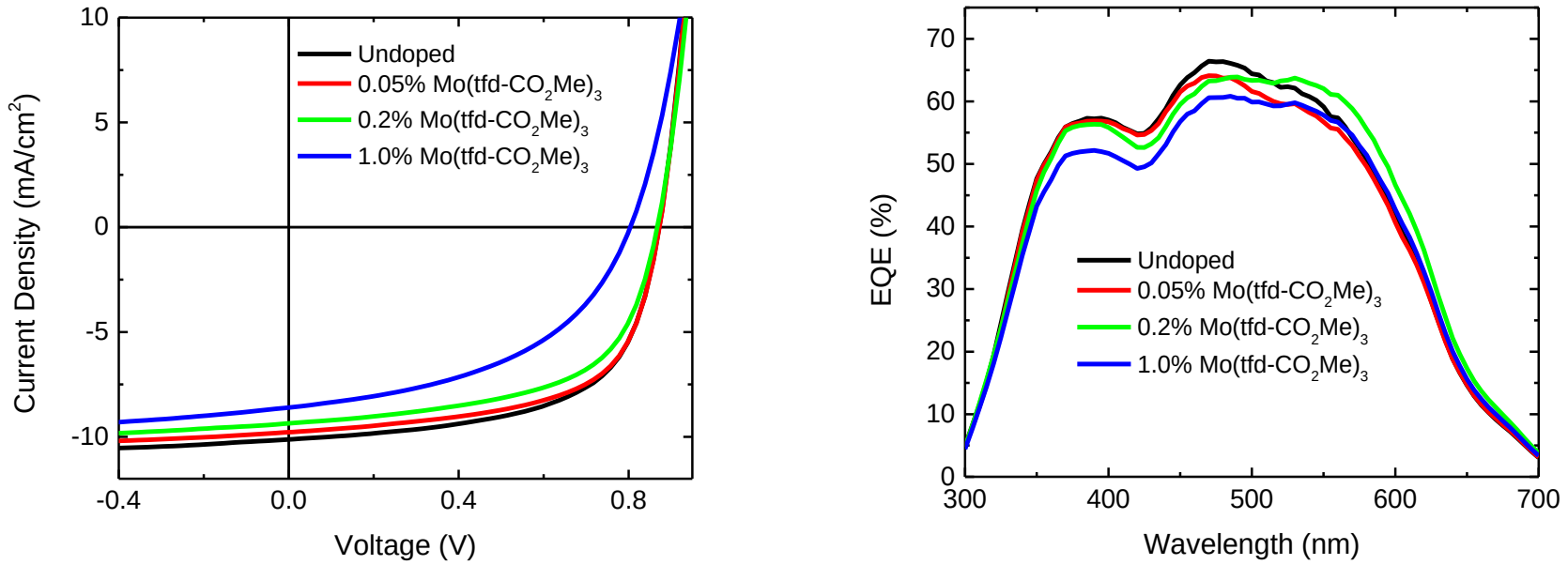

Figure 4.9. *J-V* curves (left) and IPCE (right) of PCDTBT:$PC_{71}BM$ OPV cells doped with various concentrations of Mo(tfd-$CO_2Me)_3$. No improvement in J_{SC} or PCE is observed.

4.2.4 Atomic Force Microscopy

An in-depth discussion of atomic force microscopy (AFM) relating to organic photovoltaic devices was given in Chapter 1. For the work in this chapter, AFM was conducted on a Bruker Dimension Icon in tapping mode, using Bruker RTESP-150 antimony-doped silicon tips, and analyzed with Gwyddion SPM analysis software. Doped solutions were pre-mixed by adding small volumes of 0.1 or 1 mg / mL Mo(tfd-$CO_2Me)_3$ or Mo(tfd-$COCF_3)_3$ solutions to 10 mg / mL PTB7 or PCDTBT chlorobenzene solutions and stirring for up to 1 h in inert atmosphere. Solutions were spun-cast at 1000 rpm for 60 s on UV-ozone cleaned ITO substrates to achieve films ca. 100 nm in thickness, after which samples were dried in vacuum (~10^{-6} Torr).

To explore the possibility of morphological changes upon dopant introduction, atomic force microscopy was performed on films of PTB7 and PCDTBT with concentrations of p-dopant relevant to the trends observed in the conductivity, UPS, and OPV results. The full series of height and phase images can be observed in Figures 4.9 and 4.10. Generally, no observations in the height or phase images would lead one to conclude that the presence of the dopant results in a substantial change in the surface morphology of the film, such as new features or changes in roughness. The root-mean-squared roughness (R_{RMS}) of the undoped films is 0.26 ± 0. 1 and 0.21 ± 0.01 nm for PTB7 and PCDTBT respectively, and deviates by less than 0.01 nm across any of the doped samples.

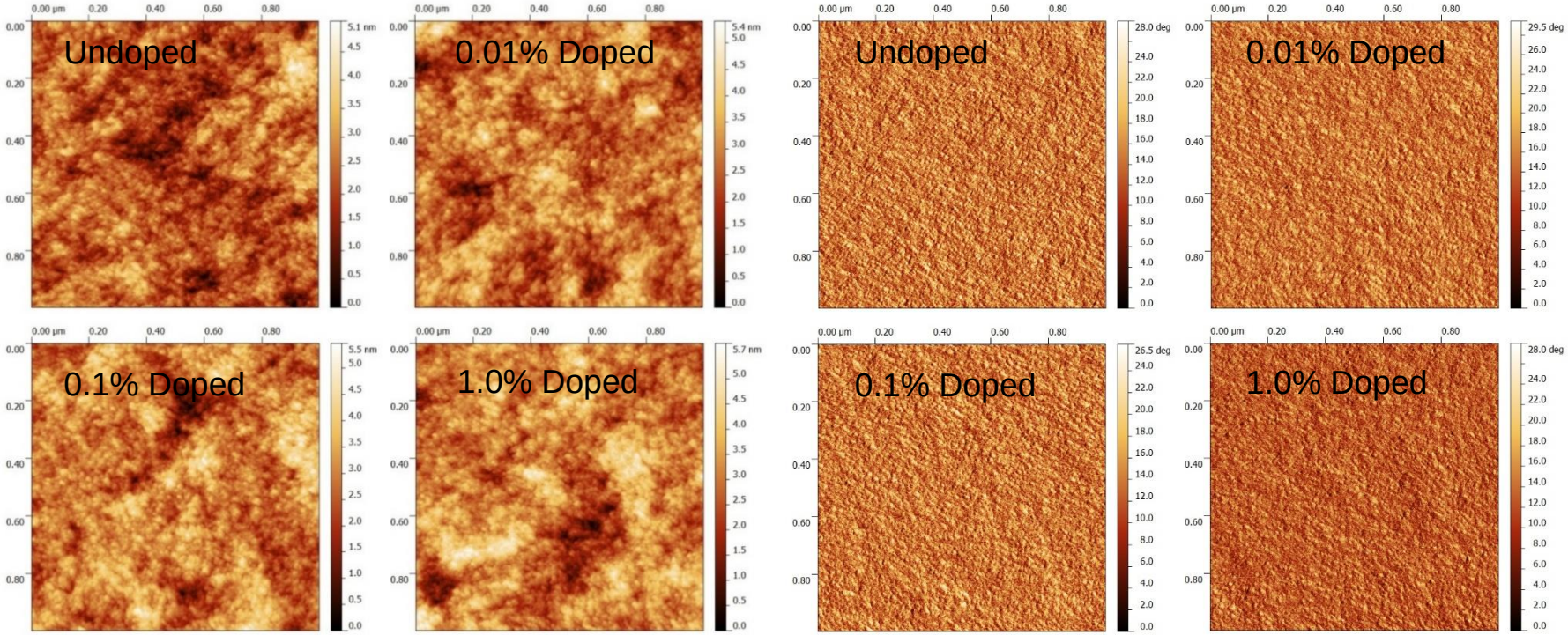

Figure 4.10. Atomic force microscopy topography (left) and phase (right) images of PTB7 films with 0, 0.01, 0.1, and 1 wt. % Mo(tfd-CO_2Me)$_3$.

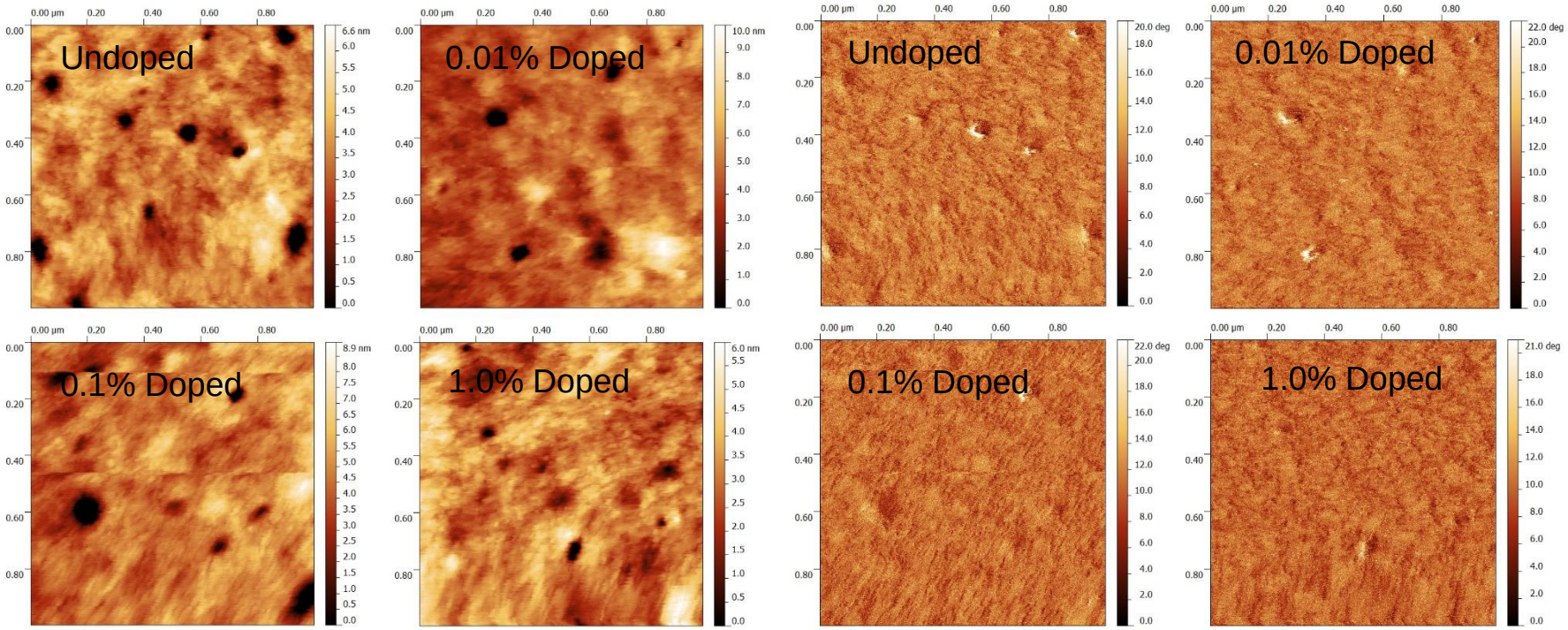

Figure 4.11. Atomic force microscopy topography (left) and phase (right) images of PCDTBT films with 0, 0.01, 0.1, and 1 wt. % $Mo(tfd\text{-}COCF_3)_3$.

4.2.5 Grazing-Incidence Wide Angle X-Ray Scattering

The effect of dopant introduction on the molecular ordering of the donor polymer phase was studied with grazing-incidence wide angle x-ray scattering (GIWAXS). A detailed discussion of GIWAXS in BHJ OPV active layers was given in Chapter 1. The experiment was conducted at the EAST – D1 beamline (http://www.chess.cornell.edu/chess/east/D1.htm) at the Cornell High Energy Synchrotron Source (CHESS) at Cornell University by Rahim Munir. The detector used was Pilatus 200K (combination of two 100K detectors). The blind spot of the detector appears in the result as a black horizontal line in the middle. The experimental parameters define the sample to detector distance as 100.25 mm, the X-ray wavelength as 1.155 Å, and the detector angle as 0.17°. Data were analyzed using Fit 2d. (http://www.esrf.eu/computing/scientific/FIT2D/) Samples were prepared in the following manner: Doped solutions were pre-mixed by adding small volumes of 0.1 or 1 mg / mL Mo(tfd-$CO_2Me)_3$ or Mo(tfd-$COCF_3)_3$ solutions to 10 mg / mL PTB7 or PCDTBT chlorobenzene solutions and stirring for up to 1 h in inert atmosphere. Solutions were spun-cast at 1000 rpm for 60 s on plasma-cleaned silicon substrates to achieve films ca. 100 nm in thickness, after which samples were dried in vacuum (~10^{-6} Torr).

As described in the previous paragraph, GIWAXS (spectra shown in Figure 4.11) was performed on polymer films deposited at similar conditions to those used in the OPVs. Weak (100) lamellar and (010) π-π stacking peaks are observed for both polymers, as has been observed in literature.[49–51] Exposure time for each shot was at 2 and 1.2 s for PTB7 and PCDTBT films respectively, and the incident angle was at 0.17° for maximum resulting intensity. There is no appearance of additional peaks or peak changes, in intensity or position, upon the introduction of the dopants up to 1 wt. %.

The lack in change of crystallographic properties upon doping supports the conclusions that the improvement in OPV performance with doping is not because of a change in morphology, but because of the reduction in trap states of the thin film.

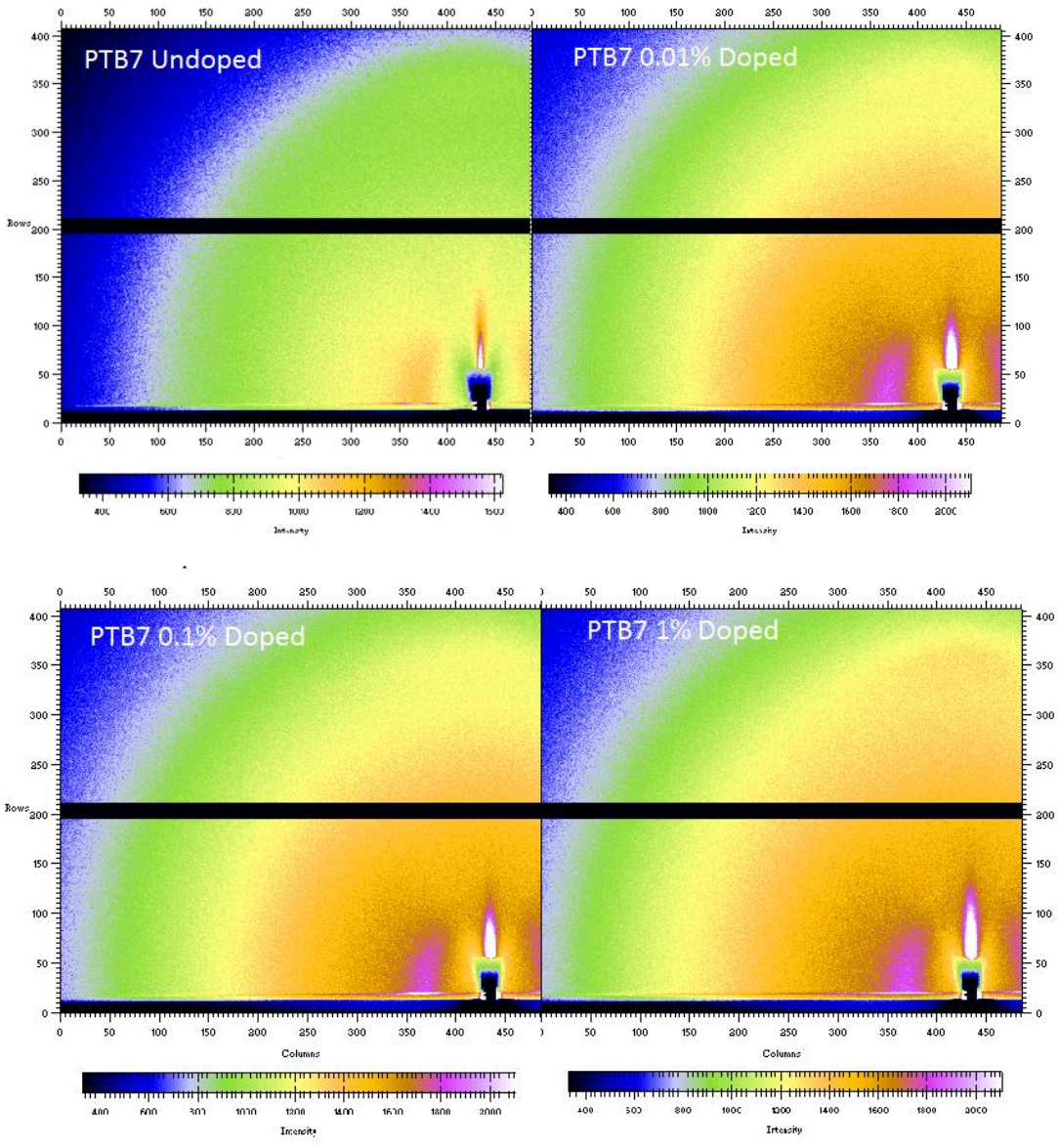

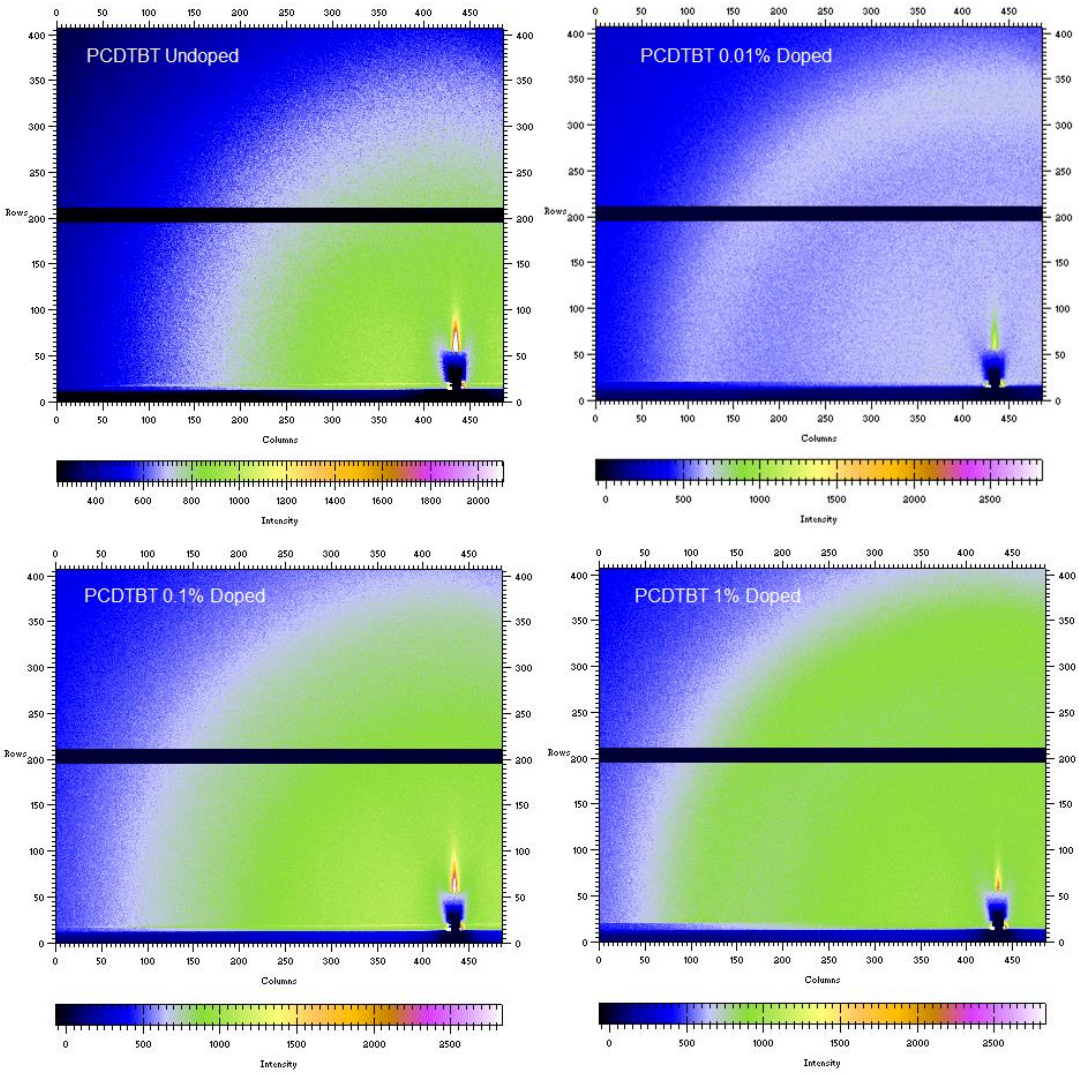

Figure 4.12. GIWAXS images of PTB7 (top) and PCDTBT (bottom) films on silicon wafers p-doped with relevant concentrations of Mo(tfd-$CO_2Me)_3$ and Mo(tfd-$COCF_3)_3$ respectively. GIWAXS was conducted at the Cornell High Energy Synchrotron Source (CHESS) at Cornell University by Rahim Munir.

4.3 Conclusion

Evidence of trap passivation in two different low-order copolymers, PTB7 and PCDTBT, upon the introduction of molecular dopants was established by conductivity and photoelectron spectroscopy. Doping of the polymers with the respective dopants in OPV active layers with $PC_{71}BM$ yielded an improvement in the J_{SC} for both material systems, with an increase of over 20% for PTB7/$PC_{71}BM$. The increase can be seen

clearly in the IPCE, the increasing values accompanied by a change in shape to favor high wavelength photons as well as a red-shifting of the low energy tail. However, increased carrier concentration also resulted in a penalty of degraded *FF* and V_{OC}, which led to significantly reduced performance at higher dopant concentrations, over ca. 1 wt. %. AFM and WAXS suggest that the dopants are well-dispersed in the film and do not appear to be interrupting or changing polymer morphology in any significant manner.

While the increase in OPV photocurrent was the expected result of trap passivation, the reduction in *FF* is inconsistent with increased charge transport on its own. It is possible that the introduction of the molecular dopants into the organic thin films has slightly changed its thickness or refractive index, which would also manifest in the observed evolution of the IPCE. An increase in thickness can also explain the lower fill factors. However, as the recorded PTB7:$PC_{71}BM$ J_{SC} is among the highest in literature, and the electron affinity of the dopant has a direct effect on the performance of doped PCDTBT:$PC_{71}BM$ devices, it is unlikely that the PCE improvements are unrelated to ultra-low doping. In this case, it is possible that the results are a product of trap passivation, refractive index and thickness changes, as well as new recombination pathways due to localized increased carrier densities, if dopants are not well dispersed on the nanoscale. The deconvolution of these effects is not straightforward for the imperfect systems being studied, and can be the focus of future work. Ultimately, relative to the previous chapter, these results can support the conclusion that ultra-low p-doping in OPVs can result in PCE and J_{SC} improvements when employed with materials that have low intricate short-range order, unlike homopolymer polythiophenes for example, and could be applicable to a number of other devices employing bulk heterojunction films with low-order organic materials.

4.4 Works Cited

[1] C. J. Brabec and J. R. Durrant, "Solution-Processed Organic Solar Cells," *MRS Bull.*, vol. 33, no. 07, pp. 670–675, Jan. 2011.

[2] S.-L. Lim, E.-C. Chen, C.-Y. Chen, K.-H. Ong, Z.-K. Chen, and H.-F. Meng, "High performance organic photovoltaic cells with blade-coated active layers," *Sol. Energy Mater. Sol. Cells*, vol. 107, pp. 292–297, Dec. 2012.

[3] R. Søndergaard, M. Hösel, D. Angmo, T. T. Larsen-Olsen, and F. C. Krebs, "Roll-to-roll fabrication of polymer solar cells," *Mater. Today*, vol. 15, no. 1–2, pp. 36–49, Jan. 2012.

[4] B. H. Wunsch, M. Rumi, N. R. Tummala, C. Risko, D.-Y. Kang, K. X. Steirer, J. Gantz, M. Said, N. R. Armstrong, J.-L. Brédas, D. Bucknall, and S. R. Marder, "Structure–processing–property correlations in solution-processed, small-molecule, organic solar cells," *J. Mater. Chem. C*, vol. 1, p. 5250, 2013.

[5] C. Girotto, B. P. Rand, J. Genoe, and P. Heremans, "Exploring spray coating as a deposition technique for the fabrication of solution-processed solar cells," *Sol. Energy Mater. Sol. Cells*, vol. 93, no. 4, pp. 454–458, Apr. 2009.

[6] T. K. An, I. Kang, H. Yun, H. Cha, J. Hwang, S. Park, J. Kim, Y. J. Kim, D. S. Chung, S.-K. Kwon, Y.-H. Kim, and C. E. Park, "Solvent additive to achieve highly ordered nanostructural semicrystalline DPP copolymers: toward a high charge carrier mobility.," *Adv. Mater.*, vol. 25, no. 48, pp. 7003–9, Dec. 2013.

[7] D. Khatiwada, S. Venkatesan, E. C. Ngo, and Q. Qiao, "Versatile Role of Solvent Additive for Tailoring Morphology in Polymer Solar Cells for Efficient Charge Transport.," *J. Nanosci. Nanotechnol.*, vol. 15, no. 9, pp. 7040–4, Sep. 2015.

[8] J. Y. Na, B. Kang, D. H. Sin, K. Cho, and Y. D. Park, "Understanding Solidification of Polythiophene Thin Films during Spin-Coating: Effects of Spin-Coating Time and Processing Additives.," *Sci. Rep.*, vol. 5, p. 13288, Jan. 2015.

[9] L. A. Perez, J. T. Rogers, M. A. Brady, Y. Sun, G. C. Welch, K. Schmidt, M. F. Toney, H. Jinnai, A. J. Heeger, M. L. Chabinyc, G. C. Bazan, and E. J. Kramer, "The Role of Solvent Additive Processing in High Performance Small Molecule Solar Cells," *Chem. Mater.*, vol. 26, no. 22, pp. 6531–6541, Nov. 2014.

[10] T. Salim, L. H. Wong, B. Bräuer, R. Kukreja, Y. L. Foo, Z. Bao, and Y. M. Lam,

"Solvent additives and their effects on blend morphologies of bulk heterojunctions," *J. Mater. Chem.*, vol. 21, no. 1, pp. 242–250, Dec. 2011.

[11] X. Zhu, F. Zhang, Q. An, H. Huang, Q. Sun, L. Li, F. Teng, and W. Tang, "Effect of solvent additive and ethanol treatment on the performance of PIDTDTQx:$PC_{71}BM$ polymer solar cells," *Sol. Energy Mater. Sol. Cells*, vol. 132, pp. 528–534, Jan. 2015.

[12] W. Kim, J. K. Kim, E. Kim, T. K. Ahn, D. H. Wang, and J. H. Park, "Conflicted Effects of a Solvent Additive on PTB7:PC 71 BM Bulk Heterojunction Solar Cells," *J. Phys. Chem. C*, vol. 119, no. 11, pp. 5954–5961, Mar. 2015.

[13] N. D. Treat, J. A. Nekuda Malik, O. Reid, L. Yu, C. G. Shuttle, G. Rumbles, C. J. Hawker, M. L. Chabinyc, P. Smith, and N. Stingelin, "Microstructure formation in molecular and polymer semiconductors assisted by nucleation agents.," *Nat. Mater.*, vol. 12, no. 7, pp. 628–33, Jul. 2013.

[14] K. R. Graham, J. Mei, R. Stalder, J. W. Shim, H. Cheun, F. Steffy, F. So, B. Kippelen, and J. R. Reynolds, "Polydimethylsiloxane as a macromolecular additive for enhanced performance of molecular bulk heterojunction organic solar cells.," *ACS Appl. Mater. Interfaces*, vol. 3, no. 4, pp. 1210–1215, Apr. 2011.

[15] G. J. Chae, S.-H. Jeong, J. H. Baek, B. Walker, C. K. Song, and J. H. Seo, "Improved performance in TIPS-pentacene field effect transistors using solvent additives," *J. Mater. Chem. C*, vol. 1, no. 27, pp. 4216–4221, Jun. 2013.

[16] J. Rivnay, R. Noriega, J. E. Northrup, R. J. Kline, M. F. Toney, and A. Salleo, "Structural origin of gap states in semicrystalline polymers and the implications for charge transport," *Phys. Rev. B - Condens. Matter Mater. Phys.*, vol. 83, no. 12, p. 121306, 2011.

[17] D. V. Lang, X. Chi, T. Siegrist, A. M. Sergent, and A. P. Ramirez, "Amorphouslike density of gap states in single-crystal pentacene," *Phys. Rev. Lett.*, vol. 93, no. 8, p. 086802, 2004.

[18] W. L. Kalb, K. Mattenberger, and B. Batlogg, "Oxygen-related traps in pentacene thin films: Energetic position and implications for transistor performance," *Phys. Rev. B - Condens. Matter Mater. Phys.*, vol. 78, p. 035334, 2008.

[19] C. Krellner, S. Haas, C. Goldmann, K. P. Pernstich, D. J. Gundlach, and B. Batlogg, "Density of bulk trap states in organic semiconductor crystals: Discrete

levels induced by oxygen in rubrene," *Phys. Rev. B - Condens. Matter Mater. Phys.*, vol. 75, no. 24, p. 245115, 2007.

[20] H. T. Nicolai, M. Kuik, G. A. H. Wetzelaer, B. de Boer, C. Campbell, C. Risko, J. L. Brédas, and P. W. M. Blom, "Unification of trap-limited electron transport in semiconducting polymers," *Nat. Mater.*, vol. 11, pp. 882–887, 2012.

[21] A. Veysel Tunc, A. De Sio, D. Riedel, F. Deschler, E. Da Como, J. Parisi, and E. von Hauff, "Molecular doping of low-bandgap-polymer:fullerene solar cells: Effects on transport and solar cells," *Org. Electron.*, vol. 13, no. 2, pp. 290–296, Feb. 2012.

[22] Y. Zhang, H. Zhou, J. Seifter, L. Ying, A. Mikhailovsky, A. J. Heeger, G. C. Bazan, and T. Q. Nguyen, "Molecular doping enhances photoconductivity in polymer bulk heterojunction solar cells," *Adv. Mater.*, vol. 25, pp. 7038–7044, 2013.

[23] H. Méndez, G. Heimel, S. Winkler, J. Frisch, A. Opitz, K. Sauer, B. Wegner, M. Oehzelt, C. Röthel, S. Duhm, D. Többens, N. Koch, and I. Salzmann, "Charge-transfer crystallites as molecular electrical dopants," *Nat. Commun.*, vol. 6, p. 8560, Oct. 2015.

[24] P. Pingel and D. Neher, "Comprehensive picture of p -type doping of P3HT with the molecular acceptor F 4 TCNQ," *Phys. Rev. B*, vol. 87, no. 11, p. 115209, Mar. 2013.

[25] C. Wang, D. T. Duong, K. Vandewal, J. Rivnay, and A. Salleo, "Optical measurement of doping efficiency in poly(3-hexylthiophene) solutions and thin films," *Phys. Rev. B*, vol. 91, no. 8, p. 085205, Feb. 2015.

[26] F. Deschler, E. Da Como, T. Limmer, R. Tautz, T. Godde, M. Bayer, E. von Hauff, S. Yilmaz, S. Allard, U. Scherf, and J. Feldmann, "Reduced Charge Transfer Exciton Recombination in Organic Semiconductor Heterojunctions by Molecular Doping," *Phys. Rev. Lett.*, vol. 107, no. 12, p. 127402, Sep. 2011.

[27] M. M. Said, Y. Zhang, R. R. Dasari, D. H. Anjum, R. Munir, H. Hu, A. Amassian, S. Barlow, and S. R. Marder, "Ultra-low p-doping of poly(3-hexylthiophene) and its impact on polymer aggregation and photovoltaic performance," *Org. Photonics Photovoltaics*, vol. 4, no. 1, pp. 1–16, Jan. 2016.

[28] A. Dai, Y. Zhou, A. L. Shu, S. K. Mohapatra, H. Wang, C. Fuentes-Hernandez, Y. Zhang, S. Barlow, Y. L. Loo, S. R. Marder, B. Kippelen, and A. Kahn, "Enhanced charge-carrier injection and collection via lamination of doped

polymer layers p-doped with a solution-processible molybdenum complex," *Adv. Funct. Mater.*, vol. 24, pp. 2197–2204, 2014.

[29] S. A. Paniagua, J. Baltazar, H. Sojoudi, S. K. Mohapatra, S. Zhang, C. L. Henderson, S. Graham, S. Barlow, and S. R. Marder, "Production of heavily n- and p-doped CVD graphene with solution-processed redox-active metal–organic species," *Mater. Horiz.*, vol. 1, no. 1, pp. 111–115, Nov. 2014.

[30] J. Belasco, S. K. Mohapatra, Y. Zhang, S. Barlow, S. R. Marder, and A. Kahn, "Molecular doping and tuning threshold voltage in 6,13-bis(triisopropylsilylethynyl)pentacene/polymer blend transistors," *Appl. Phys. Lett.*, vol. 105, no. 6, p. 063301, Aug. 2014.

[31] A. F. Stassen, R. W. I. de Boer, N. N. Iosad, and A. F. Morpurgo, "Influence of the gate dielectric on the mobility of rubrene single-crystal field-effect transistors," *Appl. Phys. Lett.*, vol. 85, no. 17, p. 3899, Oct. 2004.

[32] S.-J. Park, K.-Y. Lee, D.-H. Kim, M.-H. Shin, and Y.-J. Kim, "Improvement of electrical conductivity for high-performance organic solar cells by multi-temperature solvent annealing," *Jpn. J. Appl. Phys.*, vol. 54, no. 4S, p. 04DK07, Apr. 2015.

[33] J. Maiz, M. Muñoz Rojo, B. Abad, A. A. Wilson, A. Nogales, D.-A. Borca-Tasciuc, T. Borca-Tasciuc, and M. Martín-González, "Enhancement of thermoelectric efficiency of doped PCDTBT polymer films," *RSC Adv.*, vol. 5, no. 82, pp. 66687–66694, Aug. 2015.

[34] D. Cahen and A. Kahn, "Electron Energetics at Surfaces and Interfaces: Concepts and Experiments," *Adv. Mater.*, vol. 15, no. 4, pp. 271–277, Feb. 2003.

[35] N. Koch, "Organic electronic devices and their functional interfaces.," *Chemphyschem*, vol. 8, no. 10, pp. 1438–55, Jul. 2007.

[36] I. N. Hulea, H. B. Brom, A. J. Houtepen, D. Vanmaekelbergh, J. J. Kelly, and E. A. Meulenkamp, "Wide Energy-WindowView on the Density of States\rand Hole Mobility in Poly(p-Phenylene Vinylene)," *Phys. Rev. Lett.*, vol. 93, p. 166601, 2004.

[37] J. Hwang, E. G. Kim, J. Liu, J. L. Bredas, A. Duggal, and A. Kahn, "Photoelectron spectroscopic study of the electronic band structure of polyfluorene and fluorene-arylamine copolymers at interfaces," *J. Phys. Chem. C*, vol. 111, pp. 1378–1384, 2007.

[38] S. V Novikov, D. H. Dunlap, V. M. Kenkre, P. E. Parris, and A. V Vannikov, “Essential role of correlations in governing charge transport in disordered organic materials,” *Phys. Rev. Lett.*, vol. 81, pp. 4472–4475, 1998.

[39] O. Tal, Y. Rosenwaks, Y. Preezant, N. Tessler, C. K. Chan, and A. Kahn, “Direct determination of the hole density of states in undoped and doped amorphous organic films with high lateral resolution,” *Phys. Rev. Lett.*, vol. 95, no. 25, p. 256405, 2005.

[40] Y. Qi, S. K. Mohapatra, S. Bok Kim, S. Barlow, S. R. Marder, and A. Kahn, “Solution doping of organic semiconductors using air-stable n-dopants,” *Appl. Phys. Lett.*, vol. 100, p. 083305, 2012.

[41] Y. Zhang, B. de Boer, and P. W. M. Blom, “Trap-free electron transport in poly(p -phenylene vinylene) by deactivation of traps with n -type doping,” *Phys. Rev. B*, vol. 81, no. 8, p. 085201, Feb. 2010.

[42] M. L. Tietze, P. Pahner, K. Schmidt, K. Leo, and B. Lüssem, “Doped Organic Semiconductors: Trap-Filling, Impurity Saturation, and Reserve Regimes,” *Adv. Funct. Mater.*, vol. 25, no. 18, pp. 2701–2707, May 2015.

[43] Z. Li, K. Ho Chiu, R. Shahid Ashraf, S. Fearn, R. Dattani, H. Cheng Wong, C.-H. Tan, J. Wu, J. T. Cabral, and J. R. Durrant, “Toward Improved Lifetimes of Organic Solar Cells under Thermal Stress: Substrate-Dependent Morphological Stability of PCDTBT:PCBM Films and Devices.,” *Sci. Rep.*, vol. 5, p. 15149, Jan. 2015.

[44] L. K. Jagadamma, M. Abdelsamie, A. El Labban, E. Aresu, G. O. Ngongang Ndjawa, D. H. Anjum, D. Cha, P. M. Beaujuge, and A. Amassian, “Efficient inverted bulk-heterojunction solar cells from low-temperature processing of amorphous ZnO buffer layers,” *J. Mater. Chem. A*, vol. 2, no. 33, p. 13321, Jun. 2014.

[45] K. Vandewal, K. Tvingstedt, A. Gadisa, O. Inganäs, and J. V Manca, “On the origin of the open-circuit voltage of polymer-fullerene solar cells.,” *Nat. Mater.*, vol. 8, no. 11, pp. 904–9, Nov. 2009.

[46] S. R. Cowan, A. Roy, and A. J. Heeger, “Recombination in polymer-fullerene bulk heterojunction solar cells,” *Phys. Rev. B*, vol. 82, no. 24, p. 245207, Dec. 2010.

[47] C. Groves, J. C. Blakesley, and N. C. Greenham, “Effect of charge trapping on geminate recombination and polymer solar cell performance.,” *Nano Lett.*, vol.

10, no. 3, pp. 1063–9, Mar. 2010.

[48] C. Schwarz, S. Tscheuschner, J. Frisch, S. Winkler, N. Koch, H. Bässler, and A. Köhler, “Role of the effective mass and interfacial dipoles on exciton dissociation in organic donor-acceptor solar cells,” *Phys. Rev. B*, vol. 87, no. 15, p. 155205, Apr. 2013.

[49] W. Chen, T. Xu, F. He, W. Wang, C. Wang, J. Strzalka, Y. Liu, J. Wen, D. J. Miller, J. Chen, K. Hong, L. Yu, and S. B. Darling, “Hierarchical nanomorphologies promote exciton dissociation in polymer/fullerene bulk heterojunction solar cells.,” *Nano Lett.*, vol. 11, no. 9, pp. 3707–13, Sep. 2011.

[50] X. Lu, H. Hlaing, D. S. Germack, J. Peet, W. H. Jo, D. Andrienko, K. Kremer, and B. M. Ocko, “Bilayer order in a polycarbazole-conjugated polymer.,” *Nat. Commun.*, vol. 3, p. 795, Jan. 2012.

[51] Y. (Michael) Yang, W. Chen, L. Dou, W.-H. Chang, H.-S. Duan, B. Bob, G. Li, and Y. Yang, “High-performance multiple-donor bulk heterojunction solar cells,” *Nat. Photonics*, vol. 9, no. 3, pp. 190–198, Feb. 2015.

[52] Y. Qi, T. Sajoto, M. Kröger, A. M. Kandabarow, W. Park, S. Barlow, E.-G. Kim, L. Wielunski, L. C. Feldman, R. A. Bartynski, J.-L. Brédas, S. R. Marder, and A. Kahn, “A Molybdenum Dithiolene Complex as p -Dopant for Hole-Transport Materials: A Multitechnique Experimental and Theoretical Investigation,” *Chem. Mater.*, vol. 22, no. 2, pp. 524–531, Jan. 2010.

CHAPTER 5 ZINC OXIDE INCORPORATING PENTAMETHYL-RHODOCENE DERIVATIVES AS ELECTRON-TRANSPORT LAYERS FOR HIGHLY EFFICIENT ORGANIC SOLAR CELLS

5.1 Introduction

5.1.1 Semiconducting Oxide Interlayers in Organic Electronics

The favored transparent conducting oxide (TCO) in organic photovoltaics (OPVs), and a number of other electronic devices, has historically been indium tin oxide (ITO), owing to its high electrical conductivity and transparency in the visible region.[1,2] However, its work function (Φ) is largely dependent on surface cleaning methodology,[3] and is not always appropriately situated for electron or hole transfer to/from the valence and conduction bands of many materials that are employed in organic semiconductor devices without losses in energy. This is manifested in decreased open-circuit voltages in OPVs and higher required injection voltages in OLEDS for example.[4–7] To account for this problem, a number of interlayer materials, often semiconducting oxides with large bandgaps, have been employed to manipulate better contacts with organic materials.[8–11]

Oxides that have commonly been used for hole injection/extraction in organic electronics are molybdenum oxide (MoO_3), vanadium oxide (V_2O_5), and tungsten oxide (WO_3).[10,12–14] These layers are usually thermally evaporated to attain the most pristine layers, achieving metallic conductivities and work functions up to or above 6.0 eV. However, to realize compatibility with anticipated high-throughput roll-to-roll

manufacturing, low-temperature solution-processed MoO_X with a Φ of 5.0 eV (and up to 6.1 eV after O_2-plasma and vacuum annealing) has been reported and implemented in OPVs, the thickness minimized to offset the higher resistivity.[15]

The most common low Fermi level energy oxides are zinc oxide (ZnO) and titanium oxide (TiO_2), thin films of which, those with Φs ca. 3.5 – 4.0 eV, have found use in a number of electronic applications, including organic and inorganic photovoltaics, thin-film transistors, and liquid-crystal displays.[16–22] Using diverse film-processing methods, low-cost and facile procedures have been developed to produce amorphous to low-crystallinity ZnO layers with thicknesses of tens of nanometers and with opto-electronic properties competitive with those of their more highly-ordered relatives when employed in certain applications, such as charge-transport layers in organic photovoltaics (OPVs).[17,23,24] However, these films can still suffer from increased defect populations related to vacancies and interstitial sites relative to their more crystalline counterparts. The presence of these defects can limit charge transport and the reproducibility of device performance.[25–28]

5.1.2 Additives in Low-Temperature Solution-Processed Oxides

A method that has classically been used to augment oxide properties is the introduction of metal atoms, which can often occupy interstitial sites and/or lead to enrichment or deficiencies in charge carriers, depending on valence saturation. In zinc oxide materials processed at low temperatures the use of sodium, aluminum, and lithium have been demonstrated to improve electron mobilities, conductivities, and, ultimately, the performance of organic photovoltaic devices employing such layers.[17,24,29] However, these films require the additional step of particle formation in solution, which contributes to processing time and cost. To the best of the author's

knowledge, there has been no application of atomic doping to low-temperature zinc oxide films derived from sol-gels to date.

Robust small molecules, such as fullerene derivatives, have been co-dissolved into ZnO sol-gels, where they were incorporated into the bulk of the film and can have an influence on the oxide properties, such as carrier band energies and charge transport.[30,31] Incorporation of these organic materials into the oxide has resulted in improved OPV performance, up to 8.2 % in inverted cells with PTB7:$PC_{71}BM$, largely through increases in the *FF* and J_{SC}. The reports suggest that these improvements originate from fullerene assistance in electron extraction and transport, rather than interactions with defects.

5.1.3 Molecular Dopant Incorporation into Amorphous Zinc Oxide

Redox-active molecules, also known as molecular dopants, have already been used to modify the surface properties of metals[32,33] and oxides.[34–37] Schlesinger *et al.* used an evaporated dimeric sandwich n-dopant to reduce the work function of crystalline ZnO by up to 1.5 eV to a minimum of 2.2 eV due to electron transfer to ("surface doping" of) the oxide, allowing for more efficient energy transfer with the organic dye L4P-sp3.[37] Work-function reduction has also been demonstrated by Giordano *et al.* through solution processing of similar complexes onto metal and oxide thin films, including ZnO ($\Delta\Phi$ = –0.5 eV) formed by atomic layer deposition.[36] The use of molecular dopants has not, however, been demonstrated within the bulk of sol-gel based ZnO films, although the addition of fullerene derivatives has been shown to reduce the optical gap.[38] In addition to potentially affording a homogeneous distribution of the dopant in the oxide, such a method might also lead to greater compatibility with solution-processing of organic overlayers over surface doping approaches, in which changes in surface hydrophobicity/philicity and/or dopant transfer or passivation may

occur. Moreover, bulk doping can potentially have a more significant effect on the bulk conductivity of the oxide.

In this study, the incorporation of the molecular n-dopant 1,2,3,4,5-pentamethylrhodocene dimer ($[RhCp^*Cp]_2$)[39,40] into solution-processed ZnO thin films is demonstrated, as well as the characterization of the material properties that lead to an improvement in OPV performance. This dopant has been shown to be a reasonably air-stable, yet powerful, reductant due to the doping mechanism, which involves both cleavage of the dimer and electron transfer, resulting in the formation of two monomeric $[RhCp^*Cp]^+$ cations per dopant;[39,41–43] the effective redox potential is estimated to be ca. –2.0 V vs. ferrocene.[41] The reductant strength of the dimer and robustness of the resulting $[RhCp^*Cp]^+$ cation makes it a promising candidate for low-temperature sol-gel oxide processing.

5.2 Methods & Results

5.2.1 ZnO Preparation

The preparation method for the electron-transporting layer of amorphous ZnO (a-ZnO) was adapted from those detailed in recent publications.[17,23] For sol-gel a-ZnO, zinc acetate dihydrate (Sigma-Aldrich 379786) and ethanolamine (Sigma-Aldrich 411000) were dissolved in 2-methoxyethanol (Sigma-Aldrich 284467) to a concentration of 0.11 M. After hydrolysis in air for ca. 24 h, the sol-gel was bubbled with argon for 2 h before being transferred, in a vial with argon atmosphere, to the glove-box. 1,2,3,4,5-Pentamethylrhodocene dimer (prepared by Dr. Karttikay Moudgil as described in the literature[39,40]) was dissolved in the sol-gel solution and allowed to

stir at 60 °C for 1 h. The solutions were spin-cast onto solvent and UV-Ozone-cleaned ITO substrates in inert atmosphere, at 4000 rpm for 30 s, yielding compact ZnO films. To achieve thicker, rippled a-ZnO, the sol-gel was prepared with a zinc acetate dihydrate / ethanolamine concentration of 0.75 M and spin-cast at 3000 rpm for 30 s. In both cases, the doped films were annealed on a hotplate (PRAZITHERM PZ 28-3TD) at 100 °C for 10 min in the glovebox, then annealed in air at 150 °C for another 10 min before being allowed to cool down at room temperature.

The benefit of the low-temperature solution-processing of sol-gel ZnO is that it allows for the use of molecular dopants in ways not previously exploited, as the soluble dopants can be dissolved directly into the 2-methoxyethanol-based solution and deposited simultaneously with the sol-gel. Thermogravimetric analysis (TGA) of the $[RhCp^*Cp]_2$ powder, performed by Dr. Karttikay Moudgil, shows that the decomposition point (5% mass loss) of the dopant dimer is ca. 185 °C, seen in Figure 5.1. The thermal conversion of the sol-gel to the oxide was conducted below this decomposition point, at 150 °C for 10 min, and so has the potential to trap the dopants within the forming film, although the dimer may decompose via chemical reactions with either solvent or species created during the sol-gel deposition. It should also be noted that the doping product, the $RhCpCp^+$ cation, is among the most stable organometallic species and is expected to be stable, both thermally and in the sol-gel conditions (as has been observed via absorbance).

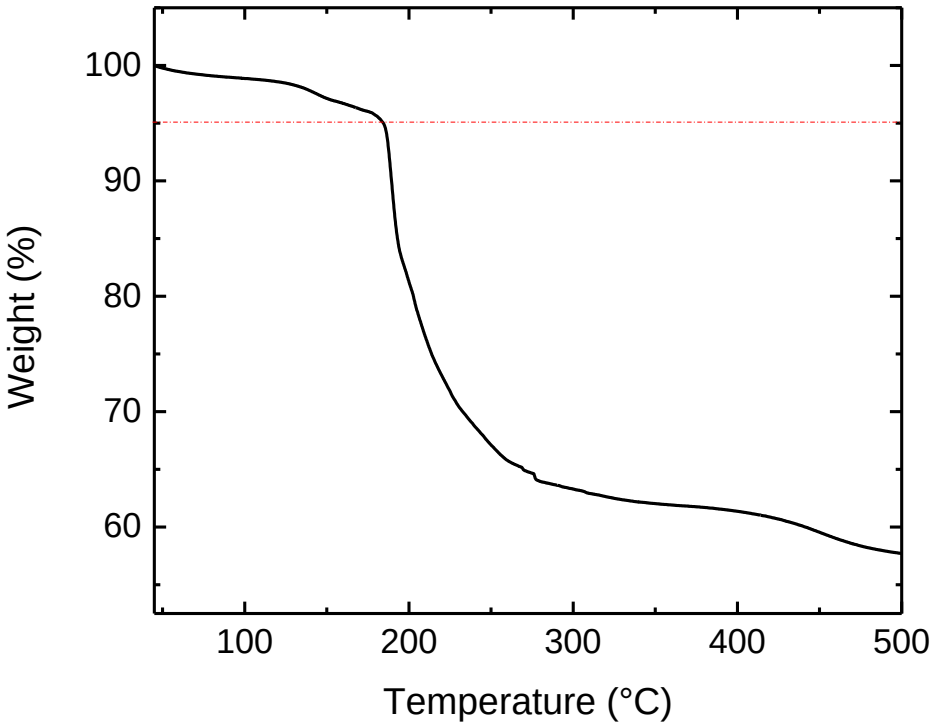

Figure 5.1. Thermogravimetric analysis of $[RhCp^*Cp]_2$ at 10 °C min^{-1}. Thermogravimetric analysis (TGA) of the $[RhCp^*Cp]_2$ powder was performed by Dr. Karttikay Moudgil.

5.2.2 Secondary Ion Mass Spectrometry

Secondary ion mass spectrometry (SIMS) is a technique that allows for surface composition analysis of solids by bombarding exposed materials with a focused beam of primary ions. Ejected secondary ions are analyzed by their mass/charge ratio in order to determine elemental or molecular composition as a function of depth. Though the first SIMS experiments were not conducted until the 1940s-1950s by Herzog, Viehböck, and Honig,[44,45] enabled by improved vacuum pump technology, the phenomenon of secondary ion ejections following primary ion collisions was first observed by J. J. Thomson in 1910.[46] Due to its ability to deliver nanometer depth resolution and elemental sensitivity down to parts per billion, SIMS has found extensive

use in the compositional characterization of electronic devices and materials that compose them, such as ZnO.[47–51]

In order to determine how well the dopant molecules are dispersed in the amorphous ZnO, thin films were studied by SIMS. Several solutions were prepared by mixing zinc oxide sol-gel solution (detailed in Section 5.2.1) with dopant molecules at concentrations ranging from 10^{-1} down to 10^{-4} mg/mL. These thin ZnO films were produced by spin coating the sol-gel solutions on top of a solvent and UV-Ozone-cleaned silicon substrate. In order to obtain a stable and reliable profile signal in this experiment, 5 layers of thin a-ZnO (from 0.11 M sol-gel solution) were deposited sequentially to a total thickness of ca. 50 nm. This film preparation was completed by Hanlin Hu at the King Abdullah University of Science and Technology.

SIMS experiments were carried out by using a Dynamic SIMS instrument from Hiden analytical company (Warrington-UK) operated under ultra-high vacuum conditions (10^{-9} Torr). Depth-profiling experiments were conducted using oxygen at energy of 4 keV for maximizing the detected rhodium signal in particular. The conversion of the sputtering time to sputtering depth scale was achieved by measuring the depth of the crater generated at the end of the depth profiling experiment. The raster of the sputtered area was estimated to be 1000 × 1000 μm^2. In order to avoid contributions from surface materials near the edge of the crater, an acquisition area of 150 × 150 μm^2 was centered in the middle of the eroded region. Throughout the sputtering process, the selected ions ascribed to rhodium and zinc were sequentially collected using a MAXIM spectrometer equipped with a quadrupole analyzer. Ions were collected from the sample by a shaped extraction field and energy filtered using a parallel plate system, with the energy resolution matched to that of the quadrupole analyzer. After passing through a triple filter system, detected ions were measured using

a pulse counting detector having a 4 keV post acceleration potential to increase the detection efficiency at high masses. SIMS experiments were conducted at the King Abdullah University of Science and Technology by Dr. Nimer Wehbe.

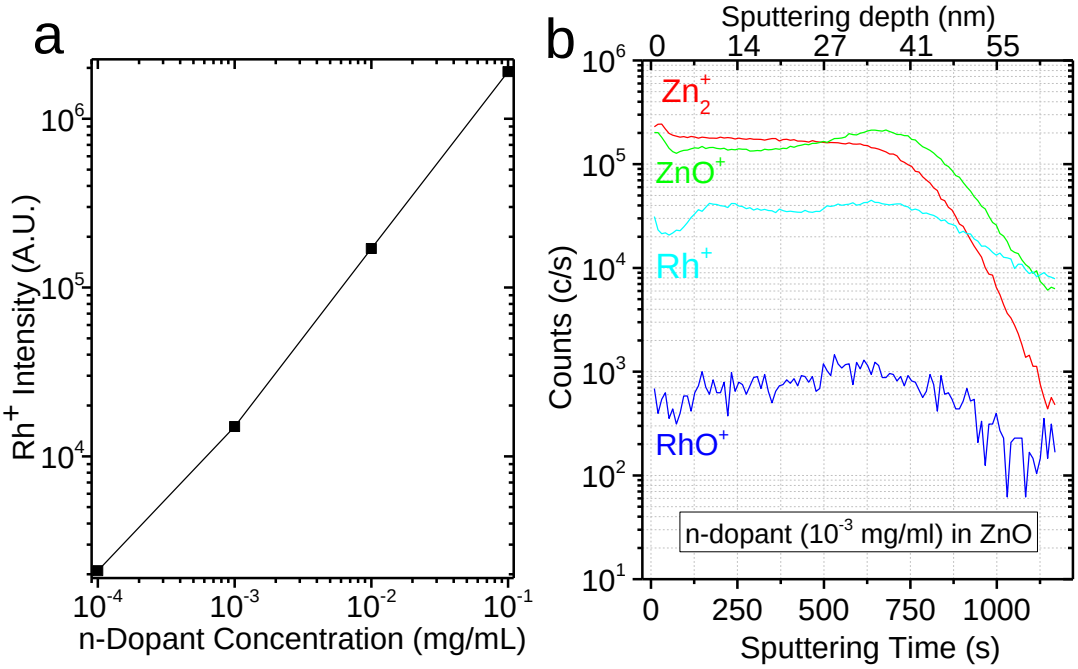

Figure 5.2. SIMS data showing (a) the Rh^+ signal intensity measured for ZnO films as a function of the rhodium concentration in the (zinc oxide precursor + dopant) solution and (b) depth profiling of a thin ZnO layer deposited from the solution containing 10^{-3} mg/mL of dopant. SIMS experiments were conducted at the King Abdullah University of Science and Technology by Dr. Nimer Wehbe.

Figure 5.2a demonstrates clearly the rhodium signals, denoted by rhodium (Rh^+) and rhodium oxide (RhO^+) ions, exhibit an approximate linear proportionality to the allotted concentration in the solution. The maximum Rh^+ intensity of 2×10^6 c/s measured from the film corresponding to the 10^{-1} mg/mL solution is decreased by almost two orders of magnitude and reaches 1.6×10^4 c/s when the dopant concentration in the solution was reduced by the same proportion. (Figure 5.3). This experimental series shows that SIMS is capable of detecting rhodium with high sensitivity in films fabricated from solutions with concentrations as low as 10^{-4} mg/mL.

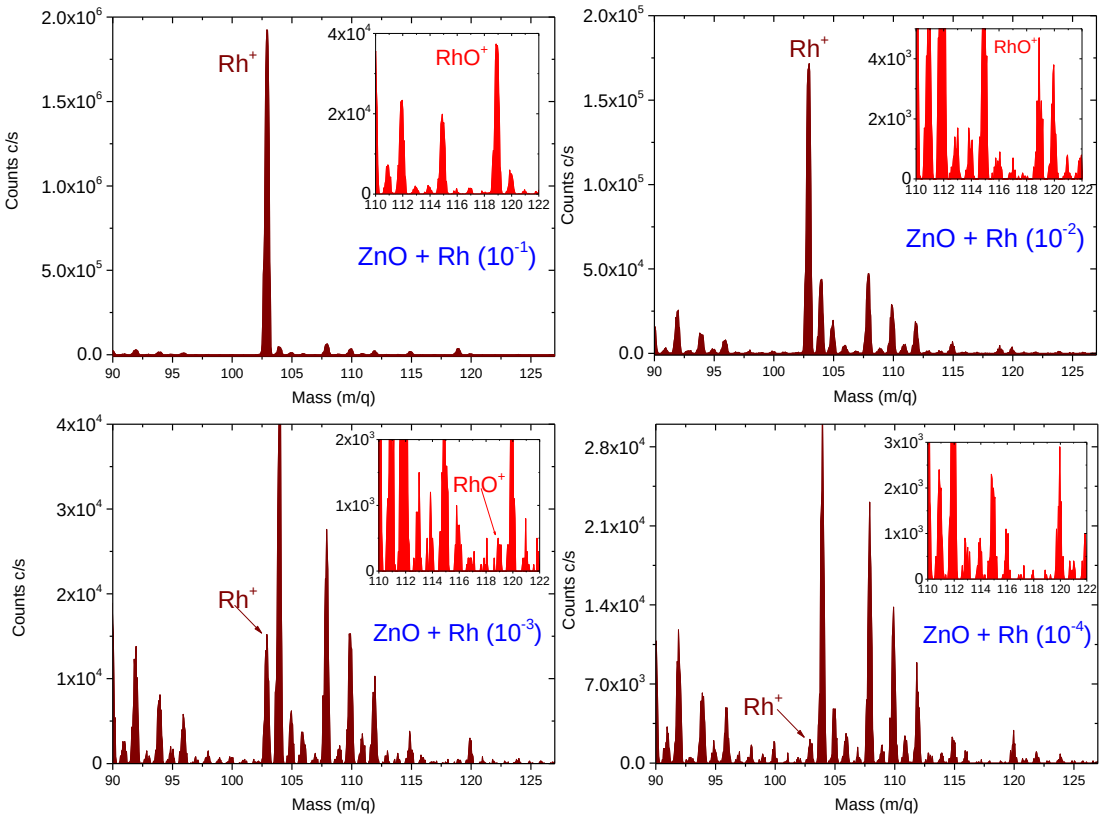

Figure 5.3. Mass spectra recorded for four thin layers produced using solutions of zinc oxide mixed with rhodium at concentration ranging from 10^{-1} down to 10^{-4} M. SIMS experiments were conducted at the King Abdullah University of Science and Technology by Dr. Nimer Wehbe.

The variation of the rhodium signal as a function of depth was investigated in order to assess the homogeneity of the rhodium distribution through the film thickness (Figure 5.2b). Following an initial drop at the beginning of the sputtering process, SIMS signals ascribed to zinc and rhodium exhibit stable intensities until the exposure of the buried silicon substrate, after which they steeply decrease. This opening surface drop is often observed in depth profiling experiments and is attributed to the presence of a contamination layer, which includes a higher oxygen content, leading to signal augmentation at the surface edge (called a matrix effect). Except for the Zn^{2+} ion, a similar enhancement effect occurs at the silicon interface and is due again to the presence of a native silicon oxide layer formed on the silicon substrate. The depth

profiling data suggests that the rhodium is homogeneously distributed throughout the deposited layer.

5.2.3 X-ray Photoelectron Spectroscopy

A detailed discussion of photoelectron spectroscopy was given in Chapter 1. For this chapter, X-ray photoelectron spectroscopy (XPS) was performed in the ultra-high vacuum environment of a Kratos Axis Ultra^{DLD} XPS/UPS system at the Georgia Institute of Technology. All samples were in contact with the detector by a metallic clip and characterizations were performed at a take-off angle normal to the film. XPS using monochromatic Al Kα line was conducted at a base pressure of 10^{-9} Torr, the Fermi level calibrated using atomically clean silver. The spot size was ca. 700 μm. Survey XPS scans were run at 160 eV pass energy and high resolution scans typically at 20 eV pass energy and 0.1 eV steps. Several solutions were prepared by mixing zinc oxide sol-gel solution (detailed in Section 5.2.1) with dopant molecules at concentrations ranging from 1 down to 10^{-4} mg/mL. These thin ZnO films were produced by spin coating the sol-gel solutions on top of solvent and UV-Ozone-cleaned ITO/glass substrate.

Atomic ratios of relevant elements in the films with differing concentrations of n-dopant are given in Table 5.1, determined by O 1s, Zn 2p, In 3d and Rh 3d peak areas. The area ratios were converted into atomic ratios after correcting for instrumental and sensitivity factors. Assuming a constant thickness, which is supported by AFM (Section 5.2.8), the effective thickness (x) of the ZnO layer was determined by integrating the expected signal decay functions[52] based on the inelastic mean free path (λ)[53] of the scattered photoelectrons relevant to the given core level orbitals, and equating to the observed In 3d and Zn 2p intensities:

$$\frac{I_{OBS}^{In\ 3d}}{I_{OBS}^{Zn\ 2p}} = \frac{\rho_{In} \int_{x}^{\infty} e^{-t/\lambda_{In\ 3d}} dt}{\rho_{Zn} \int_{0}^{x} e^{-t/\lambda_{Zn\ 2p}} dt}$$

Equation 5.1

The depth inside the sample in nm is given by t and ρ is the estimated density of an element in the given oxide. Using x which, as expected, was ca. 10 nm for each sample, oxygen contribution of the ITO substrate to the O 1s intensity was further calculated using the same integration formula and subtracted from the total signal intensity. From here, the O/Zn atomic ratio was calculated based on the remaining O 1s and Zn 2p intensities, adjusted for atomic density and signal decay to a depth of x.

Table 5.1. Atomic ratios of relevant elements in the films with differing concentrations of n-dopant, determined by O 1s, Zn 2p, and Rh 3d XPS peaks. O/Zn atomic ratio was adjusted by signal decay through the material and corrected for oxygen contribution from the ITO substrate, uncorrected values given in parenthesis.

n-Dopant Concentration	**Rh/Zn Atomic Ratio**	**O/Zn Atomic Ratio**
Undoped	-	1.08 (1.20)
10^{-3} mg/mL	-	0.92 (1.04)
10^{-2} mg/mL	-	0.92 (1.01)
10^{-1} mg/mL	0.003	0.98 (1.07)
10^{-0} mg/mL	0.030	1.10 (1.13)

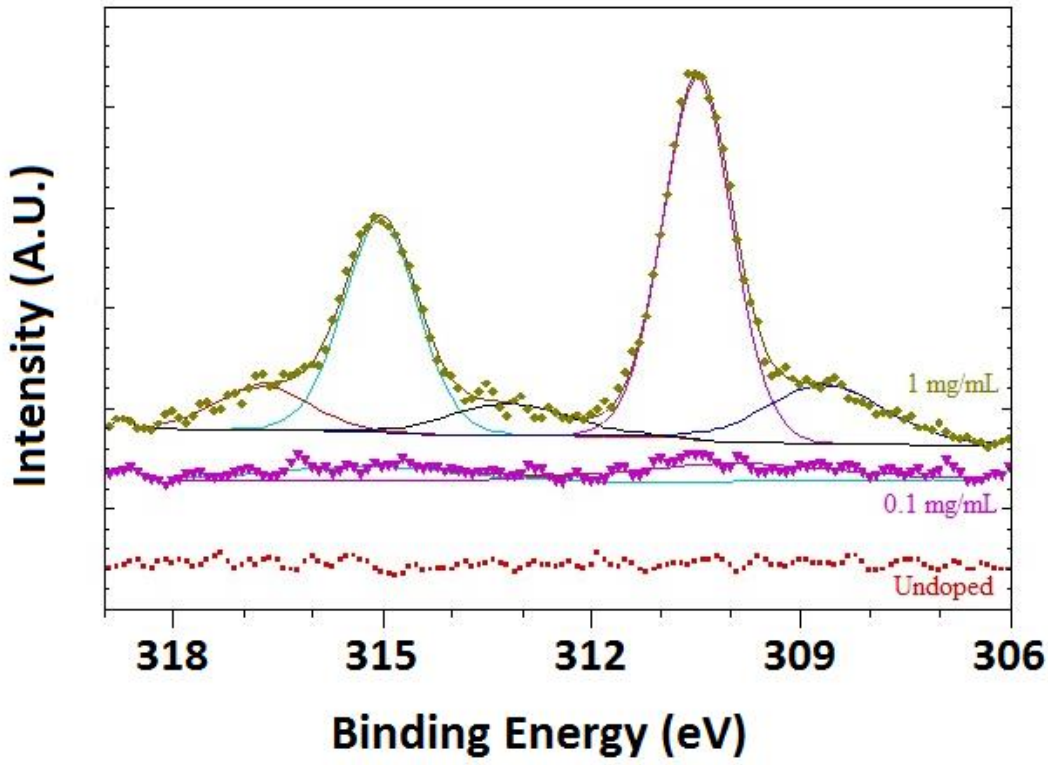

Figure 5.4. Evolution of the Rh 3d peaks is observed in the higher concentration samples.

For the oxides fabricated from 1 and 0.1 mg/mL dopant solutions, fitting of Zn 2p and Rh 3d peaks gave Rh/Zn atomic ratios of 0.030 and 0.003 respectively, consistent with the 3% and 0.3% ratio of dopant monomers to zinc acetate molecules expected from the solution concentrations. The XPS Rh 3d peaks are compared, by dopant concentration in the sol-gel, in Figure 5.4. Although the Rh signals from lower dopant concentrations cannot be detected with XPS, based on the linear decrease in Rh^+ intensity observed by SIMS (Section 5.2.2) it is reasonable to assume that the atomic ratio follows this trend as well. The 1 mg/mL film also shows two separate pairs of Rh 3d ionizations, with a difference in binding energy of ~1.8 eV. One pair, which accounts for 20.7% of the total Rh species, is seen at similar binding energy to the neutral Rh^I dimer,[34,54] while another, at higher binding energy, can be attributed to the monomeric Rh^{III} $RhCp^*Cp^+$ cation. The observation of a low-binding energy pair of Rh 3d

ionizations might indicate that the dimers are stable to the sol-gel precursor solution and do not completely react with the formed ZnO at these concentrations; however, these ionizations might also be attributable to another Rh^{I} species, such as a products of nucleophilic attack on the $RhCp^{*}Cp^{+}$ cation.

An additional, unexpected trend was the increase of the apparent O/Zn atomic ratio from the undoped to low-doped films, indicating a large change in the film composition. The increase was not uniform across the samples; the 10^{-3} and 10^{-2} mg/mL films both exhibited decreases to 0.92 from the undoped value of 1.08. These values were established by subtracting the ITO oxygen contribution from the measured O/Zn ratio, determined via the effective ZnO thickness from the In/Zn ratio and calculating the integrated signal decay.[52,53] Measured values are given in Table 1. As these films are processed at low temperatures for a short period of time, the formation of the oxide can be imperfect and the concentration of impurities can be rather high, both of which will affect the O/Zn ratio. A decrease in this ratio can indicate that the oxide is becoming more oxygen-deficient via an increase in O vacancies and Zn interstitial sites or a decrease in O interstitial sites and Zn vacancies, either situation with the potential to affect the electronic properties of the system.[55–57]

5.2.4 Ultra-violet Photoelectron Spectroscopy

A detailed discussion of photoelectron spectroscopy was given in Chapter 1. For this chapter, ultra-violet photoelectron spectroscopy (UPS) was performed in the ultra-high vacuum environment of a Kratos Axis $Ultra^{DLD}$ XPS/UPS system at the Georgia Institute of Technology. All samples were in contact with the detector by a metallic clip and characterizations were performed at a take-off angle normal to the film. Spot size was ca. 110 μm. UPS was acquired at 5 eV pass energy and 0.05 eV step size. Several solutions were prepared by mixing zinc oxide sol-gel solution (detailed in

Section 5.2.1) with dopant molecules at concentrations ranging from 1 down to 10^{-4} mg/mL. These thin ZnO films were produced by spin coating the sol-gel solutions on top of a solvent and UV-Ozone-cleaned ITO/glass substrate. The work function is determined by $WF = hv - BE_{SEE}$, where BE_{SEE} is binding energy of the secondary electron edge and hv is the He(I) photon energy (21.22 eV). The ionization energy is determined by $IE = WF + BE_{VBM}$, where BE_{VBM} is the cutoff of the valence band emission.

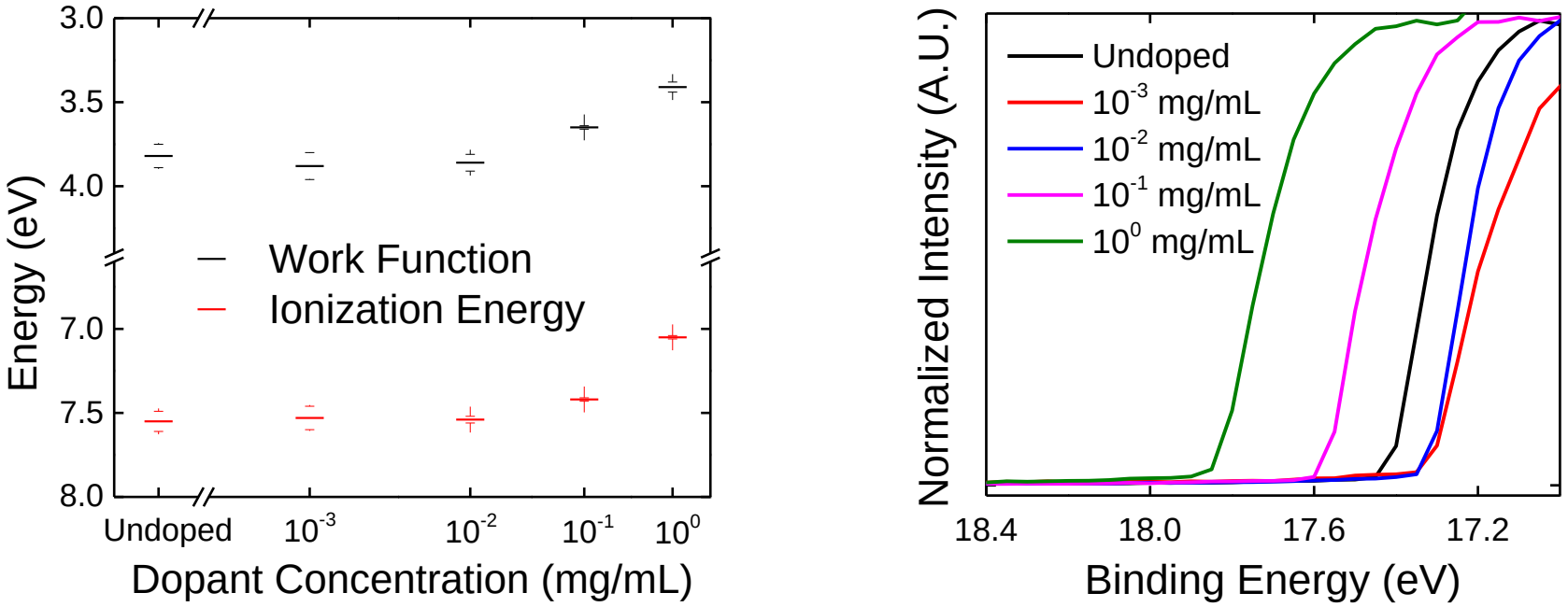

Figure 5.5. (left) Work-function and ionization-energy trends in ZnO films prepared with various concentrations of n-dopant. (right) Secondary cut-off edges illustrating the shift in work function with various concentrations of n-dopant.

UPS was used to explore shifts in the work function and ionization energy of the thin a-ZnO films; the results are shown in Figure 5.5. It was found that the lowest dopant concentrations actually result in a slight *increase* in the work function, from 3.8 to 3.9 eV. This could be explained by a compositional change in the bulk of the ZnO, indicated by the change in the O/Zn ratio shown in XPS, indicated in Section 5.2.3. Density-functional theoretical (DFT) models that account for surface defects, as opposed to termination in –OH groups, indicate an expected increase from the presence of zinc and oxygen vacancies, and from zinc interstitial sites,[56] which could account for the slight increase in the Φ at lower dopant concentrations. Only at higher concentrations does the work function decrease, down to 3.4 eV for the film with 1 mg/mL dopant, which is consistent with the dopant undergoing effective electron transfer to the conduction band, as was observed with surface doping of the oxide.[36] The ionization energy is constant at lower dopant concentrations, only shifting down with the work function at higher concentrations, with a maximum shift from 7.55 to 7.05 eV. Since the Fermi level moves little relative to the onset of the valence band (i.e. $IE - \Phi$ is roughly constant), the origin of the Φ shift is presumably the formation of interface dipoles across the surface of the ZnO particles due to the presence of positively charged $RhCp^*Cp^+$ ions on the negatively charged oxide, though one should note that an overly large Φ shift is not anticipated, as E_F is expected to be sufficiently close to the high density of states edge of the conduction band.

5.2.5 Conductivity & Mobility Measurements

An in-depth discussion regarding the methodology of conductivity and mobility (μ) measurements of semiconductors was given in Chapter 1. For this chapter, both σ and μ were measured at the King Abdullah University of Science and Technology on a-ZnO spin-cast from sol-gel solutions incorporating $[RhCp^*Cp]_2$, deposited over

plasma-cleaned pre-patterned electrodes (45 nm Au/5 nm ITO) on 230 nm silica over silicon (3×10^{17} cm^{-3} n-doped) substrates. Several solutions were prepared by mixing zinc oxide sol-gel solution (detailed in Section 5.2.1) with dopant molecules at concentrations ranging from 1 down to 10^{-4} mg/mL. The conductivity was estimated using the ohmic (linear) region of the I-V curves between the source and drain electrodes, converting current to current density using film thickness and channel width, which in all cases were 50-100 nm and 2 mm respectively, and voltage to field using channel length, which were 2, 5, 10 or 20 μm. Conductivities measured at all four channel lengths gave similar values, indicating that contact resistance is negligible relative to film resistance. σ values are averaged across at least 8 pixels from all four channel lengths. Mobility values were measured in a field-effect transistor (FET) format using an EP4 cascade microtech probe station & a Keithley 2400 source meter. Mobilities were determined by fitting the slope (m) of $I_D^{1/2}$-V_{GS} in the saturation regime by the expression $\mu = 2Lm^2/WC_i$, where L and W are the length and width of the channel, and C_i is the geometric capacitance of the gate dielectric, which is ca. 15 nF/cm^2 for the 230 nm silica over silicon (3×10^{17} cm^{-3} n-doped) substrates used in this work.[58] The threshold voltage (V_{Th}) was determined by the zero-intercept of the fitted slope. Thicknesses were determined using a Dektak 150 profilometer.

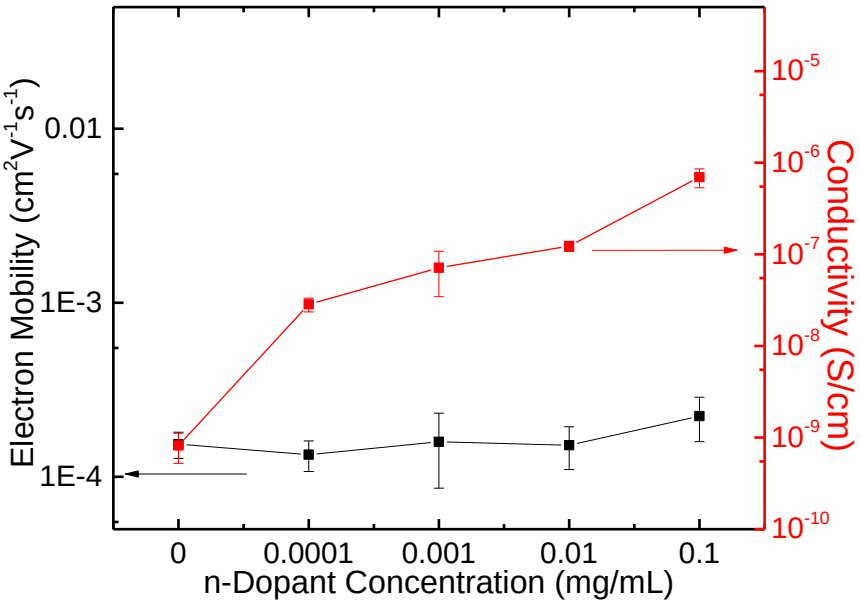

Figure 5.6. Electron mobility and conductivity values of ZnO with different concentration of dopant (as indicated) by bottom gate/bottom contact thin film filed effect transistor.

Table 5.2. Electron mobility values, threshold voltages, and On/Off ratios of the doped ZnO transistors.

Dopant Concentration	**$\mu \times 10^4$ ($cm^2\ V^{-1}\ s^{-1}$)**	**Threshold Voltage (V)**	**On/Off**
Undoped	1.5 ± 0.3	7.0 ± 6.8	10^5
0.0001%	1.3 ± 0.3	19.4 ± 6.7	10^5-10^6
0.001%	1.6 ± 0.7	9.4 ± 3.8	10^5-10^6
0.01%	1.5 ± 0.4	18.0 ± 3.7	10^5-10^6
0.1%	2.2 ± 0.6	7.0 ± 6.4	10^5-10^6

Trends of in-plane electron mobility and conductivity in a-ZnO films incorporating the n-dopant are shown in Figure 5.6. The electron mobility is in good agreement with literature values,[23,59] but does not vary significantly with doping concentrations. However, a non-trivial increase of conductivity was observed with increasing dopant concentration, approaching values measured for ZnO processed under much higher temperatures.[60] Though this is not identifiable in the threshold voltage, there appears to be an increase in the current at $V_G = 0$. This trend, combined with the unchanging electron mobility, could point to an increase of carrier density expected on increasing the doping level, assuming the mobility trend is consistent in ungated and gated saturation regimes.

5.2.6 Absorbance & Photoluminescence

UV-visible absorption spectra were acquired on a Cary 5000 (Varian) instrument. Photoemission spectra were collected using a Horiba Jobin Yvon Fluorolog-3 employing an iHR320 monochrometer, and a CCD detector. Photoluminescence lifetimes were calculated using the Horiba DAS6 Analysis software. Samples were excited at 320 nm. Spectra are corrected for fluctuations in the lamp current. Several solutions were prepared by mixing zinc oxide sol-gel solution (detailed in Section 5.2.1) with dopant molecules at concentrations ranging from 1 down to 10^{-3} mg/mL. These thin ZnO films were produced by spin coating the sol-gel solutions on top of solvent and UV-Ozone-cleaned SiOx/Si substrates.

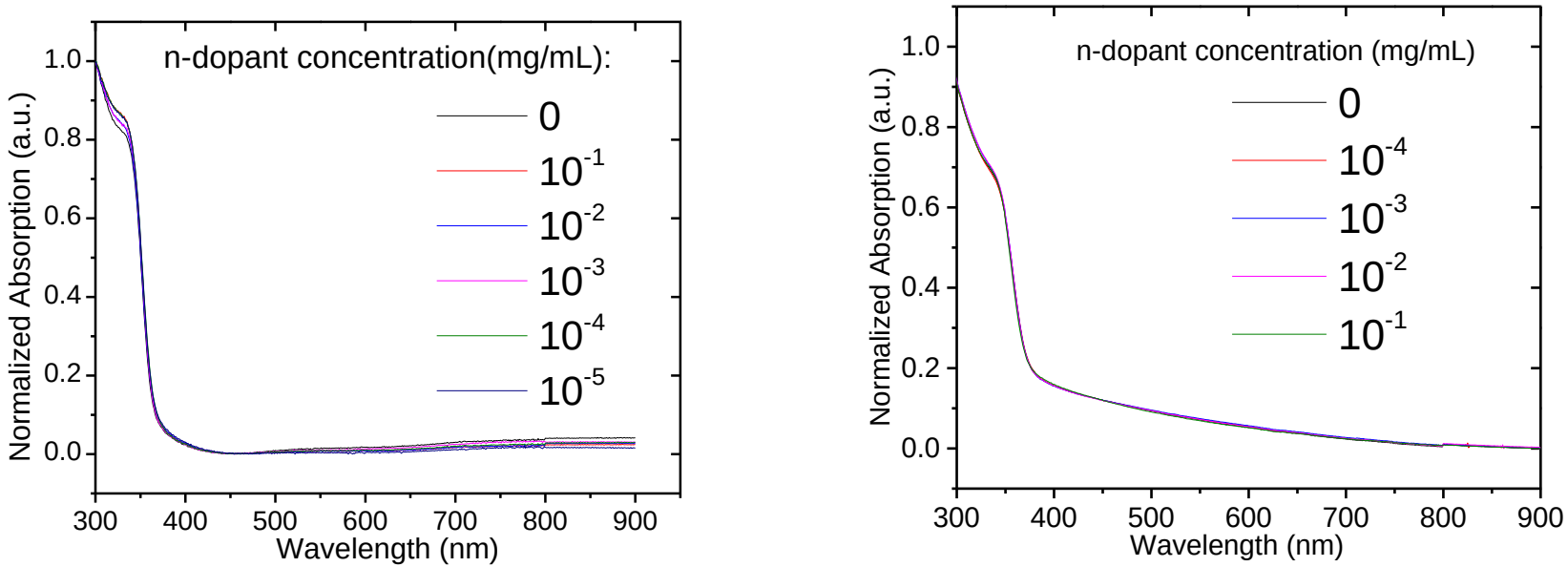

Figure 5.7. UV-Vis absorption spectra of thin, compact (left) and thick, rippled (right) ZnO doped by different concentration (mg/mL) as indicated.

The optical properties of ZnO can shed light on the nature of gap defects. Figure 5.7 shows that the introduction of dopants has a negligible effect on the absorbance of compact or rippled ZnO. The absorbance remains in the UV region, with onset ca. 360-370 nm, though the rippled ZnO displays a scattering tail in the visible region. However, it has been shown that the presence of gap states in ZnO films can be identified by photoluminescence spectroscopy, specifically by the presence of a green luminescence resulting from the recombination of shallow donors (close to the ZnO conduction band edge) and deep acceptors associated with zinc vacancies.[61–66] When normalized to the main fluorescence feature at ~360 nm, the undoped oxide film has an intense sub-gap emission, centered at 580 nm. Although doping resulted in no significant change in the absorption spectra, additions of a small amount of dopant reduce the relative intensity of the green fluorescence feature rather sharply (Figure 5.8). As this transition is thought to involve carrier relaxation into deep vacancy trap states, a reduction in the fluorescence strength could indicate a decrease in the population of vacancies, specifically of Zn vacancies, that corresponds to the observed decrease in the O/Zn atomic ratio. DFT calculations have indicated that these vacancies can act as electron-compensation centers on the surface of ZnO films that can trap mobile carriers.[56] Chen *et al.* observed a similar reduction in green luminescence in ZnO NP films upon UV-ozone treatment, and attributed this to a reduction of oxygen vacancies due to oxygen penetration during the treatment; the treatment was also found to lower charge recombination at the oxide-organic interface in OPV cells with ZnO NP electron-transport layers.[62] The average energy of both emissions decreases as well at low doping levels; the peaks are red-shifted with an energy difference of ca. 0.07 eV. At higher doping (1 mg/mL), the strength of the green luminescence increases again

and the main feature appears to broaden; this might be attributable to potential fluctuations arising from a non-uniform distribution of molecular dopants, as well as an increase in atomic vacancy sites. Both features experience a blue-shift ($\Delta > 0.05$eV), similar to that observed when ZnO is doped with donors such as gallium.[67]

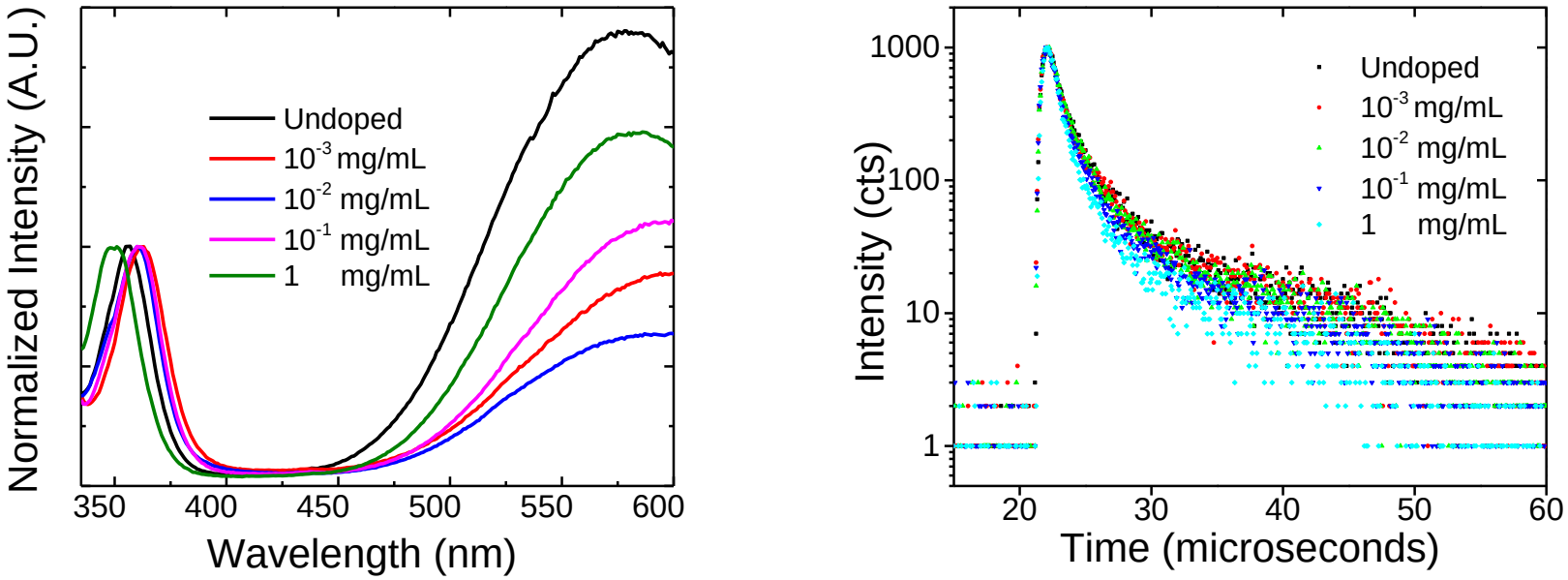

Figure 5.8. (left) Photoluminescence spectra of ZnO thin films containing molecular dopants. (right) Decay of the long-lived green photoluminescence (580 nm) of ZnO films with various dopant concentrations.

The photoluminescence decay of the green-emissive state was studied, as shown in Figure 5.8, and modelled as a biexponential. The longer component had a lifetime of 6.2 μs in the intrinsic film. The effect of low doping concentrations on this lifetime is marginal, but in the highest doped film (1 mg/mL) the lifetime is shortened to 3.0 μs, i.e. about half of its initial value. The increased rate of decay can be an indication of an increased rate in either radiative or non-radiative pathways involving shallow interstitial trap states that were previously unpopulated.

5.2.7 Organic Photovoltaic Devices

An in-depth discussion of organic photovoltaics theory and general processing procedures was given in Chapter 1. For the study in this chapter, photovoltaic devices were fabricated and tested at the King Abdullah University of Science and Technology jointly with Hanlin Hu. 200 nm-thick patterned ITO-on-glass substrates were sonicated in sodium dodecyl sulfate solution, water, acetone, and isopropanol, and then UV-ozone cleaned for 10 min. Thin a-ZnO films were produced by spin-coating zinc oxide sol-gel solutions (detailed in Section 5.2.1) that were prepared with dopant molecules at concentrations ranging from 10^{-1} down to 10^{-5} mg/mL. The active layer blend solutions were kept stirred at 60 °C overnight and filtered using PTFE 0.45 μm filters before spin casting (800 rpm, 45 s and 900 rpm, 45 s for PTB7 and PTB7-Th donor polymers respectively). For PTB7:$PC_{71}BM$ and PTB7-Th:$PC_{71}BM$, BHJs active-layer blend solutions were obtained by mixing 1:1.5 w/w donor to acceptor ratios in chlorobenzene (concentration 25 mg/mL) with a 3% volume ratio of DIO. The samples were kept in a closed Petri dish for 20 min of solvent annealing after coating the active layer, then transferred into vacuum chamber (10^{-7} Torr) for thermal evaporation of MoO_x (15 nm) and silver (Ag) (100 nm). To ensure consistent results, each series of devices were simultaneously fabricated. The active area of the devices was 0.1 cm^2.

The current density-voltage characteristics of the photovoltaic cells were measured using a Keithley 2400 under a simulated AM 1.5G solar irradiation at 100 mW cm^{-2}. The external quantum efficiency (EQE) was recorded by Oriel Quantum Efficiency Measurement Kit (Newport).

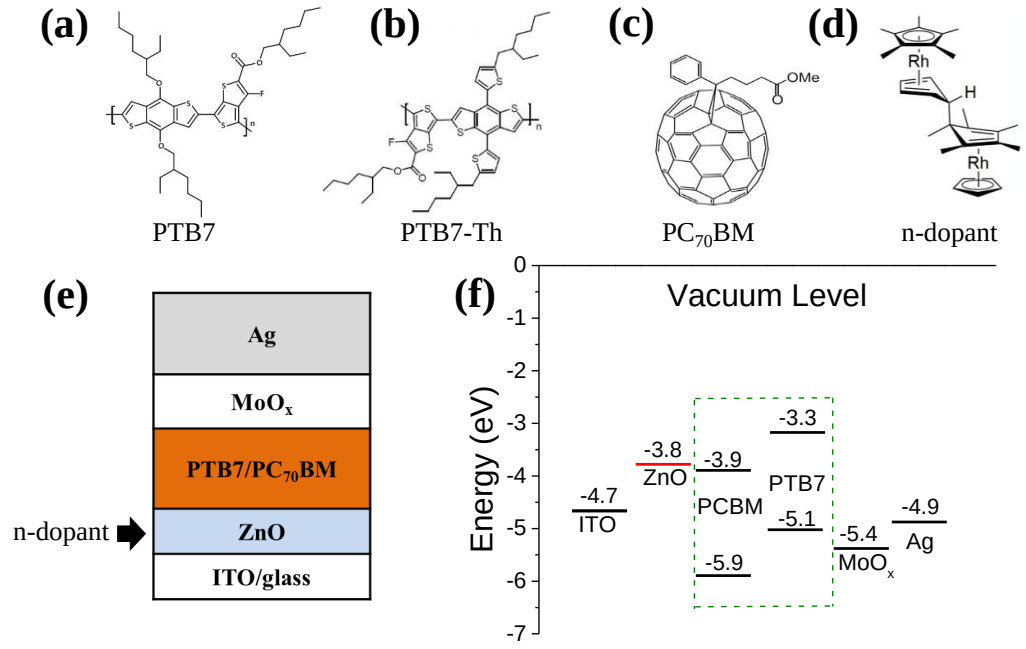

Figure 5.9. Chemical structure of (a) PTB7 polymer, (b) PTB7-Th polymer, (c) $PC_{71}BM$ fullerene and (d) the $[RhCp^*Cp]_2$ n-dopant. (e) Device architecture showing different functional layers and (f) estimated energy-level diagram of materials used in inverted BHJ device configurations.[17]

To explore the influence of dopant molecule introduction into ZnO as an electron-transport layer, organic solar cells were fabricated with high-performance polymers. The chemical structures of the materials used, PTB7, PTB7-Th, $PC_{71}BM$ and $[RhCp^*Cp]_2$, are shown in Figure 5.9 a-d respectively. With the aim of testing ZnO with different concentrations of n-dopant on the performance of organic solar cells, BHJ solar cells were fabricated with an inverted structure (Figure 5.9e); the

corresponding energy diagram is shown in Figure 5.9f, where the Φ of ZnO is measured by UPS as discussed previously, with the other estimated energy levels taken from literature values.[17]

Upon dopant incorporation into the a-ZnO layer, a sizeable improvement was seen for devices with the structure ITO/a-ZnO/PTB7:$PC_{71}BM$/MoO_3/Ag employing thin, compact a-ZnO. Figure 5.10a plots the current density-voltage (*J*-V) characteristics of these OPVs, with detailed photovoltaic parameters summarized in Table 3. The performance of OPVs with pristine ZnO is in a good agreement with literature values.[68,69] There is little effect on the V_{OC} and *FF* upon modulation of the dopant concentration within the range of 10^{-1} to 10^{-5} mg/mL; the variation in J_{SC} is the major parameter that governs the evolution of PCE with doping level. The most significant improvements appear at lower dopant concentrations, where a reduction in sub-gap fluorescence was observed in Section 5.2.6, with a maximum enhancement of J_{SC} from 16.3 mA/cm^2 (pristine ZnO) to 17.9 mA/cm^2 (with 10^{-4} mg/mL dopant in ZnO), in which the enhancement in performance is greater than 9%. Consequently, the PCE increases from 8.6% to a maximum value of 9.3%, which exceeds the record PCE of inverted PTB7:$PC_{71}BM$-based OPVs, which was previously achieved with poly[(9,9-bis(3'-(*N*,*N*-dimethylamino)propyl)-2,7-fluorene)-alt-2,7-(9,9-dioctylfluorene)] (PFN)-modified ITO.[70] As the dopant concentration increases to 10^{-1} mg/mL, the J_{SC} was reduced to 16.2 mA/cm^2, slightly below pristine values. These results seem to complement the observations from XPS and PL, corresponding to a reduction in Zn vacancies on the surface of the film that ultimately reduces charge trapping at the oxide/organic interface.[56,62] Conversely, the increases in carrier concentration and conductivity, as well as reductions in the Φ, do not appear to have a positive effect on device performance.

In order to confirm the enhancement in the J_{SC}, the incident photon-to-conversion efficiency (IPCE) spectra were measured, shown in Figure 5.10b. An increase of the spectral response across the lower wavelengths of 300-600 nm is noticed for moderately doped ZnO (10^{-5}-10^{-3} mg/mL) relative to the pristine sample with pure ZnO as ETL, followed by a uniform decrease in quantum efficiency with greater dopant concentrations, implying that the increase of current density results from more efficient electron collection in moderately doped ZnO over pristine or heavily-doped ZnO.

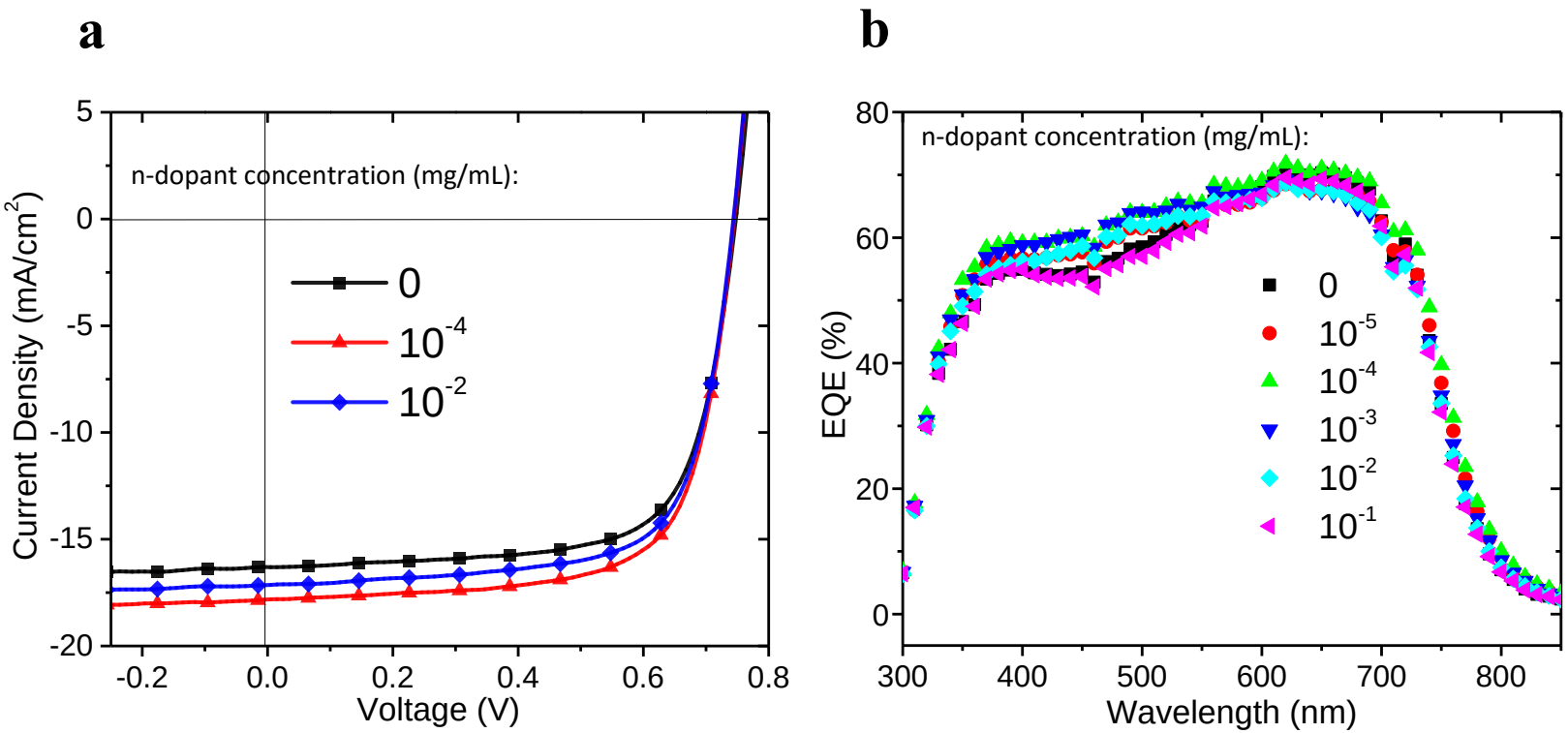

Figure 5.10. The *J-V* characteristics (a) and EQE (b) of inverted PTB7/$PC_{71}BM$ device with compact ZnO doped by different concentrations as indicated.

Table 5.3. The OPV performance values of inverted PTB7/$PC_{71}BM$ device with compact ZnO doped by different concentrations as indicated.

n-Dopant Concentrations (mg/mL)	J_{SC} (mA/cm^2)	V_{OC} (V)	*FF* (%)	PCE (%)
0	**16.3** ± 0.2	**0.74** ± 0.01	**71** ± 1	**8.6** ± 0.1
10^{-5}	**17.1** ± 0.3	**0.74** ± 0.01	**70** ± 0	**8.9** ± 0.2
10^{-4}	**17.8** ± 0.2	**0.74** ± 0.01	**70** ± 0	**9.3** ± 0.1
10^{-3}	**17.7** ± 0.2	**0.74** ± 0.01	**70** ± 1	**9.3** ± 0.2
10^{-2}	**17.1** ± 0.2	**0.74** ± 0.01	**70** ± 0	**9.0** ± 0.1
10^{-1}	**16.2** ± 0.3	**0.74** ± 0.01	**70** ± 0	**8.4** ± 0.1

In addition to the work on compact sol-gel ZnO described above, the influence of dopants on thicker, rippled ZnO, which has a greater surface area that can be taken advantage of with surface modifiers,[71,72] was also studied in OPV devices. As in the case of compact films, the dopant was introduced in solution prior to film deposition. The use of the rippled ZnO resulted in an intrinsically lower J_{SC} for PTB7:$PC_{71}BM$ devices, which is presumed to be due to light scattering evident in absorbance spectra (Figure 5.7), yielding a control efficiency of 8.0%. As expected from the results with compact ZnO, low levels of doping result in improvement in the J_{SC} and consequently the PCE, with improvements of PCE up to 8.7% (Table 5.4). Increasing the dopant concentration up to 30 mg/mL, corresponding to a 1:1 Rh/Zn atomic ratio, results in a significant photovoltaic performance decreases with concentrations of dopant over 1 mg/mL, mainly via *FF* and PCE. At 30 mg/mL, the J_{SC}, V_{OC} and *FF* decrease to 15.0 mA/cm2, 0.68 V and 58% respectively, resulting in a PCE of 6.0%.

Table 5.4. The photovoltaic parameters of inverted PTB7:$PC_{71}BM$ device with rippled ZnO doped by n-dopant with different concentration.

n-Dopant Concentration (mg/mL)	J_{SC} (mA/cm^2)	V_{OC} (V)	*FF* (%)	PCE (%)
0	**15.7** ± 0.3	**0.72** ± 0.01	**70** ± 1	**8.0** ± 0.1
10^{-4}	**17.0** ± 0.3	**0.72** ± 0.01	**68** ± 1	**8.4** ± 0.2
10^{-3}	**17.6** ± 0.2	**0.73** ± 0.01	**67** ± 1	**8.7** ± 0.2
10^{-2}	**17.3** ± 0.2	**0.73** ± 0.01	**67** ± 1	**8.5** ± 0.2
10^{-1}	**17.3** ± 0.3	**0.72** ± 0.01	**68** ± 1	**8.4** ± 0.1
1	**15.3** ± 0.3	**0.71** ± 0.01	**69** ± 1	**7.5** ± 0.2
3	**15.4** ± 0.3	**0.70** ± 0.01	**62** ± 2	**6.8** ± 0.2
10	**15.2** ± 0.3	**0.68** ± 0.01	**58** ± 1	**6.0** ± 0.2
30	**15.0** ± 0.4	**0.68** ± 0.01	**58** ± 2	**6.0** ± 0.3

To determine if the improvement could also be seen for other active layer systems, the lower-bandgap polymer PTB7-Th was employed with rippled a-ZnO, the photovoltaic parameters shown in Table 5. Again, adding the dopant up to 10^{-1} mg/mL did not change the *FF* and V_{OC} of the devices; however, J_{SC} increases from 17.5 to 19.2 mA/cm^2 between pristine rippled ZnO and a film doped using a dopant concentration of 10^{-2} mg/mL. This enhancement in J_{SC} results in a PCE improvement from 8.3% to 9.0% with a high J_{SC} of 19.2 mA/cm^2 at a slightly higher, relative to the compact films, dopant concentration of 10^{-2} mg/mL, which is expected with the higher concentration of the sol-gel. As the trends in enhancement are very similar for the compact and rippled ZnO films, it can be deduced that the improvement in the PCE and the IPCE is most likely not related to morphological/phase formation differences but to common electronic effects, such as the passivation of shallow traps, as discussed above.

Table 5.5. The parameters of inverted PTB7-Th:$PC_{71}BM$ device with rippled ZnO doped by different dopant concentration.

Concentration (mg/mL)	J_{SC} **(mA/cm^2)**	V_{OC} **(V)**	***FF*** **(%)**	**PCE (%)**
0	**17.5** ± 0.3	**0.78** ± 0.01	**61** ± 1	**8.3** ± 0.1
10^{-4}	**17.7** ± 0.3	**0.78** ± 0.01	**62** ± 1	**8.6** ± 0.1
10^{-3}	**18.4** ± 0.3	**0.78** ± 0.01	**62** ± 1	**8.8** ± 0.2
10^{-2}	**19.2** ± 0.4	**0.78** ± 0.01	**60** ± 1	**9.0** ± 0.2
10^{-1}	**18.3** ± 0.3	**0.78** ± 0.01	**60** ± 1	**8.6** ± 0.2

As the improvements in performance at lower concentrations have been linked to the population of atomic vacancies in the oxide, the role of the redox properties of the Rh dimer upon these states was explored by employing weaker reductants. Cobaltocene, which is a weaker, albeit often more reactive, metal-centered reductant (~ -1.3 V vs. ferrocene), and tetramethylammonium chloride, which has a moderately sized cation but no doping potential, were also attempted in OPVs. The separate materials were dissolved directly into ZnO sol-gels in 2-methoxyethanol in the same fashion as $[RhCp^*Cp]_2$, in relevant concentrations of 10^{-5}, 10^{-4}, 10^{-3}, and 10^{-2} mg/mL, the oxide employed in inverted PTB7:$PC_{71}BM$ devices. The anticipated increase in J_{SC} is not observed with these materials upon dopant introduction into the oxide, as is evident from the *J-V* curves in Figure 5.11, and, save a slight decrease in the *FF*, no reproducible trends can be identified, suggesting that this effect is possibly tied to the reducing strength and reaction kinetics of the Rh dimer and its effect upon the formation of the oxide.

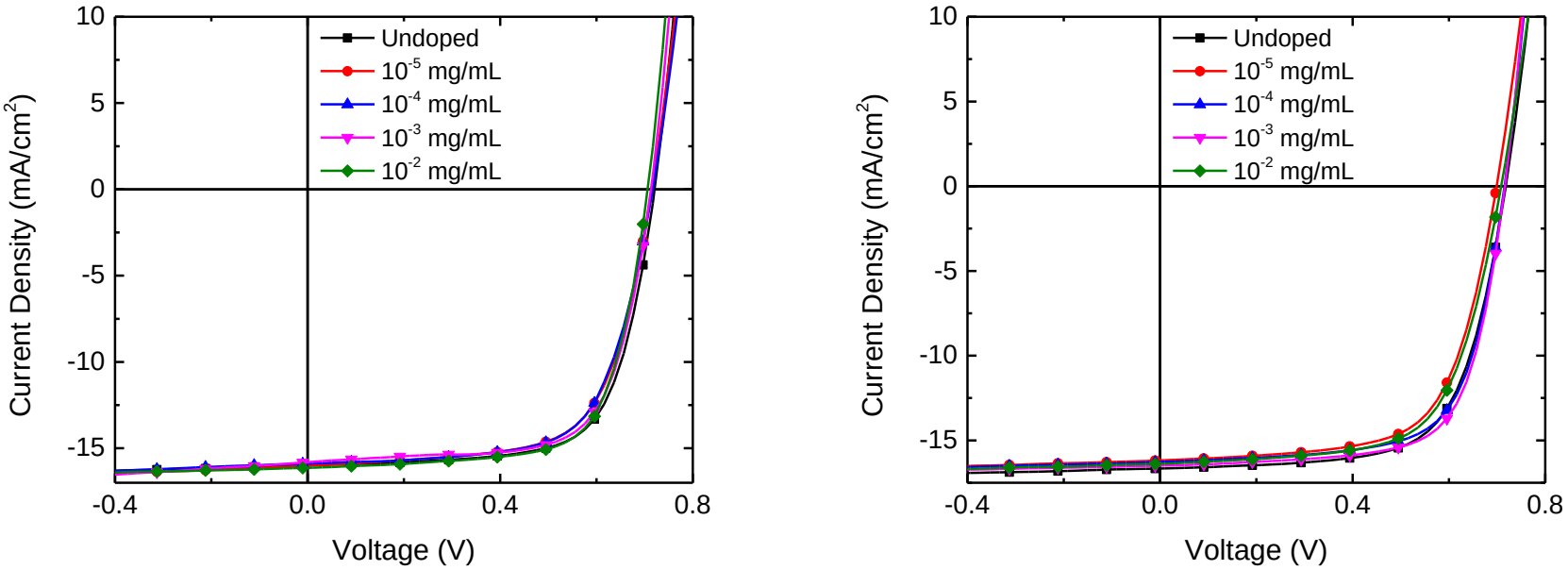

Figure 5.11. *J-V* curves and device characteristics from doping of ZnO interlayers in PTB7/$PC_{71}BM$ OPVs with cobaltocene (left) and tetramethylammonium chloride (right).

5.2.8 Atomic Force Microscopy

An in-depth discussion of atomic force microscopy (AFM) relating to organic photovoltaic devices was given in Chapter 1. For the work in this chapter, AFM was conducted at the King Abdullah University of Science & Technology by Hanlin Hu on an Agilent 5400 SPM in tapping mode, and analyzed with Gwyddion SPM analysis software. Several solutions were prepared by mixing zinc oxide sol-gel solution (detailed in Section 5.2.1) with dopant molecules at concentrations ranging from 1 down to 10^{-4} mg/mL. These thin ZnO films were produced by spin coating the sol-gel solutions on top of solvent and UV-Ozone-cleaned ITO/glass substrate.

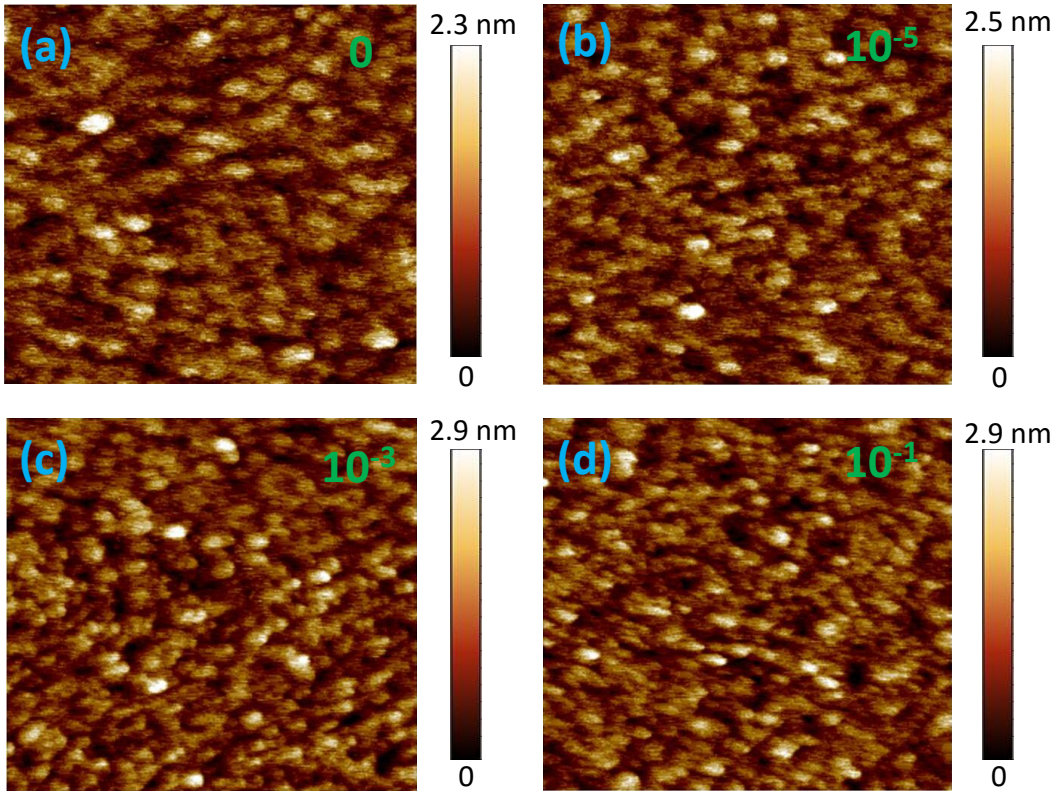

Figure 5.12. AFM (1×1 µm) images of compact ZnO with dopant concentration (mg/mL) as indicated. AFM was conducted at the King Abdullah University of Science & Technology by Hanlin Hu.

Spin-coating of 0.11 M ZnO sol-gel solutions (with and without dopant) on ITO-coated glass at a high speed (4000 rpm) for 30 s results in a compact a-ZnO layer with a thickness of ca. 10 nm, measured by ellipsometry and confirmed by XPS (as described in Section 5.2.3). The surface morphology of the ZnO thin films, with and without dopant, have been characterized by atomic force microscopy (AFM), as shown in Figure 5.12. The pristine and doped ZnO thin films display minimal differences in morphology and roughness, with nearly identical ZnO particulate size, even at higher concentrations of the n-dopant.

In contrast to the particulate morphology of compact ZnO, the rippled ZnO shows much higher roughness with sharp protrusions and shallow valleys. Compared with pristine rippled ZnO however, no significant surface morphological changes were observed for the samples with dopant regardless of concentration. AFM topography images of pristine rippled ZnO and 10^{-1} mg/mL doped, rippled ZnO were characterized as seen in Figure 5.13, which confirms the lack of structural change upon dopant incorporation.

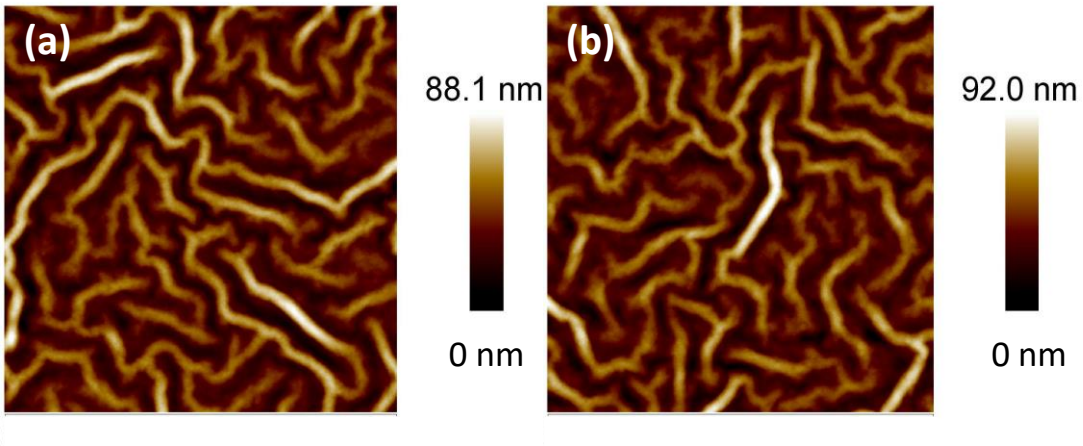

Figure 5.13. AFM (5×5 μm) images of rippled ZnO, (a) without and (b) with 10^{-1} mg/mL dopant. AFM was conducted at the King Abdullah University of Science & Technology by Hanlin Hu.

5.3 Conclusion

A method of incorporating a dimeric molecular dopant $[RhCp^*Cp]_2$ at various concentrations into ZnO sol-gels and producing low-temperature-processed thin films, has resulted in an improvement in OPV performance via the short-circuit current density for lower dopant concentrations. Although increased conductivity and large shifts in work

function are observed at high concentrations of dopant, it is not these properties that lead to a better OPV in this minimally processed system, and indeed the precise activity of the dopant is not clear in the sol-gel at these concentrations. Subtle changes in ZnO composition occur as a result of added dopant, as observed via a change in the apparent O/Zn ratio from XPS, leading to a reduction in Zn and/or O vacancy populations indicated by the photoluminescence.

Due to the possibly of reactions between the dopant and the solvent or sol-gel components, the nature of the rhodocene derivative in the forming oxide, and its effect upon this process, have not been elucidated. As such these amorphous oxides cannot be described as electrically doped, yet, as attempts with other additives have not produced the same results, the changes in oxide formation appear to be related to the dopant's reductive strength. As indicated by previous literature, it is possible that the compositional changes in the ZnO film have led to decreased charge trapping at the oxide/organic interface of OSCs, resulting in enhanced current density and consequently improving the PCE. This ZnO modification shows promise of universality, with improvements found for two contrasting preparations of ZnO films and for different donor/acceptor blends, reaching a maximum PCE of 9.4% (9.3% average) for PTB7:$PC_{71}BM$, exceeding the current record for inverted ZnO-on-ITO devices with this active layer. Continued studies of the effect of additives on low-order solution-processed oxides may afford a greater understanding of atomic ratios and vacancy/interstitial sites in these interlayers and their effects on OPV performance.

5.4 Works Cited

[1] K. Ellmer, "Past achievements and future challenges in the development of optically transparent electrodes," *Nat. Photonics*, vol. 6, no. 12, pp. 809–817, Nov. 2012.

[2] I. Hamberg and C. G. Granqvist, "Evaporated Sn-doped In_2O_3 films: Basic optical properties and applications to energy-efficient windows," *J. Appl. Phys.*, vol. 60, no. 11, p. R123, Dec. 1986.

[3] K. Sugiyama, H. Ishii, Y. Ouchi, and K. Seki, "Dependence of indium–tin–oxide work function on surface cleaning method as studied by ultraviolet and x-ray photoemission spectroscopies," *J. Appl. Phys.*, vol. 87, no. 1, p. 295, Jan. 2000.

[4] P.-R. Huang, Y. He, C. Cao, and Z.-H. Lu, "The origin of the high work function of chlorinated indium tin oxide," *NPG Asia Mater.*, vol. 5, no. 8, p. e57, Aug. 2013.

[5] A. Sharma, B. Kippelen, P. J. Hotchkiss, and S. R. Marder, "Stabilization of the work function of indium tin oxide using organic surface modifiers in organic light-emitting diodes," *Appl. Phys. Lett.*, vol. 93, no. 16, p. 163308, Oct. 2008.

[6] W. Tress, *Organic Solar Cells: Theory, Experiment, and Device Simulation*, vol. 22. Springer, 2014.

[7] Y. Zhou, J. W. Shim, C. Fuentes-Hernandez, A. Sharma, K. A. Knauer, A. J. Giordano, S. R. Marder, and B. Kippelen, "Direct correlation between work function of indium-tin-oxide electrodes and solar cell performance influenced by ultraviolet irradiation and air exposure.," *Phys. Chem. Chem. Phys.*, vol. 14, no. 34, pp. 12014–21, Sep. 2012.

[8] M. G. Helander, Z. B. Wang, J. Qiu, and Z. H. Lu, "Band alignment at metal/organic and metal/oxide/organic interfaces," *Appl. Phys. Lett.*, vol. 93, no. 19, p. 193310, Nov. 2008.

[9] T.-H. Lai, S.-W. Tsang, J. R. Manders, S. Chen, and F. So, "Properties of interlayer for organic photovoltaics," *Mater. Today*, vol. 16, no. 11, pp. 424–432, Nov. 2013.

[10] J. Meyer, S. Hamwi, M. Kröger, W. Kowalsky, T. Riedl, and A. Kahn, "Transition metal oxides for organic electronics: energetics, device physics and applications.,"

Adv. Mater., vol. 24, no. 40, pp. 5408–27, Oct. 2012.

[11] S. Chen, J. R. Manders, S.-W. Tsang, and F. So, "Metal oxides for interface engineering in polymer solar cells," *J. Mater. Chem.*, vol. 22, no. 46, p. 24202, Nov. 2012.

[12] I. Hancox, L. A. Rochford, D. Clare, P. Sullivan, and T. S. Jones, "Utilizing n-type vanadium oxide films as hole-extracting layers for small molecule organic photovoltaics," *Appl. Phys. Lett.*, vol. 99, no. 1, p. 013304, Jul. 2011.

[13] J. Meyer, "Electronic structure of molybdenum-oxide films and associated charge injection mechanisms in organic devices," *J. Photonics Energy*, vol. 1, no. 1, p. 011109, Jan. 2011.

[14] M. Vasilopoulou, G. Papadimitropoulos, L. C. Palilis, D. G. Georgiadou, P. Argitis, S. Kennou, I. Kostis, N. Vourdas, N. A. Stathopoulos, and D. Davazoglou, "High performance organic light emitting diodes using substoichiometric tungsten oxide as efficient hole injection layer," *Org. Electron.*, vol. 13, no. 5, pp. 796–806, May 2012.

[15] S. R. Hammond, J. Meyer, N. E. Widjonarko, P. F. Ndione, A. K. Sigdel, A. Garcia, A. Miedaner, M. T. Lloyd, A. Kahn, D. S. Ginley, J. J. Berry, and D. C. Olson, "Low-temperature, solution-processed molybdenum oxide hole-collection layer for organic photovoltaics," *J. Mater. Chem.*, vol. 22, no. 7, p. 3249, Jan. 2012.

[16] T. Hirao, M. Furuta, H. Furuta, T. Matsuda, T. Hiramatsu, H. Hokari, M. Yoshida, H. Ishii, and M. Kakegawa, "Novel top-gate zinc oxide thin-film transistors (ZnO TFTs) for AMLCDs," *J. Soc. Inf. Disp.*, vol. 15, no. 1, p. 17, 2007.

[17] L. K. Jagadamma, M. Al-Senani, A. El-Labban, I. Gereige, G. O. Ngongang Ndjawa, J. C. D. Faria, T. Kim, K. Zhao, F. Cruciani, D. H. Anjum, M. A. McLachlan, P. M. Beaujuge, and A. Amassian, "Polymer Solar Cells with Efficiency >10% Enabled via a Facile Solution-Processed Al-Doped ZnO Electron Transporting Layer," *Adv. Energy Mater.*, vol. 5, no. 12, p. 1500204, Apr. 2015.

[18] D. Liu and T. L. Kelly, "Perovskite solar cells with a planar heterojunction structure prepared using room-temperature solution processing techniques," *Nat. Photonics*, vol. 8, no. 2, pp. 133–138, Dec. 2013.

[19] G. B. Murdoch, S. Hinds, E. H. Sargent, S. W. Tsang, L. Mordoukhovski, and Z. H.

Lu, “Aluminum doped zinc oxide for organic photovoltaics,” *Appl. Phys. Lett.*, vol. 94, no. 21, p. 213301, May 2009.

[20] B.-Y. Oh, M.-C. Jeong, T.-H. Moon, W. Lee, J.-M. Myoung, J.-Y. Hwang, and D.-S. Seo, “Transparent conductive Al-doped ZnO films for liquid crystal displays,” *J. Appl. Phys.*, vol. 99, no. 12, p. 124505, Jun. 2006.

[21] B. Ecker, H.-J. Egelhaaf, R. Steim, J. Parisi, and E. von Hauff, “Understanding S-Shaped Current–Voltage Characteristics in Organic Solar Cells Containing a TiOx Interlayer with Impedance Spectroscopy and Equivalent Circuit Analysis,” *J. Phys. Chem. C*, vol. 116, no. 31, pp. 16333–16337, Aug. 2012.

[22] J. Kong, J. Lee, Y. Jeong, M. Kim, S.-O. Kang, and K. Lee, “Biased internal potential distributions in a bulk-heterojunction organic solar cell incorporated with a TiOx interlayer,” *Appl. Phys. Lett.*, vol. 100, no. 21, p. 213305, May 2012.

[23] L. K. Jagadamma, M. Abdelsamie, A. El Labban, E. Aresu, G. O. Ngongang Ndjawa, D. H. Anjum, D. Cha, P. M. Beaujuge, and A. Amassian, “Efficient inverted bulk-heterojunction solar cells from low-temperature processing of amorphous ZnO buffer layers,” *J. Mater. Chem. A*, vol. 2, no. 33, p. 13321, Jun. 2014.

[24] K. Kim, S. Y. Park, K.-H. Lim, C. Shin, J.-M. Myoung, and Y. S. Kim, “Low temperature and solution-processed Na-doped zinc oxide transparent thin film transistors with reliable electrical performance using methanol developing and surface engineering,” *J. Mater. Chem.*, vol. 22, no. 43, p. 23120, Oct. 2012.

[25] T. Hu, F. Li, K. Yuan, and Y. Chen, “Efficiency and air-stability improvement of flexible inverted polymer solar cells using ZnO/poly(ethylene glycol) hybrids as cathode buffer layers.,” *ACS Appl. Mater. Interfaces*, vol. 5, no. 12, pp. 5763–70, Jun. 2013.

[26] Z. R. Khan, M. S. Khan, M. Zulfequar, and M. Shahid Khan, “Optical and Structural Properties of ZnO Thin Films Fabricated by Sol-Gel Method,” *Mater. Sci. Appl.*, vol. 02, no. 05, pp. 340–345, May 2011.

[27] P. A. Rodnyi and I. V. Khodyuk, “Optical and luminescence properties of zinc oxide (Review),” *Opt. Spectrosc.*, vol. 111, no. 5, pp. 776–785, Dec. 2011.

[28] Z. Wu, T. Song, Z. Xia, H. Wei, and B. Sun, “Enhanced performance of polymer

solar cell with ZnO nanoparticle electron transporting layer passivated by in situ cross-linked three-dimensional polymer network.," *Nanotechnology*, vol. 24, no. 48, p. 484012, Dec. 2013.

[29] H. P. Kim, A. R. B. M. Yusoff, H. M. Kim, H. J. Lee, G. J. Seo, and J. Jang, "Inverted organic photovoltaic device with a new electron transport layer.," *Nanoscale Res. Lett.*, vol. 9, no. 1, p. 150, Jan. 2014.

[30] T. Hu, L. Chen, K. Yuan, and Y. Chen, "Amphiphilic fullerene/ZnO hybrids as cathode buffer layers to improve charge selectivity of inverted polymer solar cells.," *Nanoscale*, vol. 7, no. 20, pp. 9194–203, May 2015.

[31] S.-H. Liao, H.-J. Jhuo, Y.-S. Cheng, and S.-A. Chen, "Fullerene derivative-doped zinc oxide nanofilm as the cathode of inverted polymer solar cells with low-bandgap polymer (PTB7-Th) for high performance.," *Adv. Mater.*, vol. 25, no. 34, pp. 4766–71, Sep. 2013.

[32] B. Bröker, R.-P. Blum, J. Frisch, A. Vollmer, O. T. Hofmann, R. Rieger, K. Müllen, J. P. Rabe, E. Zojer, and N. Koch, "Gold work function reduction by 2.2 eV with an air-stable molecular donor layer," *Appl. Phys. Lett.*, vol. 93, no. 24, p. 243303, Dec. 2008.

[33] L. Lindell, M. Unge, W. Osikowicz, S. Stafström, W. R. Salaneck, X. Crispin, and M. P. de Jong, "Integer charge transfer at the tetrakis(dimethylamino)ethylene/Au interface," *Appl. Phys. Lett.*, vol. 92, no. 16, p. 163302, Apr. 2008.

[34] K. Akaike, M. V. Nardi, M. Oehzelt, J. Frisch, A. Opitz, C. Christodoulou, G. Ligorio, P. Beyer, M. Timpel, I. Pis, F. Bondino, K. Moudgil, S. Barlow, S. R. Marder, and N. Koch, "Effective Work Function Reduction of Practical Electrodes Using an Organometallic Dimer," *Adv. Funct. Mater.*, vol. 26, no. 15, pp. 2493–2502, Mar. 2016.

[35] W. Osikowicz, X. Crispin, C. Tengstedt, L. Lindell, T. Kugler, and W. R. Salaneck, "Transparent low-work-function indium tin oxide electrode obtained by molecular scale interface engineering," *Appl. Phys. Lett.*, vol. 85, no. 9, pp. 1616–1618, 2004.

[36] A. J. Giordano, F. Pulvirenti, T. M. Khan, C. Fuentes-Hernandez, K. Moudgil, J. H. Delcamp, B. Kippelen, S. Barlow, and S. R. Marder, "Organometallic dimers: application to work-function reduction of conducting oxides.," *ACS Appl. Mater. Interfaces*, vol. 7, no. 7, pp. 4320–6, Feb. 2015.

[37] R. Schlesinger, F. Bianchi, S. Blumstengel, C. Christodoulou, R. Ovsyannikov, B. Kobin, K. Moudgil, S. Barlow, S. Hecht, S. R. Marder, F. Henneberger, and N. Koch, "Efficient light emission from inorganic and organic semiconductor hybrid structures by energy-level tuning.," *Nat. Commun.*, vol. 6, p. 6754, Jan. 2015.

[38] S.-H. Liao, H.-J. Jhuo, P.-N. Yeh, Y.-S. Cheng, Y.-L. Li, Y.-H. Lee, S. Sharma, and S.-A. Chen, "Single junction inverted polymer solar cell reaching power conversion efficiency 10.31% by employing dual-doped zinc oxide nano-film as cathode interlayer.," *Sci. Rep.*, vol. 4, p. 6813, Jan. 2014.

[39] S. Guo, S. K. Mohapatra, A. Romanov, T. V Timofeeva, K. I. Hardcastle, K. Yesudas, C. Risko, J.-L. Brédas, S. R. Marder, and S. Barlow, "n-Doping of organic electronic materials using air-stable organometallics: a mechanistic study of reduction by dimeric sandwich compounds.," *Chem. Eur. J.*, vol. 18, no. 46, pp. 14760–72, Nov. 2012.

[40] O. V. Gusev, L. I. Denisovich, M. G. Peterleitner, A. Z. Rubezhov, N. A. Ustynyuk, and P. M. Maitlis, "Electrochemical generation of 19- and 20-electron rhodocenium complexes and their properties," *J. Organomet. Chem.*, vol. 452, no. 1–2, pp. 219–222, Jun. 1993.

[41] S. K. Mohapatra, A. Fonari, C. Risko, K. Yesudas, K. Moudgil, J. H. Delcamp, T. V Timofeeva, J.-L. Brédas, S. R. Marder, and S. Barlow, "Dimers of nineteen-electron sandwich compounds: crystal and electronic structures, and comparison of reducing strengths.," *Chem. Eur. J.*, vol. 20, no. 47, pp. 15385–94, Nov. 2014.

[42] Y. Qi, S. K. Mohapatra, S. Bok Kim, S. Barlow, S. R. Marder, and A. Kahn, "Solution doping of organic semiconductors using air-stable n-dopants," *Appl. Phys. Lett.*, vol. 100, p. 083305, 2012.

[43] A. Higgins, S. K. Mohapatra, S. Barlow, S. R. Marder, and A. Kahn, "Dopant controlled trap-filling and conductivity enhancement in an electron-transport polymer," *Appl. Phys. Lett.*, vol. 106, no. 16, p. 163301, Apr. 2015.

[44] R. F. K. Herzog and F. P. Viehböck, "Ion Source for Mass Spectrography," *Phys. Rev.*, vol. 76, no. 6, pp. 855–856, Sep. 1949.

[45] R. E. Honig, "Sputtering of Surfaces by Positive Ion Beams of Low Energy," *J. Appl. Phys.*, vol. 29, no. 3, p. 549, Jun. 1958.

[46] J. J. Thomson, “LXXXIII. Rays of positive electricity,” *Philos. Mag. Ser. 6*, vol. 20, no. 118, pp. 752–767, Oct. 1910.

[47] J.-N. Audinot, P. Lévêque, R. Bechara, N. Leclerc, J. Guillot, H.-N. Migeon, G. Hadziioannou, and T. Heiser, “Characterization of P3HT/PCBM bulk heterojunction photovoltaic devices using advanced secondary ion mass spectrometry techniques,” *Surf. Interface Anal.*, vol. 42, no. 6–7, pp. 1010–1013, Mar. 2010.

[48] H. Haneda, “A study of defect structures in oxide materials by secondary ion mass spectrometry,” *Appl. Surf. Sci.*, vol. 203–204, pp. 625–629, Jan. 2003.

[49] A. Laufer, N. Volbers, S. Eisermann, K. Potzger, S. Geburt, C. Ronning, and B. K. Meyer, “Determination of secondary ion mass spectrometry relative sensitivity factors for polar and non-polar ZnO,” *J. Appl. Phys.*, vol. 110, no. 9, p. 094906, Nov. 2011.

[50] N. Saito, H. Haneda, M. Komatsu, and K. Koumoto, “Time-of-Flight Secondary Ion Mass Spectrometry Study of Zinc Oxide Micropatterning on Self-Assembled Monolayer Template,” *J. Electrochem. Soc.*, vol. 153, no. 3, p. C170, Mar. 2006.

[51] F. Stevie, *Secondary Ion Mass Spectrometry: Applications for Depth Profiling and Surface Characterization*. Momentum Press, 2015.

[52] S. A. Paniagua, E. L. Li, and S. R. Marder, “Adsorption studies of a phosphonic acid on ITO: film coverage, purity, and induced electronic structure changes.,” *Phys. Chem. Chem. Phys.*, vol. 16, no. 7, pp. 2874–81, Feb. 2014.

[53] M. P. Seah and W. A. Dench, “Quantitative electron spectroscopy of surfaces: A standard data base for electron inelastic mean free paths in solids,” *Surf. Interface Anal.*, vol. 1, no. 1, pp. 2–11, Feb. 1979.

[54] S. A. Paniagua, J. Baltazar, H. Sojoudi, S. K. Mohapatra, S. Zhang, C. L. Henderson, S. Graham, S. Barlow, and S. R. Marder, “Production of heavily n- and p-doped CVD graphene with solution-processed redox-active metal–organic species,” *Mater. Horiz.*, vol. 1, no. 1, pp. 111–115, Nov. 2014.

[55] M. Gruenewald, L. K. Schirra, P. Winget, M. Kozlik, P. F. Ndione, A. K. Sigdel, J. J. Berry, R. Forker, J.-L. Brédas, T. Fritz, and O. L. A. Monti, “Integer Charge Transfer and Hybridization at an Organic Semiconductor/Conductive Oxide

Interface," *J. Phys. Chem. C*, vol. 119, no. 9, pp. 4865–4873, Mar. 2015.

[56] H. Li, L. K. Schirra, J. Shim, H. Cheun, B. Kippelen, O. L. A. Monti, and J.-L. Bredas, "Zinc Oxide as a Model Transparent Conducting Oxide: A Theoretical and Experimental Study of the Impact of Hydroxylation, Vacancies, Interstitials, and Extrinsic Doping on the Electronic Properties of the Polar ZnO (0002) Surface," *Chem. Mater.*, vol. 24, no. 15, pp. 3044–3055, Aug. 2012.

[57] P. Winget, L. K. Schirra, D. Cornil, H. Li, V. Coropceanu, P. F. Ndione, A. K. Sigdel, D. S. Ginley, J. J. Berry, J. Shim, H. Kim, B. Kippelen, J.-L. Brédas, and O. L. A. Monti, "Defect-driven interfacial electronic structures at an organic/metal-oxide semiconductor heterojunction.," *Adv. Mater.*, vol. 26, no. 27, pp. 4711–6, Jul. 2014.

[58] A. F. Stassen, R. W. I. de Boer, N. N. Iosad, and A. F. Morpurgo, "Influence of the gate dielectric on the mobility of rubrene single-crystal field-effect transistors," *Appl. Phys. Lett.*, vol. 85, no. 17, p. 3899, Oct. 2004.

[59] H.-C. Chen, S.-W. Lin, J.-M. Jiang, Y.-W. Su, and K.-H. Wei, "Solution-processed zinc oxide/polyethylenimine nanocomposites as tunable electron transport layers for highly efficient bulk heterojunction polymer solar cells.," *ACS Appl. Mater. Interfaces*, vol. 7, no. 11, pp. 6273–81, Mar. 2015.

[60] M. Caglar, S. Ilican, Y. Caglar, and F. Yakuphanoglu, "Electrical conductivity and optical properties of ZnO nanostructured thin film," *Appl. Surf. Sci.*, vol. 255, no. 8, pp. 4491–4496, Feb. 2009.

[61] D. C. Reynolds, D. C. Look, and B. Jogai, "Fine structure on the green band in ZnO," *J. Appl. Phys.*, vol. 89, no. 11, p. 6189, May 2001.

[62] S. Chen, C. E. Small, C. M. Amb, J. Subbiah, T. Lai, S.-W. Tsang, J. R. Manders, J. R. Reynolds, and F. So, "Inverted Polymer Solar Cells with Reduced Interface Recombination," *Adv. Energy Mater.*, vol. 2, no. 11, pp. 1333–1337, Nov. 2012.

[63] H. Chen, S. Gu, K. Tang, S. Zhu, Z. Zhu, J. Ye, R. Zhang, and Y. Zheng, "Origins of green band emission in high-temperature annealed N-doped ZnO," *J. Lumin.*, vol. 131, no. 6, pp. 1189–1192, Jun. 2011.

[64] D. C. Reynolds, D. C. Look, B. Jogai, and H. Morkoç, "Similarities in the bandedge and deep-centre photoluminescence mechanisms of ZnO and GaN," *Solid State*

Commun., vol. 101, no. 9, pp. 643–646, Mar. 1997.

[65] D. C. Reynolds, D. C. Look, B. Jogai, J. E. Van Nostrand, R. Jones, and J. Jenny, "Source of the yellow luminescence band in GaN grown by gas-source molecular beam epitaxy and the green luminescence band in single crystal ZnO," *Solid State Commun.*, vol. 106, no. 10, pp. 701–704, Apr. 1998.

[66] B. Lin, Z. Fu, and Y. Jia, "Green luminescent center in undoped zinc oxide films deposited on silicon substrates," *Appl. Phys. Lett.*, vol. 79, no. 7, p. 943, Aug. 2001.

[67] T. Makino, Y. Segawa, S. Yoshida, A. Tsukazaki, A. Ohtomo, and M. Kawasaki, "Gallium concentration dependence of room-temperature near-band-edge luminescence in n-type ZnO:Ga," *Appl. Phys. Lett.*, vol. 85, no. 5, p. 759, Jun. 2004.

[68] C. Liu, K. Wang, X. Hu, Y. Yang, C. H. Hsu, W. Zhang, S. Xiao, X. Gong, and Y. Cao, "Molecular weight effect on the efficiency of polymer solar cells," *ACS Appl. Mater. Interfaces*, vol. 5, no. 22, pp. 12163–12167, 2013.

[69] L. Lu, T. Zheng, Q. Wu, A. M. Schneider, D. Zhao, and L. Yu, "Recent Advances in Bulk Heterojunction Polymer Solar Cells," *Chem. Rev.*, vol. 115, no. 23, pp. 12666–12731, 2015.

[70] Z. He, C. Zhong, S. Su, M. Xu, H. Wu, and Y. Cao, "Enhanced power-conversion efficiency in polymer solar cells using an inverted device structure," *Nat. Photonics*, vol. 6, no. September, pp. 593–597, 2012.

[71] K.-D. Kim, D. C. Lim, J. Hu, J.-D. Kwon, M.-G. Jeong, H. O. Seo, J. Y. Lee, K.-Y. Jang, J.-H. Lim, K. H. Lee, Y. Jeong, Y. D. Kim, and S. Cho, "Surface modification of a ZnO electron-collecting layer using atomic layer deposition to fabricate high-performing inverted organic photovoltaics.," *ACS Appl. Mater. Interfaces*, vol. 5, no. 17, pp. 8718–23, Sep. 2013.

[72] S. Nho, G. Baek, S. Park, B. R. Lee, M. J. Cha, D. C. Lim, J. H. Seo, S.-H. Oh, M. H. Song, and S. Cho, "Highly efficient inverted bulk-heterojunction solar cells with a gradiently-doped ZnO layer," *Energy Environ. Sci.*, Nov. 2016.

CHAPTER 6 **CONCLUSION AND OUTLOOK**

6.1 Overview

The field of organic photovoltaics has been moving incredibly fast; during the years that the work in this thesis was completed, it has expanded to include new techniques, such as the widespread use of solvent additives, and new materials, such new heteropolymer donors and non-fullerene acceptors, with constant challenges to the contemporary understanding of the photophysical processes involved and of desired microstructures, and, ultimately, to its potential as competitive source of alternative energy. In mid-2010 the record efficiency was 8.1%;[1] now power conversion efficiencies have exceeded 10%,[2–8] long considered to be the barrier to industrial applications of the technology and, despite Konarka's bankruptcy in 2012, dozens of companies are working on OPV modules, the earliest of which, Mitsubishi Chemical's Solar Windows, are due to be released in late 2016.[9] New developments regarding the topics of OPV morphological control, non-fullerene acceptors, and electrical doping, which are relevant to this thesis, have also emerged.

This thesis has explored the introduction of additives with the intention of addressing key barriers to electronic transport in organic photovoltaics, including the anisotropicity of non-fullerene acceptor charge-transport in BHJ active layers, trap states in hole-transporting polymers, and the low order and purity of solution-processed interlayer oxides. The employment of these additives often had an effect on the morphology and

microstructure of the active layer; these effects and their influence on the success of the work were characterized. The purpose of this section will be to review the conclusions, and accomplishments, in the previous chapters from the perspective of the OPV field, as well as their limitations and some ideas for future improvements.

6.2 Non-fullerene Acceptors in Organic Photovoltaics

In Chapter 2, the poor performance of planar molecular perylene diimide (PDI) derivative acceptors was discussed.[10–12] As a result of their planarity and rigidity, many organic small-molecule semiconductors such as these tend to phase segregate[10] and exhibit anisotropic charge transport,[13–17] which in OPV BHJs leads to inadequate pathways for charge carrier transport to the electrodes. The attempted solution was the incorporation of two PDI-derived acceptors, a small molecule and a polymer, into a ternary blend with the well-studied P3HT; the hypothesis being that the polymer would provide suitable electron pathways to the electrode and thus increase the probability of leaving the active layer and reaching the appropriate electrodes.

Though the materials demonstrated compelling blending behavior, as evidenced by DSC, ternary organic photovoltaic devices prepared with P3HT, the small-molecule PDI, and the polymer did not produce efficient OPV devices, indicating that the original hypothesis was overly simplistic. Devices of P3HT with the polymer PDI gave acceptable performances, ca. 0.7% PCE, for all-polymer OPV active layers at the time, but incorporation of the small-molecule PDI into these active layers led to a reduction in device performance via V_{OC} and *FF*. To understand these performance decreases, a morphological

study was conducted with AFM, DSC, and GIXRD, which offered evidence that the small-molecule and polymer PDIs, originally selected for their miscibility, were blending together to form a new, near homogeneous phase. Square wave voltammetry demonstrated that an as-cast blended acceptor film shared a first reduction onset with the pure polymer PDI, but annealing the film resulted in a cathodic shift of this onset, which could coincide with an interruption of the polymer's intermolecular electronic coupling. This hypothesis was supported by a significant drop in the charge mobility of the acceptor phase observed by TOF mobility upon blending of the two acceptors.

V_{OC} and *FF* are affected by a number of properties, such as the carrier generation/recombination rate at the donor/acceptor interface and transport through what should typically be pure domains. Efficient charge separation in P3HT:PDI blends has been established by Shoaee *et al.* using transient absorption spectroscopy;[10] future work could include similar experiments for the blends in this work, to determine more conclusively if the hampered charge transport is facilitating a bimolecular recombination process. As many of the materials employed in modern organic photovoltaics now have fairly low short-range order,[18–24] an understanding of the carrier transport of blended amorphous phases could lead to superior molecular design and film-processing methods.

As a result of the incorporation of complex heterocycles and branched side-chains, modern donor polymers have moved away from a reliance on short-range, π-π stacking order for effective charge transport in BHJs, and it has been suggested that charges are primarily transported along the backbone.[25–29] Along with this decrease in the short-range order of donor materials, non-fullerene acceptors have returned to prominence with PCEs over 11%, rivaling fullerene-based devices.[8,30–34] To achieve isotropic carrier transport

through the BHJ, these small molecules exhibit non-planar, twisted structures to suppress the tendency to form well-ordered, segregated domains. However, as a result they have somewhat lower electron mobilities, ca. 10^{-4} cm^2 V^{-1} s^{-1} by SCLC. Conversely, high mobility naphthalene diimide-based acceptor polymers have also been used with newer donor heteropolymers to achieve efficiencies up to 7.7%, their main issue being poor absorbance compatibility, reducing effective overlap of the solar spectrum.[35–38] Future work could include the incorporation of rylene-based polymers into OPV BHJs composed of newer donor heteropolymers, such as PTB7-Th, and these twisted acceptors, to take advantage of their high mobility backbone-based transport, provided they can be processed in such a way as to reduce phase blending with the other materials.

6.3 Electrical Dopants in Organic Photovoltaic Devices

Chapters 3 and 4 explored the use of ultra-low concentrations of p-dopants in OPV active layers in an effort to passivate in-gap trap states that hinder hole transport in OPV BHJs. In Chapter 3, trap passivation in doped P3HT thin films was identified by conductivity & photoelectron spectroscopy measurements. However, this effect did not lead to an improvement in OPV performance of doped P3HT in BHJ active layers with $PC_{61}BM$, instead lowering performance. To understand this result, TEM, AFM, UV-vis absorbance modelling, GIWAXS, and RBS were performed, and offered evidence that the dopant was aggregating in amorphous regions, with increasing dopant loading leading to increasingly large and well-separated aggregates. There was no compelling evidence of dopant diffusion into P3HT crystalline phases, where hole transport is thought to occur.

The non-uniform in-plane and out-of-plane distribution of the dopants was seen to interrupt the long-range order of P3HT phases by AFM, and possibly manifests itself in over-doped pockets that increase energetic disorder inside the active layer, resulting in the decrease in device performance. It was concluded that the use of these somewhat large (ca. 1 nm diameter), nonplanar dopants could consistently lead to significant complications in well-ordered systems.

For this reason, p-doping was attempted in two polymers known to exhibit low short-range order: PTB7 and PCDTBT. Evidence of trap passivation in these two low-order heteropolymers upon the introduction of molecular dopants was established again by conductivity and photoelectron spectroscopy, however the implementation of these polymer/dopant systems in OPV active layers with $PC_{71}BM$ yielded an improvement in the J_{SC}, increasing over 20% for devices with PTB7:$PC_{71}BM$ active layers. The photocurrent growth was also identified in the IPCE, in which quantum efficiency increases for high wavelength photons, as well as a red-shift of the low energy tail, were observed. However, sufficiently high dopant concentrations, ca. 1 wt. % dopant and greater, led to a decrease in *FF* and V_{OC}, which could potentially be due to increased carrier concentrations.[39] Structures of thin film microstructure, carried out by AFM and GIWAXS, did not offer any evidence of dopant aggregation or interruptions of polymer morphology. Thus, the hypothesis of this chapter was realized, ultra-low p-doping of OPV active layers resulted in PCE and J_{SC} increases in attempted material systems exhibiting low short-range order; this approach has the potential to be applicable in other bulk heterojunction films with low-order organic materials.

Despite the photocurrent improvements observed in chapter 4, the reduction in *FF* remains to be explained. A possible hypothesis involves changes in film thickness and refractive index upon additive introduction. Such an effect, although not substantialized by profilometry or other methods, could account for the observed evolution of the IPCE and the lower fill factors. However, several facts would oppose this theory as the sole mechanism of OPV performance evolution. The performance improvements of doped PCDTBT:$PC_{71}BM$ devices has been shown to be linked to the electron affinity of the applied dopant, and the photocurrents in the PTB7:$PC_{71}BM$ devices exceed those in literature exhibiting the same device structure. It is therefore more likely that the results are a product of several effects, including trap passivation, refractive index and thickness changes, and even morphological changes and new recombination pathways due to localized increased carrier densities, that could be related to inhomogeneous dopant distributions beyond the sensitivity of the performed experiments. Deconvoluting the effects of the many properties that could be altered by dopant introduction could be the focus of future work, such as attempting to adjust processing conditions to negate film thickness changes or the introduction of non-dopant additives to alter the refractive index, although such an endeavor might not be straightforward for the imperfect systems being studied.

Based on the improvements produced in Chapter 4, there are a number of other low-order polymers that ultra-low doping could be applied to, such as those in the poly(benzodithiophene-co-thienothiophene) and poly(dithienobenzodithiophene-co-benzodithiophenedione) families,[7,40] which generate high efficiencies with a range of acceptors, to determine if the success of this technique is truly order-limited. Low n-dopant

concentrations could also then be used to passivate electron traps in BHJs with fullerenes and the aforementioned new rylene-based acceptor small molecules and polymers, which tend to exhibit low short-range order due to their non-planarity. Finally, this method of trap passivation can be applied to other types of photovoltaic materials, such as perovskites and quantum-dot PVs, work that is currently being explored with our collaborators, reinforcing the impactful applicability of molecular dopants in solution-processed PVs as a whole.

6.4 Amorphous Oxide Interlayers in Organic Photovoltaics

Chapter 5 focused on the incorporation of a dimeric molecular n-dopant $[RhCp^*Cp]_2$ at various concentrations into thin amorphous ZnO films, solution-processed from sol-gels at low-temperatures, in an attempt to negate charge-transport and reproducibility issues that originate from large defect concentrations. The introduction of this dopant resulted in an improvement OPV efficiency, using the ZnO as an interlayer in an inverted device, through the short-circuit current density, which was reflected in the IPCE, but only for lower dopant concentrations. Increased conductivity and large shifts in work function were found with high concentrations of incorporated dopant, but it was not these properties that lead to a better OPV in this minimally processed system. XPS revealed a progression in the ZnO composition, manifesting in a change in the apparent O/Zn ratio, correlated to changes in the Zn and/or O vacancy populations as indicated by photoluminescence experiments, which have been shown to decrease charge trapping at the oxide/organic interface of OPVs.

Though this methodology of dopant introduction was based on the thermal stability of organic compounds under the processing conditions, the possibly of reactions between the dopant and the solvent, 2-methoxyethanol, or sol-gel components is still possible. Unfortunately, these sol-gels are typically cast from an alcohol which, if acidic, can lead to dopant degradation via numerous pathways. Thus the nature of the rhodocene derivative in the solution and in the forming oxide, and its effect upon sol-gel processing and oxide growth, are not currently known. However, since this work was initiated, other methods for ZnO manipulation via the introduction of organic species, such as fullerene derivatives, decamethylcobaltocene, and 1H-benzoimidazole, have emerged; yet, these have not shown OPV efficiencies as high as those included in this work,[41,42] and ZnO layers incorporating cobaltocene did not lead to OPV efficiency increases when fabricated in the present work, indicating that correlations between dopant reductive strength, additive behavior and film formation still need to be established.

In future work, the origin of the achieved ZnO compositional control in Chapter 5, as well as the nature of the rhodocene derivative within the solution, sol-gel, or oxide can be probed; further detailed studies of low-temperature solution-processed oxide formation are required, ideally observing particle formation and growth with in-situ absorbance and X-ray scattering, to properly understand how the introduced molecules are manipulating film properties. Such an understanding may afford greater control of atomic ratios and vacancy/interstitial sites in this and other low-temperature sol-gel oxide interlayers, such as titanium, molybdenum, and vanadium oxides. Finally, this ZnO modification technique exhibits the potential for universality in low-temperature sol-gel preparations, as it has led to improvements in two differing formulations of ZnO films and for different

donor/acceptor blends, reaching a maximum PCE of 9.4% for PTB7:$PC_{71}BM$, exceeding the current record for ZnO ETLs in inverted devices employing this active layer.[19,41] Beyond OPVs, these techniques should be applied to other types of photovoltaic devices that implement these types of interlayers, including again perovskites and quantum-dots, to explore if and for what reasons these effects might be limited to OPV devices.

6.5 Outlook

Conclusively, this thesis has studied the incorporation of additives into systems that contained a number of impurities and imperfections previous to their addition. While the imperfection of these systems contributes to their appeal, as low-energy and facile processing conditions are attractive for the eventual scale-up of organic solar cells, it has increased the difficulty of determining the influence of the additives and their correlation to material properties, as well as separating intended effects, such as electronic doping, from unintended effects, such as refractive index or compositional alteration. Performance improvements have been observed in certain systems, which can have industrial applications if their universality is established in additional material systems, as has been mentioned in previous sections. Though the electronic and morphological properties of these systems have been thoroughly studied, the connection of efficiency improvements to intended electrical doping has yet to be firmly established, and will require additional studies. With such work, a greater command of the properties in these imperfect systems may be realized which, at this time, seems to be a barrier that must be overcome in the commercialization of these organic semiconductor devices.

6.6 Works Cited

[1] "Solarmer achieves 8.13 percent OPV efficiency," *PV Magazine*, 2010. [Online]. Available: http://www.pv-magazine.com/news/details/beitrag/solarmer-achieves-813-percent-opv-efficiency_100000604/#axzz4AFxnldNj. [Accessed: 31-May-2016].

[2] L. K. Jagadamma, M. Al-Senani, A. El-Labban, I. Gereige, G. O. Ngongang Ndjawa, J. C. D. Faria, T. Kim, K. Zhao, F. Cruciani, D. H. Anjum, M. A. McLachlan, P. M. Beaujuge, and A. Amassian, "Polymer Solar Cells with Efficiency >10% Enabled via a Facile Solution-Processed Al-Doped ZnO Electron Transporting Layer," *Adv. Energy Mater.*, vol. 5, no. 12, p. 1500204, Apr. 2015.

[3] S.-H. Liao, H.-J. Jhuo, P.-N. Yeh, Y.-S. Cheng, Y.-L. Li, Y.-H. Lee, S. Sharma, and S.-A. Chen, "Single junction inverted polymer solar cell reaching power conversion efficiency 10.31% by employing dual-doped zinc oxide nano-film as cathode interlayer.," *Sci. Rep.*, vol. 4, p. 6813, Jan. 2014.

[4] J. Zhao, Y. Li, G. Yang, K. Jiang, H. Lin, H. Ade, W. Ma, and H. Yan, "Efficient organic solar cells processed from hydrocarbon solvents.," *Nat. Energy*, vol. 1, no. 2, p. 15027, Feb. 2016.

[5] L. Lu, T. Zheng, Q. Wu, A. M. Schneider, D. Zhao, and L. Yu, "Recent Advances in Bulk Heterojunction Polymer Solar Cells," *Chem. Rev.*, vol. 115, no. 23, pp. 12666–12731, 2015.

[6] S. Nho, G. Baek, S. Park, B. R. Lee, M. J. Cha, D. C. Lim, J. H. Seo, S.-H. Oh, M. H. Song, and S. Cho, "Highly efficient inverted bulk-heterojunction solar cells with a gradiently-doped ZnO layer," *Energy Environ. Sci.*, Nov. 2016.

[7] S. Zhang, L. Ye, and J. Hou, "Breaking the 10% Efficiency Barrier in Organic Photovoltaics: Morphology and Device Optimization of Well-Known PBDTTT Polymers," *Adv. Energy Mater.*, p. n/a–n/a, Mar. 2016.

[8] W. Zhao, D. Qian, S. Zhang, S. Li, O. Inganäs, F. Gao, and J. Hou, "Fullerene-Free Polymer Solar Cells with over 11% Efficiency and Excellent Thermal Stability.," *Adv. Mater.*, Apr. 2016.

[9] "New power source: Mitsubishi Chem, 3M team on solar cell window films for

buildings- Nikkei Asian Review," *Nikko AM*, 2015. [Online]. Available: http://asia.nikkei.com/Business/Companies/Mitsubishi-Chem-3M-team-on-solar-cell-window-films-for-buildings. [Accessed: 28-May-2016].

[10] S. Shoaee, T. M. Clarke, C. Huang, S. Barlow, S. R. Marder, M. Heeney, I. McCulloch, and J. R. Durrant, "Acceptor energy level control of charge photogeneration in organic donor/acceptor blends.," *J. Am. Chem. Soc.*, vol. 132, no. 37, pp. 12919–26, Sep. 2010.

[11] W. S. Shin, H.-H. Jeong, M.-K. Kim, S.-H. Jin, M.-R. Kim, J.-K. Lee, J. W. Lee, and Y.-S. Gal, "Effects of functional groups at perylene diimide derivatives on organic photovoltaic device application," *J. Mater. Chem.*, vol. 16, no. 4, pp. 384–390, Jan. 2006.

[12] J. E. Anthony, "Small-Molecule, Nonfullerene Acceptors for Polymer Bulk Heterojunction Organic Photovoltaics," *Chem. Mater.*, vol. 23, no. 3, pp. 583–590, Feb. 2011.

[13] V. Coropceanu, J. Cornil, D. A. da Silva Filho, Y. Olivier, R. Silbey, and J.-L. Brédas, "Charge transport in organic semiconductors.," *Chem. Rev.*, vol. 107, no. 4, pp. 926–52, Apr. 2007.

[14] K. Han, J. Huang, S. Chai, S. Wen, and W. Deng, "Anisotropic Mobilities in Organic Semiconductors," *Protoc. Exch.*, p. doi:10.103/protex.2013.070, 2013.

[15] V. Stehr, J. Pfister, R. F. Fink, B. Engels, and C. Deibel, "First-principles calculations of anisotropic charge-carrier mobilities in organic semiconductor crystals," *Phys. Rev. B*, vol. 83, no. 15, p. 155208, Apr. 2011.

[16] W. Hourani, K. Rahimi, I. Botiz, F. P. V. Koch, G. Reiter, P. Lienerth, T. Heiser, J.-L. Bubendorff, and L. Simon, "Anisotropic charge transport in large single crystals of π-conjugated organic molecules.," *Nanoscale*, vol. 6, no. 9, pp. 4774–80, May 2014.

[17] B. Fraboni, R. DiPietro, A. Castaldini, A. Cavallini, A. Fraleoni-Morgera, L. Setti, I. Mencarelli, and C. Femoni, "Anisotropic charge transport in organic single crystals based on dipolar molecules," *Org. Electron.*, vol. 9, no. 6, pp. 974–978, Dec. 2008.

[18] N. Blouin, A. Michaud, and M. Leclerc, "A Low-Bandgap Poly(2,7-Carbazole)

Derivative for Use in High-Performance Solar Cells," *Adv. Mater.*, vol. 19, no. 17, pp. 2295–2300, Sep. 2007.

[19] Z. He, C. Zhong, S. Su, M. Xu, H. Wu, and Y. Cao, "Enhanced power-conversion efficiency in polymer solar cells using an inverted device structure," *Nat. Photonics*, vol. 6, no. September, pp. 593–597, 2012.

[20] Y. Liang, Z. Xu, J. Xia, S.-T. Tsai, Y. Wu, G. Li, C. Ray, and L. Yu, "For the bright future-bulk heterojunction polymer solar cells with power conversion efficiency of 7.4%.," *Adv. Mater.*, vol. 22, no. 20, pp. E135–8, May 2010.

[21] M. P. Paranthaman, W. Wong-Ng, and R. N. Bhattacharya, *Semiconductor Materials for Solar Photovoltaic Cells*. Springer, 2015.

[22] D. H. Wang, J. K. Kim, J. H. Seo, I. Park, B. H. Hong, J. H. Park, and A. J. Heeger, "Transferable graphene oxide by stamping nanotechnology: electron-transport layer for efficient bulk-heterojunction solar cells.," *Angew. Chem. Int. Ed. Engl.*, vol. 52, no. 10, pp. 2874–80, Mar. 2013.

[23] L. Ye, S. Zhang, W. Zhao, H. Yao, and J. Hou, "Highly Efficient 2D-Conjugated Benzodithiophene-Based Photovoltaic Polymer with Linear Alkylthio Side Chain," *Chem. Mater.*, vol. 26, no. 12, pp. 3603–3605, Jun. 2014.

[24] J. Zhao, Y. Li, G. Yang, K. Jiang, H. Lin, H. Ade, W. Ma, and H. Yan, "Efficient organic solar cells processed from hydrocarbon solvents," *Nat. Energy*, vol. 1, no. 2, p. 15027, Jan. 2016.

[25] R. Noriega, A. Salleo, and A. J. Spakowitz, "Chain conformations dictate multiscale charge transport phenomena in disordered semiconducting polymers.," *Proc. Natl. Acad. Sci. U. S. A.*, vol. 110, no. 41, pp. 16315–20, Oct. 2013.

[26] V. Skrypnychuk, G.-J. A. H. Wetzelaer, P. I. Gordiichuk, S. C. B. Mannsfeld, A. Herrmann, M. F. Toney, and D. R. Barbero, "Ultrahigh Mobility in an Organic Semiconductor by Vertical Chain Alignment," *Adv. Mater.*, vol. 28, no. 12, p. 10.1002/adma.201503422, Jan. 2016.

[27] D. Venkateshvaran, M. Nikolka, A. Sadhanala, V. Lemaur, M. Zelazny, M. Kepa, M. Hurhangee, A. J. Kronemeijer, V. Pecunia, I. Nasrallah, I. Romanov, K. Broch, I. McCulloch, D. Emin, Y. Olivier, J. Cornil, D. Beljonne, and H. Sirringhaus, "Approaching disorder-free transport in high-mobility conjugated polymers,"

Nature, vol. 515, no. 7527, pp. 384–388, Nov. 2014.

[28] W. Zhang, Y. Han, X. Zhu, Z. Fei, Y. Feng, N. D. Treat, H. Faber, N. Stingelin, I. McCulloch, T. D. Anthopoulos, and M. Heeney, "A Novel Alkylated Indacenodithieno[3,2-b]thiophene-Based Polymer for High-Performance Field-Effect Transistors.," *Adv. Mater.*, Oct. 2015.

[29] X. Zhang, H. Bronstein, A. J. Kronemeijer, J. Smith, Y. Kim, R. J. Kline, L. J. Richter, T. D. Anthopoulos, H. Sirringhaus, K. Song, M. Heeney, W. Zhang, I. McCulloch, and D. M. DeLongchamp, "Molecular origin of high field-effect mobility in an indacenodithiophene-benzothiadiazole copolymer.," *Nat. Commun.*, vol. 4, p. 2238, Jan. 2013.

[30] K. Cnops, G. Zango, J. Genoe, P. Heremans, M. V. Martinez-Diaz, T. Torres, and D. Cheyns, "Energy Level Tuning of Non-Fullerene Acceptors in Organic Solar Cells," *J. Am. Chem. Soc.*, vol. 137, no. 28, pp. 8991–8997, Jul. 2015.

[31] O. K. Kwon, M. A. Uddin, J.-H. Park, S. K. S. Y. Park, T. L. Nguyen, H. Y. Woo, and S. K. S. Y. Park, "A High Efficiency Nonfullerene Organic Solar Cell with Optimized Crystalline Organizations.," *Adv. Mater.*, vol. 28, no. 5, pp. 910–6, Feb. 2016.

[32] Y. Lin and X. Zhan, "Non-fullerene acceptors for organic photovoltaics: an emerging horizon," *Mater. Horizons*, vol. 1, no. 5, p. 470, Apr. 2014.

[33] Y. Lin, F. Zhao, Q. He, L. Huo, Y. Wu, T. C. Parker, W. Ma, Y. Sun, C. Wang, D. Zhu, A. J. Heeger, S. R. Marder, and X. Zhan, "High-Performance Electron Acceptor with Thienyl Side Chains for Organic Photovoltaics.," *J. Am. Chem. Soc.*, vol. 138, no. 14, pp. 4955–61, Apr. 2016.

[34] C. B. Nielsen, S. Holliday, H.-Y. Chen, S. J. Cryer, and I. McCulloch, "Non-fullerene electron acceptors for use in organic solar cells.," *Acc. Chem. Res.*, vol. 48, no. 11, pp. 2803–12, Nov. 2015.

[35] Y.-J. Hwang, B. A. E. Courtright, A. S. Ferreira, S. H. Tolbert, and S. A. Jenekhe, "7.7% Efficient All-Polymer Solar Cells.," *Adv. Mater.*, vol. 27, no. 31, pp. 4578–84, Aug. 2015.

[36] J. W. Jung, J. W. Jo, C.-C. Chueh, F. Liu, W. H. Jo, T. P. Russell, and A. K.-Y. Jen, "Fluoro-Substituted n-Type Conjugated Polymers for Additive-Free All-Polymer

Bulk Heterojunction Solar Cells with High Power Conversion Efficiency of 6.71.," *Adv. Mater.*, vol. 27, no. 21, pp. 3310–7, Jun. 2015.

[37] C. Lee, H. Kang, W. Lee, T. Kim, K.-H. Kim, H. Y. Woo, C. Wang, and B. J. Kim, "High-performance all-polymer solar cells via side-chain engineering of the polymer acceptor: the importance of the polymer packing structure and the nanoscale blend morphology.," *Adv. Mater.*, vol. 27, no. 15, pp. 2466–71, Apr. 2015.

[38] D. Mori, H. Benten, I. Okada, H. Ohkita, and S. Ito, "Highly efficient charge-carrier generation and collection in polymer/polymer blend solar cells with a power conversion efficiency of 5.7%," *Energy Environ. Sci.*, vol. 7, no. 9, p. 2939, Jun. 2014.

[39] G. Lakhwani, A. Rao, and R. H. Friend, "Bimolecular recombination in organic photovoltaics.," *Annu. Rev. Phys. Chem.*, vol. 65, pp. 557–81, Jan. 2014.

[40] L. Huo, T. Liu, X. Sun, Y. Cai, A. J. Heeger, and Y. Sun, "Single-junction organic solar cells based on a novel wide-bandgap polymer with efficiency of 9.7%.," *Adv. Mater.*, vol. 27, no. 18, pp. 2938–44, May 2015.

[41] T. Hu, L. Chen, K. Yuan, and Y. Chen, "Amphiphilic fullerene/ZnO hybrids as cathode buffer layers to improve charge selectivity of inverted polymer solar cells.," *Nanoscale*, vol. 7, no. 20, pp. 9194–203, May 2015.

[42] S. P. Schießl, H. Faber, Y.-H. Lin, S. Rossbauer, Q. Wang, K. Zhao, A. Amassian, J. Zaumseil, and T. D. Anthopoulos, "Hybrid Modulation-Doping of Solution-Processed Ultrathin Layers of ZnO Using Molecular Dopants.," *Adv. Mater.*, vol. 28, no. 20, pp. 3952–9, May 2016.